Titre: Title:	Hybrid integration of synthesized dielectric image waveguides in substrate integrated circuit technology and its millimeter wave applications
Auteur: Author:	Andreas Patrovsky
Date:	2008
Type:	Mémoire ou thèse / Dissertation or Thesis
Référence: Citation:	Patrovsky, A. (2008). Hybrid integration of synthesized dielectric image waveguides in substrate integrated circuit technology and its millimeter wave applications [Thèse de doctorat, École Polytechnique de Montréal]. PolyPublie. https://publications.polymtl.ca/8164/

UNIVERSITÉ DE MONTRÉAL

HYBRID INTEGRATION OF SYNTHESIZED DIELECTRIC IMAGE WAVEGUIDES IN SUBSTRATE INTEGRATED CIRCUIT TECHNOLOGY AND ITS MILLIMETER WAVE APPLICATIONS

ANDREAS PATROVSKY
DÉPARTEMENT DE GÉNIE ÉLECTRIQUE
ÉCOLE POLYTECHNIQUE DE MONTRÉAL

THÈSE PRÉSENTÉE EN VUE DE L'OBTENTION
DU DIPLÔME DE PHILOSOPHIÆ DOCTOR
(GÉNIE ÉLECTRIQUE)
MAI 2008

Your file Votre référence
ISBN: 978-0-494-46113-6
Our file Notre référence
ISBN: 978-0-494-46113-6

UNIVERSITÉ DE MONTRÉAL

ÉCOLE POLYTECHNIQUE DE MONTRÉAL

Cette thèse intitulée:

HYBRID INTEGRATION OF SYNTHESIZED DIELECTRIC IMAGE WAVEGUIDES IN SUBSTRATE INTEGRATED CIRCUIT TECHNOLOGY AND ITS MILLIMETER WAVE APPLICATIONS

présentée par: PATROVSKY Andreas

en vue de l'obtention du diplôme de: Philosophiæ Doctor

est présentée au jury d'examen constitué de:

M. BOSISIO Renato G., M.Sc.A, président

M. VOLAKIS John L., Ph.D., membre externe

M. TATU Serioja O., Ph.D., membre

M. WU Ke, Ph.D., membre et directeur de recherche

À ma famille et à Rosa.

ACKNOWLEDGMENT

First of all, I would like to express my gratitude to my PhD advisor, Dr. Ke Wu, who offered me support whenever I needed it. His passion for research, his persistence, and his innovative ideas gave me the drive and the motivation to explore new frontiers and to accomplish this thesis.

I would also like to thank all the personnel at the Poly-Grames Research Center, in particular Mr. Jules Gauthier, Mr. Steve Dubé, and Mr. Roch Brassard, whose technical assistance was essential for the realization of the prototypes. A special thanks is extended to Mrs. Ginette Desparois and Mrs. Nathalie Lévesque for guiding me through the administrative jungle and to Mr. Jean-Sébastien Décarie for assistance with computer trouble.

A special thanks goes to the members of the examination jury, who took their time to read the thesis and provided very valuable comments. I am especially grateful to Dr. John L. Volakis, who came the long way from Ohio, USA, and to Dr. Serioja O. Tatu, who postponed his vacation to be present at the oral examination.

I am also indebted to my student colleagues and friends for all the professional and personal advice, and to everybody who contributed directly or indirectly to this thesis.

Finally, I would like to extend my gratitude to my parents and my brother, who supported my decision to go abroad, to Rosa, for being by my side, and to all my friends with whom I spent a wonderful time here in Montreal.

RÉSUMÉ

L'avancement technologique permet de réduire les coûts des composants et des systèmes opérés dans la bande des ondes millimétriques du spectre électromagnétique. L'intégration est la clé pour abaisser les coûts et pour réaliser des dispositifs petits et légers. À cette fin, la technologie basée sur le guide d'ondes rectangulaire traditionnel est abandonnée en faveur de circuits planaires intégrés. Cependant, l'apparition de pertes importantes dans les lignes de transmission conventionnelles à fréquences élevées, comme par exemple la ligne microruban ou coplanaire (CPW), est un défi majeur. Pour cette raison, ces dernières sont souvent un choix inapproprié, parce que les pertes excessives dans la partie frontale d'un système à ondes millimétriques peuvent affecter considérablement sa performance.

Cette thèse se penche sur un nouveau type de guide d'ondes diélectrique, qui est synthétisé sur un substrat planaire par perforation des zones adjacentes à un canal de guidage au centre. Le guide résultant, nommé guide image intégré au substrat (SIIG), ne permet pas seulement la transmission efficace des ondes électromagnétiques comme le guide image conventionnel, mais satisfait également les exigences de coûts réduits et de facilité d'intégration. Un premier objectif était l'analyse détaillée des propriétés de propagation des différents modes existants, concernant l'atténuation, le comportement dispersif, la largeur de bande, les effets de fuite et l'impact des tolérances de fabrication. Pour ce faire, des techniques d'analyse spécifiquement adaptées sont présentées, car les méthodes établies pour le guide image standard ne peuvent pas être appliquées au SIIG. Des logiciels commerciaux de simulation sont utilisés conjointement avec une approche à deux sections de guide, qui implique l'extraction de la constante de propagation à partir des paramètres S (de dispersion). Alternativement, la solution du problème des modes propres d'une seule cellule unitaire aboutit au même résultat. Les deux techniques fournissent des valeurs précises et concordantes, ce qui est confirmé par mesures de proto-

types fabriqués au laser. Il est montré que l'atténuation minimale possible est beaucoup plus petite que celle des technologies intégrées standards et que les pertes dépendent principalement des matériaux diélectriques choisis. Par conséquent, le SIIG est aussi une technologie attirante pour des applications au-delà de la bande millimétrique, soit dans la bande terahertz. Les recommandations pour les paramètres géométriques du SIIG sont discutées et un modèle équivalent simplifié avec zones diélectriques homogènes est introduit en vue d'accélérer la conception de composants passifs.

Les transitions à faibles pertes d'insertion entre guides d'ondes différents sont des éléments-clé indispensables pour une plate-forme hybride intégrée. Afin de permettre le branchement des instruments de mesure dans la bande W (75 GHz à 110 GHz), une transition du guide rectangulaire au SIIG a été développée. Une autre transition vers une ligne microruban ou CPW est essentielle pour rendre possible des mesures par sondes (sous pointes) et afin d'obtenir une compatibilité avec des circuits intégrés monolithiques hyperfréquences. La ligne microruban et le guide d'image ont des exigences très différentes quant à l'épaisseur du substrat. En conséquence, les efforts ont été concentrés sur une transition entre le SIIG et le CPW. La transition conçue fonctionne dans une large bande de fréquences avec des pertes de radiation minimales. D'autres transitions vers le guide rectangulaire intégré au substrat (SIW) sont également présentées dans le contexte des circuits intégrés sur substrat (SICs). La technologie SIC combine des lignes de transmission planaires et des structures de guide d'ondes non-planaires qui sont synthétisées d'une façon planaire sur un substrat commun. Cette approche est accompagnée d'une haute précision d'alignement, ce qui élimine le besoin d'ajuster certaines parties du circuit après coup.

En tant que guide d'ondes ouvert ayant des pertes de transmission basses, le SIIG est particulièrement approprié pour la conception d'antennes et des lignes d'alimentation correspondantes. La similarité du SIIG à d'autres guides d'ondes diélectriques, spécialement au guide image, suggère un transfert des connaissances depuis les antennes

diélectriques déjà connues. Une antenne cierge SIIG de nature planaire a été conçue et fabriquée comme dérivé de l'antenne polyrod. Sa structure est simple et compacte, et offre un gain moyen dans une région autour de 10 à 15 dBi. Un second type est une antenne SIIG linéaire d'onde progressive, dont le faisceau peut être dirigé dans la direction de rayonnement transversal en raison du design adapté des éléments de radiation. Le design novateur d'une antenne de mode à plaque diélectrique forme un faisceau de rayonnement longitudinal à l'aide d'une configuration à lentille planaire. Basées sur des technologies diélectriques, toutes les antennes présentées sont très efficaces.

Il est bien connu qu'une radiation excessive se produit aux courbures prononcées dans les guides d'ondes diélectriques ouverts. Cependant, des approches qui utilisent un nouvel excitateur de modes de plaque et une lentille planaire peuvent diviser et combiner la puissance électromagnétique dans un substrat diélectrique d'une façon efficace au moyen de méthodes quasi-optiques. Un exemple qui démontre le principe de fonctionnement et la faisabilité de cette technique est étudié théoriquement.

Étant donné que le SIIG est synthétisé sur un substrat planaire, il peut être combiné d'une manière hybride à d'autres structures guides sur le même substrat en circuits intégrés sur substrat (SICs). Il joint ainsi le SIW ainsi que le guide diélectrique non-rayonnant intégré au substrat (SINRD) et apporte des caractéristiques uniques comme son atténuation encore inférieure. Sa fabrication est par ailleurs plus tolérante à l'erreur et simplifiée à cause des trous non-métallisés. Dans ce contexte, le SIW est modifié pour une fabrication sur substrats électriquement épais afin d'obtenir une compatibilité avec le SIIG à très hautes fréquences. Basés sur une nouvelle géométrie, des coupleurs SIW-CPW hybrides ont été conçus et la théorie fournie est apte à prédire précisément le comportement de couplage. Finalement, une antenne SIIG a été intégrée conjointement avec un amplificateur à faible bruit en technologie monolithique à 60 GHz afin de prouver le concept des circuits actifs intégrés sur substrat.

Les résultats prometteurs obtenus avec la technologie diélectrique SIIG démontrent

son potentiel concernant ses faibles pertes et ses coûts peu élevés. Ceci est valide en particulier pour une opération à fréquences dans la bande millimétrique où des technologies traditionnelles n'offrent pas la performance désirée. La combinaison de ces avantages à d'autres technologies sur une plate-forme SIC hybride va fournir aux concepteurs de systèmes la flexibilité, le rendement, et les faibles coûts dont ils ont besoin.

ABSTRACT

Technological progress is expected to drastically reduce costs for components and systems in the attractive millimeter wave (mmW) band of the electromagnetic spectrum. Integration is the key to achieve cost-efficiency as well as small and lightweight devices. To this end, the traditional rectangular waveguide technology is abandoned in favor of planar integrated circuits. A major challenge, however, is the occurrence of extensive conductor losses at mmW frequencies in conventional planar transmission lines, such as microstrip or coplanar waveguide (CPW). For this reason, the latter are often an inappropriate choice, because excessive losses in key components of mmW front-ends can significantly affect the system performance.

This thesis deals with a novel type of integrated dielectric waveguide which is synthesized on a planar grounded substrate by perforation of the zones adjacent to a guiding channel in the center. The resulting Substrate Integrated Image Guide (SIIG) not only allows for low-loss guidance of electromagnetic waves in a similar way as the standard image guide, but also meets the requirements of low cost and ease of integration. A first objective was the detailed analysis of the propagation properties of fundamental and higher order modes in this waveguide structure, regarding attenuation, dispersion behavior, bandwidth, leakage effects, and the impact of fabrication tolerances. For this purpose, specifically adapted techniques of analysis are presented, since established methods for the conventional image guide can not be applied to the more complex periodic SIIG. Commercial electromagnetic full-wave software is used along with a dual-line approach involving a subsequent extraction of the propagation constant from simulated S-parameters. Alternatively, the solution of the eigenmode problem of a single SIIG unit cell also performs the task. Both techniques are in good agreement and provide accurate results, which is supported by measurements on laser-fabricated prototypes. It is shown that the achievable attenuation is much lower than in the standard integrated technolo-

gies and that losses mainly depend on the chosen dielectric material. As a consequence, the SIIG also is an attractive technology for applications beyond the mmW band, i. e. in the terahertz range. Design recommendations for the geometric parameters of the SIIG are discussed and a simplified equivalent model with homogeneous dielectric regions is introduced to speed up the design of passive components.

Low-loss transitions between dissimilar waveguide structures are indispensable key components for a hybrid integrated platform. In order to enable the connection of standard measurement equipment in the W-band (75 GHz to 110 GHz), a transition from rectangular waveguide to SIIG was developed. Another transition to either microstrip or CPW is essential to enable coplanar probe measurements and to achieve compatibility with monolithic millimeter wave integrated circuits (MMICs). Microstrip and image guide have very different requirements for the substrate thickness, for which reason efforts were concentrated on a wideband transition between the SIIG and CPW. The designed transition shows good broadband performance and minimal radiation loss. Other transitions from the SIIG to the Substrate Integrated Waveguide (SIW) are also presented in the context of substrate integrated circuits (SICs). The latter technology combines planar transmission lines and originally non-planar waveguide structures that are synthesized in planar form on a common substrate. High alignment precision is a direct consequence, which eliminates the necessity for additional tuning.

As an open dielectric waveguide technology with very small transmission loss, the SIIG is particularly suitable for antennas and corresponding feed lines. The similarity of the SIIG with other dielectric waveguides and especially with the image guide suggests a knowledge transfer from known dielectric antennas. A planar SIIG rod antenna was designed and fabricated, as a derivative of the established *polyrod* antenna. The structural shape is simple and compact, and it provides a medium gain in the range of 10 dBi to 15 dBi. A second developed type, an SIIG traveling-wave linear array antenna, is frequency-steerable through broadside due to special radiation elements. The novel

design of a slab-mode antenna forms an endfire beam by a planar lens configuration. In addition, all of those dielectric-based antennas are highly efficient.

As is well-known for open dielectric waveguides, excessive radiation occurs at sharp bends and discontinuities. However, new techniques involving a novel slab-mode launcher and a laminated planar lens can split and combine electromagnetic power efficiently by quasi-optical means in a dielectric substrate. An example is studied, which shows the working principle and the feasibility of this approach.

Being synthesized on a planar substrate, the SIIG can be combined in a hybrid way with other waveguide structures on the same substrate in so-called substrate integrated circuits (SICs). It joins the SIW and the Substrate Integrated Non-Radiative Dielectric guide (SINRD) and adds unique features like even lower loss and more tolerant, eased fabrication, since only non-metallized air holes are needed. In this context, the SIW is modified for fabrication on electrically thick substrates to achieve compatibility with the SIIG at exceedingly high frequencies. Based on a novel topology, hybrid SIW-CPW forward couplers were designed and the provided theory accurately predicts the coupling behavior. Finally, an SIIG antenna was integrated together with an MMIC low-noise amplifier at 60 GHz to prove the concept of active SICs.

The promising results obtained by the dielectric SIIG technology demonstrate its low-loss and low-cost potential, especially at frequencies in the upper mmW spectrum, where traditional technologies do not offer the required performance. Combining these advantages with other technologies on a hybrid SIC platform will provide system designers with the required flexibility, performance, and cost frame.

CONDENSÉ EN FRANÇAIS

Contexte des travaux de recherche

Un nombre croissant de domaines d'applications industrielles émergent dans la bande des ondes millimétriques, qui s'étend de 30 GHz à 300 GHz. Si cette bande était auparavant utilisée uniquement pour des applications militaires à cause des coûts immenses des composants, elle attire aujourd'hui l'intérêt des industries automobiles, des communications sans fil, des technologies médicales, de sécurité et de beaucoup d'autres. Les avantages des ondes millimétriques, comme la disponibilité d'une énorme largeur de bande, leurs propriétés uniques de propagation, de réflexion et diffraction suggèrent par exemple la conception de nouveaux systèmes de communication, de radar et d'imagerie. Pour ces applications industrielles, les coûts de fabrication jouent un rôle primordial. Ils s'ajoutent aux exigences quant à la compacité, à la légèreté et à l'efficacité, toutes étant indispensables pour un succès sur le marché. L'expérience avec les produits micro-ondes à plus basses fréquences a montré que l'intégration à grande échelle est indispensable pour satisfaire toutes ces conditions initiales. C'est pourquoi la plupart des circuits micro-ondes utilisent la ligne microruban ou le guide coplanaire (*coplanar waveguide* – CPW), qui sont simples à fabriquer et peu coûteux. Cependant, ces technologies intégrées génèrent trop de pertes de conduction aux fréquences millimétriques au dessus de 30 GHz. Leur emploi pour les éléments-clé dans une partie frontale (*front-end*) peut réduire considérablement la performance d'un système.

Une solution pour répondre aux besoins mentionnés est l'utilisation des guides diélectriques intégrés dont le mécanisme de guidage est basé sur la réflexion totale à la surface de séparation entre deux milieux diélectriques différents et non sur l'interaction avec les courants dans un ou plusieurs conducteurs. Pratiquement tous les guides d'ondes optiques fonctionnent de cette manière. De telles technologies ont été inves-

tiguées intensément dans les années soixante-dix et quatre-vingt pour l'application dans la bande des ondes millimétriques. Dû à sa simplicité, le guide image est un des résultats les plus populaires. Il consiste en une barre diélectrique posée sur un plan de masse et présente une atténuation très faible de l'onde guidée. Le plan de masse cause toujours des pertes de conduction, toutefois largement réduites. Ce dernier a plusieurs fonctions importantes, entre autre il sert comme blindage et constitue le support des circuits diélectriques planaires. Bien que le guide image présente les avantages d'intégration et de faibles pertes, il est difficile et coûteux de réaliser des circuits complets, parce que l'intégration hybride reliée aux autres technologies standards et la haute précision d'alignement nécessaires présentent un grand défi. En conséquence, le guide image conventionnel n'est pas particulièrement adapté à la production en masse.

Une version modifiée du guide image est proposée dans cette thèse, qui facilite largement l'intégration hybride de composants à ondes millimétriques. Cette nouvelle structure est nommée Guide Image Intégré au Substrat (*Substrate Integrated Image Guide* – SIIG). Le point de départ est un substrat diélectrique planaire de haute permittivité ($\varepsilon_r \approx 10$) qui est perforé dans les zones adjacentes à un canal de guidage au centre. Cette perforation entraîne une réduction de la permittivité effective, ce qui génère un effet de guidage presque identique à celui du guide image uniforme, à l'exception de quelques particularités à cause de la périodicité.

Plusieurs méthodes de micro-fabrication sont disponibles afin d'effectuer la perforation du substrat d'une façon très précise. Entre autres, il y a la coupure par laser, la gravure humide et sèche (DRIE), et la cuisson des céramiques dans leur état final (LTCC, HTCC). Comme toutes les structures SIIG synthétisées restent connectées par les murs de substrat entre les trous de perforation, la précision d'alignement est assurée d'une manière inhérente. Les surfaces libres et non-perforées sur le substrat sont disponibles pour accommoder d'autres parties d'un circuit, par exemple des éléments actifs. Un avantage additionnel par rapport au guide image standard est la faisabilité de tran-

sitions intégrées entre guides d'ondes différents sur le substrat commun. Ceci épargne l'ajustement mécanique ultérieur, car la précision de fabrication est largement suffisante dans la plupart des cas. Il devient ainsi facile de connecter un circuit monolithique (*monolithic millimeter wave integrated circuit* – MMIC) actif à une technologie diélectrique comme le guide image, ce qui était très coûteux avant.

Analyse, design, et mesures du SIIG

Avant d'utiliser le SIIG pour la conception de composants et de circuits, il faut connaître exactement ses propriétés de guide d'ondes. La constante de propagation du guide image peut être approximée par des méthodes quasi-analytiques relativement simples. Ils existent aussi des méthodes rigoureuses, qui sont applicables aux guides diélectriques uniformes dans la direction de propagation, ce qui n'est pas le cas pour le SIIG. Ainsi, il est nécessaire de concevoir des méthodes d'analyse qui sont applicables au SIIG avec sa géométrie tridimensionnelle et périodique. À cette fin, deux techniques étant compatibles avec des logiciels commerciaux sont présentées dans cette thèse. Une méthode est basée sur la simulation de la transmission d'ondes par deux sections de guide ayant une longueur différente. Ensuite, la constante de propagation est extraite des paramètres S obtenus. L'autre méthode est basée sur la solution du problème aux valeurs propres d'une seule cellule unitaire du SIIG. Les deux techniques sont très générales, peuvent tenir compte des pertes diélectriques ou de conduction, et montrent une très bonne concordance des résultats. Dû au maillage flexible des modèles simulés, elles sont aussi applicables à d'autres structures guides comparables.

À l'aide de ces techniques, le SIIG a été analysé en détail et une série de recommandations pour les divers paramètres de design ont été élaborées. Il est démontré que l'épaisseur du substrat a un impact décisif sur la bande d'opération monomode utilisable. Une largeur de bande maximale praticable est d'environ 25 %. L'intervalle périodique de la perforation ne devrait pas être choisi trop grand afin d'éviter les bandes interdites

du SIIG ainsi qu'une radiation partielle par onde de fuite. Il est aussi impératif de former des zones perforées assez larges afin d'éviter des fuites latérales vers le substrat. Pour faciliter la conception des composants passifs, le SIIG peut être remplacé par un modèle équivalent. Ce modèle remplace les zones perforées réelles par des régions homogènes ayant une permittivité effective réduite. Un film d'isolation mince de basse permittivité ($\varepsilon_r \approx 2$) entre le substrat et le plan de masse réduit significativement les pertes de conduction. Pour cette raison et puisque ce film aide à relaxer la tolérance à l'erreur de fabrication, il est avantageux de l'inclure. Le SIIG est dispersif et l'atténuation simulée et mesurée d'un prototype sur silicium de haute résistivité est autour de 35 dB/m à 94 GHz. D'autres simulations ont montré que des niveaux d'atténuation encore plus faibles sont possibles si on utilise des matériaux diélectriques ayant des facteurs de dissipation plus petits aux fréquences millimétriques.

Excitation de mode dans le SIIG

Pour effectuer des mesures et combiner le SIIG à d'autres guides d'ondes intégrés, il faut disposer de transitions qui rendent possible l'excitation du mode fondamental, soit le mode E_{11}^{y}. Une transition du guide rectangulaire déjà couramment utilisée pour le guide image standard a été modifiée pour le SIIG. Elle consiste en un cornet pyramidal posé sur un plan de masse dans lequel s'étend une extrémité taillée du SIIG. Ainsi, il est possible d'adapter les champs des modes TE_{10} du guide rectangulaire et E_{11}^{y} du SIIG graduellement, sans provoquer des pertes de radiation significatives. Une telle transition est importante afin d'effectuer des mesures de paramètres S d'un composant passif ou le diagramme de rayonnement d'une antenne, car le guide rectangulaire est l'interface standard des instruments de mesure en ondes millimétriques. Les pertes d'insertion mesurées d'une seule transition du prototype sont autour de 0.5 dB à 94 GHz.

Cependant, la transition décrite n'est pas appropriée pour l'intégration au substrat. Une autre transition vers un CPW a été conçue à cette fin. Le CPW est compatible avec

des substrats électriquement épais dont le SIIG est dépendant. Étant une technologie standard aux fréquences millimétriques, le CPW permet la connexion de MMICs par microcâblage ou par connexion par billes. La transition développée contient un ou deux larges trous métallisés, qui réfléchissent l'onde vers la direction désirée. L'excitation d'un mode à plaque diélectrique s'effectue par un résonateur à plaque dans lequel une sonde de couplage coplanaire est gravée. La transformation au mode E_{11}^{y} se fait par des trous percés dans le substrat. Les simulations de la structure tridimensionnelle montrent une radiation parasitique de moins de -0.15 dB par transition, un niveau de réflexion inférieur à -20 dB et une perte d'insertion inférieure à -0.4 dB. À cause de difficultés de fabrication, ces valeurs ne pouvaient pas tout à fait être obtenues avec un prototype mesuré sous pointes. Pourtant, le fonctionnement est démontré et cette transition a été utilisée plus tard avec succès pour un projet d'intégration hybride entre un MMIC et une antenne SIIG diélectrique.

Antennes diélectriques intégrées

En conséquence de son caractère de guide d'ondes ouvert, le SIIG est particulièrement approprié pour la conception des antennes diélectriques intégrées. Ses faibles pertes d'atténuation suggèrent aussi son utilisation comme ligne d'alimentation des éléments de rayonnement. Trois antennes ont été développées, elles trouveront des applications dans les parties frontales de systèmes à ondes millimétriques. L'une d'elles est une version planaire de l'antenne cierge diélectrique ou *polyrod*. Elle est constituée d'un guide d'alimentation SIIG qui aboutit à une pointe taillée. Cette configuration permet une très bonne adaptation des champs entre le SIIG et la pointe d'antenne et par conséquent des réflexions peu élevées. Le plan de masse donne à l'antenne son diagramme de rayonnement caractéristique, dont le lobe principal a une inclinaison d'environ 30° par rapport à l'horizontale, comparativement au rayonnement longitudinale de l'antenne cierge diélectrique standard. Deux variantes sont étudiées théoriquement à

94 GHz, une avec de faibles lobes secondaires et une qui maximise le gain. La première a été fabriquée et mesurée dans une chambre anéchoïque afin de vérifier les résultats simulés. Le gain dépend principalement de la longueur de la pointe diélectrique et se situe typiquement entre 10 dBi et 15 dBi. La longueur du prototype est de 6 mm et le gain correspondant est de 13 dBi. Les résultats de mesure et de simulation sont presque identiques. Ce n'est pas la perte par réflexion qui limite la largeur de bande, mais la dégradation du diagramme de rayonnement. Le rendement de l'antenne décrite a été déterminé à 74 % par des simulations qui tiennent compte des pertes diélectriques et conductrices.

Le deuxième type d'antenne SIIG conçu est une antenne linéaire à onde de fuite. L'onde qui se propage dans le SIIG en tant que guide d'alimentation est perturbée par des éléments de radiation métallisés, qui sont arrangés périodiquement sur le canal de guidage. La théorie disponible pour ce genre d'antennes concernant le balayage du lobe principal en fonction de la fréquence est complétée. Elle permet de prédire les limites de l'angle d'élévation du lobe principal sans que des lobes de périodicité soient générés. Contrairement à d'autres antennes possédant des éléments de rayonnement périodiques qui sont alimentés en série, ce design est capable de balayer le faisceau principal à travers la direction de rayonnement transversal. Ceci devient possible avec des éléments spéciaux, qui suppriment les réflexions distribuées vers l'entrée de l'antenne, faute de quoi apparaîtrait une bande interdite. En plus, le niveau de rayonnement par élément est ajustable sur une grande étendue, ce qui permet la conception d'antennes compactes avec un petit nombre d'éléments. L'antenne a été réalisée sur un substrat d'alumine pour une bande d'opération autour de 94 GHz. Les résultats de mesures de ce prototype concordent bien avec les résultats de simulation, sauf un décalage causé par les tolérances de fabrication. Cette antenne SIIG à onde progressive génère un faisceau plat étroit avec un gain de 11 dBi, soit 2.4 dB moins que la directivité simulée. Ces pertes incluent une transition de guide rectangulaire au SIIG. Le rendement de l'antenne, in-

cluant la transition de guide rectangulaire au SIIG, se situe ainsi autour de 60 %. Il est possible d'augmenter le gain par un rallongement de l'antenne ou par un arrangement de plusieurs antennes en parallèle.

Un troisième type d'antenne diélectrique intégrée est basée sur une conception novatrice. Ce design n'a pas recourt au SIIG, mais il contient un excitateur de mode similaire à celui qui est utilisé pour la transition CPW-SIIG. L'onde à plaque excitée est approximativement cylindrique et se propage avec une atténuation très faible dans le substrat. Elle peut être focalisée par une lentille planaire placée directement sur le substrat. Afin de rayonner l'onde vers la direction longitudinale dans l'espace libre, le plan de masse est courbé, ce qui entraîne une transition d'une plaque diélectrique métallisée à une plaque non-métallisée libre dans l'air. Comme le confinement des champs guidés est beaucoup moins fort, l'ouverture effective de l'antenne s'agrandit de sorte que le gain augmente et la dispersion au bord du substrat diminue. La largeur de bande est limitée par l'excitateur d'onde et est supérieure à 20 %. Bien que cette antenne soit destinée aux applications à fréquences millimétriques, un prototype agrandi a été réalisé à 12 GHz en vue de faciliter la fabrication et les mesures. Son gain mesuré est de 12 dBi, une valeur qui peut être changée par modification de la lentille ou de l'épaisseur de substrat. Le fait que le champ électrique soit orienté perpendiculairement à la plaque diélectrique permet l'utilisation de substrats électriquement épais et de haute permittivité. En même temps, le substrat utilisé peut également accommoder des circuits intégrés, ce qui rend cette antenne à mode de plaque diélectrique compacte et simple à fabriquer à un coût peu élevé. Comme les autres antennes diélectriques présentées, elle a une efficacité très élevée. Par conséquent, ce type d'antenne est bien adapté aux systèmes portables à ondes millimétriques.

Diviseurs de puissance SIIG

Faire passer une onde électromagnétique par un coude étroit est un problème général dans le contexte de guides diélectriques ouverts. Même si un bon confinement des champs est obtenu par un contraste élevé de l'indice de réfraction, une partie significative de la puissance est rayonnée au niveau de ces discontinuités, entraînant des pertes de transmission excessives et de la diaphonie. Une recherche bibliographique et des études de simulation ont été effectuées afin de trouver une solution applicable à la technologie SIIG. Dans la plupart des cas, un rayon de courbure minimal est recommandé, qui réduit les pertes par radiation à un niveau acceptable. Bien que ce choix soit souvent fait dans le domaine optique, les dimensions nécessaires dans un circuit intégré à ondes millimétriques ne seraient pas justifiables. Une autre possibilité de réduire la radiation parasitique est la variation graduelle de la permittivité effective des zones perforées. Cependant, cette approche nécessite une perforation très fine afin d'assurer la quasi-homogénéité, ce qui n'est possible qu'avec une technique de fabrication ultra-précise et coûteuse. Une troisième approche implique une cavité résonante diélectrique à l'endroit du coude du guide diélectrique. Cette configuration a été étudiée avec succès par d'autres chercheurs en deux dimensions, mais elle génère encore trop de radiation dans une structure tridimensionnelle comme le SIIG. Dans ce cas, la cavité fonctionne comme une antenne à résonateur diélectrique, à moins que la permittivité du substrat ne soit extrêmement élevée. En général, les méthodes capables de réduire la radiation aux coudes du SIIG sont complexes et c'est pour cette raison que les applications préférées sont celles qui sont réalisables uniquement avec des sections linéaires.

La situation est différente pour les diviseurs de puissance. Il est montré qu'une division à deux branches est faisable si l'angle d'ouverture est petit. Toutefois, une telle jonction en "Y" est limitée à deux sorties SIIG. S'il y a besoin d'une division à un nombre plus élevé de canaux, un principe similaire à celui de l'antenne à plaque diélectrique peut être appliqué. L'onde cylindrique excitée dans un substrat est transformée en une onde

ayant des fronts d'ondes droits à l'aide d'une lentille planaire posée sur le substrat. Par la suite, l'onde est facilement divisée aux canaux de guidage en technologie SIIG, avec un faible niveau de radiation. De tels diviseurs peuvent être utilisés pour des réseaux d'antennes ou pour des groupeurs de puissance quasi-optiques à fréquences millimétriques.

Le SIIG dans le contexte des circuits intégrés sur substrat

Dans le cadre de la technologie des circuits intégrés sur substrat (*substrate integrated circuits* – SICs), deux types de guides synthétisés sont déjà développés : le guide rectangulaire intégré (*substrate integrated waveguide* – SIW) et le guide diélectrique non-rayonnant (*substrate integrated non-radiative dielectric guide* – SINRD). Ainsi, le SIIG est le troisième qui se joint aux SICs. L'objectif final poursuivi avec la technologie SIC est de combiner ces structures synthétisées avec les lignes de transmission standards (microruban et CPW) sur un substrat commun, afin de profiter des avantages spécifiques à chaque guide d'ondes. Cette approche permet une haute performance du circuit à ondes millimétriques ainsi qu'une intégration à grande échelle et à faible coût. Le SIIG est comparé avec le SIW et le SINRD pour justifier son utilisation par ses caractéristiques uniques. Il est surtout le guide ayant les pertes d'atténuation les plus faibles aux fréquences millimétriques. Par rapport aux autres structures intégrées, les pertes conductrices du SIIG augmentent moins rapidement avec la fréquence et il possède ainsi le plus grand potentiel d'application à des fréquences encore plus élevées, c'est-à-dire dans la bande sous-millimétrique/terahertz.

Le SIIG n'est pas facile à combiner avec le SINRD, car les deux guides exigent une épaisseur de substrat différente à la même fréquence d'opération. En plus, l'orientation du champ modal est orthogonale, ce qui complique l'adaptation. Par contre, le SIW est flexible par rapport à l'épaisseur du substrat et ne pose pas de problèmes de compatibilité. Cependant, sa fabrication sur un substrat électriquement épais de haute permittivité, requis par le SIIG, est problématique. Pour cette raison, la forme ronde des trous

métallisés a été abandonnée en faveur des contours rectangulaires. La stabilité structurelle est assurée par une plus grande distance entre les vias, entraînant ainsi des réflexions plus importantes vers l'entrée du guide. Cependant, il est montré que l'adaptation peut être améliorée d'une façon significativement en tenant compte de l'impédance "Bloch" réelle de la structure périodique. Une transition novatrice entre le SIW et le CPW qui est adaptée aux substrats épais a été conçue. Elle est constituée d'un dipôle de couplage coplanaire et d'une cavité résonante qui sert d'élément de couplage entre le SIW et le CPW. Un prototype a été réalisé à 50 GHz sur un substrat d'alumine. Cette transition possède une large bande passante de plus de 30 % et la perte d'insertion simulée et mesurée est de -0.4 dB et -0.55 dB, respectivement. Une configuration dos-à-dos de cette transition avec la transition CPW-SIIG proposée précédemment permet de relier le SIW avec le SIIG, ou directement ou avec un MMIC intégré dans la section CPW.

Un concept novateur de coupleur hybride à été élaboré, qui comporte un CPW gravé dans la métallisation du côté supérieur d'un SIW. Le couplage entre le mode quasi-TEM du CPW et le mode TE_{10} du SIW est évalué avec une théorie des modes couplés. Le calcul difficile du coefficient de couplage est évité par l'application précédente d'une théorie des modes normaux. Un tel coupleur peut être conçu pour un niveau de couplage arbitraire allant jusqu'à 0 dB, ce qui correspond à un transfert entier de la puissance guidée. Autrement dit, il est possible d'opérer le coupleur en mode transition. Plusieurs prototypes réalisés à 50 GHz confirment les résultats calculés et de simulation. Basés sur le même principe, des coupleurs hybrides CPW-SIIG ou SIW-SIIG peuvent être conçus.

Un exemple simplifié d'un circuit hybride actif a été fabriqué pour démontrer la faisabilité et l'utilité de la technologie SIC. À cette fin, un amplificateur MMIC à faible bruit est connecté à l'antenne cierge SIIG développée précédemment par une transition CPW-SIIG. Le MMIC est monté sur le même tenon métallique (connecté à la base métallique) qui est utilisé pour la transition et il est microcâblé aux lignes CPW sur le substrat d'alumine. Les mesures de pertes de transmission entre l'antenne active fabriquée et une

antenne cornet ont été effectuées sur une station de sondes à l'aide d'un analyseur de réseau. Les résultats confirment une très bonne performance et suggèrent l'implantation de telles technologies dans les parties frontales de systèmes à ondes millimétriques.

TABLE OF CONTENTS

LIST OF TABLES

LIST OF FIGURES

LIST OF ACRONYMS AND ABBREVIATIONS

2-D	Two-Dimensional
3-D	Three-Dimensional
CAD	Computer Aided Design
CMOS	Complementary Metal Oxide Semiconductor
CPW	Coplanar Waveguide
CST-MWS	Microwave Studio® (Computer Simulation Technology GmbH)
DBR	Distributed Bragg Reflection/Reflector
DRIE	Deep Reactive Ion Etching
EBG	Electromagnetic Band Gap
FEM	Finite Element Method
FEP	Fluorinated Ethylene-Propylene copolymer (Dupont™)
FDFD	Finite-Difference Frequency-Domain
FDTD	Finite-Difference Time-Domain
FSPL	Free-Space Path Loss
HFSS	High Frequency Structure Simulator® (Ansoft Corp.)
HR	High Resistivity
HTCC	High-Temperature Co-fired Ceramics
ISM	Industrial, Scientific, and Medical
LNA	Low Noise Amplifier
LRM	Line-Reflect-Match (calibration)
LTCC	Low-Temperature Co-Fired Ceramics
MMIC	Monolithic Microwave/Millimeter-wave Integrated Circuit
mmW	Millimeter Wave
NRD	Non-Radiative Dielectric guide
OFDM	Orthogonal Frequency Division Multiplex

PTFE	Polytetrafluoroethylene (also known as Teflon®)
SIC	Substrate Integrated Circuit
SIIG	Substrate Integrated Image Guide
SINRD	Substrate Integrated Non-Radiative Dielectric waveguide
SIW	Substrate Integrated Waveguide
TE	Transverse Electric
TM	Transverse Magnetic
V-band	Standard waveguide band from 50 GHz to 75 GHz
VCO	Voltage Controlled Oscillator
VNA	Vector Network Analyzer
W-band	Standard waveguide band from 75 GHz to 110 GHz
WR10	Electronic Industries Association (EIA) waveguide designation for the W-band
WR15	Electronic Industries Association (EIA) waveguide designation for the V-band

INTRODUCTION

A rapidly growing number of commercial applications stimulate the development of new technologies for the millimeter wave (mmW) band of the electromagnetic spectrum, which spans the frequency range from 30 GHz to 300 GHz. Important target applications include personal communications and high capacity wireless data links, various automotive and aircraft radar systems, sensors and spectroscopy, medical imaging, and security scanners. A comprehensive overview is given in [1]. All these future products will take advantage of one or more of the unique characteristics of millimeter waves, which include the broad available bandwidth, the good spatial resolution being realizable with comparatively small antenna apertures, the ability to penetrate dust, smoke, or fog, the specific resonance frequencies of important atmospheric molecules in this frequency range, and last but not least the vast resources of so far unused frequencies.

High-density integration is the key to mass-producible, cost-efficient, small and lightweight commercial products. Microstrip is the dominant integrated waveguide structure in the microwave range up to about 30 GHz. Its simplicity, low-cost fabrication by printed circuit technology, and the vast available amount of design information cast in accurate empirical formulas for the use in circuit synthesis software have led to its popularity. At mmW frequencies (30 GHz – 300 GHz), however, the coplanar waveguide (CPW) is often preferred because the microstrip line then requires very thin substrates due to the potential overmoding and power leakage into substrate modes and because good ground connections by metallized vias become increasingly difficult to realize. CPW is suitable for the mmW range, but inefficient wave guidance by metal-based waveguides constitutes a general problem in this frequency range. The increasing influence of the skin effect causes the currents to flow in a very thin region below a metal surface and the surface roughness becomes a critical factor. In addition, the cross-sectional dimensions of the guide need to be scaled down towards higher frequencies to suppress

higher order modes and potential leakage or radiation. Both circumstances entail high current densities and hence significant conductor losses. The situation is even worse for the traditional integrated planar transmission lines, microstrip and CPW, because the existent electromagnetic field singularities at the conductor strip edges deteriorate the loss problem. In the past, researchers attempted to reduce the dielectric losses in the substrate material by applying techniques such as micro-machining, but the conductor-related losses are by far dominant and could not be lowered significantly. Although this drawback is usually tolerated in miniature MMICs with very short transmission lines, it becomes a serious problem for the design of larger passive devices like antenna arrays and corresponding feeding networks, power dividers or combiners, directional couplers, phase shifters, resonators, and filters. For this reason, the preferred technology for such components at mmW frequencies traditionally was and still is rectangular waveguide due to its superior performance. Its wave attenuation is low because the modal fields are well distributed over the relatively large air cross-section without any field singularities present. Unfortunately, the rectangular waveguide is extremely expensive, heavy and bulky, and hardly integrable.

Wave propagation on purely dielectric rods was first investigated at the beginning of the 20th century in a theoretical paper [2]. Experiments [3] and a general theory showing the existence of *TE*, *TM*, and hybrid modes [4] were published later. Dielectric rod antennas came into use [5] and research on dielectric waveguides continued because of their promising low-loss properties and flexibility [6, 7]. In contrast to metallic waveguides, where electromagnetic waves are guided by interaction of the fields with currents flowing on conductors, the guidance effect of dielectric waveguides is based on total internal reflection at the dielectric-air interface. Since the actual wave guidance takes place at the surface of the dielectric material, those waves are referred to as surface waves. A guidance effect is also achieved when a dielectrically denser material is surrounded by a material of lower permittivity. Undoubtedly, the biggest story of success in this area is

that of the optical fiber, which can transport signals in the form of electromagnetic waves in the optical range over extremely long distances and thus rendered the Information Age possible, including the Internet.

On the one hand, optical waveguides are generally purely dielectric, because metals have a plasma-like character at these wavelengths and would introduce too much transmission loss. On the other hand, radio frequency and microwave technology is traditionally based on metallic waveguide structures, because dielectric-based technologies do not provide the needed compactness and are more difficult to design. The mmW and terahertz ranges are located between those parts of the spectrum and suffer from a technology gap, as illustrated in Figure 1. This lack of a practical technology initiated the research for *integrated* dielectric waveguides. Examples include the image guide [8] and its rectangular strip version [9], the inverted strip guide [10], the non-radiative dielectric (NRD) guide [11], and the inset guide [12]. All these structures have a metallic ground plane, but the conductor loss is small because there are no field singularities as found in the case of microstrip or CPW and the field concentration is comparatively small. They can be regarded as mixed metallic-dielectric and are therefore well adapted

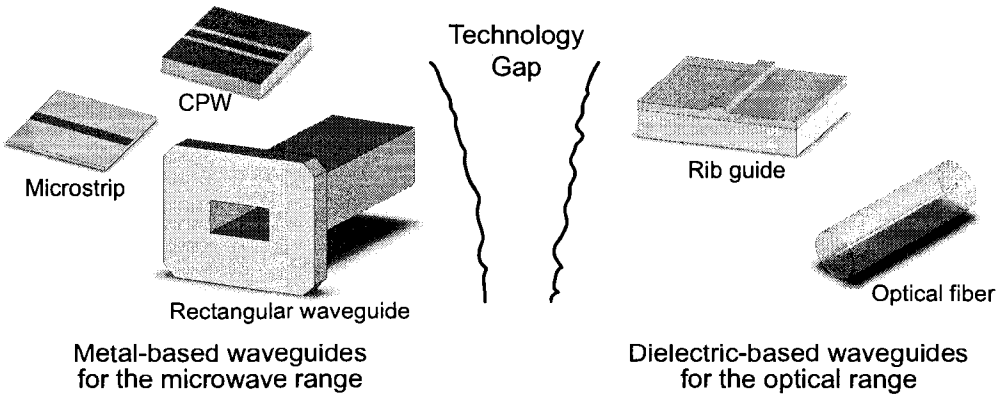

Figure 1 Technology gap between the microwave and optical parts of the electromagnetic spectrum: Waveguides for long wavelengths are metal-based, whereas they are purely dielectric for short wavelengths.

to the transition region between the microwave part and the infrared/optical parts of the electromagnetic spectrum. Although wave guidance would be possible in the absence of any conductor, the use of a ground plane at mmW frequencies has several significant advantages. It provides an appropriate mechanical support for the dielectric lines, it acts as a one-sided shielding, and it can be used for biasing and dissipating heat from active devices. Furthermore, the ground plane has the effect of shifting higher-order and degenerate modes to higher frequencies, thus increasing the useable single-mode bandwidth. Of all the mentioned integrated dielectric guides, the image guide is the simplest and probably the most widely used. It obtained its name from the "mirror" effect of the ground plane. King [8] was mainly interested in the low-loss properties of the image guide with very loosely bound waves, whereas Knox [9] concentrated on the rectangular, high-permittivity image guide with the objective of integration. For the latter type, insertion of an optional insulating dielectric film of low permittivity between the substrate and the metallic ground plane additionally reduces conductor losses [13]. Figure 2(a) shows a graphic of the resulting insulated image guide.

A rich variety of passive and active components as well as circuits were realized in image guide technology, which prove the benefits of the integrated dielectric technology. Among them are leaky-wave antennas [14], filters [15], couplers [16], mmW oscillators [17], a V-band communications receiver [13], a W-band receiver [18] and a 94-GHz radar system [19]. Despite the fact that image guide is known for decades, it was not intensively used in microwave or mmW integrated circuits. One reason was the absence of mass-producible MMICs for the mmW range, which are the basis for any cost-efficient commercial product today. This is changing now with the advances in technology and the increasing pressure of expansion to the mmW bands as a result of the shortage of frequency resources in the microwave range. Especially the low-cost CMOS technology will play an important role and it becomes available for ever increasing frequencies. Even though the standard image guide offers very low attenuation loss, it has substan-

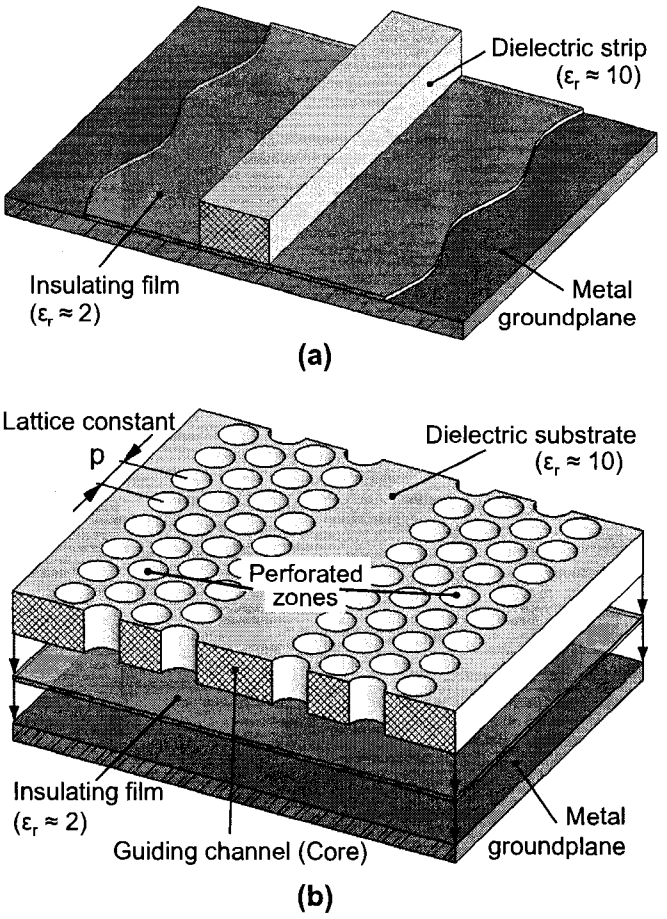

Figure 2 (a) Insulated image guide and (b) exploded view of substrate integrated image guide (SIIG).

tial drawbacks concerning integration and manufacturing. The single dielectric strips, which are very small at short wavelengths, have to be placed precisely on the support, i. e. the metallic ground plane. Not only tight control of the image guide's dimensions is required, but also a very demanding alignment precision of the guides relative to each other. The interconnection of image guide circuits to other transmission lines is probably the most serious limitation. In fact, it is difficult to combine different technologies due to the varying requirements for the support (e. g. ground plane versus dielectric substrate)

and the very high precision needed at mmW frequencies, not to mention the multiple fabrication steps.

The above argumentation led to the proposal of a hybrid approach that accommodates diverse waveguide technologies on a common substrate [20]. In order to solve the mentioned problems, the substrate should not only serve as a support for hybrid circuits, it should also be the medium out of which three-dimensional waveguides are formed. This technology was baptized the "Substrate Integrated Circuits" (SICs), a combination of various planar and synthesized non-planar waveguides, which complement one another in their favorable properties [20]. The most popular and widely used of such waveguide structures is the Substrate Integrated Waveguide (SIW), an embedded version of the dielectric-filled metal waveguide [21]. The Substrate Integrated Non-Radiative Dielectric guide (SINRD) was also investigated [22]. In this research work, the image guide was chosen as a starting point for a new synthesized version, the so-called Substrate Integrated Image Guide (SIIG) [23]. It achieves even lower transmission loss than the SIW or SINRD [24] due to its open waveguide character. The SIIG is shown in Figure 2(b). Like the standard image guide, the SIIG possesses a continuous ground plane and an optional low-permittivity insulation film to lower conductor losses in the ground plane. However, the guiding channel is formed in a planar substrate by regular perforation of the adjacent regions instead of using an isolated dielectric strip. Removing parts of the high-permittivity substrate material ($\varepsilon_r \approx 10$) has the effect of lowering the efficient permittivity in the corresponding zones. Therefore, the SIIG produces basically the same guiding effect as the standard image guide, except for particularities due to the periodic structure. Despite the many similarities, the SIIG possesses several key advantages over the standard image guide with respect to eased fabrication at lower cost. First, a planar substrate is used, which is industry standard and the cheapest way to manufacture all kinds of electronic circuits. Second, the interconnection with other waveguide technologies on the same substrate is substantially simplified. Dielectric technologies are never

stand-alone in transceivers that comprise active devices with metal pins as inputs and outputs. Third, the proposed SIIG geometry is robust and allows for low tolerances and a high alignment precision. The outcome is a high-performance technology for small, lightweight, and cost-efficient circuits and systems.

The first chapter of this thesis deals with the geometry of the SIIG, its dimensional parameters, and their effect on the propagation properties. The various methods used in the past to determine the propagation constant of standard image guide are reviewed. It is pointed out that those methods are not applicable to the SIIG and that rigorous three-dimensional (3-D) methods are necessary for a valid analysis of the periodic structure instead. Two techniques of analysis, based on a driven modal simulation and on an eigenmode solution using commercial software, were developed and are presented along with their advantages and drawbacks. Important design guidelines are deduced from the observed interdependencies and an equivalent SIIG model for simplified passive component design is discussed. Fundamental differences between the SIIG and similar looking 2-D photonic band gap defect waveguides are explained to avoid confusion. The chapter closes with detailed information on possible fabrication techniques and employed experimental methods.

In the second chapter, topologies for efficient SIIG mode excitation are presented. Such waveguide transitions are key components in every hybrid circuit or system, necessary for interconnections between dissimilar technologies on a common substrate. Transition design is a challanging task, because the SIIG, in contrast to SIW or SINRD, is a completely open waveguide and therefore prone to excessive radiation at discontinuities. First and foremost, a transition between SIIG and rectangular waveguide is essential to connect standard measurement equipment in the W-band. Based on a tapered horn design, the presented version provides very low return and radiation loss. Another transition to CPW was developed in integrated planar form. Its outstanding wideband

performance enables coplanar probe measurements and hybrid SICs including active components.

Novel dielectric-based antennas that use the SIIG as low-loss feed line are addressed in the third chapter. Two types of antennas, a planar dielectric rod antenna and an SIIG array antenna, are demonstrated along with their measured performance at 94 GHz. An extended theory regarding the limitations for single beam frequency scanning of the latter type is established. Special radiation elements are proposed, which allow scanning through broadside without suffering from high return loss due to the well-known effect of distributed Bragg reflection (DBR) in periodic leaky-wave antennas. In addition, an entirely novel dielectric antenna concept is presented, which comprises a slab-mode waveguide and a planar lens configuration to focus the generated quasi-optical beam.

The fourth chapter covers the topic of power dividing and combining in open dielectric technologies. As with conventional image guide, an unacceptable level of radiation occurs in an SIIG at discontinuities like bends or Y-branches. Since the remedial requirement of a large radius of curvature cannot be fulfilled due to certain design constraints, an alternative technique is investigated to direct the guided electromagnetic waves into several SIIG channels. Quasi-optical power splitting and combining in a grounded planar substrate is a compact and efficient solution to this problem.

In the fifth chapter, the SIIG is put in the context of substrate integrated circuits. Its characteristics are compared with those of the already existing synthesized waveguides, the SIW and the SINRD. This is followed by a discussion on how these technologies can be combined with each other in order to exploit all the beneficial properties of a hybrid SIC. In particular, modifications of the SIW are suggested in order to achieve compatibility with the SIIG. In this regard, a new transition from the modified SIW to CPW is proposed for use on electrically thick high-permittivity substrates. Another transition was designed for direct interconnection of SIW and SIIG. A novel concept for hybrid SIW-CPW forward couplers with arbitrary coupling level up to 0 dB is presented, ac-

companied by a suitable coupled-mode theory and a study of the most important design parameters. 0-dB couplers allow for nearly complete complete power transfer and can also be used as transitions. Finally, the implementation of the SIIG in SICs is addressed in a conceptual study. A real example of hybrid integration of a 60-GHz mmW MMIC low-noise amplifier proves the anticipated feasibility and performance, also in conjunction with active devices.

CHAPTER 1

ANALYSIS, DESIGN, AND FABRICATION OF THE SIIG

This chapter deals with the SIIG geometry, the influence of important design parameters, techniques for analysis, as well as SIIG fabrication. Existent modes in image guide and their notation are addressed in the following section.

1.1 Image guide modes and notation

The theory of dielectric waveguide modes is discussed for example in [4] and [25]. Only some general remarks for better understanding will be made here. A waveguide mode is generally understood as a particular solution of Maxwell's equations (or more specific the derived wave equation) for the electromagnetic fields that propagate along a wave-guiding structure. In a hollow metal waveguide, an infinite number of discrete modes can exist. Some of these modes may be above cut-off, the others below cut-off (i. e. the propagation constant γ is purely real and therefore the mode does not propagate but is attenuated in an exponential manner). All these modes together form a complete set, i. e. any possible field configuration inside the metal waveguide is a superposition of the modes.

The situation is somewhat different for open dielectric waveguides like the image guide. Here, the guided modes also form a discrete spectrum, i. e. the modes have discrete propagation constants for a given frequency. However, the finite number of discrete modes cannot fully describe any possible field configuration in the dielectric waveguide and therefore cannot be said to form a complete set. They are complemented by a continuous spectrum of radiation modes and reactive modes [26]. For this reason, a real cut-off frequency as known from metal waveguides below which mode propagation is

not possible does not exist. A certain mode may not be guided but still can propagate in the surroundings of the guide. Non-guided modes do not have an exponentially declining field in the lateral direction and hence propagation also occurs in lateral direction away from the guide. Therefore, the term "divergence frequency" was suggested [27] instead of the well known cut-off frequency for metal waveguides. Nevertheless, the term "cut-off" is widely used today for dielectric waveguides. The discrete spectrum of guided modes and the continuous spectrum of radiation modes and reactive modes together form a complete set of modes which can describe any possible electromagnetic field configuration in an open dielectric waveguide. A detailed discussion of the different kinds of modes and their characteristics is presented in [26] on the basis of a planar slab waveguide.

Two different notations for indexing of the guided hybrid modes in image guide are used in the literature. One uses HE_{nm} for modes whose cross-sectional fields resemble that of an *H*- (*TE*-) wave and EH_{nm} if they are similar to an *E*- (*TM*-) wave in a corresponding metal waveguide. Indices n and m count the field maxima in horizontal and vertical direction, respectively. Another notation was used in this thesis because it is more widely used. It specifies the modes as E^x_{nm} and E^y_{nm}, where the capital E stands for the electric field, the indices count the maxima in horizontal and vertical direction, and the dominant direction of the transverse electric field is indicated by x (horizontal) or y (vertical). Figure 1.1 shows the transverse electric fields of some lowest order modes of image guide and insulated image guide.

The actually used mode should be easy to excite, have low loss, and show the smallest dispersion possible. It is usually a good idea to choose the fundamental mode of a waveguide and operate it in a frequency range where no other mode is guided. Then, the danger of mode conversion and disturbing interference is drastically reduced. For this reason, the E^y_{11} mode is preferred, even though the E^x_{11} mode has lower loss because its field concentration in the vicinity of the ground plane is lower [28]. Moreover, all modes

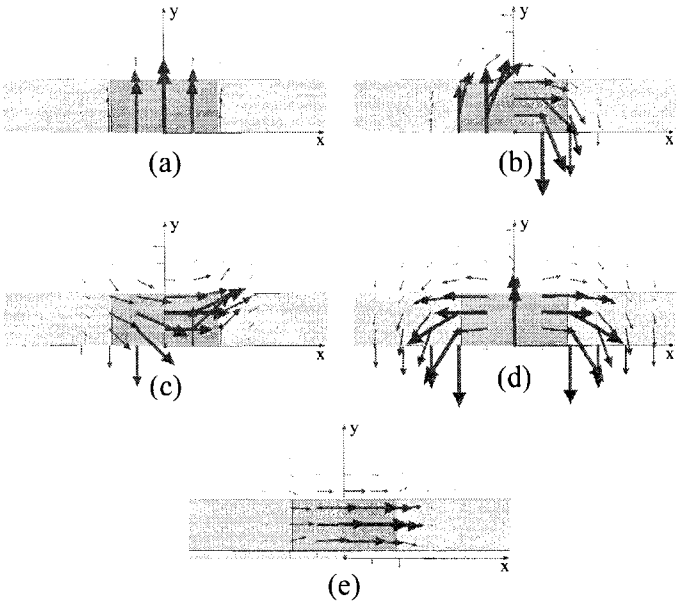

Figure 1.1 Transverse electric fields of some modes of image guide: (a) E_{11}^{y}, (b) E_{21}^{y}, (c) E_{11}^{x}, (d) E_{31}^{y} modes in image guide, (e) E_{11}^{x} mode in insulated image guide

of insulated image guide except the fundamental one have the potential to leak at certain frequencies because of the supported substrate modes [29].

The field distribution of all modes in image guide changes with frequency, i. e. it is more concentrated in the dielectric strip for increasing frequencies. As a result, propagation is highly dispersive. Towards higher frequencies, the phase constant β asymptotically approaches the wave number in the strip, the medium with the highest permittivity. Figure 1.2 graphically illustrates the dispersion of image guide modes qualitatively. The phase constant β is close to the vacuum wave number k_0 at low frequencies and asymptotically approaches the wave number of the medium with the highest relative permittivity ε_r, namely the dielectric strip. Multiple guided modes exist at high frequencies and therefore the operating frequency range is usually chosen to be in the region with the strongest dispersion for single-mode operation.

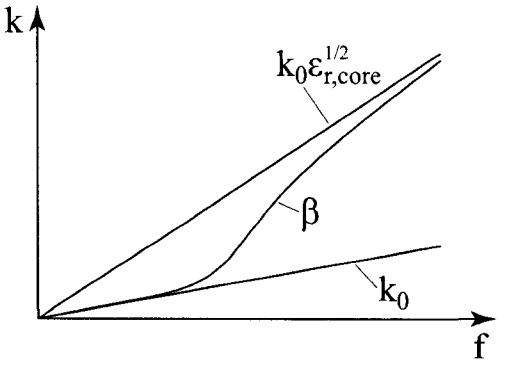

Figure 1.2 Qualitative dispersion behavior of image guide modes.

1.2 SIIG topology

The SIIG was first proposed in a paper on hybridization of waveguide technologies [20] and demonstrated for the first time in [30]. The starting point is a high-permittivity dielectric substrate of a certain, required thickness. Such a dielectric slab, which may be grounded on one side, is capable of vertically confining and guiding a mode. A refractive index contrast in the horizontal plane is necessary in order to achieve additional horizontal confinement. This can be achieved by total (equivalent to the standard image guide) or partial removal of the substrate material adjacent to a guiding channel in the center. One way to partially remove dielectric material is perforation of the substrate by cutting or etching vertical holes into it. This technique was used before to improve the operation of patch antennas on high-permittivity substrates [31,32]. If the voids and their distance to each other are much smaller than a wavelength, then the guided wave "sees" a homogeneous region of artificially lowered effective permittivity compared to the substrate material. An optional low-permittivity insulation film between the ground plane and the high-permittivity substrate further reduces the already low conductor losses. This is because the magnetic fields are less intense at the ground plane surface, thus inducing smaller current densities. Figure 1.3 shows the topology of a typical SIIG with important design parameters such as the width w and height d of the

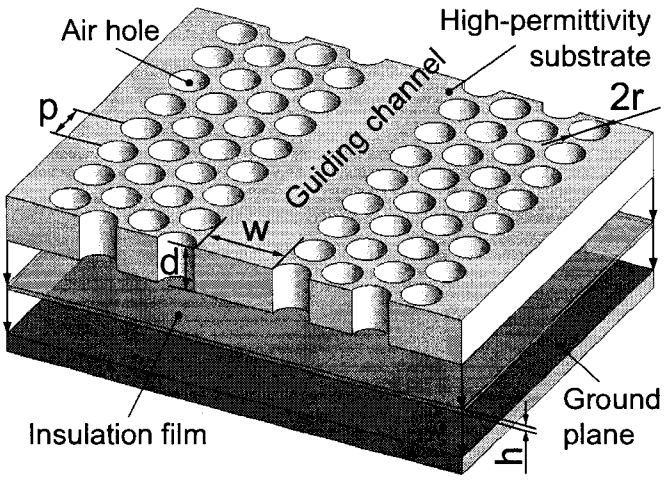

Figure 1.3 Geometry and important design parameters of the SIIG.

guiding channel (core dimensions), the hole diameter $2r$, the lattice constant p, and the insulation film thickness h.

A relevant aspect of the SIIG technology is the mechanical stability of the entire circuit. This means that the SIIG must stay connected in a rigid way with the rest of the substrate in order to build the mentioned hybrid circuits. To this end, a narrow wall between the holes needs to be maintained to keep everything connected. The thickness of this wall is equal to the difference $p - 2r$. For a given minimum wall thickness, an equilateral pattern of equal-sized air holes allows to remove most of the substrate and thus provides the highest refractive index contrast between the guiding channel and the surrounding zones [33]. It is for this reason that an equilateral hole pattern was employed for all SIIGs throughout the thesis. A high refractive index contrast is required for good field confinement and guidance by the SIIG. This is in contrast to optical technology, where large radii of curvature are feasible and where lower coupling efficiency (i.e. higher radiation) is usually accepted. The influence of the dimensional parameters on the SIIG's propagation properties is addressed in section 1.4, after the following section which deals with numerical analysis.

1.3 Modal analysis of SIIG propagation properties

This section first reviews some of the most important analysis techniques for uniform dielectric waveguides. Two methods for the specific analysis of SIIG modes are presented subsequently.

1.3.1 Approximate methods for dielectric waveguides

Only dielectric waveguides that are uniform in one of the lateral coordinates (this includes circular cross-sections that are uniform in one cylindrical coordinate) possess an analytical solution of Maxwell's equations. The presence of corners, edges or roundings in open dielectric waveguides with other shapes effect the coupling of the electromagnetic fields in a way that no solution in a separable form exists and all guided modes are of hybrid character, i. e. all six field components $E_x, E_y, E_z, H_x, H_y, H_z$ are present. Therefore, these shapes are much more difficult to treat and need to be solved by numerical means if high accuracy is needed. In many practical cases, however, engineers need to know the propagation constants within a certain accuracy and can renounce on highly accurate results if an approximate analysis leads to much faster results. The first semi-analytic technique was presented for rectangular dielectric waveguides [34]. It is based on the assumptions that the modes are well confined in the core region, so that fields in the corner regions can be neglected and that the fields are separable in the various regions of interest. Those assumptions are not valid in many practical cases and thus strongly limits the method's applicability. A more accurate method, the so-called effective dielectric constant (EDC), was introduced for the analysis of the propagation properties of rectangular image guide [9] and was also widely used afterwards for other dielectric waveguides with rectangular sub-regions. In contrast to the first method, the EDC method takes into account coupling of the two transverse directions and also the fields in the corner regions are not completely neglected. Despite its simplicity, the lat-

ter technique provides fairly accurate results for the propagation constant in most cases. Both methods are described and compared in more detail in [26]. It is important to notice that the described approximate methods are only useful to calculate modal phase constants and cannot provide any information on guided electromagnetic fields.

1.3.2 Overview of numerical methods for uniform dielectric waveguides

As mentioned before, the accurate calculation of propagation constants of guided modes on arbitrarily shaped uniform dielectric waveguides is a difficult problem. Nevertheless, several numerical methods were developed to achieve this task. The first rigorous methods applied to a rectangular dielectric guide [35, 36] were point-matching techniques (today better known as mode-matching method). This method is one of the oldest and simplest for the accurate solution of dielectric waveguides and is based on harmonic expansion of the fields in the various dielectric regions. Within the procedure, the fields are explicitly matched at certain certain points on the dielectric interface(s). A similar method was later applied to single and coupled image guides [37]. In contrast to the methods in subsection 1.3.1, the mode-matching technique also provides the field distribution and orientation of the guided modes. It constitutes an efficient technique for simple, homogeneous structures, but its formulation becomes tedious for more complex structures and good convergence is not assured in that case. An additional variational formulation or moment method for more accurate field matching at dielectric interfaces can improve convergence and accuracy. Another method which was used for the analysis of inhomogeneous dielectric guides transforms Maxwell's equations first into a set of generalized telegraphists equations for mode voltages and mode currents [38]. This approach was not widely used later. A comprehensive treatment of guidance and leakage effects in open dielectric waveguides together with a combined mode-matching and generalized transverse resonance method is given in [29]. A somewhat different efficient transverse resonance diffraction method is described in [26, 39]. Such transverse reso-

nance approaches allow the development of equivalent circuits for step discontinuities. The method of lines has also found applications in dielectric waveguide calculations [40]. Semi-analytical integral equation methods have shown to be efficient candidates for calculating the fields and propagation constants of dielectric waveguides [41, 42]. Satisfying the boundary conditions is guaranteed by derivation of appropriate integral representations of the fields. Treatment of anisotropic media is also possible. The most versatile rigorous methods are fully numerical finite-difference frequency-domain (FDFD) methods [43–45], finite-difference time-domain (FDTD) methods [46–48], and finite-element methods (FEM) [49–51], which discretize the cross section of the guide. Arbitrary shapes can be dealt with, including anisotropic media. Due to the discretization with triangular or rectangular elements, they yield more accurate results if applied to linear rather than curved boundaries. Hybrid methods such as a FEM-method-of-lines approach [52] attract more attention recently. They can combine the advantages of complementary techniques and therefore provide increased efficiency at comparable or better accuracy. In [52], the FEM is used to deal with the complex part of a dielectric structure whereas the method-of-lines is used to solve the fields efficiently in the surrounding homogeneous part.

1.3.3 Methods of analysis for the SIIG

The numerical methods listed in the preceding subsection were used to analyze dielectric waveguides which are uniform in the direction of propagation. In this case it is sufficient to carry out the calculations in only two dimensions on the cross-sectional plane of the guide because the dielectric distribution in the cross-section contains all information about the guide. The scenario is different for the SIIG, which is a non-uniform, periodic waveguide with non-constant cross-section. It is therefore necessary to conduct the analysis at least on a full unit cell, which contains the complete information on the geometry of the periodic structure. The above listed two-dimensional methods of anal-

ysis for dielectric waveguides - approximate or rigorous - are therefore not suitable for the calculation of propagation characteristics of the SIIG. A three-dimensional technique which is capable of handling such a relatively complex structure is required for this task. The finite-difference (FDFD, FDTD) and finite-element methods (FEM) are the most versatile fully numerical methods and allow to discretize the SIIG structure quite accurately. Commercial software based on these methods was therefore used for the simulation of the SIIG propagation properties and a variety of passive SIIG components studied in this thesis. The High Frequency Structure Simulator (HFSS®) from Ansoft Corporation served as finite-element tool in the frequency domain whereas Microwave Studio® from Computer Simulation Technology (CST-MWS) covers the finite integration technique (FIT) [53], which is equivalent to the FDTD method, but is based on the integral representation of Maxwell's equations instead of the differential form, implicating some numerical differences. Figure 1.4 shows the FEM mesh of one half of an SIIG unit cell (symmetry is exploited in the HFSS® simulation). Curved boundaries like the air holes in the substrate are well approximated by the tetrahedral FEM mesh, but not discretized in an exact way. This discretization error is typically small and can be neglected for practical cases. The cubical FDTD mesh used in CST-MWS constitutes a rather course approximation of curved boundaries. However, the perfect boundary approximation, a proprietary algorithm included in CST-MWS, projects the staircase mesh on the actual structure and thus renders an accurate simulation of complex curved structures possible. Other FDTD software often uses conformal meshing for comparable improvement.

The propagation properties of a certain mode in a straight SIIG are described by its complex propagation constant

$$\gamma = \alpha + j\beta \,, \tag{1.1}$$

where α is the attenuation constant and β the phase constant. Two different techniques were used to obtain γ [23], in particular that of the most important fundamental E_{11}^{y} mode.

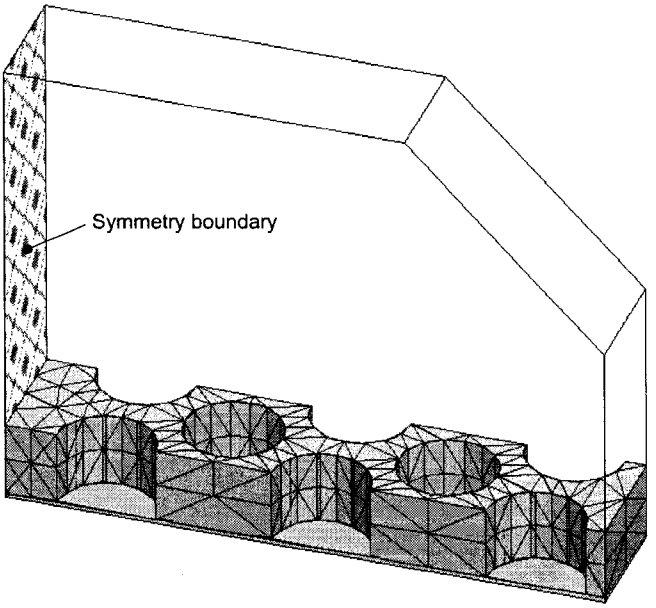

Figure 1.4 SIIG unit cell (substrate) discretized by FEM mesh. Only one half of the unit cell has to be simulated by use of a symmetry boundary.

The dual-line technique

The first method is a dual-line technique, i. e. two SIIG sections differing in length are simulated by driven modal analysis and the propagation constant is extracted subsequently from the pair of S-parameters. Such an approach was applied before to the analysis of the substrate integrated non-radiative dielectric guide [54]. Wave ports are applied to excite the structure and to receive the system response. However, the transverse electromagnetic modal fields are calculated by a two-dimensional eigenmode analysis therefore are valid only for a uniform waveguide without structural change in the direction of propagation. As a consequence, those excitation ports cannot be defined directly on a cross-sectional plane of the periodic SIIG directly. Short sections of uniform equivalent dielectric image guide are therefore added on each side to fulfill this precondition. Perforated zones are replaced by homogeneous material with reduced permittivity. In [54], a mathematical technique [55] was employed to compensate the imperfect field matching

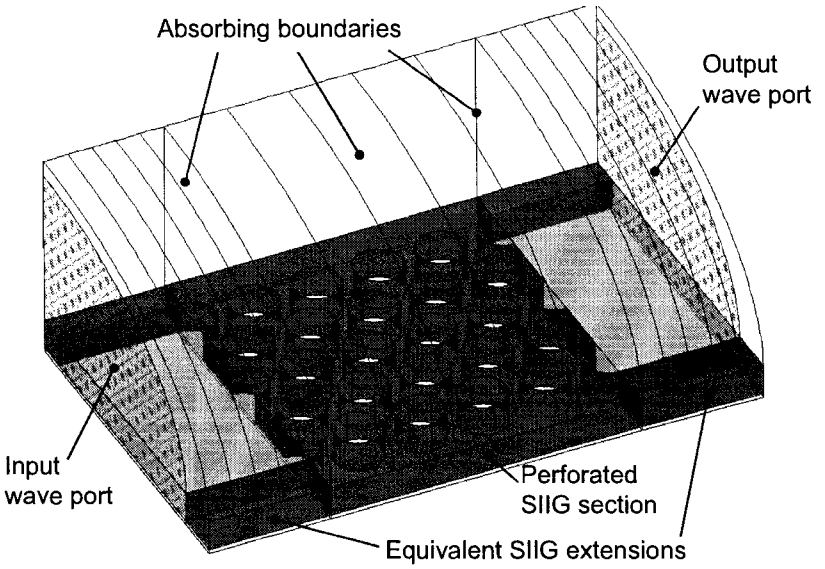

Figure 1.5 One half of the short SIIG section with uniform port extensions for the simulation of the complex propagation constant by the dual-line method.

between the uniform model and the real 3-D periodic SINRD. However this technique can only be applied to non-radiative models which can be treated as two-ports without restriction. Since the occurring radiation in an open structure like the SIIG cannot be assessed, this technique is not valid in this case. For this reason it is very important that the uniform sections are well matched to the actual SIIG, so that reflections and radiation at the interface are minimized. More details on how to choose the width of the equivalent guiding channel and the lowered uniform permittivity for optimized matching are given in subsection 1.4.5. Figure 1.5 shows the simulated shorter SIIG section having a length of five unit cells. Only one half of the geometry is considered in the simulations because of the structural symmetry. The symmetry boundary is then either a magnetic wall for analysis of even modes or an electric wall for odd modes. The length of the uniform extensions should be around half a wavelength for smooth transition to the wave ports. Absorbing boundaries were applied to the outer surfaces of the open structure in order to maintain the open waveguide character and allow radiation and leakage to take place.

Results for the attenuation constant will only be accurate if the absorbing boundaries are situated far enough from the guide core to avoid interaction with the guided waves. A 3-mm radius around the core was found to be sufficient for practical situations at 94 GHz. Power absorption will always occur at lower frequencies where field confinement of the dielectric guide is less pronounced. The length difference between the short and the long line sections was chosen two periodic intervals. A longer difference can help to average numerical imprecision or mismatching phenomena, but produces higher computational effort. After obtaining a pair of complex transmission S-parameters ($\boldsymbol{S}_{21}$) for the two differing line sections, the propagation constant is calculated from the phase difference as follows:

$$\beta = \frac{\left|\angle\left(\boldsymbol{S}_{21,\mathrm{long}}\right) - \angle\left(\boldsymbol{S}_{21,\mathrm{short}}\right)\right|}{\Delta l} \,. \tag{1.2}$$

$\angle\left(\boldsymbol{S}_{21,\mathrm{long}}\right)$ and $\angle\left(\boldsymbol{S}_{21,\mathrm{short}}\right)$ denote the absolute phase in radian of the simulated complex transmission S-parameters of the long and short SIIG sections, respectively. Δl is the difference in length in meters. Provided that the uniform port extensions and the perforated SIIG sections are well matched, the attenuation constant α is readily extracted from the magnitude ratio of the pair of $\boldsymbol{S}_{21}$-parameters:

$$\begin{aligned} \left|\boldsymbol{S}_{21,\mathrm{long}}\right| &= \left|\boldsymbol{S}_{21,\mathrm{short}}\right| \mathrm{e}^{-\alpha\cdot\Delta\mathrm{l}} \\ \alpha &= \frac{-\ln\left(\left|\boldsymbol{S}_{21,\mathrm{long}}\right| / \left|\boldsymbol{S}_{21,\mathrm{short}}\right|\right)}{\Delta l} \,. \end{aligned} \tag{1.3}$$

The 3-D eigenmode technique

Another useful technique that was successfully applied to the analysis of the SIIG is a 3D eigenmode analysis of a single SIIG unit cell. Compared to the two-line technique, it is more efficient with regard to simulation time and resources. Moreover, results for the complex propagation constant are more precise in general since no field matching between homogeneous and perforated sections are required. Figure 1.6 shows half of the SIIG unit cell (symmetry) and the simulated electric vector field on the cross-sectional

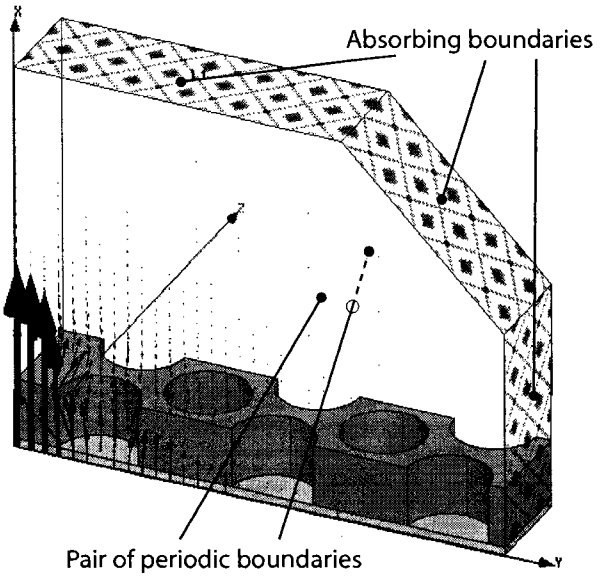

Figure 1.6 One half of the symmetric SIIG unit cell used for 3-D eigenmode simulation. The electric vector field is shown in the cross section.

plane. The distribution of the scalar electric and magnetic field in the SIIG cross section is presented in Figure 1.7. The field confinement in and around the guiding channel is strongly dependent on frequency and is shown here for the "worst case" at a minimum usable frequency. Even though the fundamental mode of the image guide theoretically has no cutoff frequency, operation at lower frequencies is not advisable due to unacceptable leakage and radiation at discontinuities and also because distances to keep between guiding channels in integrated circuits would become excessive. This topic is discussed in more detail in subsection 1.4.1.

The 3-D eigenmode technique demands for input of the phase difference between the pair of periodic boundaries prior to simulation. As a result, the phase constant β at the obtained eigenfrequency f is simply calculated from this phase difference and the length of the unit cell, which is equal to lattice constant p. The waveguide dispersion $\gamma = \gamma(f)$ is then computed in an inverse way, i. e. the eigenfrequency as a function of the complex propagation constant, $f = f(\gamma)$. The propagation constant is predefined to be purely

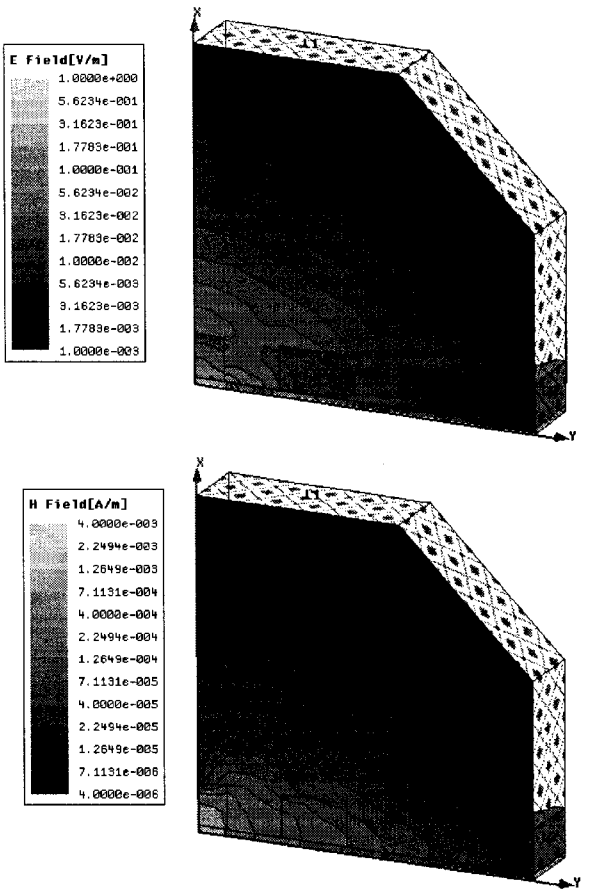

Figure 1.7 Electric (upper graphic) and magnetic field distribution in and around the SIIG guiding channel at the lowest practical frequency.

imaginary for numerical analysis, i.e. $\boldsymbol{f} = \boldsymbol{f}(\beta)$. Any kind of loss, which would normally result in a complex propagation constant, yields a complex eigenfrequency $\boldsymbol{f}_0 = f_{0,\text{real}} + f_{0,\text{imag}}$. An unloaded Q-factor as defined for transmission-line resonators is derived by HFSS as follows:

$$Q = \left| \frac{\Re\{\boldsymbol{f}_0\}}{2 \cdot \Im\{\boldsymbol{f}_0\}} \right| . \tag{1.4}$$

This is a valid approximation for weak line attenuation [56]. In general, for a dispersive

transmission line, the Q-factor is related to the attenuation constant by

$$\begin{aligned} Q &= 2\pi f \frac{\text{energy/unitlength}}{\text{powerloss/unitlength}} \\ &= 2\pi f \frac{P/v_g}{-\mathrm{dP/dz}} = \frac{2\pi f}{v_g 2\alpha}, \end{aligned} \tag{1.5}$$

where P is the real power flowing through the waveguide in z-direction and v_g is the group velocity which is equal to the velocity of energy transportation. Since β is already known, the attenuation constant α can readily be extracted by

$$\alpha = \frac{f}{2Q} \cdot \frac{2\pi}{v_g} = \frac{f}{2Q} \cdot \frac{\mathrm{d}\beta}{\mathrm{d}f}. \tag{1.6}$$

The validity of this technique for extracting the attenuation constant α was later shown in [57].

Comparison of both techniques

Simulation results presented in the following are based on a SIIG made of 380 µm thick high-resistivity (HR) silicon substrate (ε_r = 11.7, ρ > 10 kΩ·cm) with a guiding channel width of 510 µm. The holes of 0.5 mm diameter are arranged in an equilateral pattern with p = 0.645 mm inter-hole spacing and the thickness h of the FEP (fluorinated ethylene-propylene copolymer, a PTFE-like plastic, ε_r = 2.08) insulation film is 50 µm. The two described methods of analysis are compared in Figure 1.8 with regard to SIIG dispersion. Both computed curves are virtually identical, which proves the accuracy of the different approaches.

SIIG attenuation properties are closely related to the material properties, i.e. dissipation factors of the insulating film and the substrate, as well as the conductivity of ground plane. All simulation results in this section are based on dissipation factors of $\tan\delta = 1 \cdot 10^{-3}$ for the FEP film and $\tan\delta = 7 \cdot 10^{-4}$ for the HR-silicon. The conductivity of

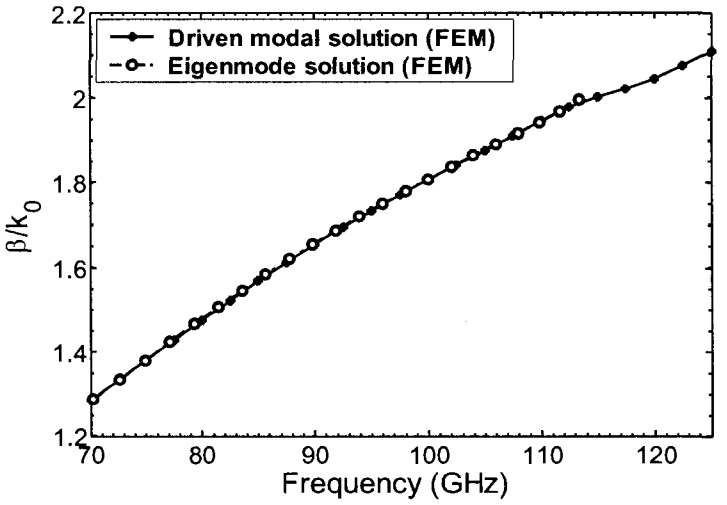

Figure 1.8 Comparison of the SIIG dispersion (normalized phase constant) obtained by a driven modal solution and a 3-D eigenmode solution with HFSS, respectively. Core dimensions are 510 μm × 380 μm ($w \times d$) on HR-silicon.

the aluminum ground plane is $3.8 \cdot 10^7$ S/m although conductor losses tend to be higher in reality due to the surface roughness. Figure 1.9 shows the simulated guide attenuation. A distinct stop-band can be observed at a center frequency of 116 GHz. Such a phenomena is often called electromagnetic band gap (EBG) or photonic band gap and is caused here by distributed Bragg reflection at the one-dimensional periodic discontinuities (the air holes) of the SIIG. The lowest EBG occurs when the guided wavelength λ_g equals twice the periodic interval p, i. e.

$$\lambda_g = 2p = \lambda_{\text{Bragg}} \frac{k_0}{\beta} = \frac{\lambda_{\text{Bragg}}}{n_{\text{eff}}} \,. \tag{1.7}$$

λ_{Bragg} is called the Bragg-wavelength and n_{eff} is the effective refractive index of the waveguide. In this case, the reflected electromagnetic waves add up constructively towards the waveguide input. Amongst others, the width of such an EBG depends on the amount of reflected power from a single discontinuity. The more the discontinuity is pronounced, the wider is the band gap. Since the attenuation in the direction of propagation

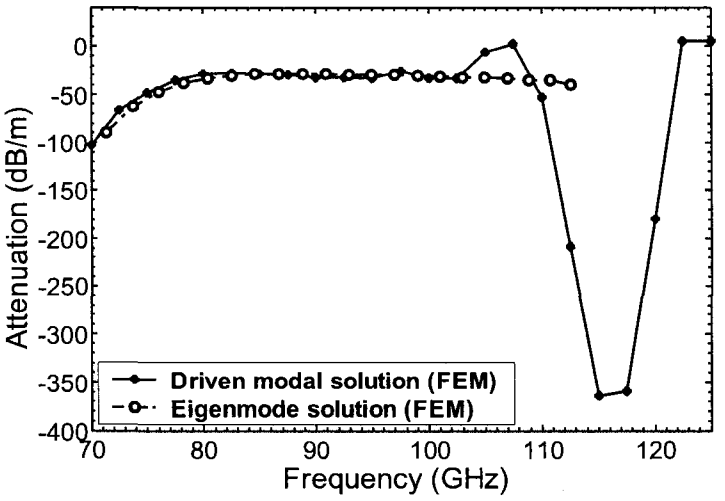

Figure 1.9 Comparison of the SIIG waveguide attenuation obtained by HFSS driven modal solution and 3-D eigenmode solution.

follows an exponential function, an effective depth of penetration can be introduced and therefore it is possible to speak of an effective length of distributed reflection. Advantage is taken of this sort of periodic reflections for certain filter and coupling applications in optics [58] and in the same way it provides an opportunity for the design of band-stop and band-pass filters at millimeter-wave frequencies [15]. Figure 1.10 shows the lattice constant's relation to the center frequency of the EBG for specific SIIG dimensions. Every single curve point was obtained by setting the phase difference between the periodic boundaries in the 3-D eigenmode analysis to π, thus yielding a standing wave. Since the EBG has a certain width, which is also dependent on the guide length, a certain guard distance is to be kept between its center frequency and the highest operation frequency.

The curve in Figure 1.9 obtained from the two-line method shows overshooting next to the stop band. The reason is the wider band gap produced by the shorter SIIG section in comparison to the longer one. Results obtained from the 3-D eigenmode solution implicitly involve the solution of an infinite periodic structure. Reflections are not con-

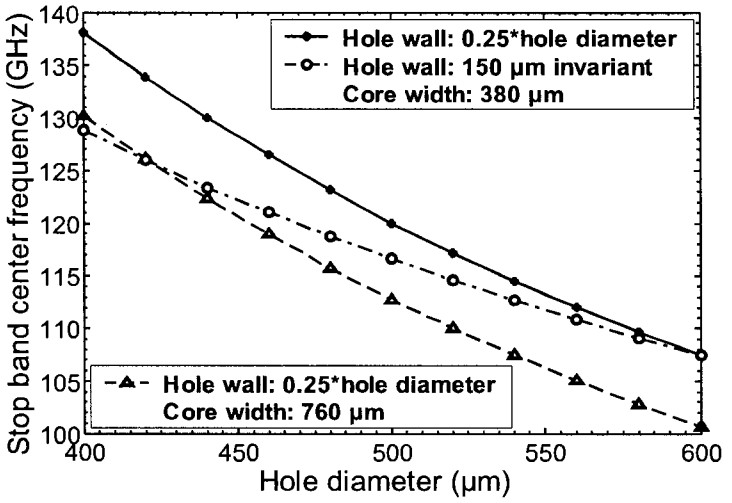

Figure 1.10 Center frequency of the EBG in dependence on the air hole diameter and the lattice constant. The thickness d of the HR-silicon substrate is 380 µm for all curves.

sidered in the eigenmode approach and therefore no stopband is visible in the attenuation graph. For both analysis methods, line attenuation increases dramatically towards low frequencies as a consequence of the weak field concentration around the guiding channel. When fields touch on the outer absorbing boundaries, energy is absorbed and leads to attenuation. This relation gives an indication on the lowest usable frequency in order to obtain good guiding properties. A limitation of the 3-D eigenmode unit cell analysis is given by the fact that the insertion loss due to superimposed reflections is not taken into account. Only material and leakage losses can be extracted from the results because the solution type is not of the excitation-response type and S-parameters are not available as a consequence. The EBG that occurs if the Bragg condition (1.7) is fulfilled is thus not visible in the eigenmode results. As a concluding statement, it can be said that the two-line method is more general and is applicable to a wider range of problems, whereas the 3-D eigenmode solution is faster and more precise, but is limited to infinite periodic structures and cannot take into account distributed reflection phenomena.

1.4 Design guidelines for SIIG dimensional parameters

As illustrated in Figure 1.3, the SIIG involves many design parameters that can be changed independently. This leads to an enormous flexibility but also to a higher design complexity. The influence of the diverse dimensions is demonstrated by means of parametric simulations.

1.4.1 The bandwidth of SIIG

The single-mode bandwidth of an image guide of specific geometry is a question of definition. A clear and unambiguous answer is therefore not possible and it is recommended to refer to a "useable" or "practical" bandwidth for the specific case.

In theory, the fundamental E_{11}^{y} mode has no cut-off frequency and is (very loosely) guided even at very low frequencies. However, the wave is very loosely bound in that case, the fields extend very far from the dielectric core, and radiation would occur at the slightest discontinuity. Such a scenario cannot be accepted in practice, especially in integrated circuits, where available space is scarce. A paper discusses the question of image guide bandwidth [59] and several other definitions for the lower bandwidth limit are proposed. A definition for the lower bandwidth limit could be the maximum allowable field extension from the core or a specified ratio of the power guided in the dielectric to the power guided in the surrounding air. Other proposed definitions, based on a limitation of dispersion or change of characteristic impedance, seem to be very vague and not useful to apply to an integrated waveguide technology.

The upper limit of the single mode bandwidth can be defined by the cut-off frequency of the next higher-order mode, usually the E_{21}^{y} mode for small aspect ratios of width and height of the guiding channel. On the one hand, this cut-off is, in general, not easy to determine exactly by numerical methods. On the other hand, mode coupling is negligi-

ble at frequencies near cut-off, where the higher-order mode is very loosely bound. A reasonable choice for the upper bandwidth limit is therefore close to the point where the field confinement of the higher-order mode starts to rise noticeable with frequency.

Agreement is found in the literature to the statement that the widest bandwidth can be achieved for the standard image guide with a guiding channel aspect ratio of 2:1 (width $\times$ height) [13, 59]. The insulated image guide, on which the SIIG is based, should have an aspect ratio close to unity for a maximum practical bandwidth [13]. The reason is the influence of the low-permittivity insulation film which decreases the cut-off frequency of the E^y_{21} mode relative to the E^y_{11} mode. This decrease can be compensated with a somewhat narrower guiding channel. Nevertheless, a narrower bandwidth has to be accepted for the insulated image guide in comparison to its counterpart without insulation film.

As for the SIIG, a maximum refractive index contrast between the unperforated guiding channel and the perforated adjacent zones is beneficial not only for well confined wave guidance but also to maximize the usable single-mode bandwidth. Thus, it is desirable to use a high-permittivity material and to remove as much of the substrate material as possible in the perforated zones. The equilateral hole pattern is the most effective and was therefore used for the SIIG. The operating frequency range of an SIIG is strongly dependent on the substrate thickness d. High-permittivity substrates ($\varepsilon_r \approx 9...13$) of approximately 400 µm thickness are a good choice for the 94-GHz range. Such dimensions are good to handle in contrast to much thinner substrates needed for microstrip, for example. The width of the guiding channel w (core width) has a smaller influence on the fundamental mode, but plays a major role in maximizing the usable single-mode bandwidth, since it strongly affects the E^y_{21} mode. The dispersion diagram in Figure 1.11 shows this interrelation graphically. Relating to original core dimensions of 760 µm $\times$ 530 µm ($w \times d$), the phase constant β does not change dramatically for a 33 % decrease

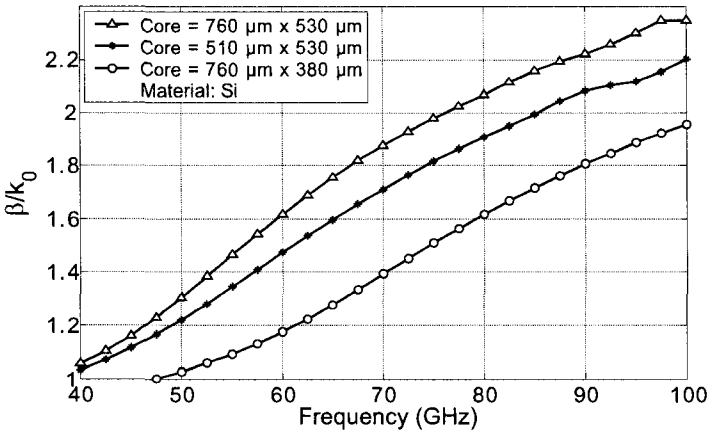

Figure 1.11 E_{11}^{y} mode dispersion behavior for SIIGs of differing core dimensions. Modifying the substrate thickness d has much more influence than altering the guiding channel width w.

in width. However, the response is much more significant if the substrate thickness is reduced by 28 %.

The lower SIIG bandwidth limit is determined by requirements on the field confinement around the guiding channel. Too weak confinement results in high radiation levels at discontinuities and must be avoided. The upper limit is given by the cut-off or divergence frequency of the next higher order mode E_{21}^{y}. However, the transition from divergence to guidance is not sharp. Coupling to this mode becomes possible at discontinuities if the field confinement increases towards higher frequencies. Figure 1.12 shows the unloaded transmission line Q-factor for the first and second modes obtained by 3-D eigenmode simulation with HFSS. Derived from the computed curves in Figure 1.12, the lower limit of the useable single-mode bandwidth is at the frequency where the Q-factor has nearly reached its quasi-constant value for the fundamental mode. This limit depends on how far the outer absorbing boundaries are away from the SIIG center. A clearance of 3 mm was chosen as the basis of our simulations because bigger distances do not, in practice, make sense for integrated circuits. The upper bandwidth limit is the

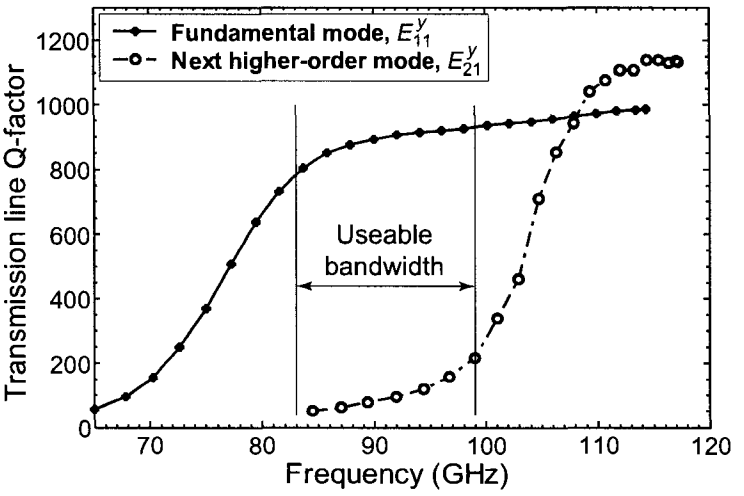

Figure 1.12 Unloaded transmission line Q-factor for the fundamental and the first higher order mode of a silicon SIIG. Core dimensions: 510 μm × 380 μm

frequency where the factor for the second mode starts to rise quickly, indicating that this mode has passed the divergence frequency. Following these definitions of the bandwidth limitations (which are used in this entire thesis), the useable single-mode bandwidth of the example SIIG ranges from 83 GHz to 99 GHz, which yields a relative bandwidth of 17.6 %. The values given here are related to engineering practice and slightly depend on numerous parameters. In this way, by analyzing SIIGs with various core dimensions, the graphs in Figure 1.13 were generated. They show the relative bandwidth in dependence on core width and insulating film thickness as a parameter. An optimum is obtained if the width and height of the guiding channel are approximately equal, which is in agreement with statements for the conventional insulated image guide [13].

1.4.2 SIIG attenuation

The use of a thin insulation film entails a broad useable bandwidth. However, a trade-off has to be made because a thicker film can significantly reduce conductor losses.

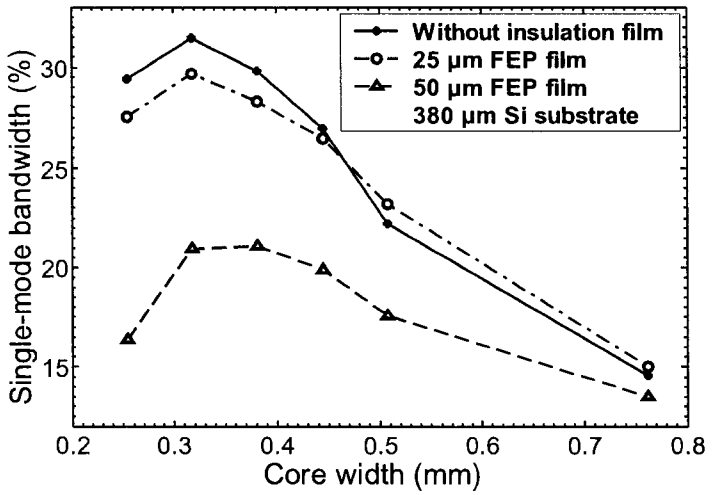

Figure 1.13 Useable (practical) SIIG single-mode bandwidth in dependence on the core width w and the insulation film thickness h as a parameter.

Attenuation for silicon SIIGs with different insulation film thickness on an aluminum ground plane is shown in Figure 1.14. As expected, the highest attenuation is observed in the absence of an insulation film. Increasing the film thickness reduces attenuation, but no relevant improvement can be observed above a certain value. A thickness of about one-tenth of the substrate height is a reasonable compromise, which is a confirmation of the findings in [13]. In other HFSS simulations, the aluminum ground plane was replaced by a perfect conductor, so as to remove all conductor loss. The results are shown in Figure 1.15. It can be noticed that all three configurations approximately possess the same loss level, only somewhat shifted in frequency. In another experiment, the dielectric losses were removed, the effect being shown in Figure 1.16. This time there is a clear difference in attenuation loss. For the employed materials (HR-silicon, FEP insulation film, and aluminum ground plane), it was found that about two-thirds of the losses can be attributed to dielectric losses. Only in the case without the insulation film, the dielectric losses are approximately equal to the conductor losses. This fact

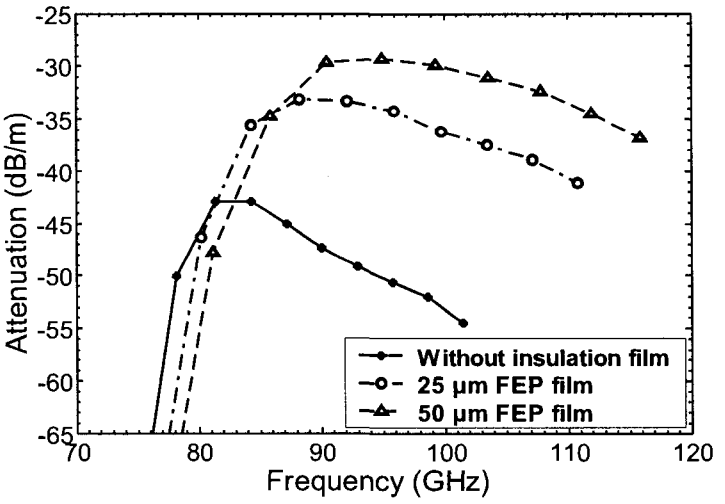

Figure 1.14 Waveguide attenuation of an HR-silicon SIIG for different insulation film thicknesses. Core dimensions: 380 μm × 380 μm.

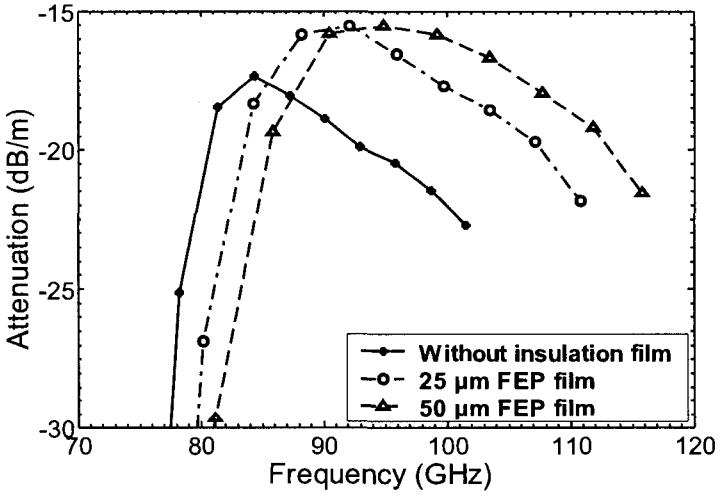

Figure 1.15 SIIG attenuation without taking into account conductor losses.

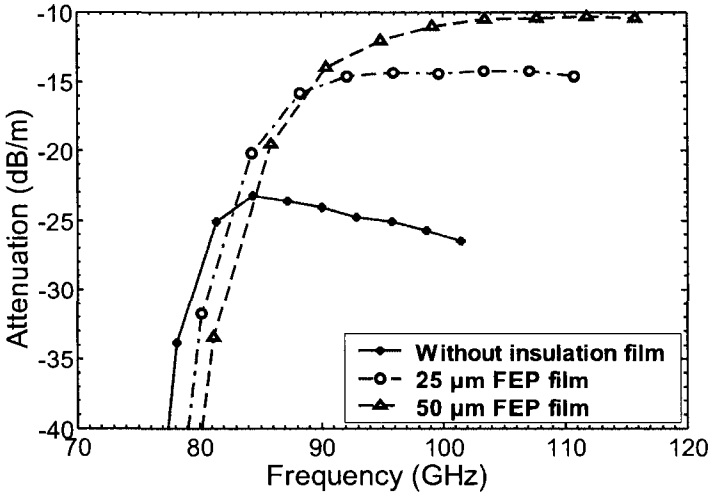

Figure 1.16 SIIG attenuation without taking into account dielectric losses.

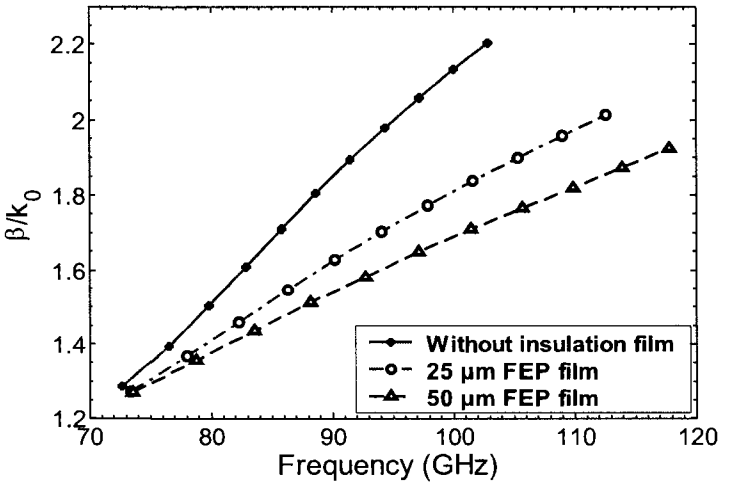

Figure 1.17 SIIG dispersion for different insulation film thicknesses.

emphasizes that low-loss dielectrics are essential for low SIIG attenuation. The use at higher frequencies is possible, because this mostly affects conductor losses.

Dispersion curves are drawn in Figure 1.17 for the three different insulation film thicknesses. It can be observed, that dispersion is less pronounced for thicker insulation

films.

1.4.3 Substrate leakage

Avoidance of leakage in connection with substrate modes is another important design criterion for SIIGs. In principle, the E_{11}^{y} mode is guided without leakage and is not disturbed by the periodic arrangement of holes. The electromagnetically denser core region keeps the guided wave on track, at least in straight sections. However, if guided-wave fields reach the unperforated substrate material beyond the perforated zones, energy leaks away into the surrounding substrate. This is due to the slower propagation velocity in the surrounding substrate (= grounded slab) compared to the guided wave in the SIIG core. The unloaded transmission line Q-factor was simulated for SIIGs with varying width of the perforated zones. Figure 1.18 shows the influence of the perforation width. Five rows of air holes, corresponding to a distance of approximately 3 mm between the SIIG center and the absorbing boundaries, were used for all prior simulations

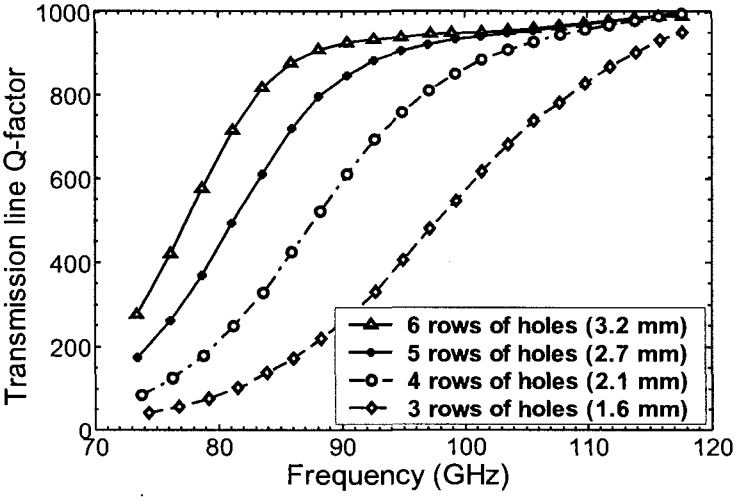

Figure 1.18 Unloaded transmission line Q-factor over frequency for various widths of the perforated zones adjacent to the guiding channel.

in this chapter. As can be seen, further increase yields only slight improvement and the field confinement must be sufficient in any case for applications in integrated circuits. Narrower perforated zones, however, limit the useable bandwidth unnecessarily and are therefore not recommended unless part of the bandwidth can be sacrificed for a specific application.

1.4.4 Essential differences between the SIIG and 2-D photonic crystal defect waveguides

It is very important to realize that the SIIG is *not* a photonic crystal defect waveguide. Even though it looks similar to previously proposed photonic crystal slab waveguides [60, 61], the SIIG is not operated in an EBG region of the periodic hole lattice, but at frequencies inferior to the bandgap. The periodic pattern of equally sized holes is chosen for design and fabrication convenience and the perforation only serves to reduce the effective permittivity in these regions in order to achieve *total internal reflection*. For instance, foam-like statistically distributed cavities of irregular shape would also do as long as the guided wave sees a dielectric with quasi-homogeneous lowered effective permittivity in this area. The difference between the two guiding mechanisms was discussed in [62, 63]. Besides the disadvantages of inferior field confinement and guidance along bends, the SIIG has two substantial advantages over the class of corresponding photonic crystal slab waveguides presented in [61]. It provides a broader operating bandwidth and low or no radiation. For operation in the bandgap region of a photonic crystal, the lattice period must be chosen slightly longer than half a guided wavelength. which generates fast-wave spatial harmonics that radiate in vertical directions, in which the wave is only bound by a refractive index step. This limitation is explained in more detail in the following.

Leaky-wave radiation occurs if fast-wave space harmonics exist at a certain frequency. According to Floquet's theorem for periodic structures, the expansion into space

harmonics β_n is given by

$$\beta_n = \beta + \frac{2n\pi}{p} \,, \tag{1.8}$$

where β is the phase constant of the guided wave, n is an index, and p is the periodic interval. Fast wave space harmonics exist for

$$\underbrace{\left|\beta + \frac{2n\pi}{p}\right|}_{\beta_n} < k_0 \,, \tag{1.9}$$

i. e. when the phase velocity of the space harmonic is higher than that of a wave propagating in the vacuum with wave number k_0. The backfire condition for leaky-wave radiation is

$$\begin{aligned} p\,(\beta + k_0) &= 2\pi \\ \frac{1}{\lambda_g} + \frac{1}{\lambda_0} &= \frac{1}{p} \,, \end{aligned} \tag{1.10}$$

where λ_0 is the free space wavelength and λ_g the guided wavelength. The following condition has to be fulfilled in order to avoid leaky-wave radiation:

$$p < \frac{\lambda_0 \lambda_g}{\lambda_0 + \lambda_g} \,. \tag{1.11}$$

In other words, the periodic interval p between the air holes must be smaller than this distance which depends on the dispersion characteristics and consequentially on the substrate material used for the SIIG. Since λ_g is always somewhat greater than λ_0, leaky-wave radiation only occurs at frequencies higher than the first electromagnetic band gap (EBG). Towards longer intervals p, or equivalent, higher frequencies or shorter wavelengths, the leaky-wave beam will move from backfire towards endfire direction. This is the typical frequency-scanning property of leaky-wave antennas, which is treated in more detail in section 3.2.

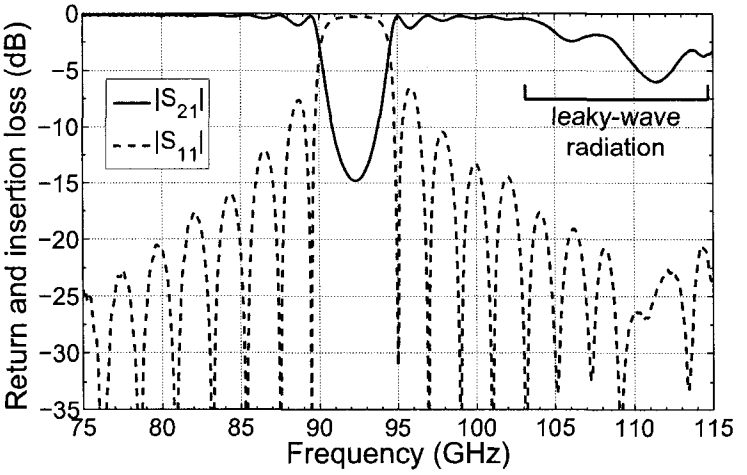

Figure 1.19 Time-domain simulation results (CST-MWS) for a HR-silicon SIIG with coarse hole lattice. Insertion loss due to leaky-wave radiation is noticeable beyond the EBG.

The theoretically predicted leaky-wave radiation at frequencies above the EBG can be observed from the simulated insertion loss graph (CST-MWS) in Figure 1.19. Since the return loss is small in that range and lossless materials were used in the simulation, the insertion loss must be a result of radiation. Dimensional parameters for the coarse HR-silicon SIIG simulation model are d = 525 μm, w = 510 μm, FEP film thickness h = 50 μm, hole diameter $2r$ = 0.6 mm, lattice constant p = 0.7725 mm, and overall length $26p \doteq 20$ mm. For this reason, the SIIG should not be operated above the first EBG of the periodic hole lattice, whereas other, shielded waveguides like the SIW can be without any difficulties [24]. It is however possible to operate the SIIG in or close to the EBG if high reflections are desired, e. g. for the design of band-pass and band-stop filters based on distributed Bragg reflection [15]. According to (1.11), no radiation leakage is expected in the vicinity of the EBG.

Another advantage of the SIIG over photonic crystal guides concerns fabrication complexity. Although tolerance requirements in the mmW-range are generally strict,

they are not comparable to those for photonic crystal defect waveguides, where an exact periodicity of the lattice is crucial to obtain the desired EBG.

1.4.5 Equivalent uniform SIIG model

An equivalent uniform SIIG model has already been introduced in subsection 1.3.3, where it was used to excite SIIG modes by means of two-dimensional wave ports. It was mentioned that good matching between the uniform and the three-dimensional periodic sections is necessary to obtain accurate results for the phase and attenuation constants by the dual-line technique. Modal fields are sufficiently similar so that low reflections at the interface between uniform and non-uniform parts can be achieved by matching the phase constant β. Extensive simulations by the 3-D eigenmode technique were conducted in order to find a simple uniform waveguide structure which allows close matching of β. A geometry that fulfills this requirement is shown in Figure 1.20. It is very similar to the actual SIIG except for the perforated regions, which are replaced by homogeneous material of lower effective permittivity ε_{eff} compared to the substrate permittivity $\varepsilon_{\text{substrate}}$.

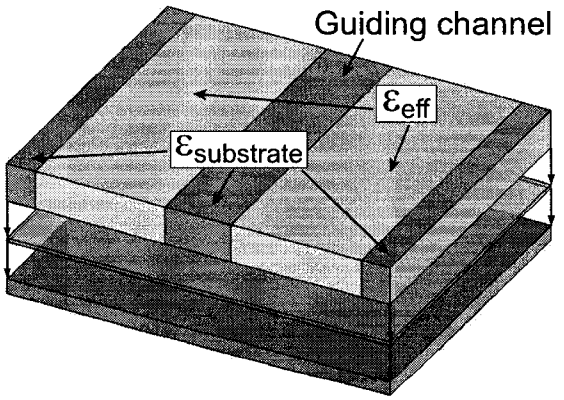

Figure 1.20 Equivalent uniform SIIG model. The perforated regions of the original SIIG are replaced by a homogeneous dielectric with lowered permittivity ε_{eff}.

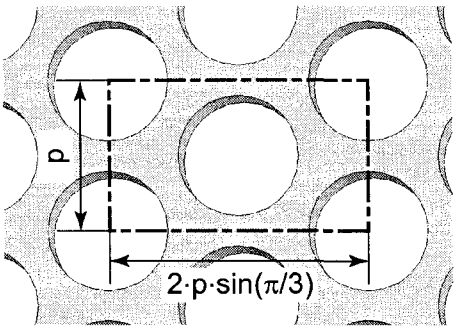

Figure 1.21 Unit cell of the equilateral hole pattern.

Insulation film and substrate thickness are left unchanged, yielding two adjustable parameters, namely the effective permittivity ε_{eff} and the effective core width w_{eff}.

It was tried to derive the optimum ε_{eff} directly by analytical methods. For an E-field polarization that is normal to the substrate plane, the calculation of the effective electrostatic permittivity is straightforward. It consists of calculating the weighted average of the filled and non-filled (air holes) substrate regions [32]. Figure 1.21 shows a unit cell of the hole lattice. The volumetric average of the relative permittivity consequently is:

$$\varepsilon_{\text{eff}\perp} = \varepsilon_{\text{substrate}} + (\varepsilon_0 - \varepsilon_{\text{substrate}}) \frac{r^2\pi}{p^2 \sin(\pi/3)} . \tag{1.12}$$

(1.12) is a good approximation as long as the wavelength is much longer than the lattice constant p. Increasing field confinement at higher frequencies leads to considerably higher values as in the electrostatic case. Figure 1.22 shows this effect for a perforated silicon substrate (ε = 11.7) with hole radius r = 230 µm and lattice constant p = 575 µm. The electrostatic value according to (1.12) is $\varepsilon_{\text{r,eff}\perp}$ = 5.49.

The electrostatic effective permittivity for in-plane E-field polarization cannot be calculated analytically. Ansoft's electrostatic FEM solver Maxwell® 2D was used to calculate $\varepsilon_{\text{eff}\parallel}$ = 4.04 for in-plane polarization based on the last-mentioned hole lattice

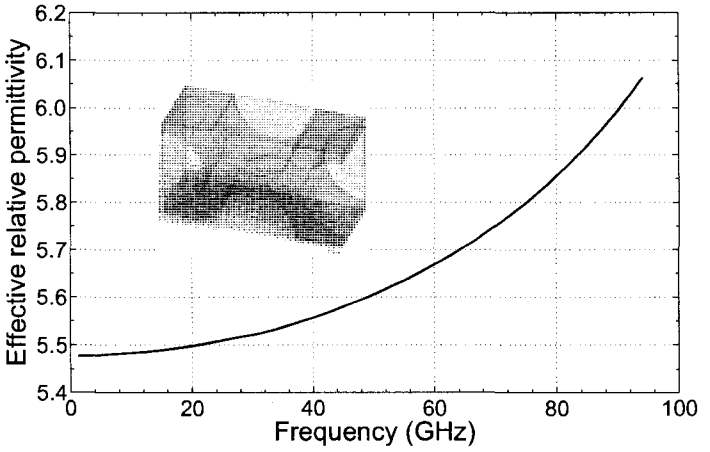

Figure 1.22 Frequency-dependent effective permittivity of a perforated silicon substrate (r = 230 μm, p = 575 μm) for E-field polarization normal to the substrate. The data was obtained by HFSS eigenmode simulation of a single unit cell.

dimensions. A graph that shows $\varepsilon_{r,eff\|}$ in dependence on frequency is shown in Figure 1.23.

When the obtained effective permittivities – either the electrostatic values or the somewhat different ones at higher frequencies – were used in the uniform SIIG model, no satisfactory matching of the phase constant β could be achieved. However, optimization led to an almost perfect phase matching over a wide frequency range, as shown in Figure 1.24. Optimized parameters are ε_{eff} = 3.7 and w_{eff} = 540 μm, whereas the core width of the the original SIIG is w = 510 μm. The substrate height d and the insulattion film height d are left at 380 μm and 50 μm, respectively. The optimized ε_{eff} is lower than expected. In fact, the modal fields are not equally distributed over the perforated zones as was falsely assumed in the above calculations. In reality, the majority of the E-field is confined in the guiding channel and exponentially declines to adjacent regions. Consequentially, the air holes right next to the guiding channel have great influence and therefore the effective permittivity has to be chosen lower. As for the effective core width, w_{eff} is slightly wider in the equivalent model. This fact can be explained by the

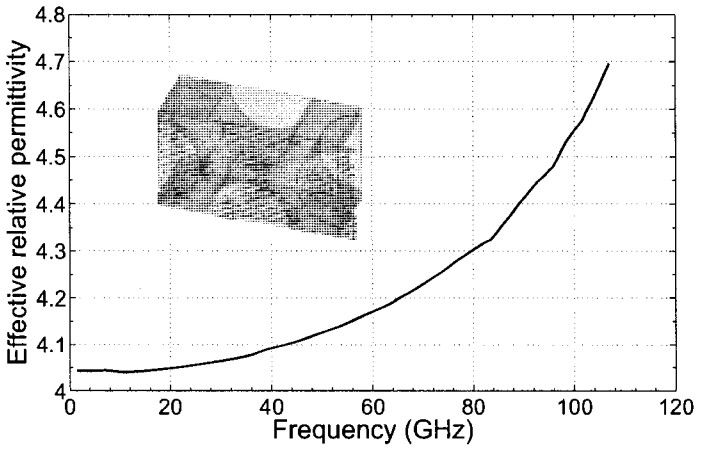

Figure 1.23 Frequency-dependent effective permittivity of a perforated silicon substrate (r = 230 μm, p = 575 μm) for E-field polarization in parallel to the substrate. The data was obtained by HFSS eigenmode simulation of a single unit cell.

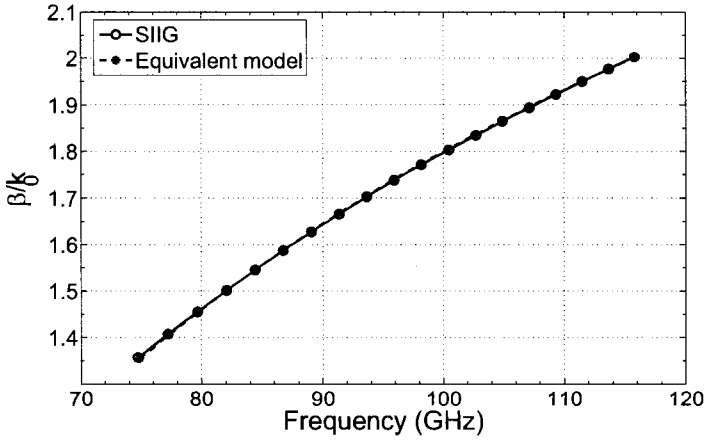

Figure 1.24 Comparison of the dispersion of the actual SIIG and its optimized equivalent model. Parameters of the equivalent are w_{eff} = 540 μm (w = 510 μm) and $\varepsilon_{\text{r,eff}}$ = 3.7.

round air holes, which lead to a meander-like delimitation of the guiding channel, similar to the SIW.

Such an equivalent uniform model is not only useful for efficient mode excitation in simulation tools, but can also serve to simplify the design of passive components. Its discretization is simpler and faster methods of analysis are available, as described in subsection 1.3.2. The equivalent model is then replaced by the actual SIIG in the final stage where usually only slight optimizations are necessary. Such a procedure was also applied successfully to SIW designs.

1.4.6 A note on the characteristic impedance of image guide

The characteristic impedance is a very useful concept for the treatment of (quasi-) TEM waveguides as transmission lines in circuit theory. However, it has to be applied with caution to other types of waveguides which have only one or no conductor involved for wave guidance. Basically, three definitions exist: the power-current impedance Z_{PI}, the power-voltage impedance Z_{PV}, and the voltage-current impedance Z_{VI}. The often used power-current definition, for example, is as follows [25]:

$$Z_{PI} = \frac{P_z}{|I_z|^2} = \frac{\int_0^\infty \int_{-\infty}^\infty (\mathbf{E} \times \mathbf{H}^*) \cdot \hat{z}\, dx\, dy}{\left| \int_{-\infty}^\infty H_x\, dx \right|^2} \tag{1.13}$$

Z_{PI}, Z_{PV}, and Z_{VI} are identical for TEM waveguides only, but can differ considerably for other waveguides, which frequently leads to erroneous results in circuit simulations. In addition, the level and phase of reflection at a waveguide discontinuity not only depends on the impedance mismatch, but also on the field mismatch. A step in a metal waveguide, for instance, introduces an inductive or capacitive effect due to the occurring field distortion and excitation of higher order modes [64, 65]. In the case of dielectric waveguides, field mismatching plays the most important role and the calculation of a

howsoever defined characteristic impedance becomes a minor issue. In this case it is the wave impedance Z_W, being defined as the ratio of the transversal field components

$$Z_W = -\frac{E_y}{H_x} , \tag{1.14}$$

which is more meaningful. Moreover, it has to be kept in mind that a discontinuity in an open waveguide cannot, in general, be described as a simple two-port because of the usually unavoidable radiation. For these reasons and by following the majority of authors in the field of dielectric waveguides, it was chosen to avoid the introduction of a characteristic impedance for the SIIG in this thesis.

1.5 Fabrication of SIIG components

Concerning fabrication, the SIIG Provides numerous advantages related to fabrication precision, design flexibility and assembly costs over the conventional image guide or insulated image guide. Instead of separate dielectric strips, SIIGs in millimeter-wave components and circuits are entirely mechanically connected to each other due to the single-substrate fabrication. Higher structural stability, but also improved alignment precision between SIIG lines and other, hybrid technologies on the same substrate are the consequence. It is therefore reasonable to invest more effort for component design in order to attain a mass-producible high-performance technology at low cost.

Standard image guide structures can be cut or milled out of sheet material, but those techniques do not lend themselves to cost-efficient mass-production. Casting resins were shown to work in an experimental prototype [66]. However low-loss liquefiable millimeter-wave materials are rare (high-permittivity in particular) and existing ones like paraffin are often not thermally stable. Cost, repeatability, and precision constitute other open questions, as is adhesion to the ground plane. The insulated image guide requires some kind of lamination technique to combine the ground plane, the insulation film, and

the substrate. Such bonding is much easier to achieve with SIIG technology because of its sheet geometry.

The SIIG can be fabricated by a variety of micro-fabrication techniques. Among them are laser cutting, micro-drilling or milling, wet etching, and dry etching, known as deep reactive ion etching (DRIE) for very high accuracy. As for high-quantity production, green state forming of ceramics and subsequent firing directly into final shape is possible. Mature technologies such as LTCC / HTCC are available for mass production.

Suitable materials for the fabrication of SIIG components and circuits include those which have very low dielectric loss at mmW frequencies and sufficient rigidity. As explained before, the substrate material should have high relative permittivity, preferably $\varepsilon_r \geq 9$, in order to obtain sufficient field confinement and compact circuits. These requirements are fulfilled by a variety of ceramics, semiconductors, and other pure, crystalline materials such as sapphire. Conventional microwave substrates such as Rogers'® high frequency laminates posses a tanδ of at least 20×10^{-4} and thus are recommended if lower performance is acceptable. In contrast, materials for the insulation film should have the lowest possible permittivity. Table 1.1 gives an overview of some suitable materials. Semiconductors like silicon or gallium arsenide offer low loss properties only in a very pure, high-resistivity state. Then, they can frequently be used to the terahertz range or even in optics. Since the level of impurities in the available float-zone wafers was not known exactly, a sample was measured with an open resonator setup from Damaskos®. This measurement method is close to its limit of sensibility when measuring the listed low-loss materials. The highest frequency at which consistent results for the dissipation factor could be achieved was 40 GHz. Alumina samples (from CoorsTek®) were also measured, since not only the alumina's purity plays a role, but also the composition of the binder [70, 71]. Data on the other listed material was extracted from [72].

Manufacturing of SIIGs on a semiconductor wafer is particularly interesting. The same semiconductor material can be used to fabricate active devices like diodes and

Table 1.1 Selection of low-loss dielectric materials suited for SIIG fabrication.

Material	f (GHz)	ε_r	$\tan\delta$	Reference
Alumina	40	9.7	5×10^{-4}	measured
Beryllia	140	6.8	7×10^{-4}	[67]
Silicon (HR)	40	11.7	7×10^{-4}	measured
Sapphire	72	9.4/11.6	0.4×10^{-4}	[68]
PTFE	100	2.07	5.3×10^{-4}	[69]
Polyethylene	100	2.3	3.7×10^{-4}	[69]
Polypropylene	100	2.25	7.3×10^{-4}	[69]

transistors or more complex monolithic integrated circuits. Such an approach would allow all-in-one integration of millimeter-wave front-ends.

Prototyping for experimental verification in the laboratory was most efficiently achieved by laser-cutting. It is a fast way to realize SIIG components of limited size on almost arbitrary substrate materials since only vertical cuts are needed. A frequency-doubled Nd:YAG laser (532 nm wavelength) served for all the realizations presented in this thesis. The laser beam diameter in the Gaussian beam focus is 40 μm, comparable to the thickness of a human hair. The step resolution of the x-y-table is 2.5 μm. Unlike PCB waveguides, the SIIG does not induce field singularities, which allows for relaxed fabrication tolerances. Therefore, the precision of the available laser micro-fabrication system is sufficient for most SIIG devices up to 100 GHz and above. The more accurate and cleaner DRIE technique was not available at Poly-Grames research center. It would be necessary for highly resonant filter structures and despite of the associated increased processing time it can be advantageous for simultaneous manufacturing of a larger number of devices.

Even though the bigger size compared to PCB transmission lines seems to be a disadvantage for miniaturization, it is advantageous for low-cost production since precision standards in manufacturing are more relaxed. Guiding channel dimensions in the order of half a wavelength in the used substrate material do not constitute significant difficulties for fabrication. The substrate height d is an important design parameter and cannot be chosen freely. However, the required thickness for the interesting bands between 60 GHz and 110 GHz is in the range of 300 µm and 600 µm, which is compact and very good to handle. Microstrip demands for much thinner substrates, which are not only very fragile but also by an important factor more expensive due to the difficult manufacturing process. The wall thickness between neighboring air holes should generally be chosen as small as the required mechanical stability of the structure permits. This is to obtain a maximum permittivity contrast between the guiding channel and the perforated zones. In practice, mechanical stability is reasonable to a wall thickness down to one-quarter of the hole diameter, which was used as a standard for most of the simulations and later realizations. This translates to 0.1 mm to 0.15 mm in the W-band. Hole diameter $2r$ and wall thickness together yield the lattice constant p. The latter must be chosen sufficiently small to avoid the already discussed EBG in the operating frequency range. Certainly, the hole lattice could always be chosen much finer than necessary, which would, however, increase the fabrication complexity and decrease the mechanical stability, so that an operation close to the EBG might be desirable.

A weakness of the standard image guide is the potential air gap between the metal ground plane and the dielectric strip, which is difficult to avoid unless special casting techniques [66] are used. The introduced insulation film in the SIIG not only reduces conductor losses but also provides a relief to that problem. Figure 1.25 shows the normalized phase constant of a typical silicon SIIG in dependence on the insulation film thickness h. The sensitivity to h is especially high for very thin films, which explains the great problems with small air gaps. It is much lower at a recommended thickness of

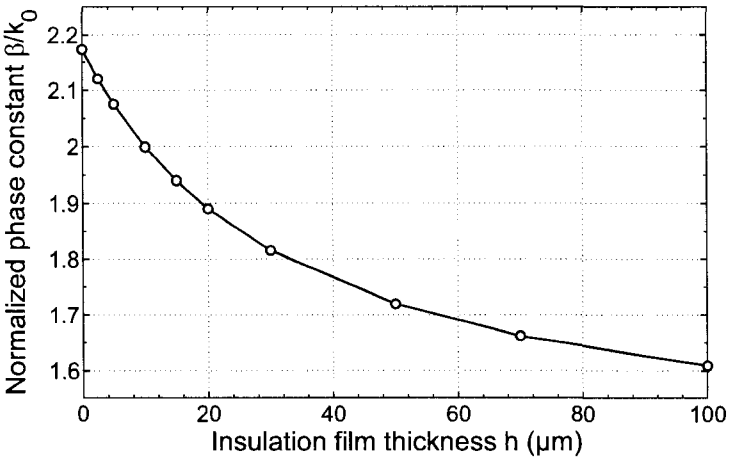

Figure 1.25 Normalized phase constant of a silicon SIIG in dependence on the insulation film thickness h at a fixed frequency of 94 GHz. Core dimensions are 510 μm × 380 μm ($w \times d$) on FEP insulation film ($\varepsilon_r = 2.08$).

one-tenth of the substrate thickness, about 40 μm in this case. The insulation film should have the lowest possible dissipation factor and permittivity (in the range of $\varepsilon_r \approx 2$). Thermal bonding of the film to the substrate and ground plane is attractive because it avoids lossy adhesives. The used FEP film has specially treated wettable surfaces and adheres well on a variety of materials after it was heated to 300 °C while sandwiched between the ground plane and substrate. A very well defined temperature as well as pressure could not be guaranteed. To this end, a heatable flatbed press is required, which was not available at Poly-Grames. As a consequence, the final insulation film thickness is liable to fluctuations, which makes up for some of the deviations in the measured results of following sections.

1.6 Experimental setup and results

Experimental determination of the complex propagation constant was carried out in the same way as the dual-line simulation method from subsection 1.3.3. Two straight

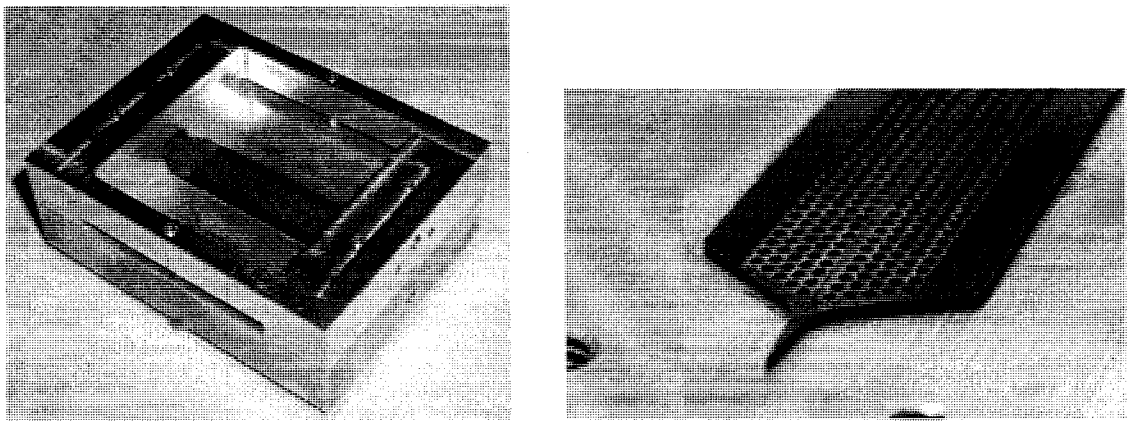

Figure 1.26 SIIG waveguide test fixture for connection to a millimeter-wave network analyzer (left) and fabricated silicon SIIG.

SIIG sections, 20 mm and 40 mm long, were fabricated out of a HR-silicon wafer in order to measure the S-parameters for subsequent extraction of the propagation constant. Another possible technique is the direct probing of guide-wave fields [73], but it involves a complexer mechanical setup and the accuracy is usually low. The dimensions were chosen as specified before for simulation. A laser was used to cut the SIIGs with matching tapers out of the wafer. Subsection 1.5 provides more details on fabrication. Aluminum test fixtures were milled with short WR-10 metal waveguide sections expanding to pyramidal horns to approximately 3 mm distance around the guiding channel. In combination with the silicon tapers, the aluminum fixtures constitute quite efficient transitions for connection to a millimeter-wave network analyzer being equipped with WR-10 waveguide ports. Further information on the waveguide-SIIG transition is provided in section 2.2. Figure 1.26 shows the described assembly and an example for an SIIG fabricated of HR-silicon.

Measured S-parameters are shown in Figure 1.27. As explained before by means of Figure 1.12, the simulated lower practical frequency limit is at approximately 83 GHz. This agrees well with the experiment where the insertion loss shows a quite smooth pro-

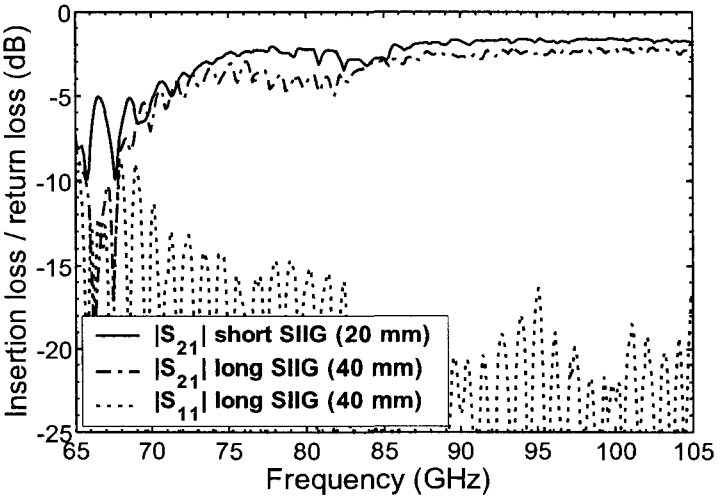

Figure 1.27 Measured insertion and return loss for the short and long SIIG sections fabricated of HR-silicon. Losses arising from the two transitions are included.

gression above 85 GHz. Small ripple is introduced by the two back-to-back transitions, which cause a not negligible amount of reflections, resonances, and radiation. This is especially true for frequencies below 85 GHz due to the poor field confinement around the guiding channel. The short SIIG section has an insertion loss mean value of 1.6 dB and the longer one of 2.3 dB in the operating frequency range, including the two transitions to WR10 metallic waveguide.

The extracted guide attenuation according to (1.3) is shown in Figure 1.28. Since the difference between the insertion loss curves of Figure 1.27 is used for calculation of the waveguide attenuation, this evaluation is very sensitive to the ripple on the insertion loss curves and therefore yields a strongly fluctuating curve. In particular, the transitions have great influence. A physically impossible *gain* at 85 GHz can be explained by the inaccuracy of this procedure. Nevertheless, the obtained attenuation should be accurate as a mean value in the operating frequency range because destructive and constructive interference as a consequence of mismatching and resonance phenomena outweigh each other over frequency. The extracted mean value of 35 dB/m above 85 GHz is close to

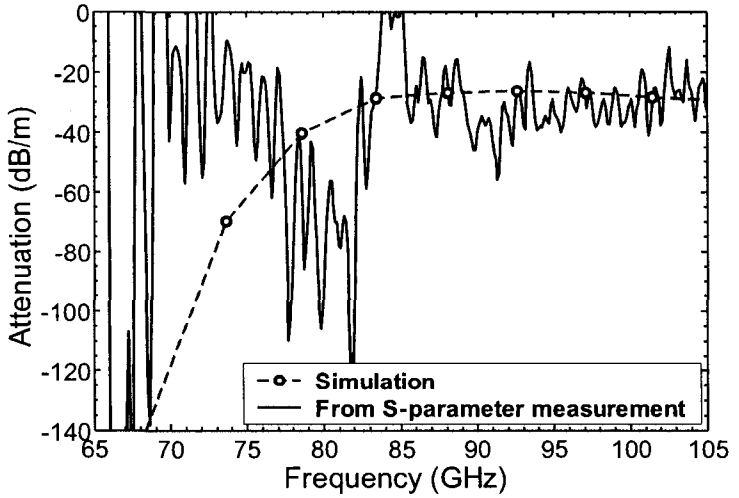

Figure 1.28 Simulated and measured guide attenuation of the HR-silicon SIIG. Experimental data was extracted from measured *S*-parameters.

the simulated value of 30 dB/m. This is reasonable because the surface roughness of the aluminum was not considered in the simulation.

Simulated and measured extracted curves for the phase constant [according to (1.2)] are shown in Figure 1.29. There is a certain deviation that can be attributed to fabrication tolerances. Due to the fragility of monocrystalline silicon and the lack of a heatable flatbed press, the SIIGs were not heat-bonded to the aluminum with the FEP insulation film in between. Instead, the perforated silicon structure was only fixed with a tape on the metal base. This obviously produces a small air gap, which, in turn, leads to a slightly lower phase constant.

Previous measurements of HR-silicon prototypes of SIIGs with a coarser hole lattice were presented in [30]. The hole diameter was 0.6 mm and the lattice constant was 0.7725 mm. A silicon substrate of thickness 0.525 mm and a 50 μm FEP insulation film were used. These dimensions entailed a deep stopband in the measured frequency range, as predicted by simulations in subsection 1.3.3. It is shown in Figure 1.30.

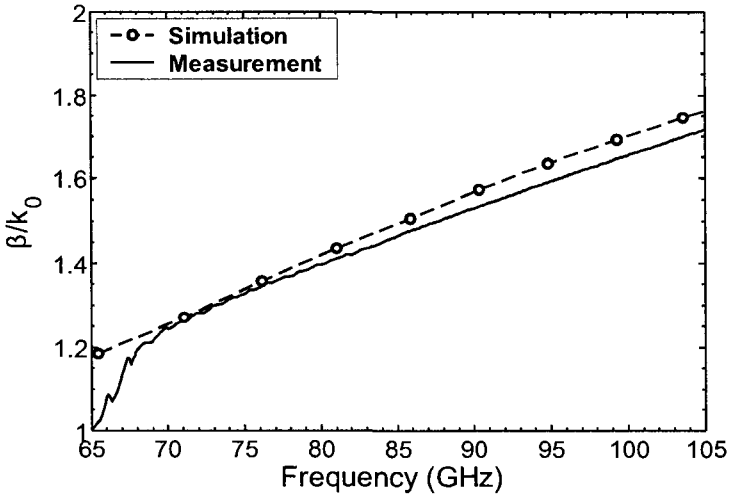

Figure 1.29 Simulated and measured normalized phase constant of the HR-silicon SIIG. Experimental data was extracted from measured *S*-parameters.

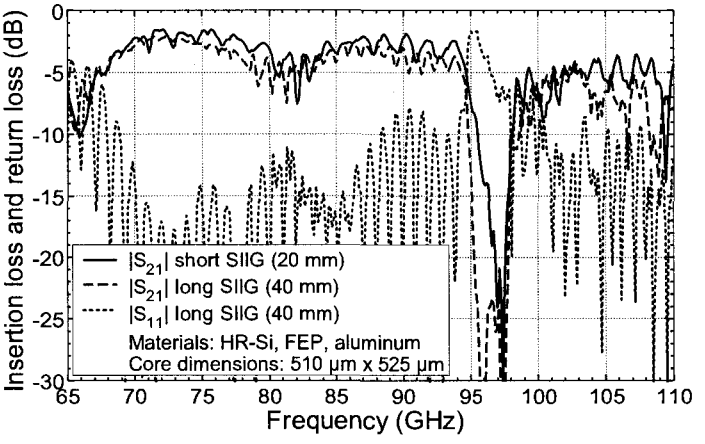

Figure 1.30 Measurement results for a HR-silicon SIIG with core dimensions 510 μm × 525 μm (w × d), hole diameter 0.6 mm, and lattice constant $p = 0.7725$ mm.

CHAPTER 2

MODE EXCITATION IN THE SIIG

This chapter presents geometries which allow the efficient launching of guided waves into the image guide. Early and more recent transitions from standard waveguide structures to image guide are reviewed. The design of a waveguide-SIIG transition that was used for measurements as well as a novel CPW-SIIG transition are described in detail. Other possible substrate integrated transitions are discussed in section 5.3 on substrate integrated circuits (SICs).

2.1 Brief review of image guide transitions

Integrated dielectric waveguides are suitable as low-loss guiding structures in the mmW range. However, they are not directly compatible with active components, since any active solid-state device has metallic inputs and outputs and therefore needs to be connected to metal-based transmission lines first. This is why transitions are required for efficient excitation of one or several modes in the corresponding dielectric waveguide.

The design of transitions to open dielectric waveguides is generally challenging for the following reasons. First, radiation occurs at discontinuities of open waveguides and a transition inherently *is* a discontinuity. Adequate methods need to be found to effectively reduce unwanted radiation and keep it at a very low level. Second, the modal field polarization and distribution of dielectric modes is in most cases very different from their metal-based counterparts. As a consequence, impedance- and field-matching are difficult to achieve. Third, a directive excitation of the surface wave towards the dielectric guide is required. Otherwise, excessive radiation and insertion loss would arise.

Several different approaches can be considered to meet all those requirements. One of them is the explicit use of consecutive abrupt steps which produce a number of reflected waves that cancel each other out by destructive interference in direction of the input. The more steps are employed, the wider the achievable bandwidth. An example is the well-known stepped impedance transformer. However, such designs are not popular for open waveguides due to the potential radiation at each abrupt step. Another possibility is the use of smooth tapers for gradual field matching. Tapers can be regarded as a special case of the stepped transformers, in which the number of steps is infinite and their individual reflections infinitesimally small. The design goal is to obtain the widest possible bandwidth with the shortest possible tapers [74,75]. A third option is the use of one or several resonant elements that serve for coupling between the different waveguides. Increased bandwidth can be achieved if the coupling to the resonant structure is strong, thereby reducing the loaded Q-factor. Wave launchers in the form of resonant antennas such as the directive Yagi-Uda antenna can be attributed to this class. Distributed, total forward-coupling by a traveling wave can also be exploited for the design of transitions, but the achievable bandwidth is inherently small and the transition itself needs to have a length in the order of several wavelengths.

One of the first and most popular transitions to dielectric image guides uses the rectangular metal waveguide as a feed line [76]. The latter is smoothly extended into a horn at its end, acting as a gradual taper to match the modal fields to those of image guide. The traditional shape of this type of transition is shown in Figure 2.1. It is widely used for measurements on image guide components, but a major drawback is its lack of compactness and ease of fabrication, which is required for the use in integrated circuits. In order to conduct measurements on single SIIG components, this transition was still adapted for use with the SIIG. It is presented in section 2.2. Other designs were reported which involve loops or monopoles embedded in the image guide itself [77] and are fed by a coaxial cable behind the ground plane. The bi-directionality and low efficiency are not

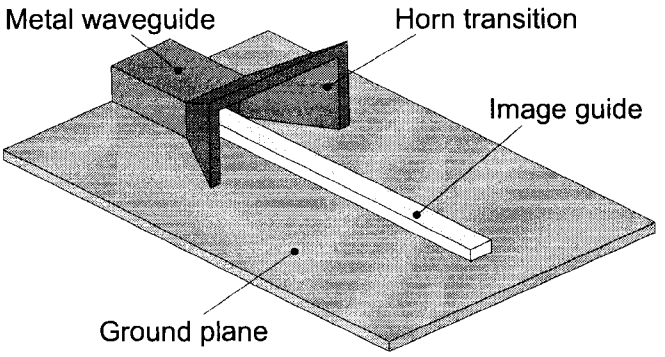

Figure 2.1 Widely used type of waveguide-to-image-guide transition.

satisfactory, however, which led to the development of a Yagi-Uda array of monopoles with improved performance [78]. Clearly, a coaxial feed is not suitable at millimeter-wave frequencies. More recently, two integrated transitions to microstrip were proposed at frequencies of 8 GHz and 20 GHz, respectively. One of them is based on a planar Yagi-Uda resonant slot array implemented in a double-layer structure [79]. Here, the microstrip feeding is formed on a thin substrate beneath the image guide, both sharing the same ground plane. Several slots arranged to an array are etched in the ground plane and coupling to one of them is established by the microstrip line. Advantages are the relative simple planar structure and the compact microstrip feed line. However, directivity and overall efficiency are acceptable only in a narrow bandwidth which is inherently limited by the Yagi-Uda topology. The other design involves smooth microstrip tapering in the horizontal and vertical dimension [80]. Although the achievable bandwidth is quite broad and the performance is satisfying, the 3-D topology renders fabrication difficult and expensive, and thus is not practical for hybrid integrated circuits. A 3-D or double-layer design is indispensable, because microstrip and image guide depend on significantly different heights of the dielectric in order to guide electromagnetic waves efficiently. Both transitions were shown to work at relatively low frequencies, but microstrip requires excessively thin substrates at higher frequencies. This limitation and the

well-known via problem with regard to ground connections favor the use of the CPW for mmW circuits. For this reason, the pursuit of an improved microstrip-SIIG transition was abandoned and a novel, compact CPW-SIIG transition based on resonant coupling was developed. The developed transition is presented in section 2.3.

2.2 SIIG transition to metal waveguide

Rectangular hollow waveguide is *the* standard technology for measurements at 60 GHz and above. Measurement instruments for that frequency range are equipped with corresponding waveguide ports. Therefore, it is desirable to have an interface between metal waveguide and SIIG in order to evaluate prototypes of SIIG components.

The field orientation of the TE_{10} waveguide mode and the E_{11}^{y} image guide mode is very similar, so that this transition constitutes an ideal, simple, and broadband launching structure. One end of the image guide extends into the waveguide. At this position, the waveguide may be entirely filled with the dielectric (often in conjunction with low-permittivity dielectrics) or only partially, leaving a surrounding space of air. In both cases, the sudden beginning of the image guide represents a discontinuity for the guided wave and as such causes reflections. Such reflections at the air-dielectric interface are particularly pronounced if the image guide is made of high-permittivity material, as it is the case for the SIIG. To keep the return loss small, the dielectric material is smoothly tapered in either the horizontal, the vertical, or both dimensions. A horizontal taper was chosen for the waveguide-SIIG transition, since a laser was used for fabrication, which only cuts 2-D outlines. The metal waveguide dimensions are narrowed in the zones where it is penetrated by the image guide. This yields improved field confinement in the dielectric and less radiation. A following horn section helps to smoothly transform the waveguide mode into a non-shielded image guide mode. The larger the horn aperture and length, the less unwanted radiation occurs. If the transition is to an SIIG instead of

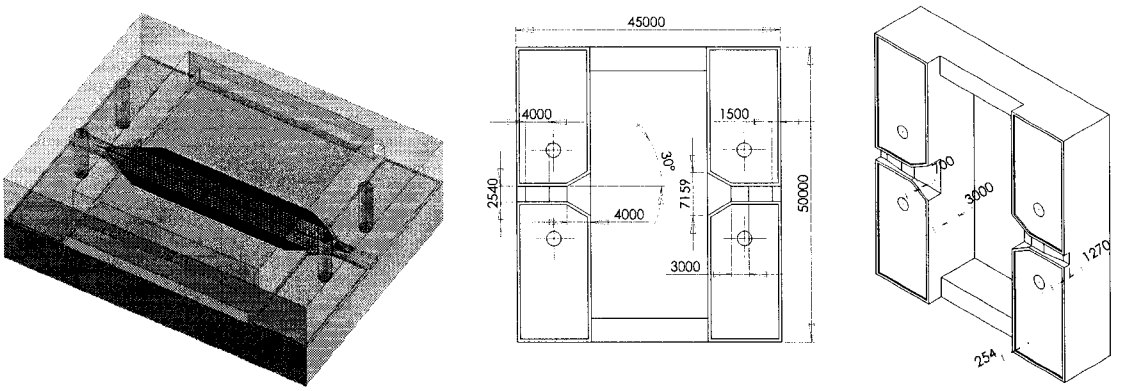

Figure 2.2 CAD model of an SIIG waveguide test fixture for connection to a millimeter-wave network analyzer (40 mm SIIG section) and drawing with dimensions in μm (20 mm SIIG section).

a standard image guide, the SIIG has to be extended to its full width, i. e. including the complete perforated zones, within the horn section. A CAD model and a corresponding drawing including the dimensions used at 94 GHz is shown in Figure 2.2.

In practice, this kind of transition exhibits between -0.75 dB and -0.25 dB insertion loss, including radiation. The lower value is typically achieved if the image guide is of low-permittivity material, which causes less matching problems. The waveguide-SIIG transition that was designed for the experiments in section 1.6 had -0.5 dB insertion loss at 94 GHz and return loss of less than -20 dB. Those are very acceptable values in the W-band and for a high-permittivity SIIG made of silicon.

2.3 Integrated transition to CPW

Despite potential problems with the excitation of the disturbing slot-line mode at discontinuities, CPW has decisive advantages over microstrip. No vias through the substrate are required for grounding, because the grounds are situated adjacent to the signal strip on the same plane. Moreover, ground strips between closely routed lines can sig-

nificantly improve isolation properties. The CPW can be operated on electrically thick substrates while maintaining the desired characteristic impedance, usually around 50 Ω. One problem, however, is not solved by the CPW: the waveguide attenuation due to conductor losses is high, roughly comparable to that of microstrip. It would therefore be desirable to merge this technology's amenities with those of a low-loss dielectric technology like SIIG. Antenna arrays, directional couplers, phase shifters, resonators, and filters are particularly important components in mmW front-ends that depend on a low-loss waveguide technology. Since the CPW is compatible with electrically thick substrates, hybrid integration of the SIIG and the CPW on the same single-layer substrate becomes feasible.

To the author's best knowledge, there is only a single publication on transitions between CPW and image guide available in the form of a patent [81]. It contains rather complex 3-D structures, based on substrates of varying thickness, variable dielectric properties, or both horizontal and vertical metallic shapes. Besides those complex geometries, which are expected to be very demanding for actual fabrication, no further performance data is provided with regard to return and insertion loss, bandwidth, or radiation loss. It is believed that none of the proposed designs is suitable for cost-efficient integration at mmW frequencies.

On that account, a novel, easy-to-integrate planar transition from CPW to SIIG should be developed. Required properties include high efficiency – in particular low radiation loss – and broadband performance. In such a scenario where a dielectric waveguide has to be interfaced with a planar transmission line, the SIIG reveals clear advantages over the standard image guide. The CPW is fabricated on the same substrate and therefore the alignment precision of CPW and SIIG is very high, associated with a rugged design. Gradual field matching by smooth tapers, as exploited in the design of the waveguide-to-SIIG transition, cannot be achieved in this case, because the modal

fields of CPW and image guide are too dissimilar. Another approach based on a resonant coupling structure was chosen for this reason.

2.3.1 Description of the transition topology

Figure 2.3 shows the proposed and realized transition in a back-to-back arrangement. A single transition is impossible to be measured due to the required CPW access for probe tip contacting. The SIIG in the center is created by substrate perforation of adjacent zones, as explained in the first chapter. Large cut-outs at the ends of the SIIG augment the refractive index contrast between the guiding channel and the surrounding area which in turn leads to a better field confinement in the channel. This is necessary to avoid excessive radiation. The electromagnetic field of the fundamental E_{11}^{y} image guide mode enters the parallel plate waveguide section that is formed by the ground plane and a metallic patch on top of the substrate. Similar to a microstrip patch antenna, this geometry can be regarded as a patch resonator that couples to the surrounding substrate regions. A microstrip patch antenna uses a thin substrate so that nearly all the power is

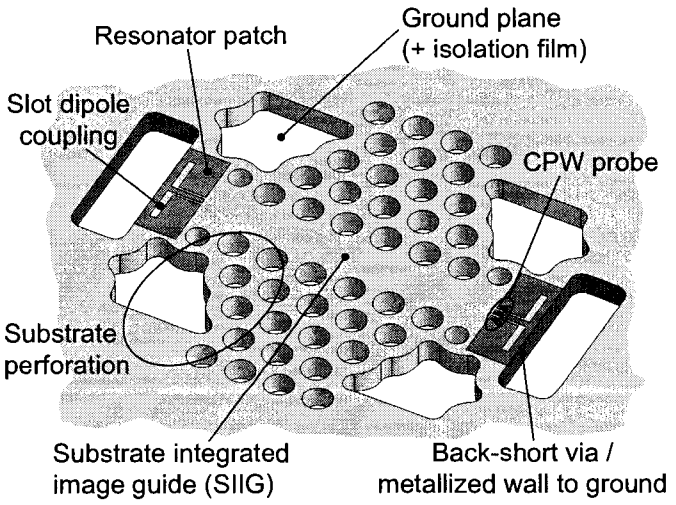

Figure 2.3 Back-to-back configuration of the proposed CPW-to-SIIG transition.

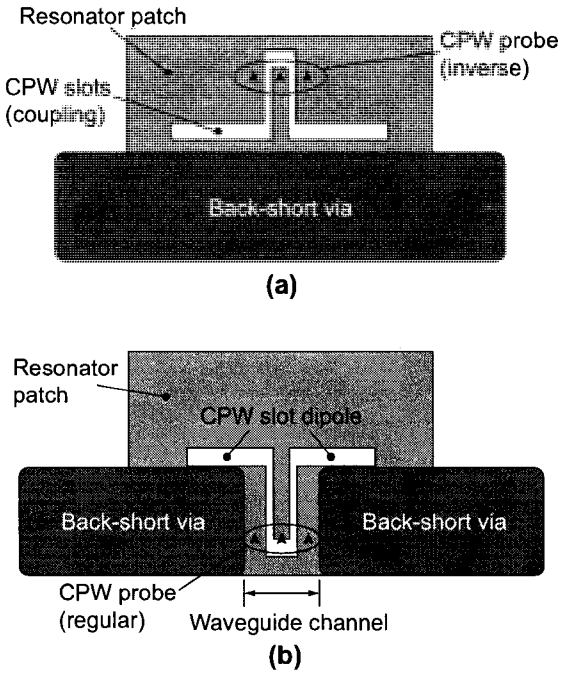

Figure 2.4 (a) Inverse dipole arrangement as used for the prototype and (b) regular configuration. Both yield almost identical performance.

coupled – or better – radiated to the air region, whereas the patch resonator in the present design couples most of the power to the TM surface wave mode in the substrate slab due to its significant thickness. The patch resonator is back-shorted by a via slot or a metallized wall that connects the patch to the ground plane. It acts as a reflector and yields the mentioned necessary directive mode excitation towards the SIIG. Hence, in contrast to the microstrip transition involving a Yagi-Uda array [79], the front-to-back ratio is ideal. Coupling is strong due to the thick substrate and the coupling efficiency is very high so that only a very small part of the injected power may be radiated. A slot dipole is etched into the patch in order to couple the resonator field to a CPW line. An enlarged view of this geometry is given in Figure 2.4(a). Due to the strong coupling on both ends, the resonator's loaded Q-factor is very low, resulting in a wide operating bandwidth of the

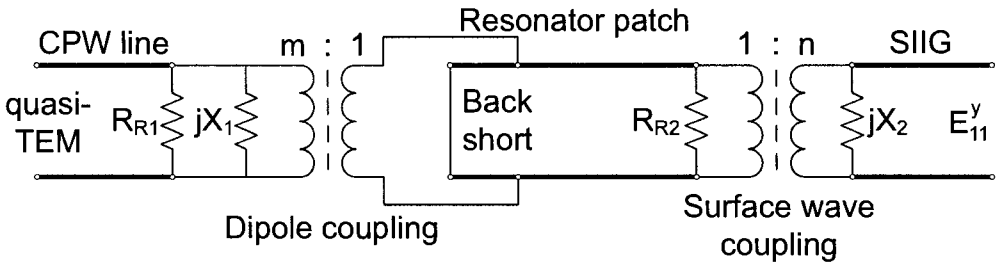

Figure 2.5 Equivalent circuit representation of a single CPW-SIIG transition.

transition. The back-short not only guarantees directive excitation of the surface wave, it also stimulates mode conversion between the patch resonator region and the CPW.

The inverse-reflective dipole configuration of Figure 2.4(a) was chosen to simplify the fabrication of the prototype. A negative consequence is that the access to the CPW input is restricted, e. g. if active devices or MMIC modules should be connected and biased. A second, but regular arrangement, as shown in Figure 2.4(b), was also simulated and exhibits almost identical results. Here, the CPW is supported by a narrow substrate channel between two vias, forming a waveguide channel below cutoff. The unwanted excitation of parasitic parallel plate modes known in conjunction with grounded CPW is therefore suppressed [82]. Simultaneously, this below-cutoff-operation also blocks backside radiation of the transition. In the latter configuration, an MMIC placed in the space above the mentioned waveguide channel can be connected to the CPW by the advantageous flip-chip technology whereas two solid vias next to the CPW can be exploited as efficient heat sinks to the ground plane.

An equivalent circuit illustration of a single CPW-SIIG transition is shown in Figure 2.5. Coupling is represented by ideal transformers and shunt admittances [64]. Radiation losses are modeled by shunt resistors R_{R1} and R_{R2}. The waveguide termination below cutoff of the regular arrangement in Figure 2.4(b) is modeled by a shunt inductance instead of the back-short [64]. It was observed that the CPW section which is

engraved in the resonator patch has no significant influence on wave propagation in the parallel-plate region, because the currents in the patch flow parallel to the CPW slots.

2.3.2 Design approach and simulations

The transition prototype ought to be fabricated on alumina substrate with supposed relative permittivity $\varepsilon_{r,S}$ = 9.7 and loss tangent tanδ = 0.0005. Those values were measured at lower frequencies around 50 GHz by an open resonator setup from Damaskos, Inc. The substrate thickness was chosen h_S = 381 µm, allowing operation of the SIIG around 94 GHz. A polyethylene insulation film of thickness h_F = 35 µm has $\varepsilon_{r,F}$ = 2.3 and tanδ = 0.001. It is inserted between the ground plane and the substrate to further decrease conductor losses, as explained in section 1.2. The SIIG guiding channel is 610 µm wide. By use of the method presented in subsection 1.4.1, the useable SIIG single-mode frequency range was determined to lie between 88 GHz and 103 GHz for the given dimensions and used materials.

Dimensions of the resonator patch and the slot dipole for 94 GHz center frequency are shown in Figure 2.6. The location as well as the length and width of the slot dipole determine the input impedance matching between the CPW line and the patch resonator. The CPW strip width is 90 µm and the slots are 43 µm wide to yield 50 Ω transmission

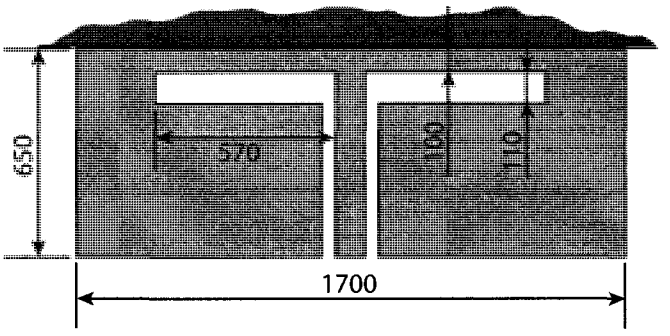

Figure 2.6 Dimensions (µm) of the metallic resonator patch and the slot dipole.

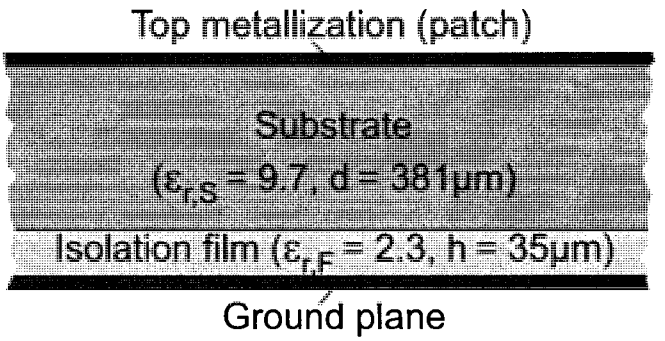

Figure 2.7 Two-layer parallel-plate waveguide region formed by the resonator patch and the ground plane.

line impedance. The length of the resonator (measured from the via wall) is approximately $3\lambda_{pp}/4$ to fulfill the short-open resonance condition, where λ_{pp} is the wavelength in the parallel plate section. The width of the patch is limited by compactness requirements. It should be chosen wide enough in order to keep lateral leakage small and to guarantee a directive surface wave excitation towards the SIIG. The total dielectric height $h_F + h_S$ between the ground plane and the resonator patch, as shown in Figure 2.7, must not exceed a certain thickness. Otherwise an orthogonal mode with horizontally oriented electrical field would also be excited, which would render the transition inoperative. The solution for the phase constant β of this mode is the same as the solution for the TE_{10} mode of a partially loaded rectangular waveguide of width equal to the total height $h_F + h_S$. In this case of a two-layer structure, the following transcendental equation [83] has to be solved numerically:

$$k_f \tan(k_s h_S) + k_s \tan(k_f h_F) = 0\,. \tag{2.1}$$

The variables k_f and k_s signify the transversal wave number in the insulation film and in the substrate, respectively. Wave number conservation requires

$$\varepsilon_{r,f} k_0^2 \;=\; \beta^2 + k_f^2$$

$$\varepsilon_{r,s} k_0^2 = \beta^2 + k_s^2 , \tag{2.2}$$

where k_0 depicts the free space wave number and β the joint phase constant of the guided wave. $\beta = 0$ applies at the TE_{10} mode cutoff frequency f_c, and therefore

$$\begin{aligned} k_f|_{\beta=0} &= k_0\sqrt{\varepsilon_{r,F}} \\ k_s|_{\beta=0} &= k_0\sqrt{\varepsilon_{r,S}} . \end{aligned} \tag{2.3}$$

In this case, the substitution

$$k_0 = \frac{2\pi f_c}{c_0} \tag{2.4}$$

with c_0 as the speed of light and equations (2.3) in (2.1) yield

$$\frac{2\pi f_c}{c_0}\sqrt{\varepsilon_{r,F}}\tan\left(\frac{2\pi f_c}{c_0}\sqrt{\varepsilon_{r,S}}h_S\right) + \frac{2\pi f_c}{c_0}\sqrt{\varepsilon_{r,S}}\tan\left(\frac{2\pi f_c}{c_0}\sqrt{\varepsilon_{r,F}}h_F\right) = 0 . \tag{2.5}$$

This final transcendental equation has to be solved numerically for the cutoff frequency f_c of the unwanted next higher order mode in the patch resonator. It was found that if the isolation film thickness is much smaller than the substrate thickness, then the higher order mode cutoff frequency of the dual-layer structure is almost equal to that of a parallel plate waveguide that is entirely filled with the substrate material, i. e. when the film layer is replaced by substrate material. Applying this simplification, the next higher order mode cutoff frequency can be determined by

$$f_c \simeq \frac{c_0}{2(h_F + h_S)\sqrt{\varepsilon_{r,S}}} . \tag{2.6}$$

For the given dimensions and materials, equation (2.6) yields f_c = 115.77 GHz, whereas the exact solution would be 115.94 GHz. A safety margin should be kept to this cutoff frequency because the resonator patch has rather small dimensions and therefore the parallel plate model has only approximate validity due to fringing fields. The slot dipole

that couples the CPW to the patch resonator has been used as an antenna elsewhere [84]. In fact, it can be said that the dipole *radiates* into the resonator region, but it also radiates to the air side. Naturally, radiation to free space is undesired and in this context the high permittivity of the substrate plays an important role. Nearly all the power is radiated into the high-permittivity substrate and only a very small fraction, approximately $\varepsilon_{r,S}^{-3/2}$, is radiated to the air side [85]. This asymptotic estimation is valid for thick, potentially grounded substrates of high permittivity. Therefore, about 3.3 % of the power or 0.15 dB have to be sacrificed as radiation loss in the case of the alumina substrate with ε_{rS} = 9.7 and even less for semiconductor substrates with higher permittivity.

A single transition was simulated in the time domain with CST-MWS without taking into account material losses. The 3-D simulation model of a single transition is shown in Figure 2.8. A discrete port was used to excite the CPW line with its input in the interior of the model. The SIIG is terminated by a wave port which requires an equivalent uniform SIIG section as explained in subsection 1.3.3. Obtained S-parameters are shown in Figure 2.9. In the range where the reflections are very low ($\leq$-25 dB), the plotted insertion loss is almost exclusively caused by radiation. The lowest insertion loss level is -0.13 dB which is in close agreement with the theoretically predicted amount of dipole radiation to the air side in the previous section. Radiation from other parts of the transition increases towards lower frequencies, because the guided surface wave fields are not sufficiently confined in the SIIG guiding channel. The radiation problem also becomes more serious towards higher frequencies due to the occurrence of mode conversion to the next higher mode in the patch resonator region.

2.3.3 Realization and measurement results

A back-to-back transition as shown in Figure 2.3 was realized. The first step was laser perforation of the alumina substrate. The upper side was then plated with a 1 µm gold layer on a 0.1 µm titanium adhesion layer. The two resonator patches including the

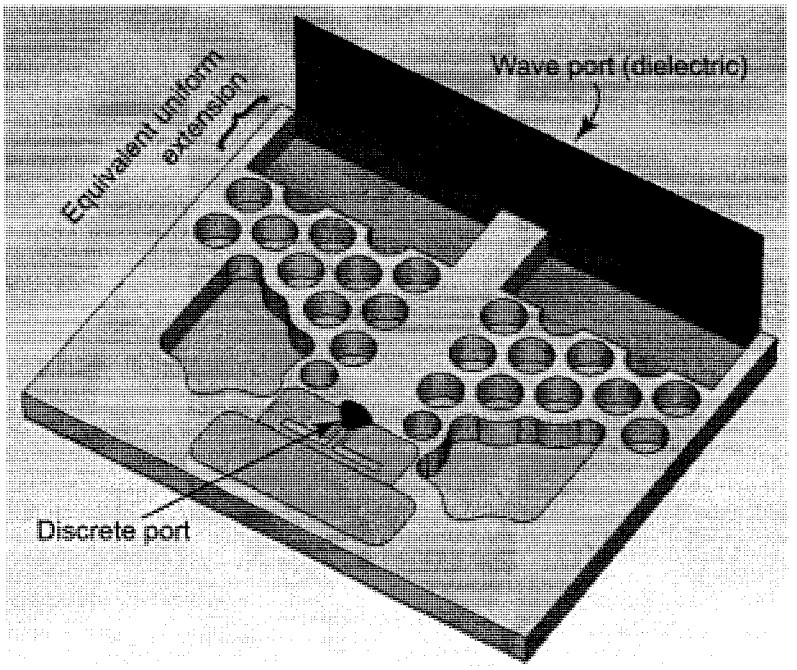

Figure 2.8 Simulation model of a single transition using a discrete port and a wave port.

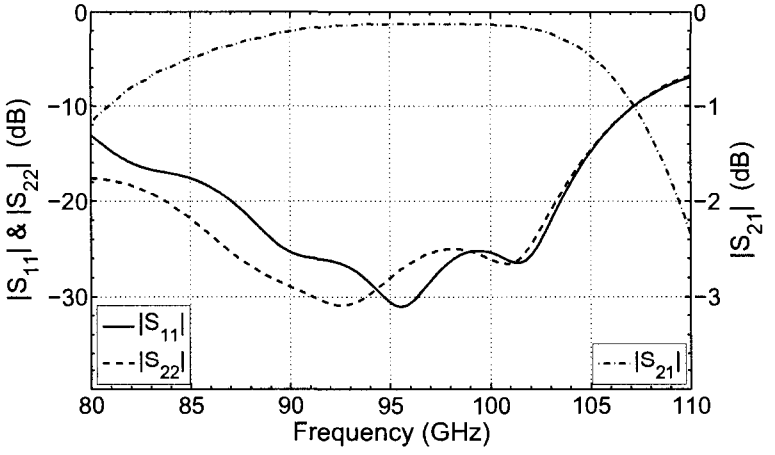

Figure 2.9 Time-domain simulation of a single transition excluding material losses. As a result, the plotted insertion loss only originates from radiation and return loss.

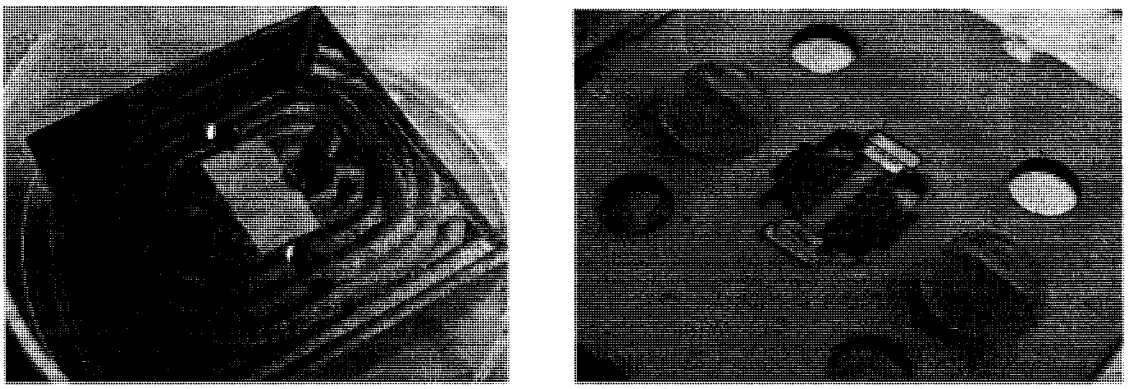

Figure 2.10 Realized CPW-SIIG transition prototype: Gold-plated brass base with milled solid vias and insulation film (l.) and the entire transition assembly (r.). The back-to-back arrangement of two transitions was necessary to conduct measurements on a probe station.

slot dipoles were subsequently etched by a photolithographic process. The subsequent fabrication procedure was improvised due to a lack of certain processes in the laboratory which are commonplace in the industry, however. Insulation film lamination or heat bonding, specific metallization of the via slots across the insulation film, and reliable electrical connections to the patches and ground plane were too demanding tasks compared to the available fabrication facilities. For this reason, another approach was pursued for the fabrication of the prototype. A metal base was milled out of a brass block, with two ridges on it serving as solid vias. Those profiles fit into corresponding cut-outs in the substrate. The gold-plated brass base is shown in Figure 2.10. The substrate was fixed on the base by nylon screws, with the mentioned polyethylene isolation film in-between. As a last step, the resonator patches had to be connected electrically to the base vias with conductive silver epoxy, as shown in Figure 2.11. Admittedly, this way of fabrication is not ideal concerning precision and conductor loss, especially in this frequency range. Nevertheless, it was still possible to show the functioning of the transition at 94 GHz.

The prototype was measured with W-band coplanar probes with waveguide input

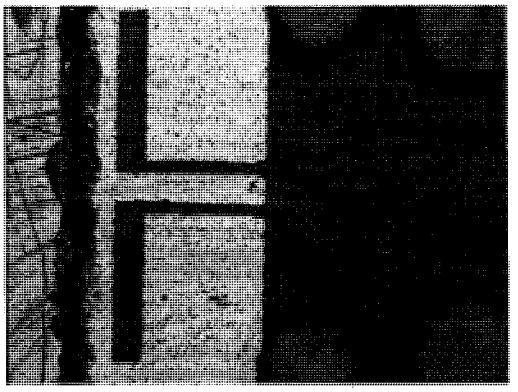

Figure 2.11 Conductive connection of the resonator patch to the back-short via with silver epoxy.

from GGB Industries™ on a Suss Microtech™ probe station. Due to the inverse arrangement of the transitions, the probes had to contact the CPW in opposite direction. This inverse probing can be compensated subsequently by de-embedding. Figure 2.12 and Figure 2.13 show measured results in comparison with simulated curves. This time, material losses were included in the simulated model. In addition to the time-domain simulation with CST-MWS, the structure was also simulated by the FEM frequency-domain solver, HFSS, to confirm the findings. The simulation results obtained by two absolutely different numerical methods agree very well. Insertion loss better than -1 dB can be observed from 88 GHz to 103.5 GHz for the back-to-back arrangement. This translates to a bandwidth of more than 15 %, which covers the entire SIIG single-mode bandwidth. The return loss stays below -20 dB. However, the measured curves significantly deviate from the expected outcome (after line-reflect-match (LRM) calibration), yielding a much higher insertion loss of about -2.8 dB. Although the structure itself is symmetric, no satisfying symmetry was observed for the S_{11} and S_{22} parameters. This is the consequence of insufficient fabrication quality and precision, which is very demanding to achieve in this frequency range. Nevertheless, the measurements confirm the principal operation of the transition.

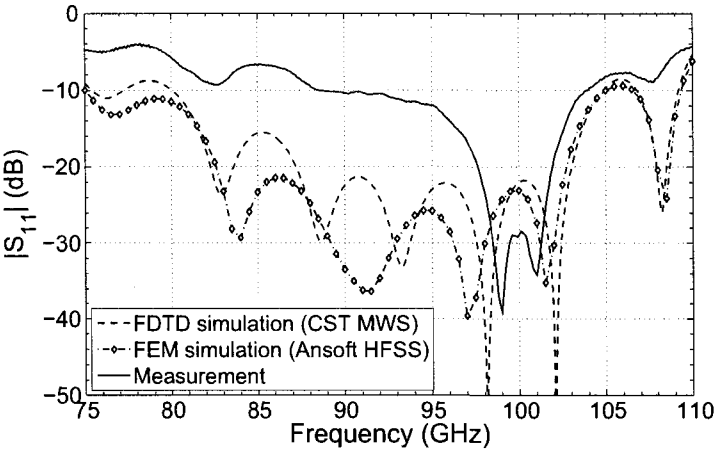

Figure 2.12 Simulated and measured return loss of the back-to-back transition. Material losses were considered in the simulations.

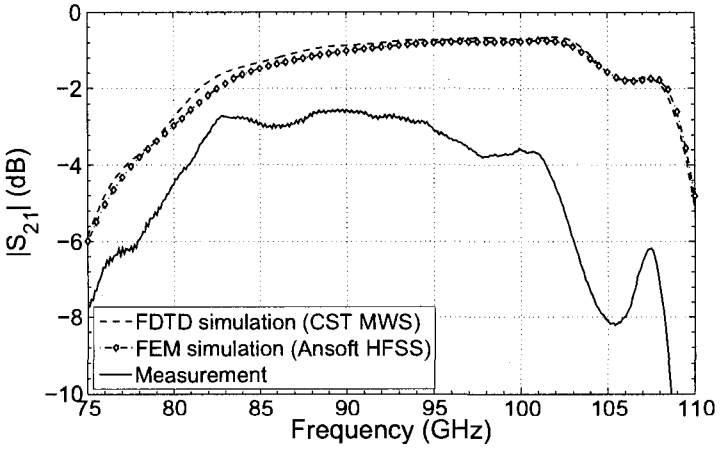

Figure 2.13 Simulated and measured insertion loss of the back-to-back transition. Material losses were considered in the simulations.

CHAPTER 3

INTEGRATED DIELECTRIC ANTENNAS

Realized examples of integrated dielectric antennas for mmW front-ends are presented in this chapter. The SIIG is particularly suitable for this application, because it allows low-loss feeding of antenna elements and because it can easily be modified to radiate due to its inherently open waveguide structure. The first section describes a planar dielectric rod antenna. An antenna involving an array of radiation elements on an SIIG feed line is presented in the following section. The last section describes a compact slab-mode antenna, which uses a dielectric substrate as wave-guiding medium and achieves directivity by means of a planar lens on top of the substrate.

3.1 SIIG rod antenna

Millimeter-wave communications, imaging, sensors and radar systems require compact and light weight antennas, which can easily be integrated and arranged into arrays. Furthermore, it is often desired to have a certain directivity, since that is easy to achieve even with relatively small antenna dimensions or because it is needed due to the high free-space loss that augments quadratically with frequency. Printed circuit board (PCB) antennas like the microstrip patch, which fulfill these requirements in the microwave range, do not provide sufficient performance in the mmW range. This is due to high conductor losses arising from high current densities at the edges of the resonator patches and the microstrip feeding network in arrays. Dielectric antennas are an auspicious alternative. They offer very low loss, which is only dependent on the used dielectric material and does not rise significantly with frequency. The dielectric rod antenna, also known as polyrod, was the first of this class to be investigated [5]. It consists of a dielectric

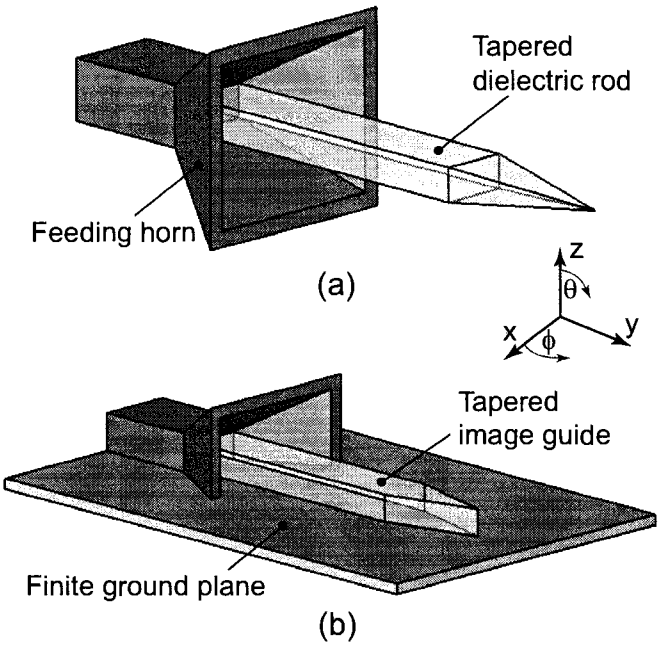

Figure 3.1 (a) Conventional dielectric rod antenna with horn feeding and (b) modified image rod antenna consisting of a tapered image guide on a metallic ground plane.

bar of cylindrical or rectangular shape, which is often tapered in some way to gradually transform a guided surface wave into a free-space wave. Antennas of this type, a few wavelengths long, typically offer medium gain around 15 dBi, high efficiency, and a broad frequency response. Feeding to the dielectric rod itself is normally achieved by means of a metallic horn as a smooth transition, as shown in Figure 3.1(a). This is very problematic, because the pyramidal horn is not compact and thus incompatible with integrated technologies. An alternative way of feeding a planar image-rod-antenna is demonstrated in this section.

In order to use the dielectric rod antenna in integrated circuits, it is necessary to convert it to a flat, planar structure, as shown in Figure 3.1(b). In this case, a ground plane acts like a mirror for the electromagnetic fields and the dielectric rod becomes an image guide. Radiation characteristics of a standard cylindrical rod antenna and a

corresponding half-cylindrical image guide rod antenna were compared by other authors [86]. Good agreement of measured radiation patterns could be shown. As far as image theory is concerned, radiation in end-fire direction tends to go to zero in connection with large ground planes, whereby the main lobe has a certain elevation relative to the ground plane. However, since the ground plane extension is finite, scattering occurs at its edges so that some energy is also radiated in the end-fire direction and into the "shielded" half space.

An assembly as shown in Figure 3.1(b) is not yet suitable for mmW integrated circuits. The horn transition is not capable of being integrated and high fabrication precision is difficult to achieve and costly. The SIIG can solve this problem in an elegant way. Direct connection of this periodic waveguide structure and the dielectric rod yields very efficient and broadband feeding, as graphically visualized by the FEM field simulation in Figure 3.2. This is a consequence of the nearly identical field distribution and orientation in the SIIG and the dielectric rod. Radiation from the discontinuity between the SIIG and the actual rod antenna is very low and therefore does not disturb the radiation pattern. The possibility of fabricating circuits and such low-loss dielectric antenna elements with high precision at low cost on the same substrate forms a distinct advantage.

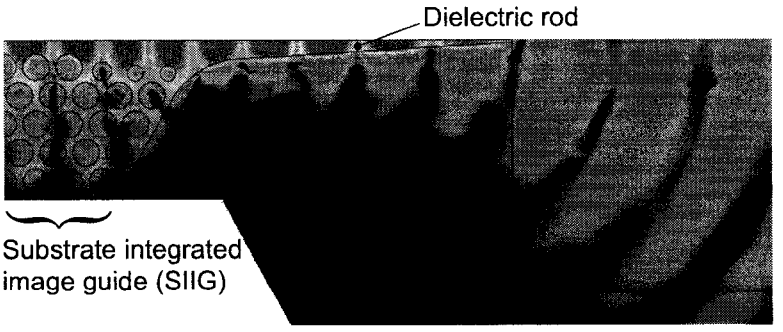

Figure 3.2 Top view of the simulated electrical field (HFSS) at ground plane level. Only half of the structure was modeled due to the even symmetry.

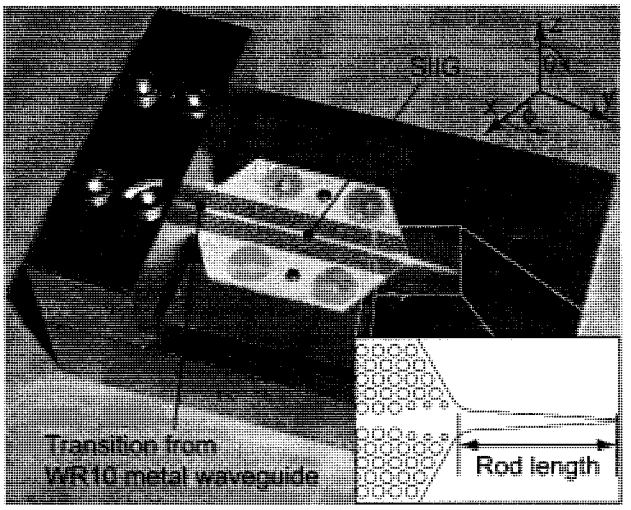

Figure 3.3 Photograph of the fabricated SIIG rod antenna. A transition from WR10 metal waveguide feeds the SIIG (for measurement purposes only) which in turn acts as feed line for the image rod antenna.

For prototyping, a laser was used to cut the structure out of 381 μm thick alumina substrate (ε_r = 9.7), but various other micro-machining techniques can be considered for high volume production. The guiding channel width w of the SIIG and the hole diameter $2r$ were each chosen 500 μm, at a lattice constant p = 625 μm. An insulating film (polyethylene; ε_r = 2.3; h = 30 μm) was added to ease fabrication tolerances and to reduce conductor losses. A photograph of the assembly is shown in Figure 3.3. In order to connect the measurement equipment, the waveguide-SIIG transition described in section 2.2 was used. About 10 % or 0.5 dB of the supplied power is radiated at this transition. This would cause a non-negligible perturbation of the radiation pattern. Therefore, absorbing foam material was put at a distance around the SIIG directly after the transition in order to damp radiated waves, but without attenuating the surface waves guided in the SIIG.

Material, length and shape of a dielectric rod antenna can strongly affect the antenna's properties. In our case, the substrate permittivity has to be high ($\varepsilon_r \approx 10$) for

a properly working SIIG feed line. The length of the rod has the strongest influence on the gain and its shape affects the radiation pattern, i. e. side lobe level and frequency-dependence. The literature does not provide accurate information on synthesis, because the effect of tapers on the total radiation pattern is very complex. Usually, the rod antenna is treated as a line source, with only a rough knowledge of the amplitude distribution. Two different designs were studied and a prototype was fabricated and measured.

3.1.1 Reduced side-lobe design

A low side lobe level can be achieved if the rod is wide at the feeding point and smoothly tapered to the end [87]. Then, the guided wave is properly bound at the feeding point so that only little power is radiated from this discontinuity and it is gradually matched to free space while propagating along the taper. Ideally, the guided wave is only radiated from the rod tip, so that interference of radiated waves occurs. Figure 3.2 provides a good insight on how the gradual transition to free space works. Some gain has to be sacrificed and a broader main lobe is obtained by the reduced side-lobe approach. However, this can be an advantage when beam steering in an array is strived for. The linear taper design was chosen for the prototype in Figure 3.3 because it guarantees sufficient mechanical stability of the very small rod. The taper width was 800 μm at the input (SIIG feeding point) and 100 μm at the end of the rod. In order to examine the influence of the rod length, the E-plane (elevation plane) radiation pattern was simulated with HFSS. Results are shown in Figure 3.4. In this case, the ground plane excess length L, as defined in Figure 3.5, was kept constant at 6 mm. It can be noticed that the directivity only slightly increases beyond a rod length of 12 mm, which corresponds to about four times the vacuum wavelength λ_0. The rod length was chosen 6 mm for the fabricated prototype to obtain sufficient ruggedness. The finite ground plane has strong influence on the radiation properties, because diffraction occurs at its edge. This mechanism is illustrated in Figure 3.5. The major part of the energy is radiated directly from the rod

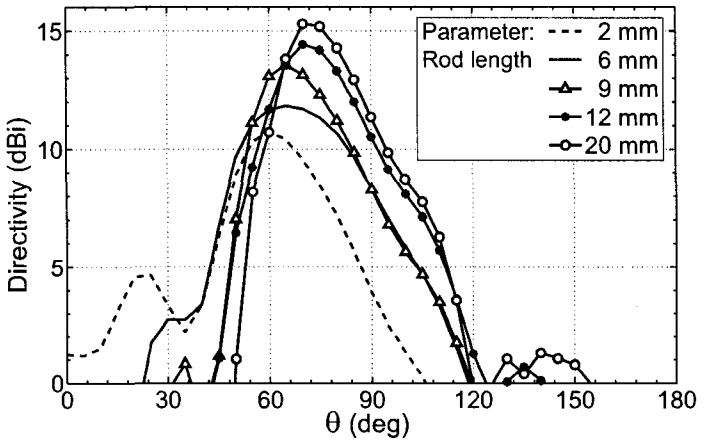

Figure 3.4 Simulated directivity in the E-plane (elevation) for varying rod lengths. Linear taper design with fixed excess length $L = 6$ mm.

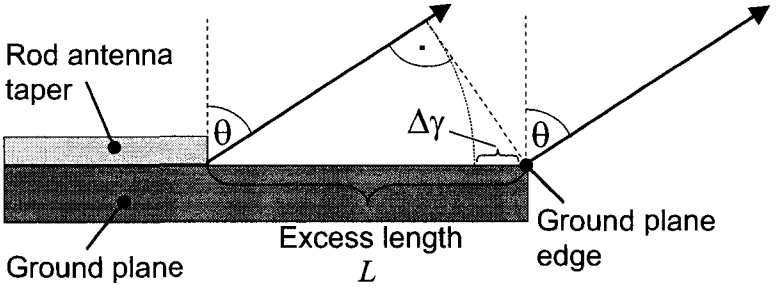

Figure 3.5 Interference and phase retardation of scattered waves from the ground plane edge, which gives rise to side lobes.

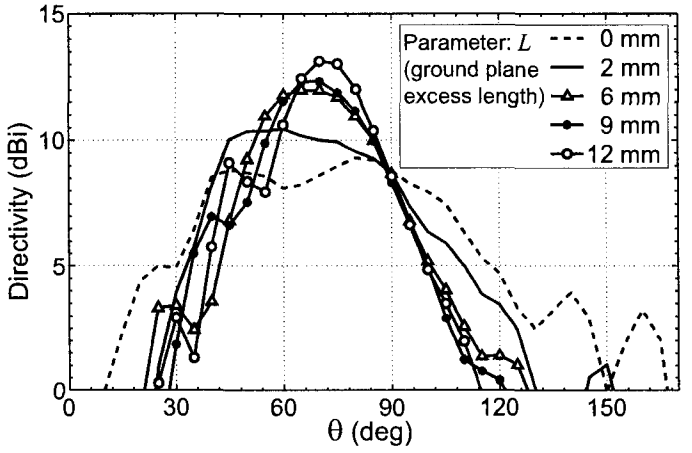

Figure 3.6 Simulated directivity in the E-plane for varying ground plane excess length L. Fixed length of linearly tapered rod: 6 mm.

antenna, but a fraction propagates to the edge and is scattered there. Although the side lobe level is small in the H-plane, there may be significant side lobes in the E-plane for that reason.

The phase retardation $\Delta\gamma$ in the far field between the two rays in Figure 3.5 is calculated from

$$\Delta\gamma = (1 - \sin(\theta)) \frac{2\pi L}{\lambda_0} . \tag{3.1}$$

For $L = 6$ mm and $\theta = 65°$, equation 3.1 results in $\Delta\gamma = 63°$. This means that the superposition is still constructive for the given elevation angle in the direction of maximum gain. The next angle of exact constructive superposition ($\Delta\gamma = 2\pi$) in this example is $\theta = 28°$, which is confirmed by the simulation results of Figure 3.6. A side lobe maximum occurs at this angle. Figure 3.6 shows the influence of the ground plane excess length L on the simulated E-plane radiation pattern. In this way, higher directivity can be achieved with longer L, but this also entails more significant side lobes. On the other hand, too short L results in a very poor E-plane pattern. In order to get a clean radiation pattern without added ripple or side lobes, the edge scattering can be diminished or avoided by absorber

material, electromagnetic bandgap substrate, or a curved ground plane. For the sake of simplicity, the original design was maintained, but only a small distance of L = 6 mm between the dielectric rod tip and the ground plane edge was chosen. Thus, interference of the radiated and diffracted waves causes only minor side lobes.

3.1.2 Maximum gain design

Maximum gain design procedures for conventional rod antennas [87,88] can as well be adopted for this planar version. Meeting the Hansen-Woodyard condition

$$l\beta - lk_0 \simeq \pi \,, \tag{3.2}$$

provides maximum super-directivity, if a long line source is assumed [87]. In (3.2), l is the rod length, β the phase constant of the guided wave, and k_0 the free space wave number. Approximately constant amplitude distribution is another precondition. The required linear phase distribution is obtained with a dielectric rod of constant cross section. Condition (3.2) for the optimum terminal phase difference can be fulfilled by proper adjustment of the cross section in dependence of the rod length. A parameter sweep was conducted over the width of the image rod. The best result at 94 GHz was obtained for a width of 275 µm at constant substrate thickness of 381 µm and rod length of 6 mm. The corresponding phase constant β was obtained by an additional eigenmode simulation: β/k_0 = 1.076. This result applied to the left side of (3.2) leads to a phase difference of 51.4°instead of π. The reason is that the antenna is not long and thus the Hansen-Woodyard condition is not directly applicable. In addition, there is an amplitude peak at the input end, very similar to a Yagi-Uda antenna, which is a comparable surface wave antenna [87]. It was experimentally shown [89] that the optimum terminal phase difference is reduced to about 60°for very short Yagi-Uda antennas and rises continuously towards π for long antennas. Moreover, the antenna presented here is not a true end-fire antenna. Peak directivity occurs at an elevation angle θ = 65°, which also reduces the

optimum terminal phase difference. HFSS simulations of a maximum gain design with a 6 mm long rod resulted in 14.4 dBi directivity at 94 GHz – a 2.4 dB increase compared to the previous linear taper design. Although this design is more narrowband-related, the simulated directivity at 90 GHz and 98 GHz was only slightly inferior, 13.7 dBi and 14.2 dBi, respectively. This second design was not realized because of its fragility due to the very thin rod.

3.1.3 Experimental results

Measurements of the prototype with linear taper, as shown in Figure 3.3, were conducted with a compact range setup in an anechoic chamber. First experiments with long ground plane excess length L = 15 mm were carried out. Pronounced side lobes predicted by equation (3.1) were observed and the ground plane was shortened subsequently to L = 6 mm. Simulated and measured H-plane and E-plane radiation patterns are compared in Figures 3.7 and 3.8, respectively. Very good agreement can be observed, even though the angular measurement range was limited due to technical constraints. The superior H-plane pattern found in the experiment (narrower beam width) can be explained by somewhat inaccurate radiation boundaries in the FEM model, which needed to be placed very close to radiating parts. The measured gain of 12.8 dBi at 90 GHz was only slightly inferior to the simulated directivity of 13 dBi. Figure 3.9 shows the half-power beam widths and gain over frequency. Reference measurements (calibration) with a pyramidal standard gain horn hold error specifications of $\pm$0.5 dB and the relative receiver accuracy for the signal strength in this case is $\pm$0.1 dB, whereas positioning errors can be neglected. Imperfect radiation boundaries in the simulation are another origin of inaccuracy. Nevertheless, the high radiation efficiency of this antenna is evident. A value of 74 % is predicted by simulations that include material loss. For the given materials, the ratio of conductor loss to dielectric loss is about 1:2. Return loss measurements were conducted with a network analyzer after offset-short calibration. The

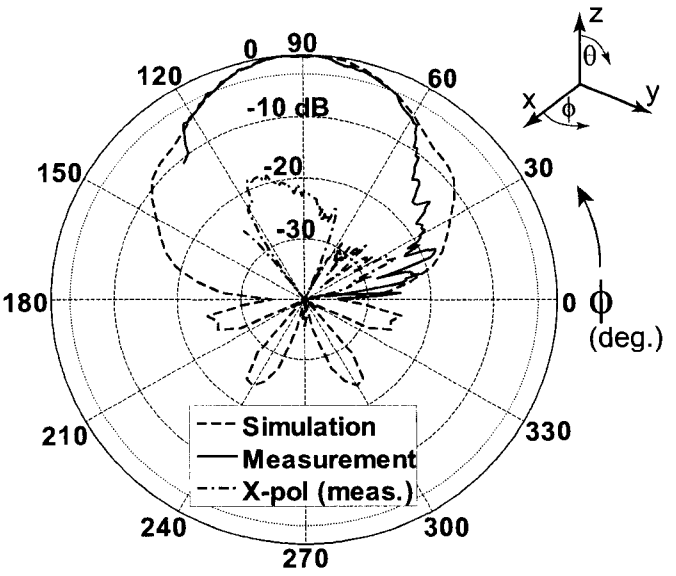

Figure 3.7 H-plane radiation pattern of the SIIG rod antenna at $\theta = 65°$.

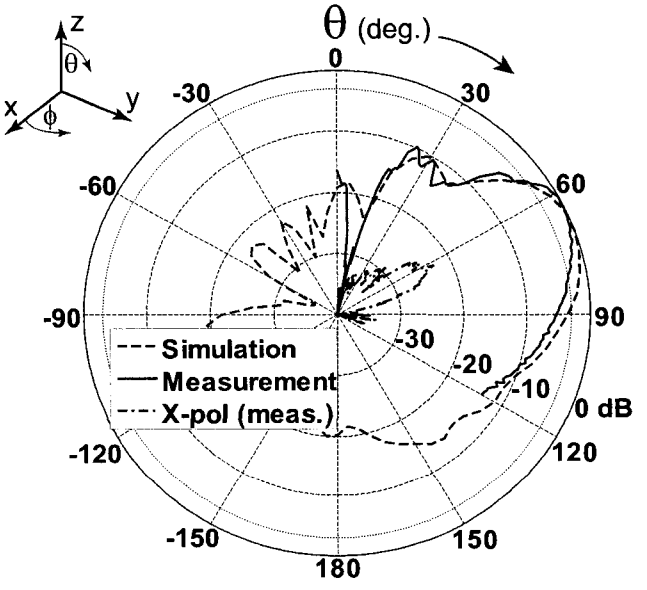

Figure 3.8 E-plane radiation pattern of the SIIG rod antenna at $\Phi = 90°$.

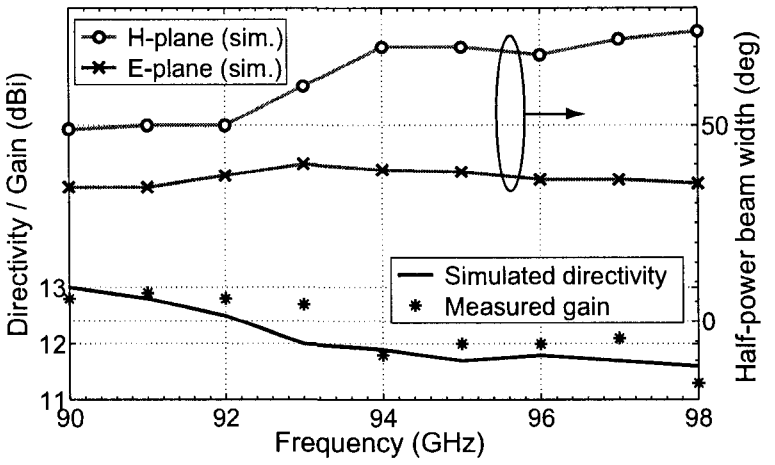

Figure 3.9 Half-power beam widths and gain over frequency.

worst value in the band from 90 GHz to 98 GHz was assessed -18 dB, in which most of the reflections probably derive from the waveguide transition and not from the antenna itself. The usable bandwidth is not limited by return loss but by the bandwidth of the SIIG and by the degradation of the radiation pattern. In the given frequency range, the elevation of the main lobe is almost frequency independent.

The SIIG rod antenna's low loss properties make it an interesting candidate for sub-millimeter and terahertz applications, which is also promoted by its low fabrication complexity. To achieve compatibility with MMICs, the rectangular waveguide feed can be replaced by a CPW feed, which allows for flip-chip mounting or wire-bond connection of the MMIC. Design, simulation, and measurements at 60 GHz including the hybrid integration of an MMIC LNA are described in section 5.5.

3.2 SIIG array antenna

The foregoing section deals with an antenna principle in which a guided wave is gradually converted into a free space wave. In this section, a low-loss, low-profile di-

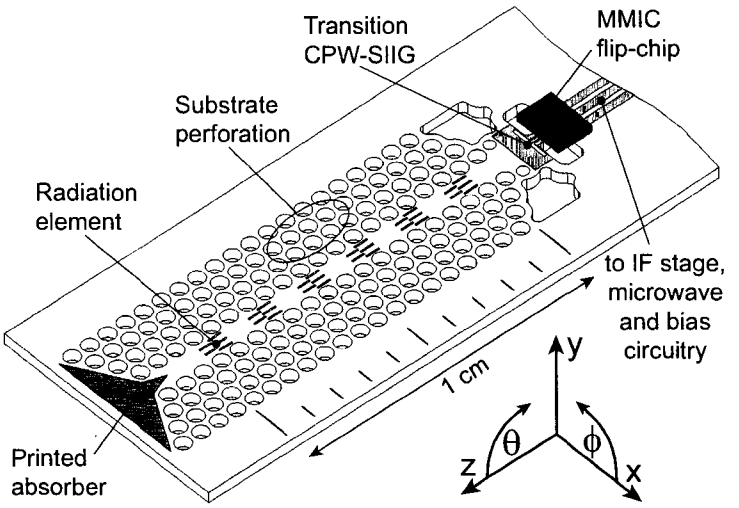

Figure 3.10 Conceivable low-loss assembly of an MMIC on an SIIG array antenna.

electric antenna is described, which can be attributed to the class of linear array antennas, or more specifically, to image line antennas. Here, radiation is caused by perturbation of the guided wave in the open SIIG. Early experiments have shown dielectric waveguides' capacity as radiators in conjunction with introduced obstacles [90]. Especially the dielectric image guide was shown to be promising for this task [91]. Such antennas are known as image line antennas, a comprehensive overview is given elsewhere [14].

The SIIG provides an integrable technology to combine the front-end circuit – most likely an MMIC – with the antenna. For example, the auspicious flip-chip technology [92] can be used to mount an MMIC chip on alumina or a similar low-loss substrate in a hybrid way. A possible assembly is shown in Figure 3.10, where the mentioned obstacles or radiation elements are placed on top of the SIIG guiding channel. The also necessary transition between CPW and SIIG is described in section 2.3. Before getting into design details, the radiation beam generation and frequency-scanning behavior is derived.

3.2.1 Extended array antenna theory

In general, linear array antennas consist of serially fed elements with equal inter-element spacing. Image line antennas belong to this class of antennas. The guided surface wave is disturbed by some kind of periodic obstacle, e. g. slots in the ground plane, dielectric gratings, or etched metallic shapes on the top side. Such discontinuities in the open dielectric waveguide cause reflection and transmission of the fundamental mode, but simultaneously excited higher-order modes at the obstacle result in radiation [93]. This can also be seen as coupling to the continuous spectrum of radiation modes in form of a leaky wave in the case of periodic obstacles [94,95]. The periodicity allows an expansion into spatial harmonics (Floquet's theorem), of which one or more are radiated in a certain direction relative to the waveguide, whereas the others are guided. Strictly speaking, Floquet's theorem can be applied only to infinite periodic structures, but it also provides good approximation for long periodic structures. The radiation condition for the m-th spatial harmonic (compare with subsection 1.4.4) is

$$\underbrace{\left|\beta + \frac{2\pi m}{p}\right|}_{\beta_m} < k_0 \,, \tag{3.3}$$

where β_m is the phase constant of the m-th spatial harmonic. The constant p is the periodic interval given by the inter-element spacing of radiation elements. Since $\beta > k_0$ for open dielectric waveguides, this condition can only be fulfilled for negative spatial harmonics (m = -1, -2, -3, etc.). Angle θ is the elevation angle measured from the axis of wave propagation as illustrated in Figure 3.10. The angle θ_m for the radiation peak of the m-th spatial harmonic is obtained from the relationship: $\cos(\theta_m) = \beta_m / k_0$.

A previously published paper [96] provides incomplete results for the scan range of the main beam without scanning adjacent grating lobes into the antenna's visible region. This is important because usually only one principal beam is desired. The lower limit of

equation (3.3), which corresponds to radiation in back-fire direction, is

$$\left|\frac{\beta}{k_0}+\frac{\lambda_0 m}{p}\right| = -1 \tag{3.4}$$

and the upper limit for end-fire radiation is

$$\left|\frac{\beta}{k_0}+\frac{\lambda_0 m}{p}\right| = 1\,. \tag{3.5}$$

The range for the m-th spatial harmonic to be radiated is therefore

$$\frac{-m}{\frac{\beta}{k_0}+1} \leq \frac{p}{\lambda_0} \leq \frac{-m}{\frac{\beta}{k_0}-1}\,, \tag{3.6}$$

where λ_0 is the free space wavelength. If only one spatial harmonic should fulfill the radiation condition (3.3), it is required that

$$\frac{-m-1}{\frac{\beta}{k_0}-1} < \frac{p}{\lambda_0} \leq \frac{-m+1}{\frac{\beta}{k_0}+1}\,, \tag{3.7}$$

With this respect, the first negative spatial harmonic (m = -1) has the largest scan range without radiating other spatial harmonics (= exclusive main lobe scan range). Fulfilling the radiation condition of (3.6) and the single beam requirement of (3.7) in parallel to achieve 180° scan coverage leads to

$$\frac{\beta}{k_0} \geq 3\,. \tag{3.8}$$

All the above is obtained by applying a leaky wave point of view, which implies an infinite or at least a long periodic structure for good approximation. Only the direction of the radiation peaks is considered, whereas the width of the grating lobes is neglected. The latter is dependent on the antenna length and accordingly on the number of radiation elements. At this point some incomplete assumptions were made in [96]. The authors

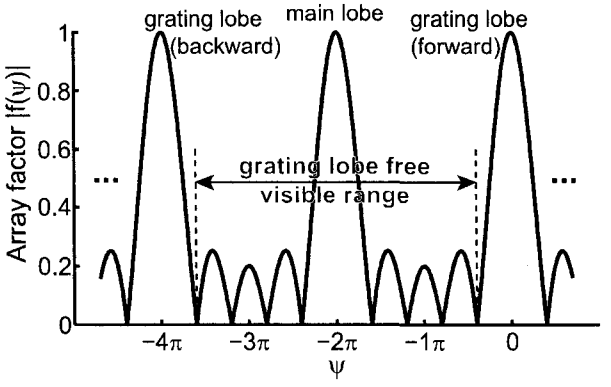

Figure 3.11 Illustration of the grating-lobe-free visible range of an example array of $N = 5$ equally excited isotropic elements.

introduce a condition that corresponds to an array of only $N = 2$ elements with accordingly wide grating lobes. Naturally, too strict limitations on the main beam scan range are the consequence. This theory is extended here for an arbitrary number of elements N. For compact antennas, like the presented SIIG array antenna, the leaky-wave approach with application of Floquet's theorem is not valid any more. Therefore, a finite array viewpoint is applied, which is suitable to describe the antenna with few elements. With the definition of a phase variable

$$\psi = k_0 p \left(\cos\theta - \frac{\beta}{k_0} \right) , \tag{3.9}$$

the width of the visible region of the array becomes [97]

$$\Delta\psi = 2k_0 p \, . \tag{3.10}$$

The grating-lobe-free visible range is illustrated in Figure 3.11. The condition

$$k_0 p(1 + \cos\theta_{min}) = 2\pi - \frac{2\pi}{N} , \tag{3.11}$$

must be satisfied for the most critical minimum scan angle θ_{min} in order to maximize the width of the visible region without including any part of the adjacent grating lobes. Furthermore, the phase difference between consecutive elements must meet

$$\beta p = k_0 p \cos\theta_{min} + 2\pi \tag{3.12}$$

so that the radiation peak ($\psi = -2\pi$) is situated at θ_{min}. Meeting both equations, (3.11) and (3.12), yields

$$\frac{p}{\lambda_0} = \frac{2 - \frac{1}{N}}{\frac{\beta}{k_0} + 1} \tag{3.13}$$

for the normalized periodic interval if the smallest θ_{min} without grating lobes is looked for. This result in (3.12) yields

$$\theta_{min} = \arccos\left(\frac{\frac{\beta}{k_0} + 1}{2 + \frac{1}{N-1}} - 1\right) . \tag{3.14}$$

If scanning up to end-fire (θ_{min} = 0°) is to be achieved, then

$$\frac{\beta}{k_0} \geq 3 + \frac{2}{N-1} , \tag{3.15}$$

which is in agreement with equation (3.8) for $N \to \infty$.

Limitations for the avoidance of an end-fire grating lobe are derived by analogous reasoning and yield equivalent to (3.13) and (3.14):

$$\frac{p}{\lambda_0} = \frac{1}{N\left(\frac{\beta}{k_0} - 1\right)} \tag{3.16}$$

$$\theta_{max} = \pi - \arccos\left(\left(\frac{\beta}{k_0} - 1\right)(N-1) - 1\right) . \tag{3.17}$$

If scanning up to backfire (θ_{max} = 180°) is to be achieved, then

$$\frac{\beta}{k_0} \geq 1 + \frac{2}{N-1}\,, \tag{3.18}$$

which evidently is a weaker requirement than (3.15). However, θ_{min} occurs at the upper scan frequency and θ_{max} at the lower and therefore β/k_0 at these frequencies has to be taken into account. Figure 3.12 graphically illustrates the above derived interrelations. The hatched area in Figure 3.13 shows the exclusive scan range of the main beam in dependence on β/k_0. It was shown here that the restrictions are less strict than previously assumed in [96], where the authors state that a slow-wave factor $\beta/k_0 \geq 5$ is necessary to cover the whole 180°-range.

3.2.2 Design and simulation

The SIIG acts as the feed line of the antenna array. Detailed analysis and design guidelines for the SIIG are provided in section 1.4. Just as for the SIIG rod antenna, alumina was used as high-permittivity substrate. The substrate thickness is 381 µm. Although the widest bandwidth is achieved with approximately equal height and width of the guiding channel, other design constraints may necessitate a broader core width. In this case, the printed radiated elements require a certain amount of space on top of the guiding channel. Therefore, an increased width of 610 µm was chosen. Hole diameter and lattice constant of the substrate perforation are 460 µm and 575 µm, respectively. Again, a 60-µm-thick polyethylene insulation film was inserted between the substrate and the ground plane. Those dimensions yield a usable SIIG single-mode frequency range of 88 GHz to 103 GHz. Such limits are found by the method described in subsection 1.4.1.

Image line antennas were built with all kind of periodic obstacles [14]. Dielectric gratings were shown to cause leaky-wave radiation, but this perturbation of the dielec-

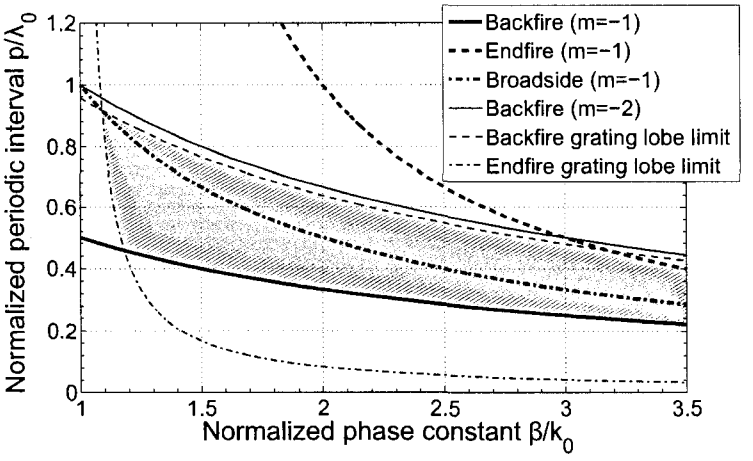

Figure 3.12 Interrelation of β/k_0, p/λ_0, and the scan limits. The grating lobe limits are calculated for a 12-element example array. No grating lobes are present in the hatched zone.

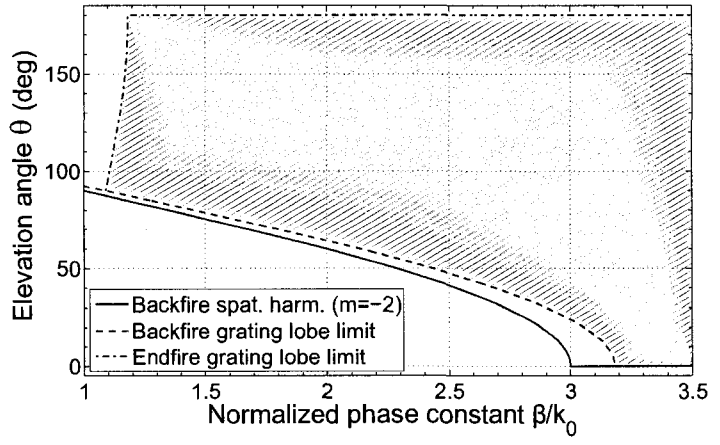

Figure 3.13 Graphical illustration of the exclusive main beam scan range in dependence on the normalized phase constant. The grating lobe limits are calculated for a 12-element example array. The hatched area identifies all possible points of operation at which grating lobes can be avoided.

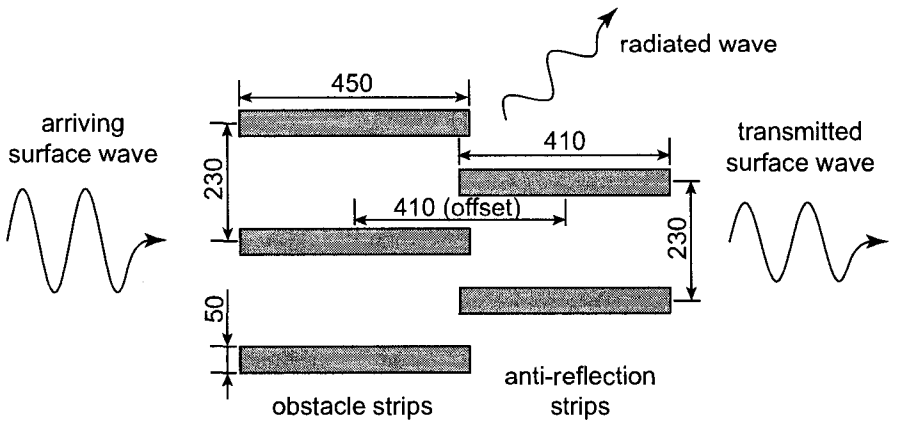

Figure 3.14 Configuration of a single radiation element as used for the SIIG array antenna. Dimensions are in μm.

tric interface cannot produce a sufficiently high leakage rate [98] to allow the design of compact antennas. Slots or grooves in the ground plane are another possibility [91,99], but they are not convenient to use for integrated circuits. Lithographically etched elements on the top side [100,101] are easy to fabricate, typically cause a stronger radiation, and provide a better control of the radiation pattern. Simple metallic strips transverse to the image guide were used in the majority of cases. The occurrence of a stop band due to distributed Bragg reflection is a well known problem in connection with periodic array or leaky-wave antennas in general and image line antennas in particular [93]. Such a stop band occurs when all elements are fed with equal phase, i.e. it coincides with broadside radiation. Since it was intended to steer the main beam through broadside, a reflection-compensating method was adopted that has previously served in microstrip traveling wave arrays [102] and image line leaky-wave antennas [103]. In addition, the element should allow a wide adjustment range for the radiation coefficient. The developed element configuration is shown in Figure 3.14. The strips, acting as shortened dipoles (below resonance), are parallel to the SIIG axis. A guided surface wave arriving from the left is disturbed by the three obstacle strips and a fraction of it is radiated. The amount of radiation increases with strip length, as do the reflections back to the input.

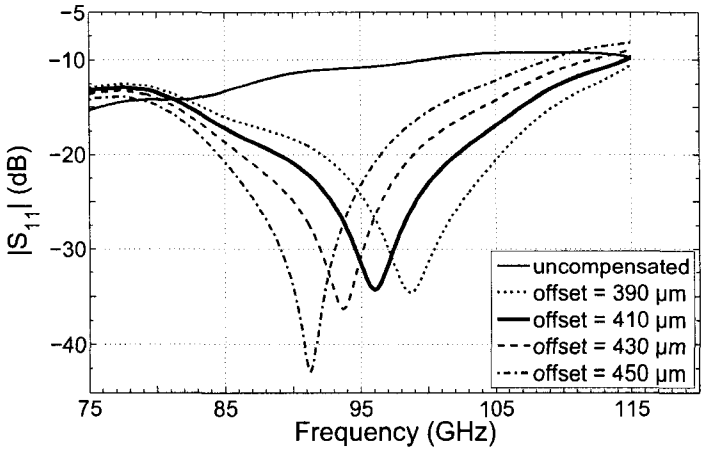

Figure 3.15 Simulation results for the return loss of a single radiation element. The offset length determines the cancellation frequency. Comparison to an uncompensated element (3 obstacle strips only) accentuate the benefits.

The following anti-reflection strips have the task to cancel those reflections by destructive interference. As shown in Figure 3.15, much lower reflected power is achieved in this way in comparison to ordinary elements without canceling mechanism.

The design procedure for a single radiation element is as follows:

1) Find initial values for the obstacle strip length and width in order to obtain the desired radiation/transmission ratio. This step was achieved by full-wave optimization (CST-MWS). A two-port model of an SIIG section as presented in subsection 1.3.3, with the obstacle strips on top of the guiding channel, is used to this end. The resonance frequency for a strip length of 550 µm is 100 GHz, as shown in Figure 3.16. As a rule of thumb, the strip length l should be shorter than

$$l \leq \frac{\lambda_0}{2\sqrt{\varepsilon_r}} \tag{3.19}$$

at the highest operating frequency to stay in the non-resonant region for broadband operation.

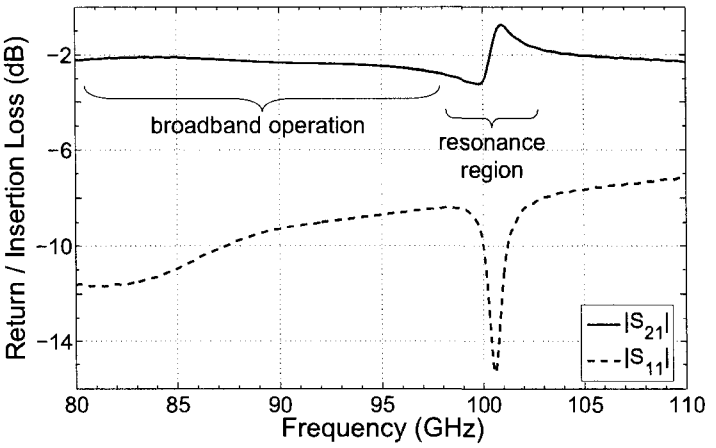

Figure 3.16 Resonance behavior of three obstacle strips with a length of 550 μm etched on top of the SIIG guiding channel. For broadband operation, the antenna has to be operated in the non-resonant region.

2) Compensate reflections by optimizing the anti-reflection strip length and offset length. As explained before, the use of twin obstacles with $\lambda_g/4$ offset can effectively reduce reflections and consequently the stop band behavior. While the offset length in Figure 3.14 is responsible for the proper phase condition to achieve destructive interference at the input port, the anti-reflection strip length has to be adjusted for the correct reflection level to accomplish quasi-complete cancelation at the broadside frequency. Since both parameters can be altered continuously, complete cancelation can always be obtained at a single frequency. Simulation results for the improved return loss are shown in Figure 3.15. Due to a certain interdependency, it may be necessary to repeat design steps *1)* and *2)* iteratively.

3) Create a database of radiation elements with different radiation coefficients. This is necessary for antenna design with shaped radiation distribution for low side lobe levels.

If broadside radiation has to be achieved at the center frequency, e. g. 94 GHz, then each of the radiation elements has to be excited with equal phase. For this purpose, the elements would be placed at a periodic interval of the guided wavelength λ_g at broadside

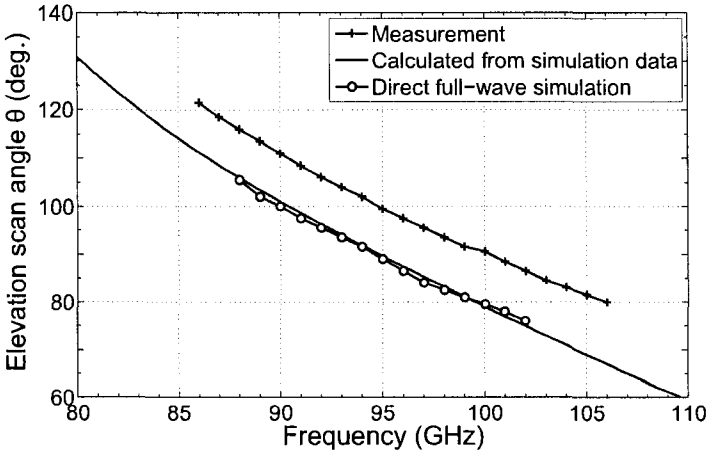

Figure 3.17 Calculated, simulated, and measured beam scan angle over frequency. The directly full-wave-simulated and phase-compensated calculated curves correspond very well with each other. Deviation of the measured curve can be attributed to fabrication tolerances and imprecisely known material constants.

frequency if the elements did not have any influence on the phase constant of the SIIG. However, inductive coupling to the elements as well as the relatively strong attenuation by radiation cause additional phase shifts. This effect has to be taken into account by placing the elements somewhat closer to each other. The phase delay caused by a single element can be obtained by comparing the simulated phase shift of an element-loaded SIIG section with an unloaded, but otherwise equal section. For example, the element shown in Figure 3.14 causes 36° additional phase shift at 94 GHz, a value that increases with frequency. As a result, the inter-element spacing of the prototype is 1.725 mm whereas λ_g of the unloaded SIIG at 94 GHz is 1.95 mm. Figure 3.17 shows the scan angle obtained by direct full-wave simulation (CST-MWS) of the complete array antenna. For comparison, another scan curve was calculated by equation (3.9) when ψ is replaced by -2π and when the above mentioned element phase shift is taken into account. Note that the simulated and calculated results agree very well with each other, thus validating the explained technique. The deviating measured curve is commented later in this section.

The prototype antenna was designed for broadside radiation at a specific frequency. If, in contrast, maximum scanning towards end-fire without generating grating lobes is looked for, the afore derived equations can be used. It was found by simulations that the given SIIGs slow wave factor at 103 GHz (highest operating frequency) with included element phase shift is β/k_0 = 1.98. The optimum inter-element spacing is calculated by (3.13) and yields p = 1.873 mm for a 12-element antenna. Then (3.14) results in θ_{min} = 65°, which means that scanning up to 25° from broadside towards end-fire is possible with this configuration.

The number of radiation elements determines one aperture dimension and consequently affects beam width and directivity. A minimum number of elements are necessary to radiate the majority of the power and to let only a small amount of residual power be dissipated in a terminal absorber. The antenna shown in Figure 3.10 was shortened to six elements for better illustration. In reality, twelve equal radiation elements were used for the designed antenna. The excitation level of the elements is exponentially decreasing towards the end due to the constant attenuation by radiation and guidance losses. Such a design is not ideal in terms of side lobe level and a more advantageous distribution of the elements' radiation coefficients is necessary for a low side lobe level. The latter can be achieved by adjusting each element's strip length appropriately. However, side-lobe optimization is not subject of this work. It was treated in many other publications, for example [96, 100, 104].

3.2.3 Measurements

The integrated assembly of Figure 3.10 is not suitable to conduct the antenna measurements. A probe station would be necessary to connect the CPW input to a receiver or transmitter, which renders the measurements in an anechoic chamber virtually impossible. Therefore, a laser-cut prototype antenna and insulation film were placed on a milled aluminum fixture that provides transitions to standard WR10 waveguide (see

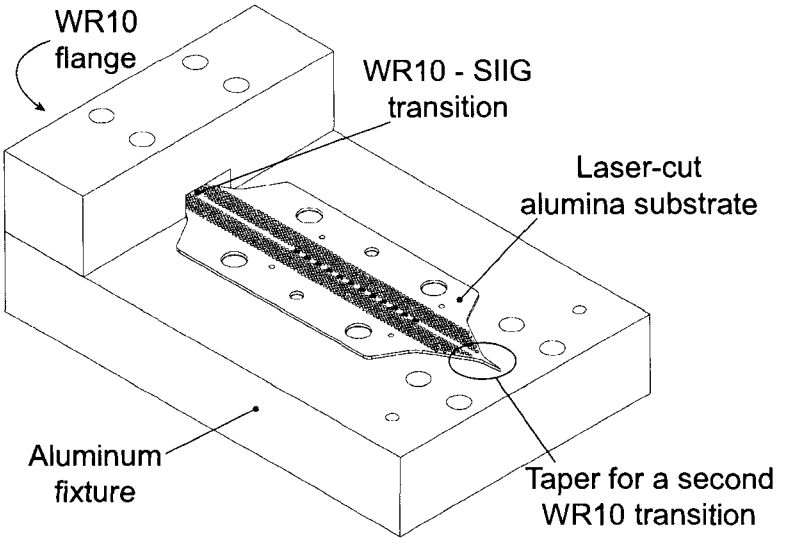

Figure 3.18 SIIG array antenna mounted on an aluminum base for measurement purposes. During measurements in the anechoic chamber, the base and the transition were clad with absorber material to avoid reflections and induced surface currents that would disturb the radiation pattern.

section 2.2). The described assembly is shown in Figure 3.18. An antenna with twelve elements is roughly 20 mm long, but the SIIG was extended on both sides to reduce the side effects caused by the transitions. Radiation pattern measurements were carried out with a compact-range setup in which the antenna under test was operated in receiving mode. Foam absorber was used to dissipate the residual guided power at the antenna output. The latter was replaced by a second transition for two-port transmission measurements by means of a VNA. Figures 3.19 and 3.20 show the simulated and measured reflected and transmitted power of the entire antenna. Significant ripple on the measured curves is a consequence of the superposition of reflected waves from the waveguide transitions and from the radiation elements. Frequency-dependent phase conditions entail either constructive or destructive interference, corresponding to reflection peaks or nulls. The transitions to WR10 waveguide as well as material losses were not modeled in the simulation. It can be noticed that the reflections are higher for reverse

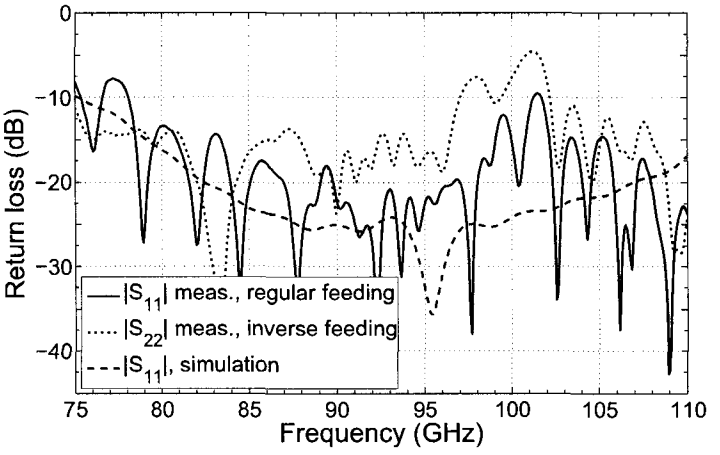

Figure 3.19 Measured and simulated antenna return loss. The non-ideal transitions to WR10 waveguide cause and increased measured reflection level.

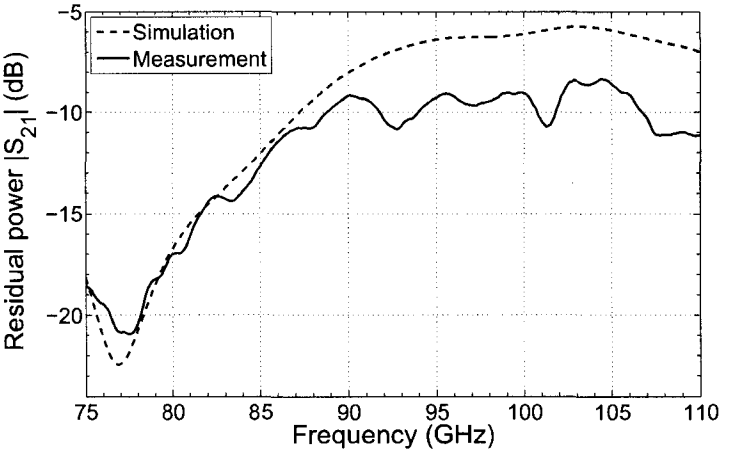

Figure 3.20 Measured and simulated residual power at the antenna termination. Material losses as well as insertion losses from the two WR10 transitions are not included in the simulation.

feeding, i. e. when the elements are fed from the output port. In this case, the reflection cancelation is not ideally adjusted any more since obstacle strips and anti-reflection strips are exchanged. A relatively high reflection level can be observed around 100 GHz. This was later found to be the frequency of broadside radiation, which had shifted from 94 GHz. In other words, the phase constant β was found to be 6 % smaller at the design frequency, which in turn deteriorates the return loss performance. This change is partly caused by fabrication tolerances and in part by not precisely known material constants in the given frequency range. Furthermore, it was observed that the high-density polyethylene film is very susceptible to humidity and that it changed its thickness over time. The deviation of the residual power in Figure 3.20 arises from dissipation losses and attenuation caused by the transitions which were not included in the simulation. The measured residual power is in the range of -8 dB after accounting -1 dB for the two WR10 transitions. This means that a fraction of 16 % is dissipated in the absorber. Also observable in Figure 3.20, the residual power is relatively constant over the operating frequency range. The field strength on top of the SIIG, where coupling to the radiation elements occurs, decreases for higher frequencies because the fields are more concentrated in the interior of the guiding channel. However, the etched strips are electrically longer at increasing frequencies, which somewhat flattens the frequency dependence of the radiation coefficient.

Figure 3.21 shows the measured radiation pattern in the H-plane at broadside angle while operated at the broadside frequency of 100 GHz and at adjacent frequencies. Due to technical restrictions, the antenna could not be measured over the full 180°-range. Shadowing effects caused by an absorber can be noticed for angles greater than 120° and diffraction occurred even before. However, since the antenna is symmetric, the first quadrant already contains all the pattern information. The maximum gain is 11 dBi at $\phi = 50°$, measured with an error tolerance of ± 0.6 dB. By comparison with the H-plane patterns at 99 GHz and 101 GHz, no relevant decrease in gain can be observed at the

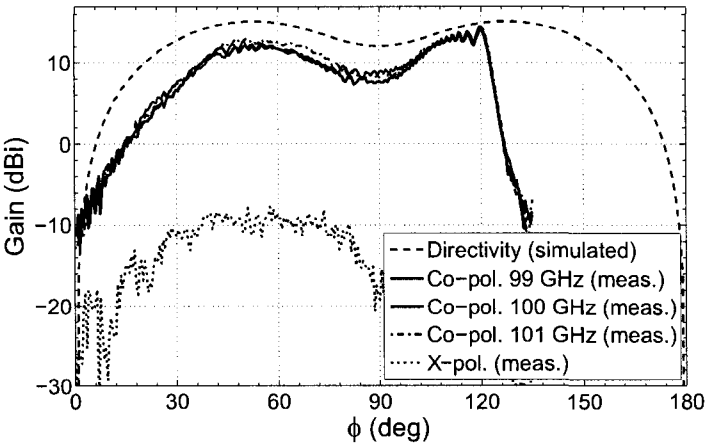

Figure 3.21 Simulated and measured H-plane radiation patterns ($\theta = 90°$).

broadside frequency of 100 GHz. This is a proof of the effectiveness of the reflection-cancelation technique. Cross-polarization is low for two reasons: The elements consisting of parallel strips are inherently linear polarized and the SIIG was designed to support only the fundamental mode, which does not couple to an incident wave of orthogonal polarization. The simulated directivity is also shown for comparison. The shape agrees well, whereas its absolute value is higher because no transition and dissipation losses are taken into account. The dent occurring at broadside direction can be explained by image theory. A radiation element over the image plane (ground plane) can approximately be modeled by two point sources with twice the distance, whereas the image source has negative sign. Constructive interference occurs at broadside if the distance between these sources is $\lambda/2$. Since the actual electrical distance in the case of our antenna is slightly more, about $0.65 \cdot \lambda$ by taking into account the effects of the substrate, constructive interference occurs at an angle of 40° away from broadside. Admittedly, this circumstance is not ideal. A combination of thinner substrate and thinner insulation film improves the pattern while it does not change the operating frequency range. Another option is to make use of only one of the two maxima when a two-dimensional array is designed. Figure 3.22 shows the measured E-plane radiation pattern at the broadside frequency

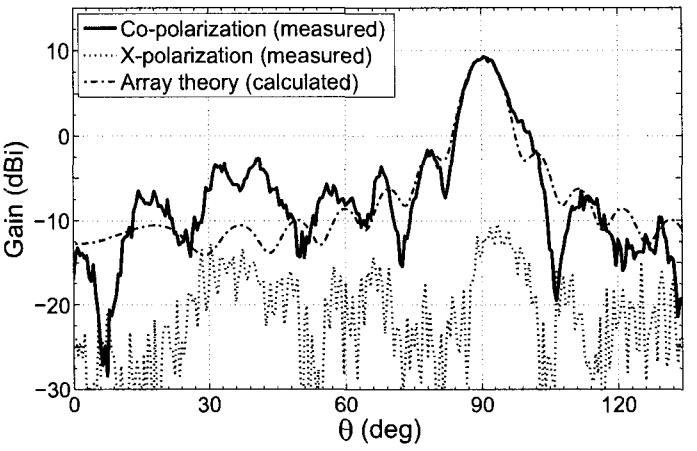

Figure 3.22 Calculated and measured E-plane radiation pattern ($\phi = 90°$). The peak of the calculated curve is fit to the peak of the measured curve.

of 100 GHz. For comparison, the expected pattern was calculated by array theory for exponentially decreasing excitation of point sources. This analytical approach allows quite accurate prediction of the shape of the main beam. The rest of the pattern matches only roughly, since the sheet absorbers applied to the free surfaces of the aluminum fixture do not totally suppress surface currents and reflections, and the transition to WR10 waveguide is also believed to cause noticeable side effects. Obtained radiation patterns show comparably good results in the entire operating frequency range from 88 GHz to 103 GHz.

It is difficult to determine the radiation efficiency experimentally. Simulations with included material loss predict a power loss of 13 % due to dissipation. Another 18 % are not radiated, but dissipated in the terminal absorber. The insertion loss of the employed WR10 transition is estimated at 0.5 dB or 11 %, which yields, altogether, a total radiation efficiency of 58 % or a loss of 2.4 dB. This theoretical result is in accordance with the difference between the measured gain and the simulated directivity in Figure 3.21. Even if insertion losses from an integrated transition between CPW and SIIG might be slightly higher than in the case of the rectangular waveguide transition, there is still room for

lowering the residual terminal power. MMIC connection losses included, the overall efficiency to achieve with this type of integrated antenna is estimated to lie between 50 % and 60 % at 94 GHz, if the same materials are used.

Figure 3.17 shows the main beam scan angle over frequency. The already mentioned deviation in the phase constant of the SIIG shifts the scan angle by 10° compared to theoretical predictions. The average curve steepness is 2°/GHz and the half power beam width of the main beam is 8.5°. Therefore, the antenna could be used as a fixed-direction fan-beam sector antenna for high-capacity data links within a bandwidth of up to 2 GHz. Higher gain can be achieved by arranging several SIIG array antennas in parallel, thus narrowing the H-plane beam. Long-range vehicular radars could use the frequency scanning ability of this antenna. By increasing the number of elements and antenna length, the main beam can be made very narrow for this application.

3.3 Dielectric slab-mode antenna

3.3.1 Design

A wideband CPW-SIIG transition that is suitable to excite a surface wave on an integrated dielectric waveguide is presented in section 2.3. In an analogous manner, a TM_0 slab mode can be launched on a grounded dielectric substrate, as illustrated in Figure 3.23. Like the CPW-SIIG transition, this type of slab-mode launcher can be used on high-permittivity substrates and has an operating bandwidth of typically more than 20 % at a return loss level of better than -20 dB. More details on the underlying mechanism of field conversion between a CPW and a dielectric waveguide are given in section 2.3. Other TM_0 slab-mode launchers can be found in the literature, e. g. with microstrip input [105] or CPW input [106]. However, the presented launcher is superior in terms of launching efficiency as well as achievable bandwidth and was therefore preferred over

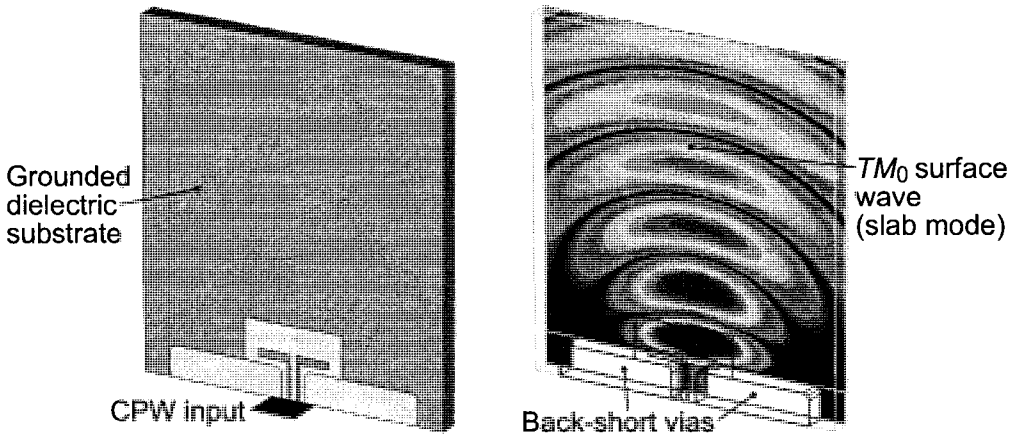

Figure 3.23 Topology of the developed TM_0 slab-mode launcher and visualization of the electric field at ground plane level.

the other designs. Moreover, its front-to-back ratio is very high as a result of the large metallic back-short vias.

Depending on the chosen substrate material, a slab wave can have very low transmission loss. Wave attenuation is particularly low if a thin low-permittivity insulation film or air gap is introduced below the substrate, as it was also done for the SIIG to reduce conductor losses in the ground plane. This simple waveguide structure was shown to be attractive for 2-D quasi-optical power combiners [105, 107], a topic that is briefly discussed in the next chapter. Directive mmW antennas constitute another interesting application, because a surface wave that originates from a point source can be spread to a large effective aperture and then be radiated efficiently into free space. An antenna based on this functional principle was realized and a photograph of the prototype including part descriptions is shown in Figure 3.24. It was fabricated from Rogers RT/duroid® 6010LM high frequency laminate (ε_r = 10.2, tanδ = 0.0023). Although the intended area of application mmW front-ends due to the efficiency advantages over conventional metal-based antennas, the antenna was designed around 12 GHz in order to allow the use of a standard SMA connector and to simplify radiation pattern measurements in the anechoic cham-

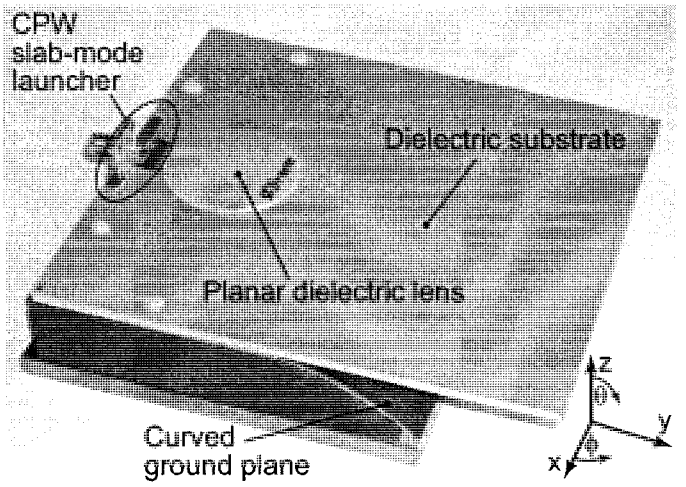

Figure 3.24 Photograph and part description of the realized slab-mode antenna prototype.

Table 3.1 Dimensions of the slab-mode antenna prototype.

Symbol	Dimension	Value [mm]
a	Substrate edge length (square)	120
d	Substrate thickness	2.54
h	Air gap (below substrate)	0.254
t	Lens thickness	1.27
D	Lens diameter	34
r	Radius of curved ground	60
l	Length of curved ground (horiz.)	40

ber. The physical dimensions are listed in Table 3.1. A planar dielectric lens being half as thick as the substrate and of the same material was attached on top of the substrate. It locally changes the thickness of the grounded substrate and therefore reduces the phase velocity of the guided wave in those regions, which leads to a focal effect. The cylindrical phase fronts of the launched surface wave are flattened in this way to augment the antenna gain. This principle is discussed more explicitly in section 4.3 together with a

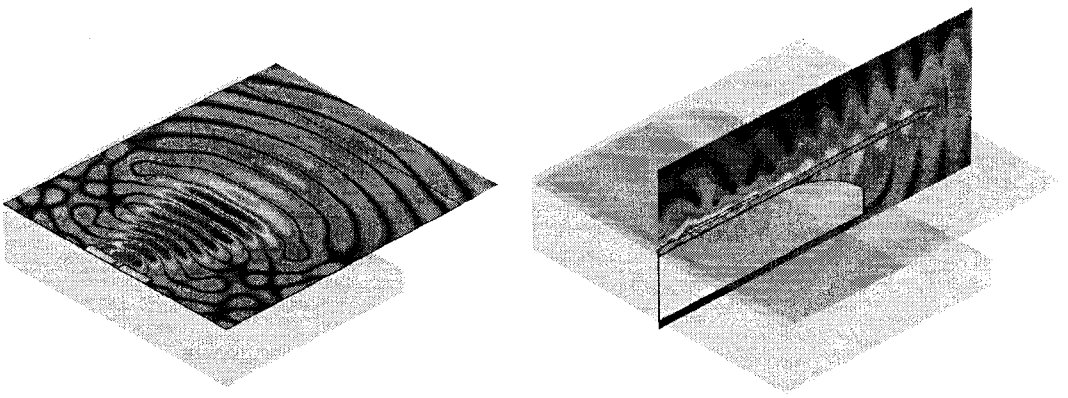

Figure 3.25 Simulated electrical field at ground plane level and on a centered vertical plane of the slab-mode antenna.

quantitative analysis of the propagation constants in the dielectric slab. The prototype's curved ground plane was milled out of a brass block. Low-cost fabrication for commercial products is feasible by plastic injection molding and subsequent electroplating, for example. Instead of an insulation film, a small air gap of $h = 0.254$ mm was created between the substrate and the ground plane. Figure 3.25 shows the simulated electric field on a horizontal and on a centered vertical plane of the antenna. The field visualizations illustrate how the guided surface wave in the grounded slab is focused by the dielectric lens, gradually transformed into an ungrounded slab mode by the curved ground plane, and finally radiated in end-fire direction at the edge of the substrate. Since the wave is loosely guided at this point (low effective permittivity), reflections from the substrate border are relatively small in spite of the high refractive index contrast. Scattering can be reduced additionally by an antireflection segment at the radiating edge, as shown in Figure 3.26. Such a segment may be of a material with a lower permittivity, between that of the high-permittivity substrate and that of the surrounding air. The best value found by iterative optimization was $\varepsilon_r = 2.2$ with a section length of 7.8 mm. An alternative and simpler manner is to thin the substrate, which leads to a lower effective permittivity of the guided slab. A comparison of the simulated reflection level with and without

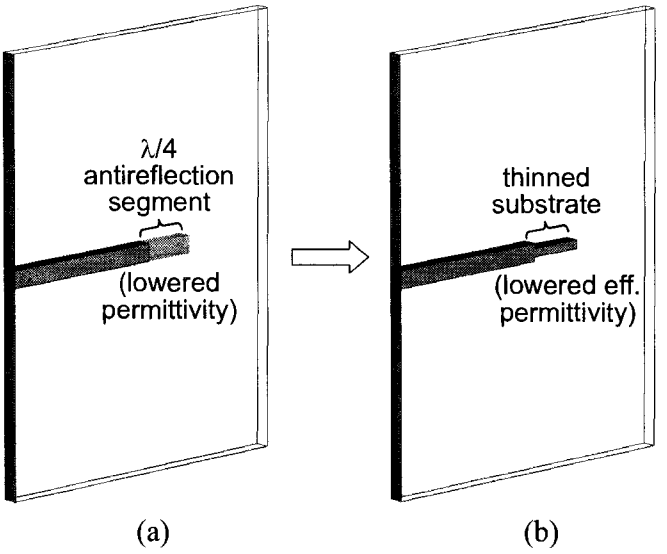

Figure 3.26 Antireflection segment at the substrate edge: (a) $\lambda/4$ substrate section of lowered permittivity or (b) thinned substrate with lowered effective permittivity.

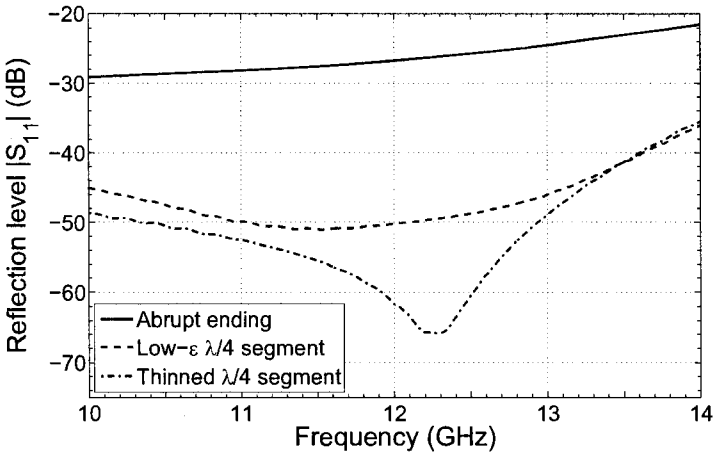

Figure 3.27 Comparison of the simulated reflection level (dielectric slab only) with and without the antireflection segment.

the antireflection segment is shown in Figure 3.27. Besides a decreased return loss, this technique also slightly improves the radiation pattern due to the improved scattering behavior at the substrate edge.

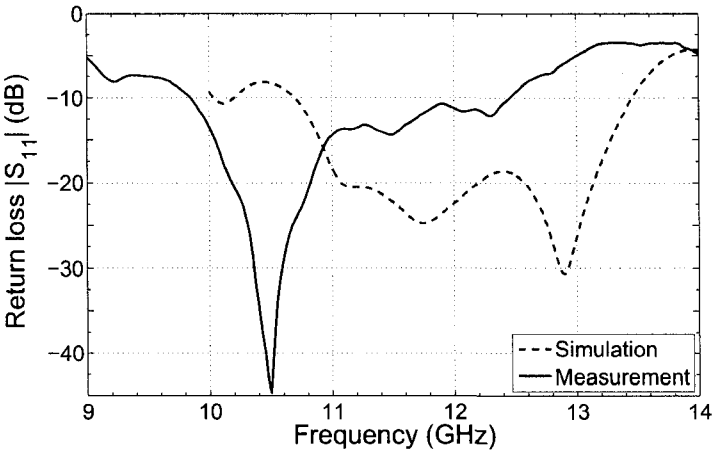

Figure 3.28 Measured return loss at the SMA connector of the slab-mode antenna in comparison with simulation results.

3.3.2 Experimental results

The return loss at the soldered SMA connector was measured by means of a network analyzer. Measurement and simulation results are shown in Figure 3.28. Despite the frequency shift and degradation of the measured return loss, which is most probably caused by fabrication tolerances and the effect of the SMA connector, the bandwidth at less than -10 dB is greater than 20 % and thus confirms the simulation result. This bandwidth is by far enough to cover the unlicensed 60-GHz band and other assigned mmW bands.

The radiation patterns in the E- and H-plane were measured in a compact range setup in an anechoic chamber. Figure 3.29 and Figure 3.30 show the results in comparison with those obtained by simulations. Very good agreement is noticeable and the measured antenna gain of 12.0 dBi differs only marginally from the simulated directivity of 12.6 dBi. The side lobe level observed in the H-plane is low, which supports the idea of slab-beam focusing by a planar lens. Significant side lobes exist in the E-plane, however. They are mainly caused by the slightly radiating slab-mode launcher (about 3 % of the power is

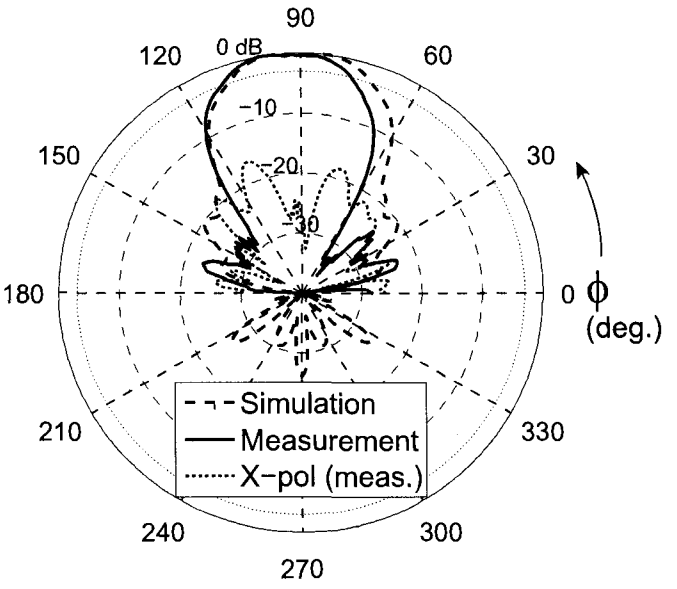

Figure 3.29 Simulated and measured H-plane radiation pattern of the slab-mode antenna at 12 GHz.

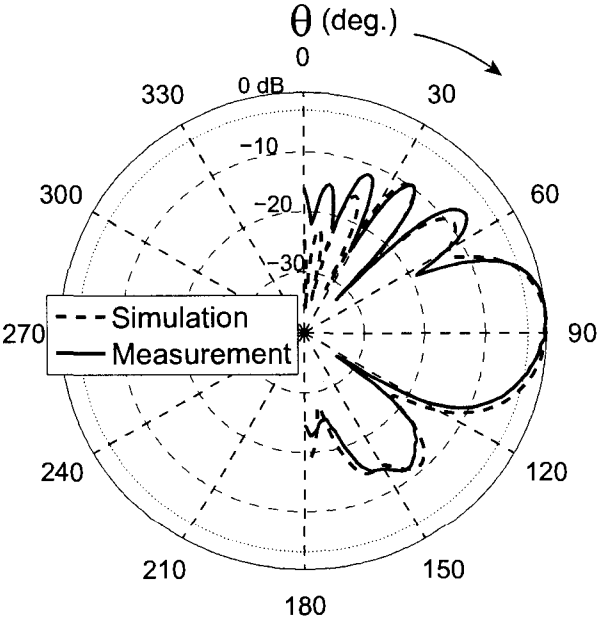

Figure 3.30 Simulated and measured E-plane radiation pattern of the slab-mode antenna at 12 GHz.

radiated to the air side instead of the substrate, see section 2.3). Absorbers could be used to suppress them, if necessary. The side lobe to the lower hemisphere is generated by the abruptly ending ground plane and can be lowered by an optimized design. A relatively small lens was used for the prototype. The antenna gain can be enhanced by a larger, optimized lens, which leads to a wider effective aperture in the horizontal dimension. The E-plane beam width depends on the vertical extension of the guided wave fields. The thinner the dielectric slab, the looser the wave guidance and the larger the effective vertical aperture. Similar to the rod antenna discussed in the foregoing section, the gain may therefore be increased by tapering the dielectric slab towards the end. An accurate theoretical solution for this kind of wedge antenna is available [108]. Applying these design optimizations, a scaled 60-GHz version of a slab-mode antenna with 15 dBi gain could be smaller than 20 mm $\times$ 20 mm.

3.3.3 Special features

The developed dielectric slab-mode antenna is well-suited for applications in the mmW range because of its low-loss dielectric construction, its wide operating bandwidth, and the customizable directivity in a range of about 5 dBi to 20 dBi. In contrast to the also very popular Vivaldi antenna, a special version of tapered slot antenna, the dominant electric field component of the slab-mode antenna is oriented perpendicularly to the substrate plane. Therefore, and due to the gradual transition to free space, it is capable of radiating efficiently even from thick high-permittivity substrates. At 60 GHz, for example, substrate thicknesses in the range of 0.5 mm are applicable and allow a good structural stability, whereas most other types of integrated antennas on high-permittivity substrates suffer from the well-known *field trapping* effect [109,110]. As a consequence, the slab-mode antenna is capable of being integrated with a silicon MMIC on the same wafer. It also differs from the Vivaldi antenna in its filtering effect. The necessary CPW slab wave launcher is inherently bandwidth limited, whereas the tapered Vivaldi design

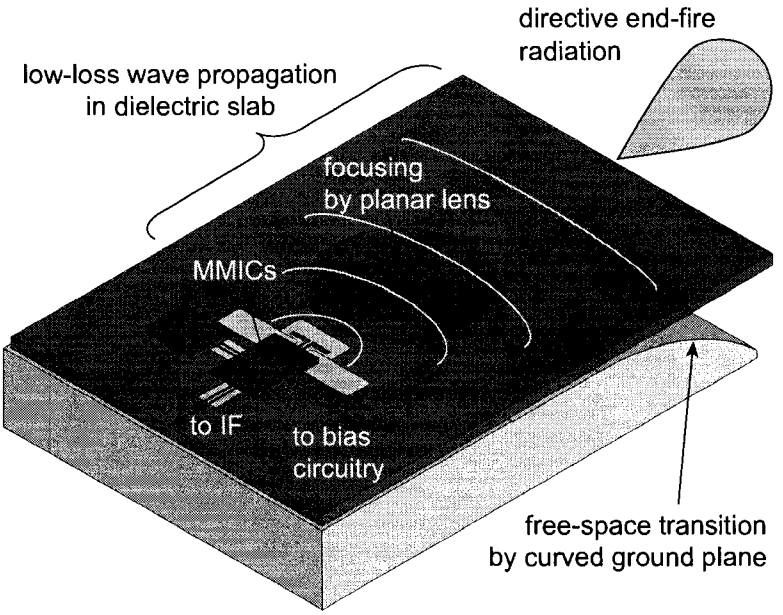

Figure 3.31 Conceptual assembly of a slab-mode antenna and flip-chip mounted MMICs.

is very broad band. In most cases, however, a certain bandwidth limitation is an advantage for filtering undesired received signals. A reasonable antenna gain of about 15 dBi – 20 dBi is required for short-haul high-speed communications as projected for the 60-GHz band for several reasons [111]. Although the aimed distances are quite small, the generated power is distributed over a large frequency range or over a large number of carriers if OFDM is used as modulation scheme. Since power amplifiers are cost-intensive at 60 GHz and battery power is scarce in portable devices, the preferred approach are efficient high gain antennas. This is further promoted by the high free space path loss and because such antennas are small at short wavelengths. More directive radiation also reduces the signal delay spread in indoor environments, which in turn lowers interference and improves the channel capacity. Another advantage is the antenna's compatibility with wire-bonding or with the flip-chip approach [112] for hybrid integration. A conceivable mmW front-end assembly is shown in Figure 3.31, where MMICs are flip-chip

mounted on a common substrate for connection to the off-chip slab-mode antenna. In this way, the interconnection losses can be kept very small to avoid a degradation of the system performance. The large solid vias that form a part of the transition can simultaneously be used for RF grounding and heat dissipation from the MMIC. The common substrate not only serves as a support for the MMICs and as wave guiding medium in the antenna, but can also accommodate other microwave and biasing circuits. By this means, planarity is maintained – one of the most important premises for low-cost processing. The simple construction of the dielectric slab-mode antenna should allow its use up to submillimeter frequencies.

CHAPTER 4

SIIG BENDS AND POWER SPLITTING/COMBINING

This chapter deals with the feasibility of bends and power splitters or combiners in SIIG technology. Although efficient wave guidance along such discontinuities is a general problem in conjunction with dielectric waveguide technologies, an alternative approach was investigated to ease those drawbacks.

4.1 SIIG bends

Electromagnetic waves on dielectric waveguides are unshielded and more loosely guided than in metal-based waveguides. As a consequence, radiation occurs at waveguide curvatures. Losses due to radiation in bends were studied theoretically [113] and experimentally for dielectric rod transmission lines in general [114] and for the image guide in particular [115, 116]. It was found that the radiation losses decrease with increasing refraction index contrast and radius of curvature. Figure 4.1 shows a 60°-bend in SIIG technology on alumina and the respective simulated electrical fields. The bend losses are unacceptably high and may lead to severe cross-talk in integrated circuits. It is therefore often recommended to maintain a minimum radius of curvature in order to keep the losses at an acceptable level. An estimate for the minimum acceptable radius R for low permittivity dielectric rod guides is [116]

$$R = \frac{8\pi^2 r_0^3}{\lambda_0^2} \,. \tag{4.1}$$

In (4.1), r_0 designates the length over which the field decays by $1/e$ in a distance of the straight guide. This would translate to $R \approx 2.5$ mm for the shown alumina SIIG

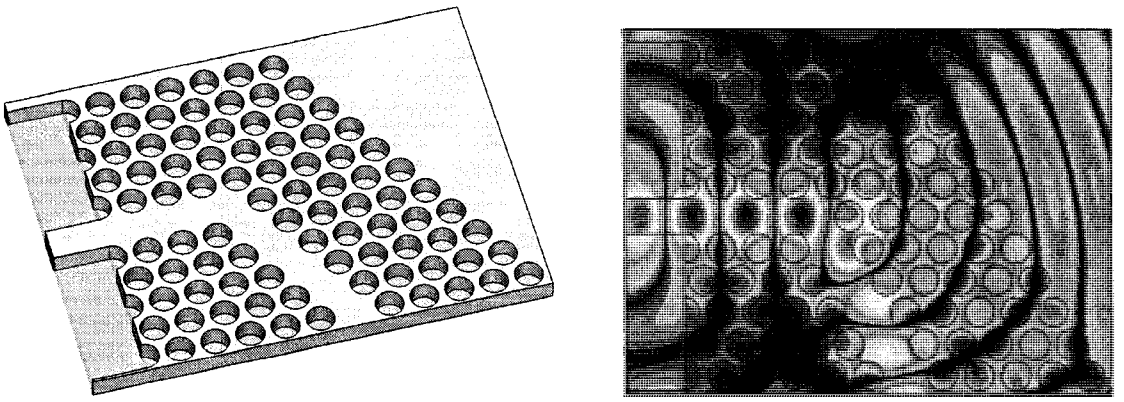

Figure 4.1 60° SIIG bend and simulated electric field.

at 94 GHz. Practical measurements have shown [116] that at least twice this radius is needed to achieve reasonably low radiation levels, even in conjunction with high-permittivity substrates. Although this option is usually chosen at optical wavelengths, resulting bend dimensions in the order of centimeters at mmW frequencies are not practical for integrated circuits. An approach that allows drastically reduced bend radii involves a laterally varying permittivity of the dielectric waveguide [117]. In the case of the SIIG, the effective permittivity in the substrate could be changed by altering the air hole radius. However, if a quasi-homogeneous medium is to be created, a very fine lattice of air holes would be necessary. This can only be achieved by a very precise fabrication technique and it is questionable if a simple waveguide bend is worth such an effort. Another option is the use of resonant cavities in the waveguide intersection regions. Such a scenario was theoretically studied in two dimensions for integrated optical circuits [118] with very convincing results. The idea was picked up for the design of image guide multiplexers [119]. Even though the basic principle was shown to work, a considerable amount of radiation still occurs, unless the index contrast is extremely high. This situation is comparable to dielectric resonator antennas, where the majority of the power is reflected at the dielectric-air interfaces and resonates in the dielectric cavity, but a part is intentionally radiated at each wave bounce. Electromagnetic band gap (EBG)

regions were also investigated for efficient wave guidance around bends in dielectric waveguides, in particular at optical frequencies [61]. However, easy-to-build 2-D EBG structures confine the electromagnetic energy in two dimensions only, so that significant radiation can still occur in the third dimension for which the guiding effect is based on a refractive index contrast. Arising leaky-wave radiation due to the long periodic interval in the EBG region was addressed in section 1.4.4. As a conclusion it has to be admitted that there is no straightforward solution to the problem of SIIG bends. Techniques to reduce radiation at bends to an acceptable level exist but involve high complexity or unreasonable dimensions. Preferred applications are those for which linear SIIG sections can be used.

4.2 SIIG Y-junctions

Although compact SIIG bends with small radius of curvature and low insertion loss are very difficult to realize, the situation is different for for Y-junctions that are used to split the guided wave power in two branches. If the the opening angle of the output branches is chosen small enough, the discontinuity seen by the incoming wave is rather small and so is the radiation of curvature [120]. Those components are important for symmetrical or asymmetrical power splitting, e. g. in parallel image line array antennas [121]. It was also found that such bifurcations can be used as couplers due to the achievable high isolation between the output ports [120]. An example for a symmetric Y-junction is given in Figure 4.2 along with the simulated electrical field. It can be observed that the power splitting is achieved with much lower radiation loss compared to the sharp SIIG bend in Figure 4.1, although the lattice of air holes is quite coarse. An insertion loss of -1 dB was achieved for this example. Applying a finer lattice or a combination of larger and smaller air holes can significantly improve the result, because the existing discontinuities in the output branches are reduced.

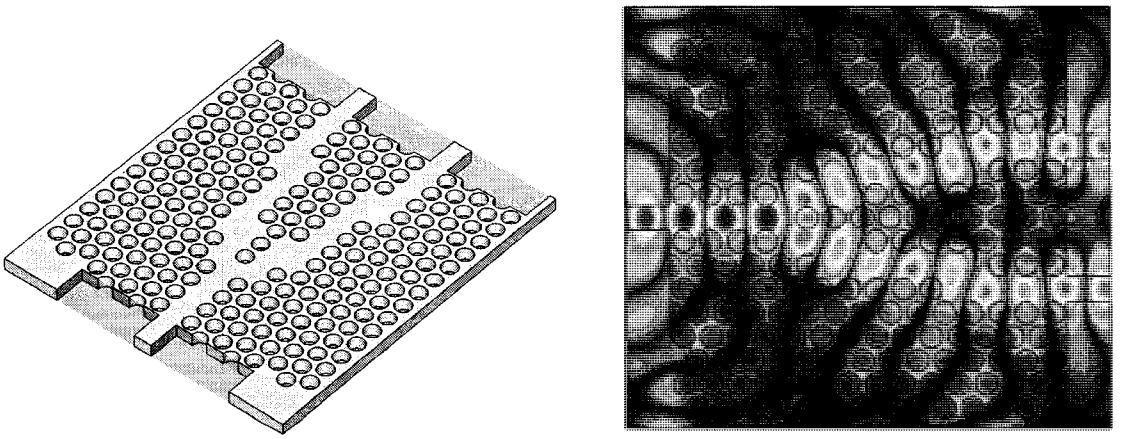

Figure 4.2 SIIG Y-junction and simulated electric field.

4.3 SIIG slab-mode splitter

The SIIG Y-branch presented in the above section is suitable exclusively for power splitting into two branches. If more output channels are required, a direct junction is not practical, because it is virtually impossible to mitigate the radiation loss problem. A more promising approach is to divide a slab wave. Those techniques also became known as 2-D quasi-optical power combining and examples in microstrip [105] and coplanar technology [107] are published. The idea of using a planar dielectric slab for quasi-optical power splitting/combining has the advantage of low loss and low radiation. A surface wave is excited on a grounded dielectric slab (substrate) by a suitable planar wave launcher in a directive manner. The wave being emitted from a single point, spreads laterally by a certain angle while it propagates in the slab without discontinuities. It is then received by an array of opposite wave transitions. The used wave launchers in both cases [105, 107] provide only narrowband performance and a limited front-to-back ratio. Another suitable wideband surface wave launcher is presented in section 3.3, where it is used as the feed of a slab-mode antenna. Low return loss in a wide bandwidth and good directivity are obtained due to the back-short vias. A TM_0-mode surface wave being excited in this way propagates in the dielectric slab and can then be divided in several

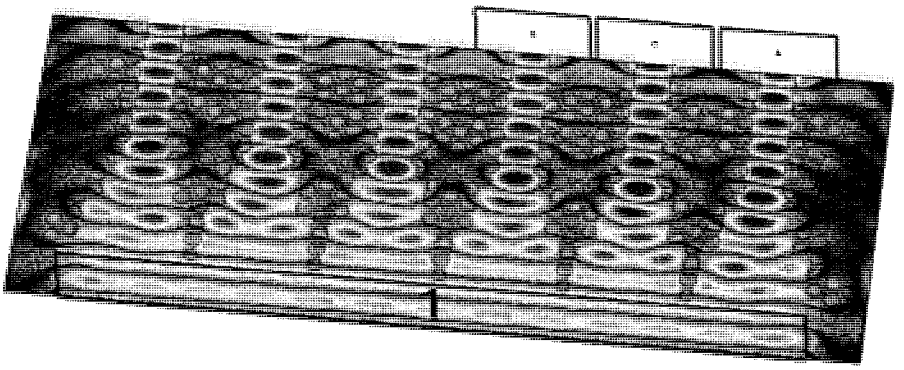

Figure 4.3 E-field visualization of an incoming slab wave that is split into several SIIG branches.

SIIG channels, as shown in Figure 4.3. To do so, however, the wave fronts of the slab wave must be straight, at least in the most common case of parallel output lines. To this end, the phase of the excited beam with cylindrical wave fronts has to be equalized either before or after reception. This requirement can be met by using either meander-shaped transmission lines of different length [105] or dielectric lenses embedded in the substrate [107]. The former has the disadvantage of being limited to lower microwave frequencies, the latter is difficult to manufacture. For this reason, a planar lens laid on top of the substrate is employed here for phase equalization, which is equivalent to focusing of the propagating wave. The same topology was also used for the dielectric slab-mode antenna in section 3.3. The lens effect is based on the differing phase velocities in grounded dielectric slabs of varying thickness. The propagation constants β of the slab modes can efficiently be calculated by the transverse resonance (TR) technique. This method uses a transmission line model of the transverse cross section of a uniform waveguide. The distinct advantage of the TR method is that boundary conditions at the dielectric interfaces can easily be handled as junctions of different transmission lines. Although the field distribution or guide attenuation are not directly accessible by this technique, the propagation constants β of the guided modes are obtained easily by finding the roots of a single characteristic equation. In the studied example, a low-permittivity insulation film

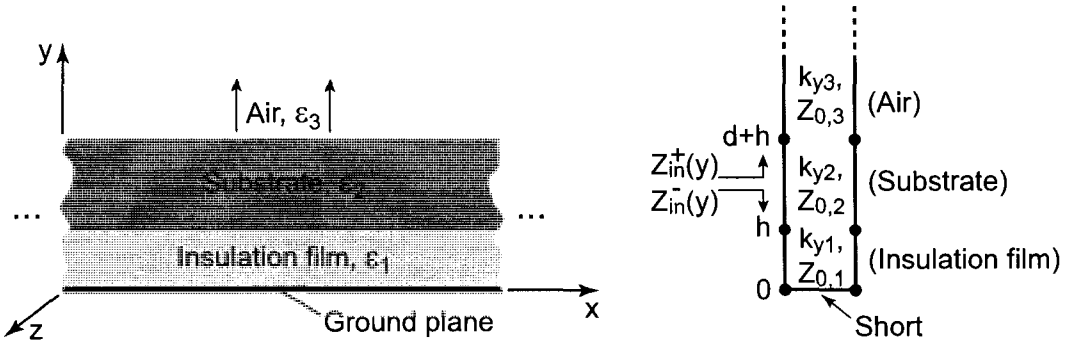

Figure 4.4 Dielectric slab waveguide and its transverse resonance representation as connected transmission lines.

was inserted between the alumina substrate and the ground plane in order to significantly reduce conductor losses in the latter. The resulting 3-layer structure (two dielectric layers and the air above) and its transmission line representation are shown in Figure 4.4.

The separability condition

$$\beta = \sqrt{k_i^2 - k_{ci}^2} \tag{4.2}$$

holds for the uniform waveguide with separable cross-sectional geometry, with wave number

$$k_i = \frac{2\pi f \sqrt{\varepsilon_{r,i}}}{c_0} . \tag{4.3}$$

in the i-th dielectric layer and transverse or cutoff wavenumber

$$k_{c,i} = \sqrt{k_{x,i}^2 + k_{y,i}^2} \tag{4.4}$$

(in Cartesian coordinates) in the respective dielectric layer with index i. Equation (4.4) reduces to $k_{c,i} = k_{y,i}$ in the case of the layered slab waveguide because of its uniformity in x-direction. For a given mode, $k_{c,i}$ is a fixed function of the waveguide geometry. In a waveguide, the fields form standing waves in the transverse plane of the guide. This situation can be modeled as a resonant transmission line circuit. The resonance condition

is

$$Z_{\text{in}}^{+}(y) + Z_{\text{in}}^{-}(y) = 0 \quad \forall y \,. \tag{4.5}$$

$Z_{\text{in}}^{+}(y)$ and $Z_{\text{in}}^{-}(y)$ are the input impedances seen at any point y on the resonant transmission line when looking towards the positive and negative y-direction, respectively. With the help of the well-known transmission line impedance equation

$$Z_{\text{in}} = Z_0 \frac{Z_L + jZ_0 \tan(\beta l)}{Z_0 + jZ_L \tan(\beta l)} \,, \tag{4.6}$$

the impedance transformed by the transmission lines can be evaluated at an arbitrary level y. Z_L is the load impedance at the end of the equivalent transmission line and Z_0 refers to its characteristic impedance. Z_0 is identical to the wave impedance of the *TM* or *TE* wave (depending on the considered mode) with transverse propagation constant k_{yi} in the respective dielectric layer [83]:

$$Z_{0,i} = Z_{TMi} = \sqrt{\frac{\mu_0}{\varepsilon_i}} \frac{k_{yi}}{k_i} \quad \text{for TM-waves} \,, \tag{4.7}$$

$$Z_{0,i} = Z_{TEi} = \sqrt{\frac{\mu_0}{\varepsilon_i}} \frac{k_i}{k_{yi}} \quad \text{for TE-waves} \,. \tag{4.8}$$

Due to the considered wave propagation in transverse direction, the propagation constant β in equation (4.6) has to be replaced by the corresponding k_{yi}. Thus, evaluating the resonance condition (4.5) at $y = h$ yields

$$Z_{in}^{-}(h) + Z_{0,2} \frac{Z_{in}^{+}(h+d) + jZ_{0,2} \tan(k_{y2}d)}{Z_{0,2} + jZ_{in}^{+}(h+d) \tan(k_{y2}d)} = 0 \,. \tag{4.9}$$

The fundamental mode of the grounded layered slab waveguide is the TM_0 mode. In this case, the *TM* wave impedances (4.7) are used. Since the slab is grounded on the bottom side, the load impedance is a short, i. e. $Z_L = 0$. Impedance $Z_{in}^{+}(h+d)$ is that of an infinitely long transmission line representing the air layer. The corresponding transverse propagation constant k_{y3} is always purely imaginary and therefore, with (4.6),

$Z_{in}^{+}(h+d) = -Z_{TM3}$. Thus, equation (4.9) yields

$$jZ_{TM1}\tan(k_{y1}h) + Z_{TM2}\frac{-Z_{TM3} + jZ_{TM2}\tan(k_{y2}d)}{Z_{TM2} - jZ_{TM3}\tan(k_{y2}d)} = 0\,. \qquad (4.10)$$

Applying (4.2), (4.3) and (4.7) results in the final characteristic equation, which allows the calculation of β by a root-finding algorithm for a given frequency. This TR algorithm can easily be extended to more dielectric layers, e. g. if the lens and the substrate are made of different materials or if the effects of a potential air gap between them need to be analyzed.

A simulation study was conducted in order to show the feasibility of slab-mode power splitting into SIIG branches. Alumina was chosen as high-permittivity substrate on a polyethylene insulation film. A substrate height of 381 µm on a 35-µm thick insulation film is suitable for operation at 94 GHz. Phase equalization of the surface wave propagating in the slab waveguide is achieved by a planar 254-µm thick alumina lens placed directly on top of the substrate. Figure 4.5 shows the normalized wavelengths of the fundamental TM_0 mode for the alumina substrate only and for combined substrate and lens thickness, resulting in $d + h$ = 635 µm. The fact that the shorter way through the center of the lens accounts for a shorter guided wavelength relative to the longer way via the lateral lens regions causes the wave fronts to be straightended, which leads to a wide, parallel beam. The mode plot in Figure 4.6 shows all guided modes, namely the fundamental TM_0 mode and the next higher TE_1 and TM_1 modes, for the increased slab thickness (substrate and lens) of 635 µm. For the given parameters, the cutoff frequency of the TM_1 mode is just below 90 GHz. However, in the 94-GHz-range it is guided so loosely that coupling to this mode hardly occurs. In contrast, the TE_1 mode with electrical field orientation parallel to the substrate is well guided and therefore mode coupling is probable at structural discontinuities such as an abrupt change in the substrate thickness. Negative consequences of this property are discussed later.

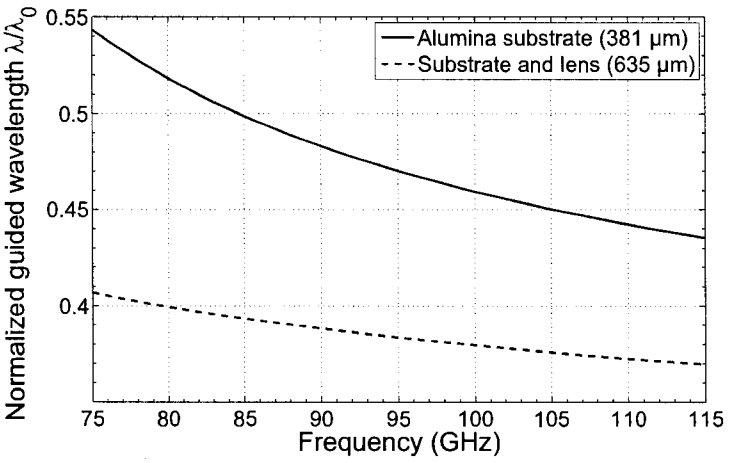

Figure 4.5 Differing guided wavelengths in the zones with alumina substrate only and in those with additional superimposed lens.

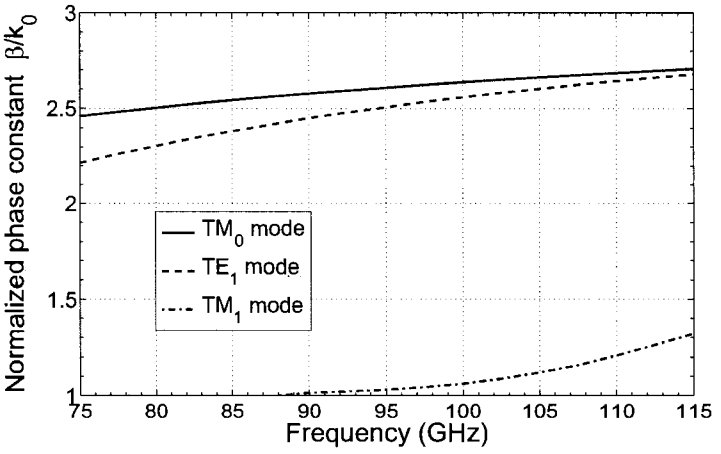

Figure 4.6 Fundamental and higher modes in the grounded slab (635 μm alumina).

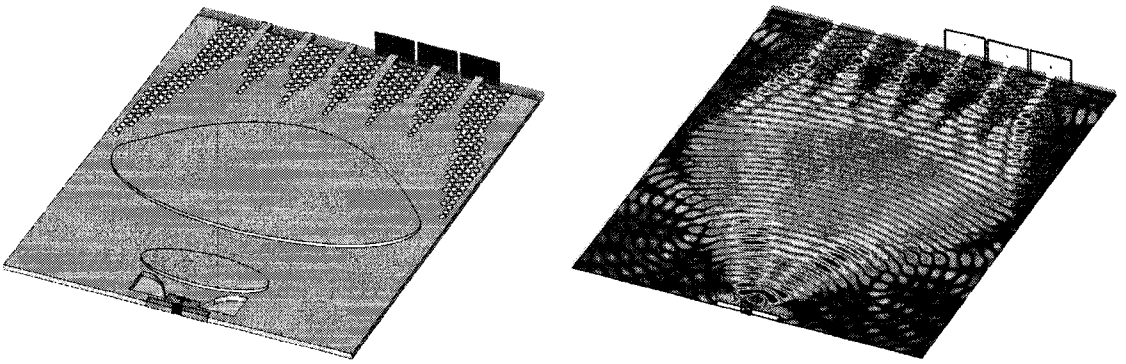

Figure 4.7 SIIG slab-mode splitter and simulated E-field.

In a next step, the slab-mode launcher of section 3.3 was combined with a planar lens on the substrate in order to achieve straight wave fronts in the grounded slab waveguide. It was observed that a single lens is not sufficient to achieve the necessary phase equalization. Furthermore, too much power was lost due to lateral radiation of the excited surface wave. For this reason, a second lens was added to the final design as well as recesses on each side of the slab-mode launcher. Finally, the entire SIIG slab-mode splitter, as shown in Figure 4.7, was simulated. Since the structure is symmetric, only three of the six output ports were evaluated. Results for insertion loss, amplitude distribution and phase equalization are shown in Figures 4.8 and 4.9. In good approximation, the insertion loss is equal to the radiation loss, because lossless materials were used in the simulation. The ideal, lossless output power for one of six equalized channels would be $10 \lg \frac{1}{6}$ = -7.8 dB. Close to 97 GHz, the output powers are almost balanced at a level of -11 dB. Consequentially, the radiation loss reaches about -3 dB, which is relatively high. The reflections from the abrupt change of slab thickness at the lens contours is one reason. They may be alleviated by a quarter-wave anti-reflection layer, possibly realized by a stepped rim. Another reason is the mentioned mode coupling to the TE_1 mode. A gradual taper instead of the abrupt step at the edge of the lens would mitigate this effect. In general, thinner lenses can also improve the reflection, radiation, and mode coupling behavior, but the focal distance then becomes very long. The phase curves in Figure 4.9

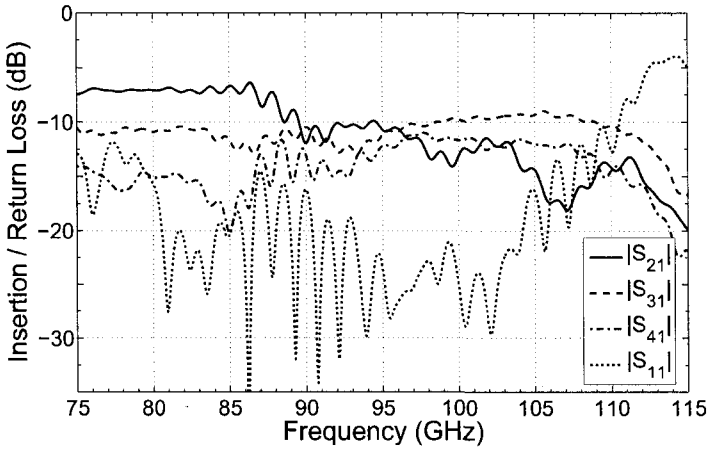

Figure 4.8 Amplitude distribution at the output ports of the SIIG slab-mode splitter.

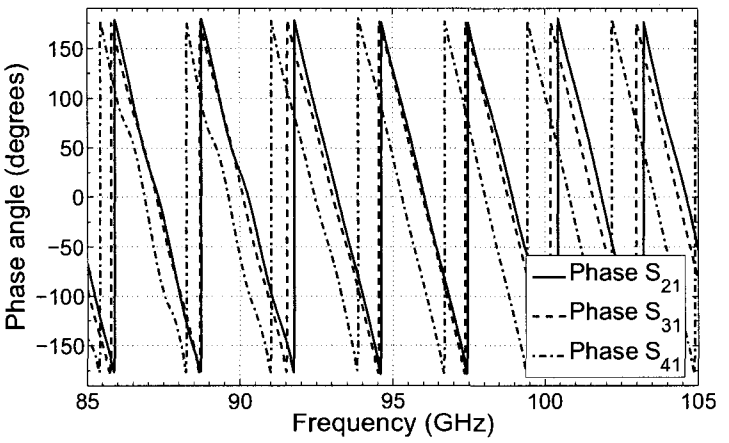

Figure 4.9 Phase conditions at the output ports of the SIIG slab-mode splitter.

indicate that the phase equalization by the pair of lenses is effective. Only the outermost channels lag behind by roughly 90°. The outputs do not necessarily have to be SIIG lines. The wave power can also be received by an array of slab-mode launchers, such as the one that is used at the input. This leads to a more compact design and provides CPW outputs to which mmW amplifiers can be connected. In this way it is possible to achieve simple but efficient planar power combining, comparable to [105, 107].

Generally speaking, this study has identified a possible way to accomplish power splitting or combining by use of a low-loss dielectric slab waveguide and SIIG output branches. A multitude of parameters still need to be optimized for improved performance. The demonstrated splitter/combiner can also be used for integrated dielectric antenna arrays or planar quasi-optical power combining at very high frequencies. Very low conductor loss and the inherent isolation of the output lines are convincing advantages compared to other techniques.

CHAPTER 5

THE SIIG IN THE CONTEXT OF SUBSTRATE INTEGRATED CIRCUITS

In this chapter, the SIIG is put into context with other integrated waveguide technologies, such as the CPW, the substrate integrated waveguide (SIW), and the substrate integrated non-radiative dielectric guide (SINRD). The different technologies' characteristics are compared and the feasibility of interconnections is demonstrated. Their hybrid integration and interconnection in substrate integrated circuits (SICs) is discussed and an active 60-GHz front-end is realized.

5.1 Comparison of substrate integrated waveguide technologies

The most popular embedded structure of an originally non-planar waveguide is the SIW. It consists of two rows of metallized vias in a dielectric substrate that is metal-clad on both sides [122]. The basic structure is shown in Figure 5.1, besides the SINRD [22] and the SIIG. Both, SINRD and SIIG, do not possess metallic side walls like the shielded

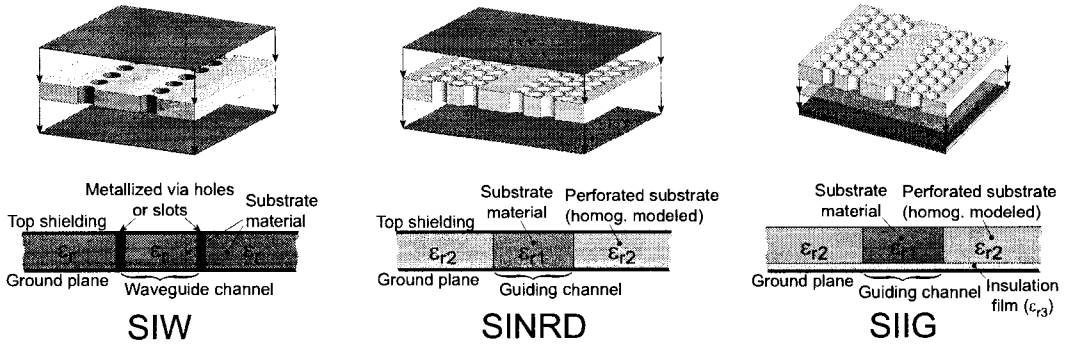

Figure 5.1 Substrate integrated waveguide structures, each with its respective equivalent model.

SIW. Wave guidance is achieved by substrate perforation which creates dielectric regions of different effective permittivity. As explained in the first chapter, the SIIG is a true surface wave guide, whereas the SINRD's mode of operation needs to be differentiated. Its first propagating *TEM* mode is actually similar to a parallel-plate mode which has no cutoff frequency. However, the SINRD is not operated in this mode due to the potential lateral leakage or radiation. The preferred mode is the LSM_{10} mode which has lower loss and does not radiate. Here, the guidance effect is achieved by a cut-off behavior in the adjacent zones of lower permittivity. The coexistent LSE_{10} mode constitutes an inconvenience because mode coupling can occur at discontinuities.

In the following, the different integrated waveguide structures are compared with each other and with traditionally used microstrip and CPW lines at a common benchmark frequency of 94 GHz. The same materials are used for all waveguides, i. e. high resistivity silicon (10 kΩ·cm), with ε_r = 11.7 and tanδ = $7 \cdot 10^{-4}$, and gold metallization with σ = $4.1 \cdot 10^{-7}$ S/m. Simulations of the attenuation of microstrip and CPW are difficult to perform without specialized simulation tools that adequately take into account the skin effect as well as field singularities. For this reason, measured values at lower frequencies [123] were taken as a basis and extrapolated to 94 GHz. Depending on the specific dimensions, a lower loss bound of at least 200 dB/m can be observed. This value can be much worse, if well-known problems like free surface charges or excitation of surface waves occur.

Wave guidance in the SIW is comparable to a conventional hollow metal waveguide, even though the overall guide attenuation is higher due to the dielectric filling and the consequential smaller cross section. Wave attenuation is calculated by a perturbation method [56] and the use of the respective equivalent model in Figure 5.1. The attenuation

constant due to dielectric losses α_d for the TE_{10} mode yields

$$\alpha_d = \frac{\sqrt{\varepsilon_r} k_0 \tan\delta}{2\sqrt{1-\left(\frac{f_c}{f}\right)^2}}, \tag{5.1}$$

with the cutoff frequency f_c and the dielectric loss tangent tanδ. This means that attenuation due to dielectric dissipation is independent from the waveguide height. Circumstances are different for the conductive attenuation constant α_c:

$$\alpha_c = \frac{2R_s}{b\sqrt{1-\left(\frac{f_c}{f}\right)^2}} \sqrt{\frac{\varepsilon_r \varepsilon_0}{\mu_0}} \left(\frac{1}{2} + \frac{b}{a}\left(\frac{f_c}{f}\right)^2\right), \tag{5.2}$$

where $R_s = \sqrt{\frac{\pi f \mu_0}{\sigma}}$ depicts the surface resistivity of the metallic waveguide walls. The waveguide width a is chosen for the desired single-mode frequency range, but its height b can be varied freely without changing the phase constant β. It can be noticed in equation (5.2) that conductor losses rapidly rise with decreasing b. In fact, for $b \ll a$, α_c is nearly inversely proportional to b. The transmission line Q-factor is inversely proportional to the total attenuation constant $\alpha = \alpha_d + \alpha_c$, as shown in equation (1.5). Consequently, the SIW height has a significant influence on the achievable quality factor in SIW components, in particular at high frequencies. For the attenuation loss comparison, width and height of the silicon SIW were chosen 735 µm × 368 µm so that lowest conductor losses are achieved at a maximum TE_{10} single-mode bandwidth. No field singularities exist in the SIW and currents flowing on the conductor walls are much better distributed compared to microstrip or CPW. Simulation results are shown in Figure 5.2. The obtained attenuation of 55 dB/m at 94 GHz should be seen as a lower bound due to the use of the equivalent model and the unconsidered surface roughness. However, measurements on fabricated SIWs have shown that the attenuation obtained in practice is only slightly higher. The dispersion behavior of the SIW is very similar to that of a standard metal waveguide, as can be seen in Figure 5.3.

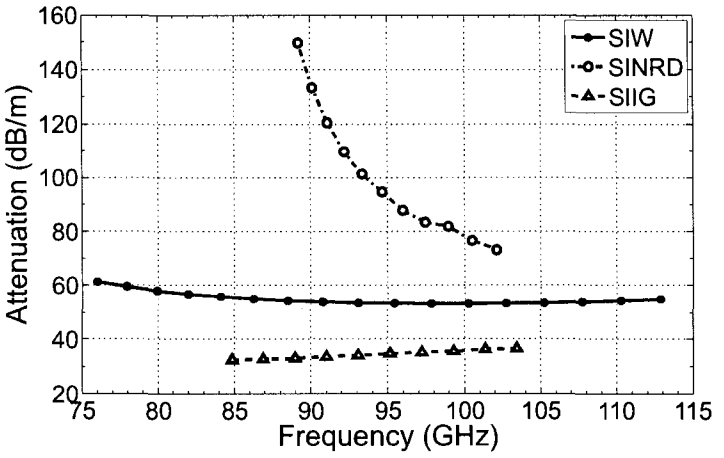

Figure 5.2 Guide attenuation of substrate integrated waveguide structures in their usable operation frequency range.

Attenuation properties of the SINRD were analyzed in an analogous manner. The core dimensions of the SINRD were 762 μm × 600 μm (width × height) with an effective relative permittivity ε_{r2} = 4.5 in the perforated zones in order to maintain the non-radiating feature around 94 GHz. This automatically implicates operation close to the LSM_{10} cutoff, causing relatively high and frequency-dependent attenuation around 100 dB/m as well as strong dispersion, as shown in Figure 5.2 and Figure 5.3.

Conductor losses in the SIIG only occur in the ground plane. Example simulations were carried out with core dimensions of 508 μm × 381 μm (width × height) and with a 30-μm polyethylene insulation film (ε_r = 2.3, tanδ = 0.001). On the basis of these numbers, the simulated attenuation accounts to 35 dB/m around 94 GHz, which corresponds to a transmission line Q-factor of about 900. As shown in Figure 5.3, the SIIG's gradient of the dispersion curve is relatively small and constant. Figure 5.4 shows the total attenuation split into a dielectric part and a conductor part. Conductor losses are clearly lower than losses by dielectric dissipation. Increasing the insulation film thickness further improves this property, thus making the SIIG a promising sub-millimeter waveguide. A

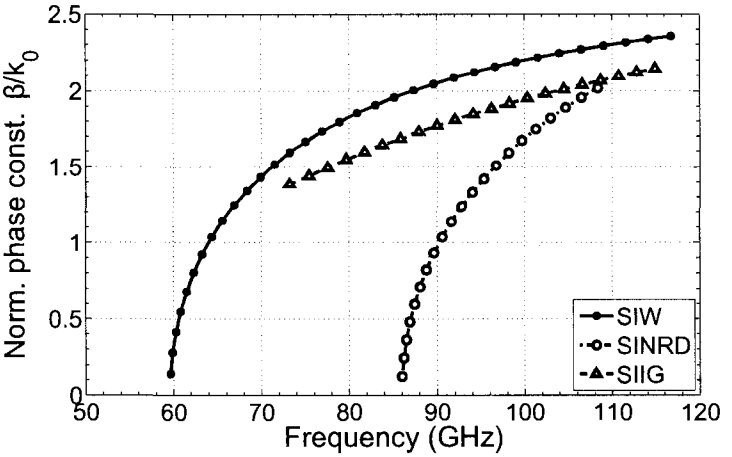

Figure 5.3 Dispersion of substrate integrated waveguides.

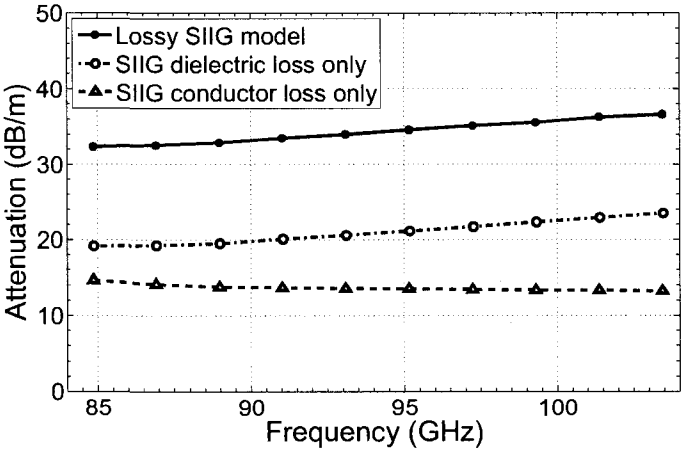

Figure 5.4 SIIG attenuation split into a dielectric part and a conductor part.

Table 5.1 Integrated waveguide properties summary.

Property	Microstrip / CPW	SIW	SINRD	SIIG
Dispersion	small / very small	high	extreme	high
Attenuation at 94 GHz	200 dB/m or more	55 dB/m or more	around 100 dB/m	35 dB/m or less
Operating bandwidth	DC – 110 GHz +	75 GHz – 110 GHz	89 GHz – 103 GHz	85 GHz – 104 GHz
Conduct. loss : dielectr. loss	10 : 1 or higher	1.5 : 1	1 : 1	0.6 : 1 or lower

recapitulating comparison of the propagation characteristics of the various synthesized waveguides on silicon substrate is given in Table 5.1.

5.2 Compatibility between SIW and SIIG

The desired operating frequency range of the SIIG dictates the substrate thickness, whereas the single-mode range of the SIW is only determined by its width. Therefore, in order to accommodate both on one electrically thick substrate, the SIW has to be adapted to these conditions. As a positive side effect, the mechanical stability increases and conductor losses decrease. Round metallized via holes are traditionally used to create the electric side walls of the SIW. Those holes are easily mechanically drilled into machinable materials. However, requirements for minimum return and leakage losses force the hole diameter to become very small at frequencies in the upper mmW or sub-millimeter-wave spectrum. This is especially true for high-permittivity materials like ceramics, semiconductors, or sapphire, which are often used because of their outstanding low-loss performance. Mechanical drilling of those materials is not feasible and therefore other micro-machining techniques such as laser perforation or wet/dry etching

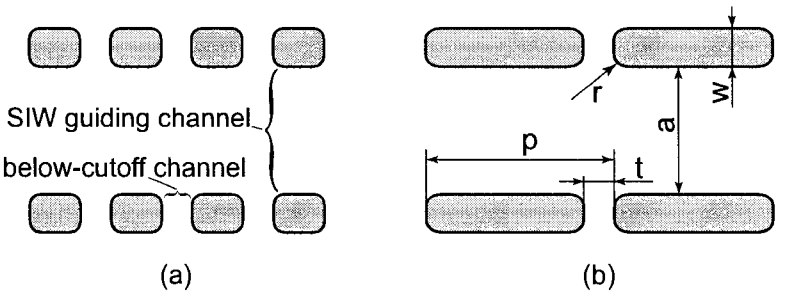

Figure 5.5 New SIW via slot configurations with (a) short slots and (b) long slots for operation below the first stop band or between the first and second stop bands, respectively.

are employed. Since those techniques are amenable to arbitrarily shaped perforations, the limitation to circular vias is not justified any more. Rectangular slots were found to be advantageous for lower leakage and better definition of the SIW side walls. Rounded corners increase the overall mechanical stability, allow for better metallization, and often cannot be totally avoided in the fabrication process (e. g. due to the finite diameter of the laser beam). Larger via dimensions that can be chosen in this way simplify fabrication, especially at very high frequencies in combination with electrically thick substrates in the range of $\lambda/4$ or more, where the aspect ratio (via depth versus diameter) is high. Figure 5.5 shows two different slot configurations, one with short slots for waveguide operation below the SIWs first stop band and another with long slots for operation between the first and second stop bands. Those stop bands or electromagnetic band gaps are unavoidable in periodic structures and occur due to distributed Bragg reflection in the vicinity of frequencies where the periodic spacing p is equal to a multiple of half a guided wavelength.

The wall thickness t between the slots plays an important role for the leakage rate. These inter-slot regions can be seen as waveguide sections below cut-off, in which the evanescent fields decay exponentially. Compared to cylindrical vias, t can be much wider, if the slot width w is increased. As a matter of fact, this can be a significant

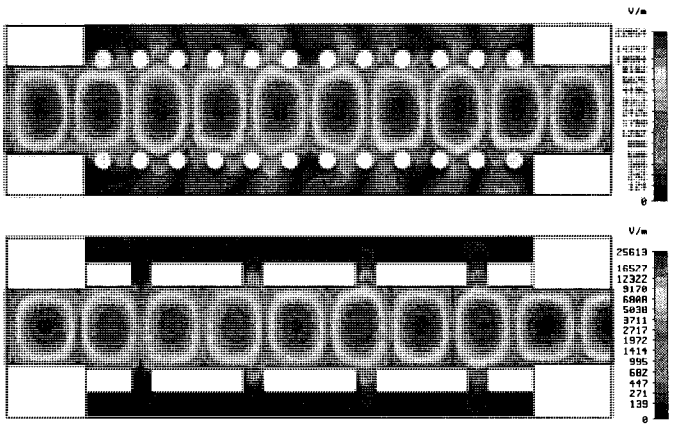

Figure 5.6 Comparison of leakage between an SIW with round vias and long via slots. The spacing between the holes is the same as that of the slots, t = 300 µm, and the hole diameter corresponds to the slot width.

advantage at mmW and sub-mmW frequencies, where feature sizes become extremely small. Figure 5.6 illustrates the difference in leakage level between an SIW with round vias and another with long slots. The leakage level is significantly higher in the case of round via holes, although the spacing t is equal. Moreover, the phase constant of an SIW consisting of long slots has a phase constant which is in much closer agreement with that of a uniform waveguide, as shown in Figure 5.7. This improved side wall definition potentially eases component design.

The slot interruptions constitute discontinuities in the substrate integrated waveguide channel and therefore cause reflections, if an SIW section is connected to a uniform waveguide (i.e. with continuous side walls and the same width a. The reflection level generally rises with increasing t and r. However, an SIW section can be regarded as uniform transmission line section with its own characteristic impedance. The characteristic impedance of periodic structures is also called the Bloch impedance by analogy with quantum-mechanical electron waves that may propagate through a periodic crystal lattice in a solid [124]. This impedance is only unambiguous if the terminal planes of

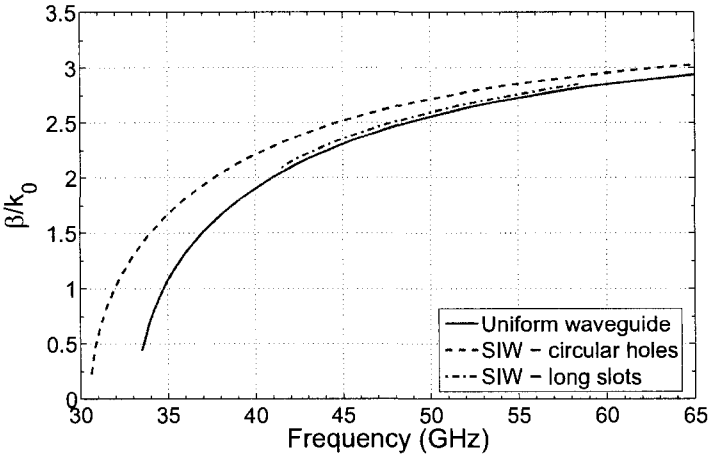

Figure 5.7 Comparison of the normalized phase constant of different SIW configurations of the same width a.

the unit cell are uniquely defined. Once the Bloch impedance is determined, standard matching techniques are available for optimized connection to uniform waveguides.

The Bloch impedance Z_B of an SIW was calculated from the simulated S-parameters s_{ij} of a single, symmetric SIW unit cell with terminal planes defined at the slot centers. A direct relation between Z_B and Z_0, the characteristic impedance of the connected uniform waveguide of equal width a, exists. It can be derived from the S-matrix of a lossless transmission line

$$\mathbf{S}|_{Z_B} = \exp(-j\beta l) \begin{pmatrix} 0 & 1 \\ 1 & 0 \end{pmatrix} , \tag{5.3}$$

which is then renormalized from Z_B to Z_0 [125]:

$$\mathbf{S}|_{Z_0} = (\mathbf{S}|_{Z_B} + \Gamma \mathbf{1})(\mathbf{1} + \Gamma \mathbf{S}|_{Z_B})^{-1} , \tag{5.4}$$

where Γ is the reflection factor defined by

$$\Gamma = \frac{Z_B - Z_0}{Z_B + Z_0} . \tag{5.5}$$

Reorganizing the linear equation system (5.4) yields the S-parameters normalized to Z_0

$$\begin{aligned} s_{11}|_{Z_0} = s_{22}|_{Z_0} &= \Gamma \frac{1 - \exp(-j2\beta l)}{1 - \Gamma^2 \exp(-j2\beta l)} \\ s_{12}|_{Z_0} = s_{21}|_{Z_0} &= \exp(-j\beta l) \frac{1 - \Gamma^2}{1 - \Gamma^2 \exp(-j2\beta l)} , \end{aligned} \tag{5.6}$$

It is then possible obtain the wanted Bloch impedance from

$$Z_B = Z_0 \sqrt{\frac{(s_{11} + s_{21} + 1)(s_{11} - s_{21} + 1)}{(s_{11} + s_{21} - 1)(s_{11} - s_{21} - 1)}} , \tag{5.7}$$

where all s_{ij} are normalized to Z_0. The dimensions as defined in Figure 5.5(b) were chosen a = 1300 µm, p = 1800 µm, t = 300 µm, w = 380 µm, and r = 50 µm for an example SIW in silicon substrate (ε_r = 11.7). A plot of the Bloch impedance over frequency is shown in Figure 5.8 in comparison to the characteristic impedance of a uniform, silicon filled waveguide with equal width a (curve X = 0) and with reduced width a-X (curve X = 92 µm). The ranges where the Bloch impedance is purely imaginary depict the stop bands. Perfect impedance matching between the uniform waveguide and the periodic SIW can only be achieved at particular frequencies. However, good matching in most of the frequency range between the two stop bands is possible by a simple adjustment of the width.

An SIW section consisting of eight long via slots (configuration Figure 5.5(b)) with dimensional parameters as specified above was analyzed. Figure 5.9 shows the simulated return loss that arises if uniform waveguides of equal width a are connected to the SIW section at both ends, whereas the connection to slightly narrower waveguides (curve X = 92 µm) yields a much better matching. This is in agreement with the

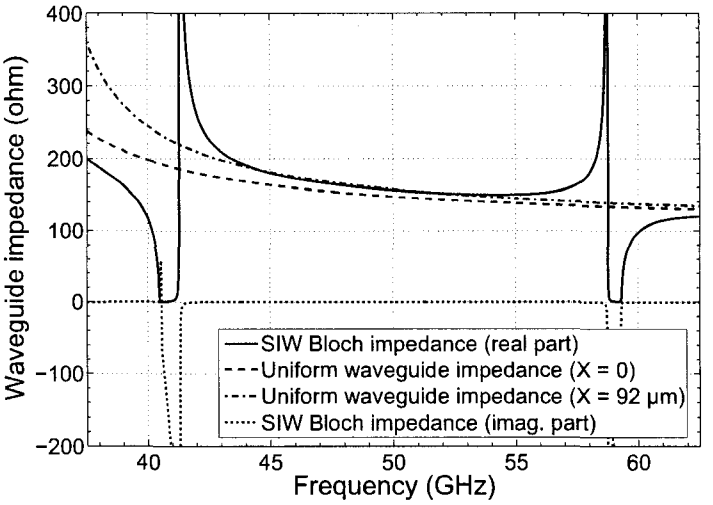

Figure 5.8 Calculated Bloch impedance of the given SIW in comparison with the characteristic impedance of uniform, dielectric-filled waveguides with equal width a and reduced width a-X.

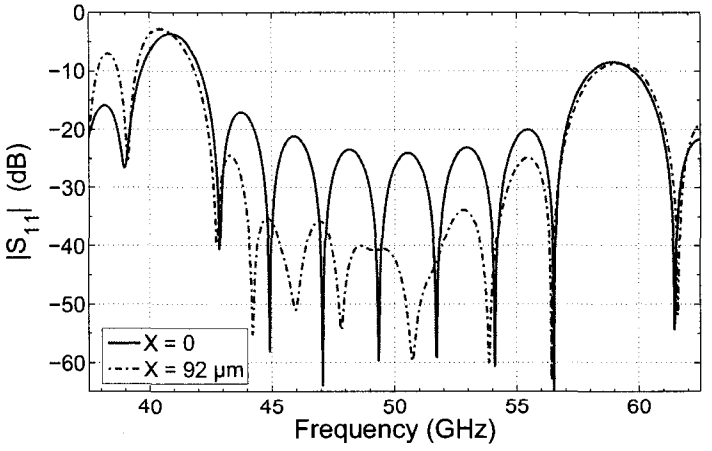

Figure 5.9 Simulated return loss for the unmatched case ($X = 0$) and for improved Bloch impedance matching ($X = 92$ μm).

impedance deviation shown in Figure 5.8. As mentioned before, the terminal planes for connection to the uniform waveguides must be strictly maintained. Also observable in Figure 5.8, the Bloch impedance of an SIW that is operated below the first stop band is lower than that of a uniform waveguide of equal width. In this case, the waveguide width must be increased for improved matching.

The reflection level increases with rising t and/or r, which may be inevitable at higher frequencies due to structural stability and fabrication requirements. In particular, constructive interference of the reflected waves can cause more serious side-effects than initially considered. Single passive components are frequently modeled with wave ports at the input and output. Those ports represent uniform waveguides of infinite length and suboptimal matching can cause deteriorations of the accuracy when the component is connected directly to another SIW later. This is especially true for circuit simulations containing a multitude of SIW components, since the error accumulates. For this reason, the above matching technique should be applied if the interruptions in the side walls of an SIW cause a significant alteration of the characteristic Bloch impedance of the periodic structure in comparison to a uniform waveguide without side wall gaps. It was shown that a simple shift of the waveguide width yields considerable improvements in a broad frequency band.

Other than the SIW, compatibility between the SINRD and the SIIG is much more difficult to achieve. The reason is that both guiding structures depend on specific substrate thicknesses to operate them in the desired frequency range. At equal frequency, the SINRD generally requires a thicker substrate than the SIIG, which can also be seen in section 5.1. In the given example on a silicon substrate, the SINRD has a thickness of 600 µm, whereas the SIIG is 381 µm thick at equal operating frequency. Another obstacle is the field orientation of the LSM_{10} mode, which is perpendicular to that of the SIIG's and SIW's fundamental modes.

5.3 Interconnection of planar and non-planar waveguides

5.3.1 Transition between CPW and SIW

Transitions from CPW to SIW are interesting because they allow interfacing of MMICs with the SIW on arbitrarily thick substrates. Due to its low-loss properties, the SIW is suitable for filters, resonators, and other passive devices that require a high quality factor. By means of two consecutive transitions, one from SIW to CPW and another from CPW to SIIG, the SIW and the SIIG can be interfaced on a common substrate. It is then possible to insert an MMIC in the connecting CPW section, e. g. between an SIIG antenna and an SIW filter. A CPW-SIIG transition is presented in section 2.3. Accommodation of both, SIIG and SIW, on the same substrate requires the SIW to be adapted for electrically thick high permittivity substrates, as described in section 5.2. In addition, SIW components with higher Q-factor are feasible on thicker substrates as justified in section 5.1. What is missing is a suitable transition from CPW to SIW. Such transitions were already demonstrated by Deslandes and Wu on substrates of low permittivity. One transition that uses a slot dipole is narrowband and the overall performance is moderate due to radiation losses [126]. Another transition using a via connection to ground [127] provides good performance in a broad bandwidth. However, it requires a metallized via hole of very small diameter (0.4 mm at 28 GHz) to which the design is very sensitive. This diameter scales down with increasing operating frequency and substrate permittivity, so that fabrication in those cases is virtually impossible.

For these reasons, a novel transition was developed which does not posses the drawbacks of the former designs. A CAD model is shown in Figure 5.10. It makes use of a slot dipole for coupling, but the radiation problem described in [126] does not play a significant role in the present design, because the increased substrate permittivity forces nearly all of the power to be radiated or coupled to the substrate region. Only a very small fraction of approximately $\varepsilon_r^{-3/2}$ is radiated to the air side [85], where ε_r is the

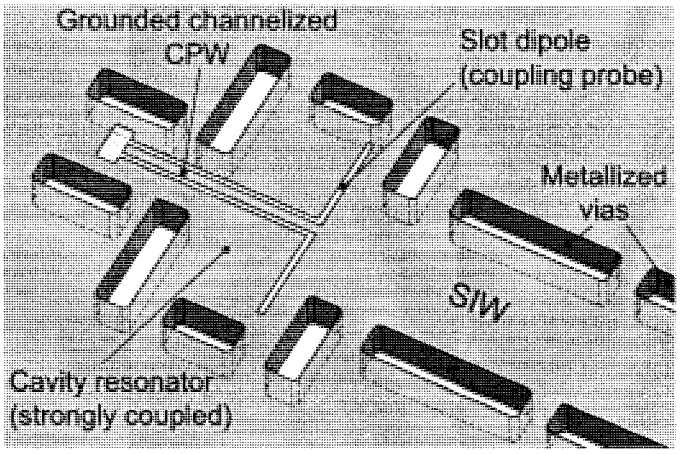

Figure 5.10 Proposed CPW-SIW transition.

relative permittivity of the substrate. The SIW is enlarged at the beginning to allow the coupling dipole to be placed on top of the substrate. This enlarged section acts as a cavity resonator which is strongly coupled to the SIW on one side and to the slot dipole on the other. A high coupling coefficient and a low loaded Q-factor is the consequence, which in turn leads to a broad operating bandwidth. The cavitys length determines the frequency range of the transition and the position, width, and length of the coupling dipole have to be optimized for wideband matching.

The transition was designed with CST-MWS and results are confirmed by HFSS, two 3-D simulation tools that are based on totally different numerical methods. CPW and SIW dimensions are chosen for the desired impedance, probe pitch and frequency range. Several other mutually influencing dimensional parameters have to be optimized iteratively. The dimensions of a transition for 50 GHz on 381-µm-thick alumina substrate (ε_r = 9.7) are shown in Figure 5.11. This transition provides a return loss of less than -20 dB within a bandwidth of over 30 %. Radiation losses amount to less than -0.15 dB insertion loss in the model without material losses. It was found that thicker substrates can be used without difficulty when the dimensional parameters are slightly adjusted.

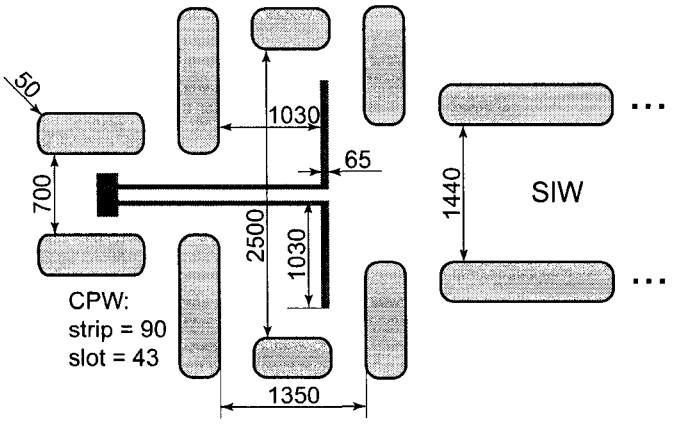

Figure 5.11 Dimensions (in μm) of the developed CPW-SIW transition.

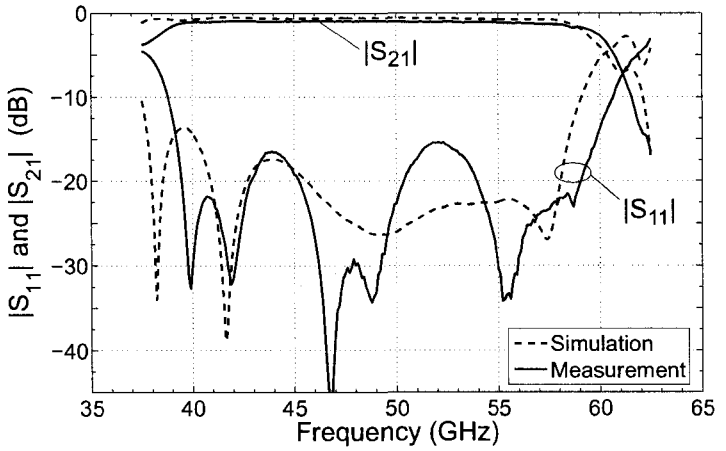

Figure 5.12 Simulation and measurement results for the back-to-back SIW transition.

A back-to-back arrangement of two transitions was fabricated by laser-cutting and subsequent sputtering to cover all surfaces, including the via walls, with a 2 μm thick layer of gold. The slot dipoles were engraved by a photolithographic etching process. CPW probe measurements were carried out on the prototype. Simulated and measured S-parameters for the back-to-back transition including a 4 mm long SIW section are shown in Figure 5.12. The expected insertion loss is less than -0.8 dB, when radiation

and material losses are taken into account. The measured insertion loss ranges between -1.0 dB and -1.2 dB. That difference between theory and practice results from underestimated conductor losses in the CPW feed lines which amount to about 0.2 dB for each of the 2 mm long sections. In later applications, such losses can be reduced by using shorter CPW lines for connection to an MMIC closer to the slot dipole. The measured return loss is below -15 dB from 39 GHz to 59 GHz, corresponding to an entire metal waveguide bandwidth of 40 %.

5.3.2 Direct transition between SIW and SIIG

As mentioned in the above section, the SIW and the SIIG can be interfaced with each other by two back-to-back CPW transitions. This is a good solution if an active device or MMIC has to be inserted in the connection between the dissimilar waveguide structures. However, a direct connection may be desired to reduce the overall insertion losses. Two geometries were studied to achieve that goal. The first employs a planar sector-horn structure in the style of the transition in section 2.2, which gradually widens the SIW in order to match the more loosely guided fields in the SIIG. It is shown in Figure 5.13(a). For simplicity, an equivalent SIIG model was used in the simulation. As other parts of the SIW, the side walls of the sector-horn can be realized by metallized vias. It was found that not only the horn is critical for low radiation and insertion loss, but also the shape of the metallization on top of the substrate. Best results were obtained by the profile in Figure 5.13(a). FEM-based simulation results by HFSS for that topology are given in Figure 5.14. Based on those simulations, the transition can be used in a very wide bandwidth with an average insertion loss by radiation of -0.6 dB. The return loss is better than -20 dB in most parts, but a weak resonance can be observed at 97.5 GHz. Careful design is necessary to avoid such resonances in the pass band.

Another type of SIW-SIIG-transition is shown in Figure 5.13(b). The design is similar to the CPW-SIIG-transition presented in section 2.3 and is based on resonant cou-

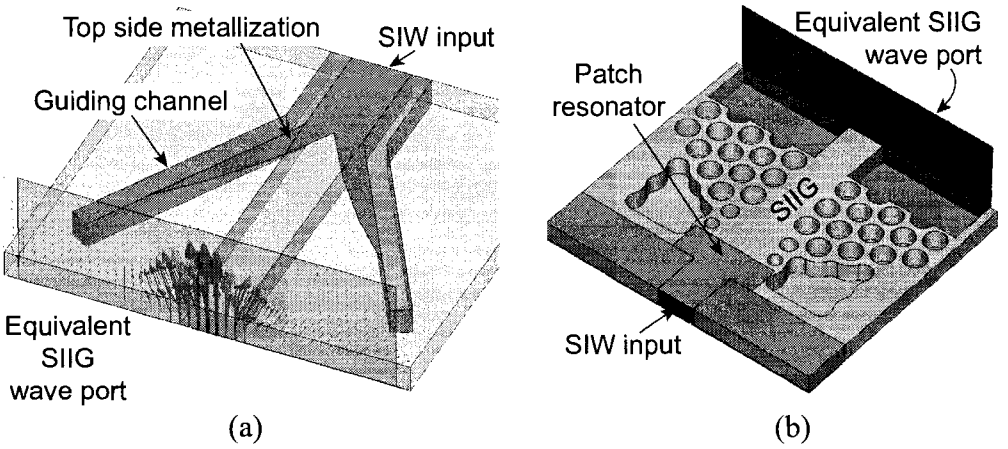

Figure 5.13 Transition from SIW to SIIG using (a) a sector horn or (b) a patch resonator.

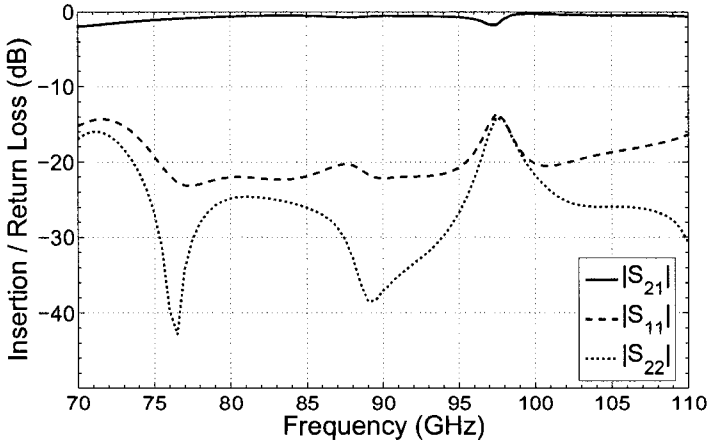

Figure 5.14 S-parameters for the horn-based SIW-SIIG-transition.

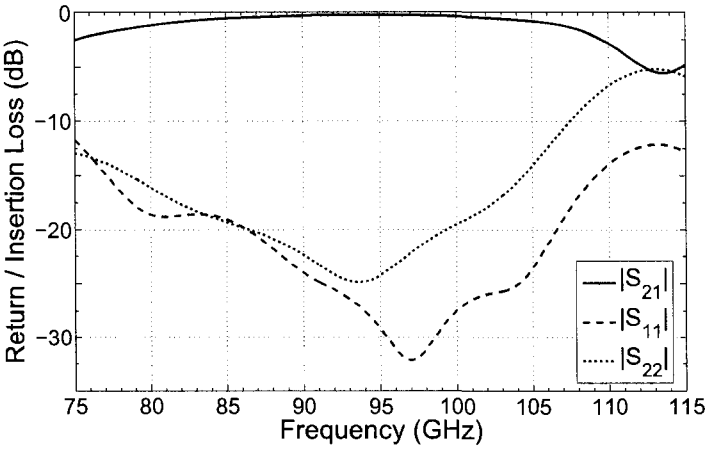

Figure 5.15 S-parameters for the patch resonator based SIW-SIIG-transition.

pling. A low-Q parallel plate resonator is formed by a patch on top of the substrate and the ground plane on the bottom. Instead of the CPW coupling dipole, the electromagnetic wave is fed to the resonator directly by the SIW. The matching can be adjusted by changing the SIW width, either smoothly or by a stepped impedance transformer. Other parts of the transition are explained in more detail in section 2.3. Figure 5.15 shows the S-parameters simulated by the time domain solver of CST-MWS. This kind of transition can be used in a relative bandwidth of about 20 % to 25 % with low return and insertion loss. Advantages of this design over the sector-horn transition are the lower radiation loss of only -0.2 dB in a limited frequency range and potentially simpler fabrication.

5.4 Hybrid SIW-CPW forward couplers

Directional couplers are fundamental components in most microwave and mmW systems. With a multitude of applications moving to mmW and terahertz frequencies, novel hybrid coupling structures can overcome the loss limitations of standard planar technologies and still be integrable in a cost-effective way. In this context, couplers based on substrate integrated waveguides like the SIW and the SIIG can drastically reduce

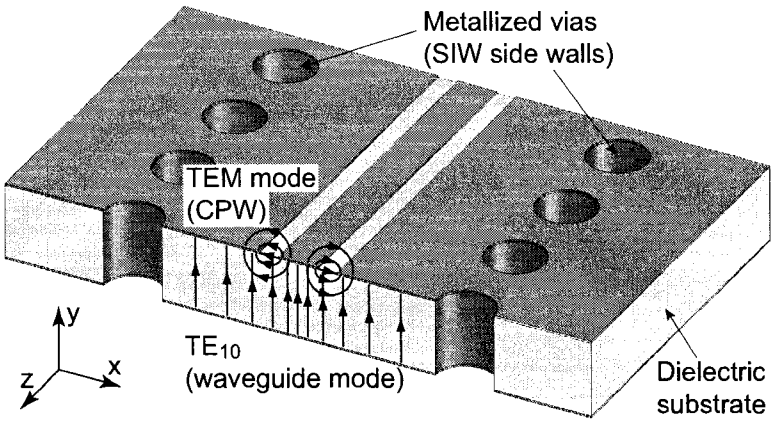

Figure 5.16 Studied hybrid coupling structure comprising a substrate integrated waveguide (SIW) and a coplanar waveguide (CPW) on top.

attenuation losses and thus improve system performance. Such couplers are particularly interesting for concatenated structures with relatively large dimensions, used for example in antenna feeding networks [128] or six-ports [129, 130]. However, the SIW and SIIG are not directly compatible with active devices or MMICs, so that additional transitions to planar transmission lines like microstrip or CPW are indispensable. In many cases, it would be desirable to combine the transition with the coupling function in a hybrid way to simplify the topology and to reduce losses and required space. Such an approach could also be interesting for distributed amplifiers and other applications which are briefly discussed at the end of this section. Figure 5.16 shows the studied hybrid coupling structure, which is equivalent to the laterally bounded conductor-backed CPW. It consists of an SIW formed by parallel rows of metallized vias and a CPW being part of the upper SIW broad wall. The electromagnetic fields of the CPW mode and the TE_{10} waveguide mode overlap so that coupling occurs between the dissimilar integrated guides. Several publications have treated the suppression of undesired power leakage or coupling to other modes in the conductor-backed CPW [131–135]. This is most effectively done by placing the lateral walls close to the CPW in order to increase the cutoff frequency of the unintentionally created waveguide channel [132, 134, 135]. By con-

trast, the topology studied here deliberately makes use of the mode-to-mode coupling effect and therefore the distance between the rows of vias is such that the dominant TE_{10} waveguide mode can propagate in the desired operating frequency range but all higher waveguide modes are attenuated.

5.4.1 Normal-mode and coupled-mode analysis

To simplify the analysis of mode coupling in the described structure, a uniform section is assumed, i. e. the rows of metallized via holes of the structure in Figure 5.16 are replaced by continuous conducting side walls. In practice, this does not lead to restrictions, because the actual SIW with periodic vias can be modeled very accurately by a dielectric-filled rectangular waveguide. The width of this equivalent waveguide needs to be slightly broadened in order to match the propagation constant of the actual SIW in a wide frequency range [136]. It is important, however, to point out that a certain group of modes, such as TM modes, cannot be guided along the actual SIW structure because of the discontinuous side walls along which current flow is impossible. The normal modes of this composite CPW-SIW topology, i. e. the modes of the coupled system, are solutions of the wave equation. As such, those modes obey orthogonality relations and therefore no mode coupling occurs as long as uniformity in the direction of wave propagation is maintained. With the dimensions given in Table 5.2 and alumina ($\varepsilon_r = 9.7$) as substrate material, only the first two even modes (magnetic center wall) and the odd coupled slotline mode can propagate. The latter is not suppressed, because the lateral walls are distant from the CPW. However, the slotline mode can be avoided by maintaining structural as well as excitation symmetry or by using air bridges.

The electric field distributions of the propagating modes in the transversal plane was simulated with CST-MWS and results are shown in Figure 5.17 for different frequencies. It may be noticed that the first mode resembles the uncoupled CPW mode and the second mode resembles the TE_{10} waveguide mode at low frequencies, whereas the situation is

Table 5.2 Dimensions of the analyzed uniform CPW-SIW coupling structure.

Symbol	Dimension	Value
a	SIW width (uniform)	1.47 mm
d	SIW substrate height	381 μm
w	CPW strip width	108 μm
s	CPW slot width	56 μm

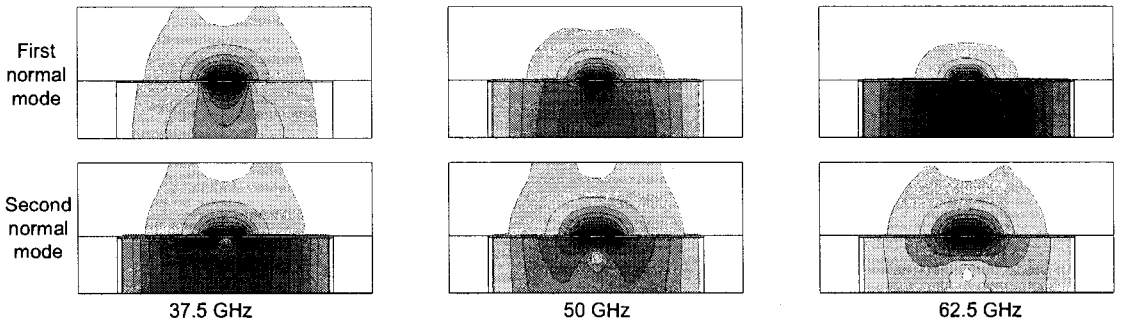

Figure 5.17 Electric field distribution of the two lowest order normal modes in the cross section of the SIW-CPW coupling structure at various frequencies.

reversed at high frequencies. This interesting property reflects in the propagation constant of the normal modes compared to the modes of the uncoupled (isolated) guides. The isolated CPW mode was analyzed by moving the SIWs side walls close enough together so that the TE_{10} mode does not propagate any more. Correspondingly, the phase constant of the uncoupled TE_{10} mode of the closed SIW (without CPW on top) can either be simulated or calculated by available analytical expressions. In Figure 5.18, the phase constants of all four modes are plotted over frequency. The phase constant of the first normal mode, being close to that of the isolated CPW at low frequencies, asymptotically approaches the isolated TE_{10} mode towards high frequencies. The contrary is true for the second normal mode, which confirms the above observation of "mode conversion". The transverse electric vector fields of the first and second normal modes are shown in Fig-

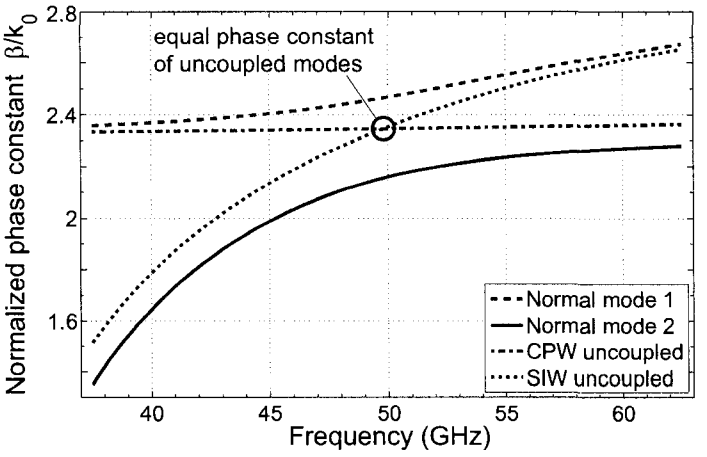

Figure 5.18 Phase constants of the isolated CPW and TE_{10} modes and of the normal modes in the coupled waveguide structure.

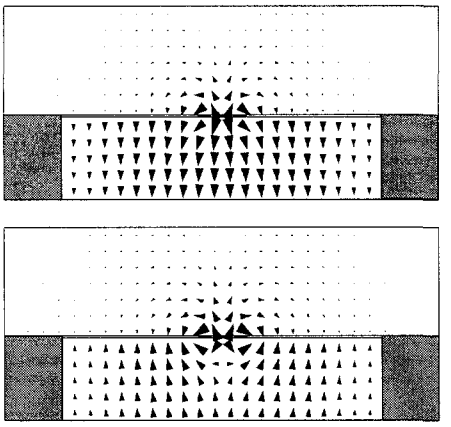

Figure 5.19 Transverse electric vector field of the first (top) and second normal mode (below) at 50 GHz.

ure 5.19. For a given field orientation in the CPW region, the field orientation of the two modes is antipodal in the SIW region. The superposition of these modes corresponds to the well-known odd- and even-mode analysis, commonly used for symmetrical couplers with waveguides placed side by side instead of on top of each other. Power transfer from the CPW to the SIW or vice versa can be explained by a simultaneous propagation

of the superposed normal modes. Due to their differing phase velocity, a part of the guided power oscillates between the CPW and the SIW while the power of each of the normal modes remains constant. An unequal phase velocity of these modes is crucial for the forward coupling mechanism, whereas it is detrimental for backward coupling. Ordinary backward couplers, such as parallel line hybrids, rely on differing odd- and even-mode impedances and unequal phase velocities have the negative effect of a decrease in the isolation level. Forward couplers, on the other hand, should match the odd- *and* even-mode impedances at the beginning and end of the coupling section to eliminate the backward coupling and to achieve a high isolation [137]. The length L of maximum power transfer over which the two normal modes accumulate a phase difference of 180° is readily calculated for the uniform coupling structure by

$$L = \frac{\pi}{\hat{\beta}_1 - \hat{\beta}_2} , \tag{5.8}$$

where $\hat{\beta}_1$ and $\hat{\beta}_2$ are the phase constants of the first and second normal mode, respectively.

Other than the normal-mode analysis, the coupled-mode theory describes the interaction of coupled guided waves from the viewpoint of the modes existing in the uncoupled waveguides. An expansion of the electromagnetic fields of a coupled system in terms of the modes of an uncoupled system leads to a set of generalized telegraphist's equations [138], which are equivalent to the coupled mode equations. Maxwell's equations are represented accurately by a complete set of those coupled-mode equations. In practice, however, only a limited number of modes are considered and therefore the coupled-mode theory remains an approximate, but usually precise mathematical description of the wave propagation in a coupled sytem. The differential equations for two loosely coupled modes (only the dominant modes of the involved waveguides are considered),

as used in the classic publication [139], are:

$$\frac{dE_1}{dz} = -(\gamma_1 + \kappa_{11})\, E_1 + \kappa_{12} E_2 \tag{5.9}$$

$$\frac{dE_2}{dz} = \kappa_{21} E_1 - (\gamma_2 + \kappa_{22})\, E_2 \,, \tag{5.10}$$

In (5.9) and (5.10), $E_{1,2}$ represent the complex normalized wave amplitudes on lines 1 and 2, so that $|E|^2$ is equal to the normalized guided power. $\gamma_{1,2}$ are the propagation constants of the uncoupled guides 1 and 2, and κ_{mn} are coupling coefficients between lines *m* and *n*. Assuming loose coupling, κ_{11} and κ_{22} can be neglected.

$$\kappa_{11} \approx 0 \; ; \; \kappa_{22} \approx 0 \,, \tag{5.11}$$

Both coupling coefficients, κ_{12} and κ_{21}, are equal if reciprocity is guaranteed (involved materials may be anisotropic, but the permittivity and permeability tensors must be symmetric). Limiting the interest to the lossless case here, κ_{12}, κ_{21}, and the propagation constants $\gamma_{1,2}$ are purely imaginary and thus it is convenient to make the following substitutions

$$\kappa_{12} = \kappa_{21} = j\kappa \tag{5.12}$$

$$\gamma_{1,2} = j\beta_{1,2} \,, \tag{5.13}$$

which lead to simplified coupled-mode equations

$$\frac{dE_1}{dz} = -j\beta_1 E_1 + j\kappa E_2 \tag{5.14}$$

$$\frac{dE_2}{dz} = j\kappa E_1 - j\beta_2 E_2 \,. \tag{5.15}$$

According to the classic theory [139], complete power transfer from one guide to the other is possible in the symmetric case only, i. e. if $\beta_1 = \beta_2$. The investigated

CPW-SIW coupling structure is asymmetric, however, except for the frequency where $\beta_{CPW} = \beta_{SIW}$, at about 50 GHz. In the following, the notation $\beta_1 = \beta_{CPW}$ and $\beta_2 = \beta_{SIW}$ is used. In the asymmetric case, the solution of differential equations (5.14) and (5.15) for the amplitude E_2 on the unexcited, coupled waveguide ($E_1 = 1$, $E_2 = 0$ at $z = 0$) is [139]:

$$E_2 = \exp\left[-j\left(\kappa + \frac{(\beta_1 + \beta_2)}{2}\right)z\right] E_2^* \,, \tag{5.16}$$

with the transfer factor

$$E_2^* = \frac{j}{\sqrt{\frac{(\beta_1-\beta_2)^2}{4\kappa^2} + 1}} \cdot \sin\left(\sqrt{\frac{(\beta_1 - \beta_2)^2}{4} + \kappa^2} \cdot z\right) \,. \tag{5.17}$$

The second term of (5.17) reflects the sinusoidal power oscillation over the coupling length z between the two isolated modes. The coupled power is maximum if the argument of the sine function is $\pi/2$ or an odd multiple thereof. By using the result for L from (5.8), the coupling coefficient is then calculated by

$$\kappa = \frac{1}{2}\sqrt{\left(\frac{\pi}{L}\right)^2 - (\beta_1 - \beta_2)^2} \,. \tag{5.18}$$

In the next step, the first term of (5.17) is evaluated to find the maximum transferred power at $z = L$:

$$|E_2|^2 = |E_2^*|^2 = \left(1 + \frac{(\beta_1 - \beta_2)^2}{4\kappa^2}\right)^{-1} \,. \tag{5.19}$$

The coupling length L for maximum power transfer and the coupling coefficient κ are plotted over frequency in Figure 5.20. The frequency-dependent maximum power transfer ratio and level are shown in Figure 5.21, in which 1 or 0 dB relates to a complete power transfer from one guide to the other. With all these variables known, equation (5.16) for the complex wave amplitude E_2 on the coupled guide is entirely determined and the coupling level as well as the phase can be predicted. The solution for the ampli-

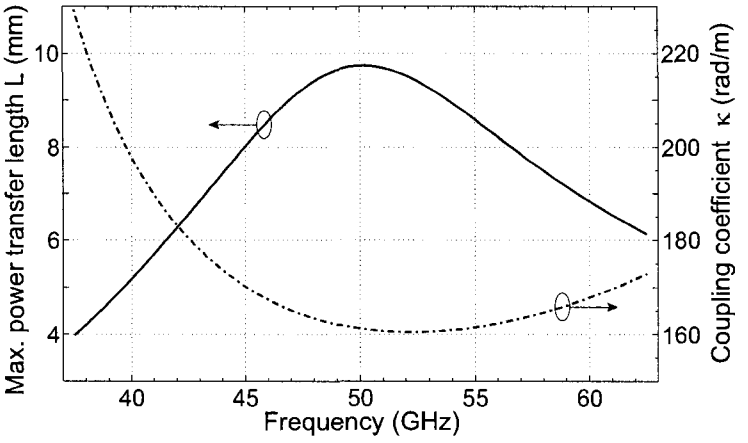

Figure 5.20 Coupling length L for maximum power transfer and coupling coefficient κ over frequency.

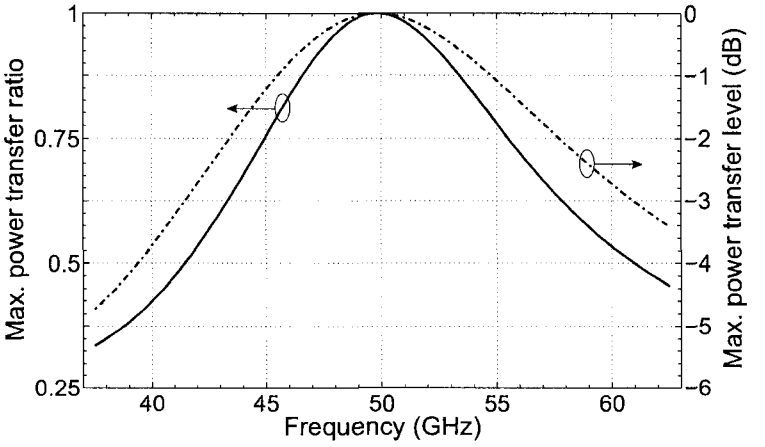

Figure 5.21 Maximum power transfer ratio and level over frequency.

tude E_1 on the excited guide is [139]:

$$E_1 = \exp\left[-j\left(\kappa + \frac{(\beta_1+\beta_2)}{2}\right)z\right] E_1^* \,, \tag{5.20}$$

with the transfer factor

$$\begin{aligned} E_1^* \;=\; & \cos\left(\sqrt{\frac{(\beta_1-\beta_2)^2}{4}+\kappa^2}\cdot z\right) \\ & -\frac{(\beta_1-\beta_2)}{2\kappa}\frac{j}{\sqrt{\frac{(\beta_1-\beta_2)^2}{4\kappa^2}+1}}\cdot\sin\left(\sqrt{\frac{(\beta_1-\beta_2)^2}{4}+\kappa^2}\cdot z\right) \,, \end{aligned} \tag{5.21}$$

and in the lossless case simply

$$|E_1|^2 = 1 - |E_2|^2 \,. \tag{5.22}$$

It should be kept in mind that this coupled-mode theory is based on the assumption of loose coupling. Any theory assuming the idea of "one and only one isolated mode is excited on one guide" in the case of tightly coupled guides is a misconception and can therefore lead to erroneous results.

Results obtained separately by normal-mode analysis and coupled-mode theory were compared in [140] for asymmetric dielectric couplers and showed a very good agreement. Here, both methods are combined, i. e. the result of (5.8) for the length L of maximum power transfer is used in the coupled-mode theory. This is done to avoid the often difficult calculation of the coupling coefficient κ by a field overlap integral, which requires a prior knowledge of the transversal fields. In this way, only the four phase constants of the two isolated modes and the two normal modes of the coupling structure have to be known in order to assess the complete coupling behavior. In comparison to the guided wave fields, phase constants are much easier to obtain by analytical expressions (waveguide mode), empirical formulas, conformal mapping (CPW),

or by specialized efficient numerical methods. For the sake of simplicity, only uniform coupling sections were studied here. By applying available theory on tapered coupling structures [141, 142], the analysis can easily be extended. In a real coupler made of lossy materials, the attenuation constants α_1 and α_2 of the coupled waveguides do not vanish. If $\alpha_1 = \alpha_2 = \alpha$, an additional factor $e^{-\alpha z}$ has to be added in (5.16), corresponding to an exponential decay of the wave amplitudes. Additional complexity is introduced if α_1 and α_2 are significantly different [139]. Realistic values for the wave attenuation in the CPW and SIW on alumina substrate at 50 GHz are in the range of 100 dB/m and 25 dB/m, respectively. This translates into a relative attenuation difference $|\alpha_1 - \alpha_2|/\kappa \approx 0.05$ for the given structure, which is small enough to be neglected.

5.4.2 Design considerations for 3-dB and 0-dB couplers

Two SIW-CPW couplers with coupling levels of 3 dB and 0 dB (= total power transfer) were designed, based on the cross-sectional dimensions of Table 5.2 and alumina substrate. After evaluating the phase constants of the four modes in Figure 5.18 by numerical simulations or analytical expressions, the required lengths of the coupling sections were calculated by (5.8) at 50 GHz, yielding 4.95 mm and 9.75 mm, respectively. The required length for a 3-dB coupler is slightly more than half the length of maximum power transfer to account for a small admissible amplitude imbalance.

Figure 5.22 and Figure 5.23 show a comparison of results obtained by this theory and by simulation of the entire three-dimensional (3-D) structure with CST-MWS. In order to excite the uncoupled modes in the simulation, lumped ports were used for the CPW, and the SIW was extended on both sides for an excitation with wave ports. Small discrepancies can be explained by numerical inaccuracies and also by reflections generated at discontinuities introduced by the abrupt beginning and end of the CPW section. Nevertheless, the agreement is very good and confirms the validity of the provided theory.

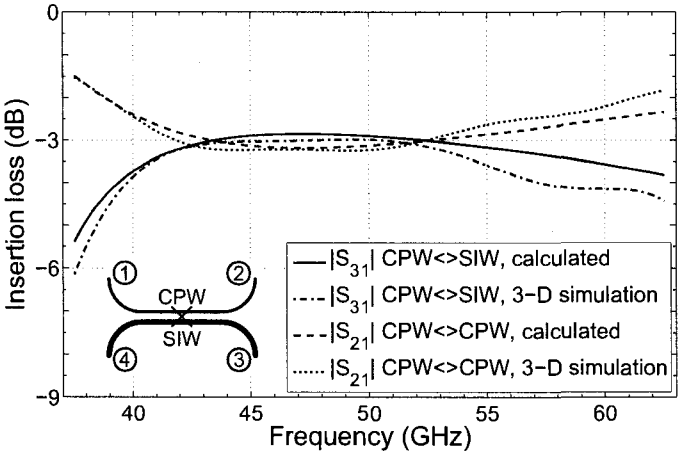

Figure 5.22 Comparison of calculated and simulated insertion losses of the lossless 3-dB coupler.

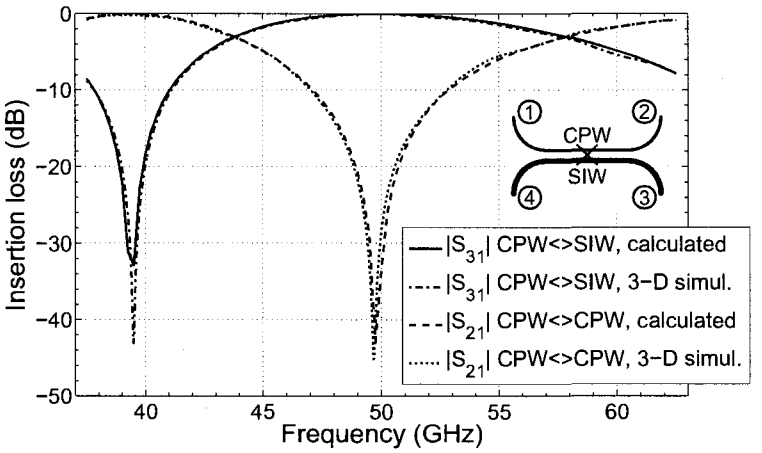

Figure 5.23 Comparison of calculated and simulated insertion losses of the lossless 0-dB coupler.

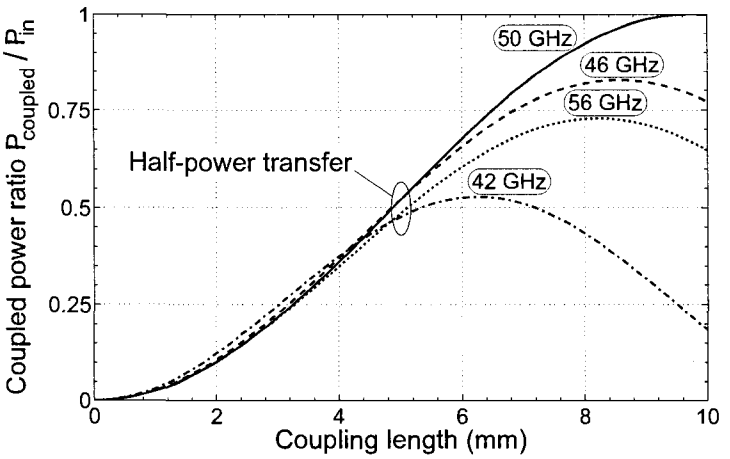

Figure 5.24 Coupled power as a function coupling length at various frequencies. 3-dB coupling is achieved in a wide bandwidth of more than 25 %.

The 3-dB coupler has a very wide relative bandwidth of 25 % at less than 0.5 dB amplitude imbalance, which is a consequence of the asymmetric coupling structure. As can be seen in Figure 5.20, the length of maximum power transfer is longest at 50 GHz, the frequency where the phase constants of the uncoupled guides are equal and the phase constants of the normal modes in the coupled system have minimum difference. At the same time, the maximum exchanged power is highest at this frequency and declines towards higher or lower frequencies, as shown in Figure 5.21. Therefore, similar to the asymmetric coupler in [140], a compensation between the coupling length and the power transfer level takes place, which leads to a wide achievable bandwidth. This effect is illustrated by the curves in Figure 5.24. It also shows that a wideband operation is possible at lower coupling levels. However, such a wide bandwidth does not appear as a matter of principle, but certain parameters must be optimized. This is especially true for the coupling strength between the CPW and the SIW. For the given structure, the coupling coefficient is particularly dependent on the CPW slot width s and the SIW or substrate height d. The influence of the latter was investigated by calculating the coupler response for three different values of d, but otherwise unchanged dimensions. Simulated phase

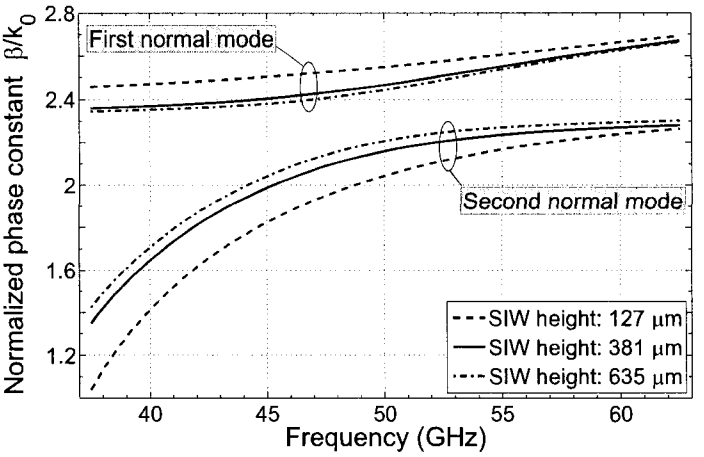

Figure 5.25 Phase constants of the first two normal modes with the SIW height d as a parameter. The coupling strength increases with decreasing d.

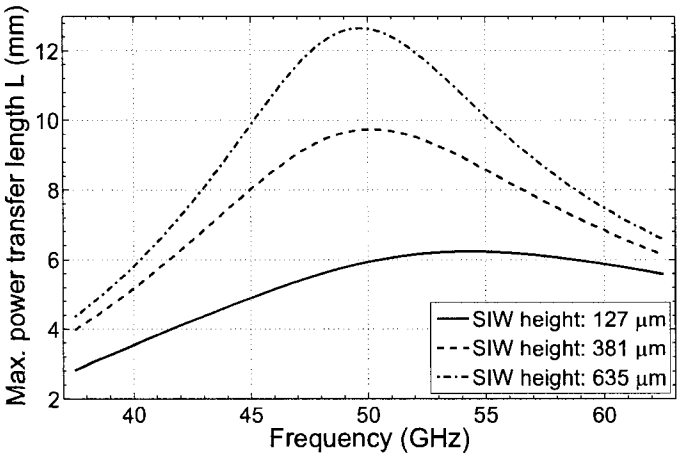

Figure 5.26 Length L for maximum power transfer with d as a parameter.

constants of the normal modes are shown in Figure 5.25. It can be observed that the difference $\hat{\beta}_1 - \hat{\beta}_1$ is greater for stronger coupling or decreased SIW height, which translates into a shorter length L of maximum power transfer. Corresponding curves for L at different values of d are shown Figure 5.26. Figure 5.27 shows coupling levels over frequency for the 3-dB coupler and the 0-dB coupler and with the SIW height as a param-

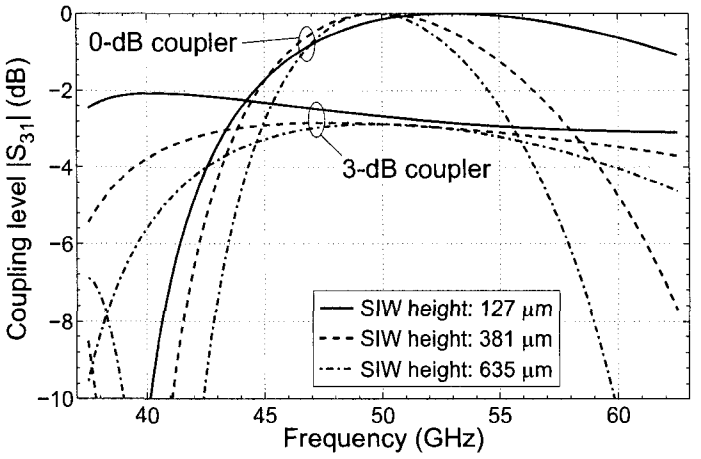

Figure 5.27 Coupling levels of the 3-dB and 0-dB couplers with the SIW height d as a parameter. The coupling strength increases with decreasing d.

eter. At d = 127 μm, complete power transfer is achieved for L = 6.2 mm at 52.9 GHz. The frequency where complete power transfer can occur shifts for varying d, because the substrate thickness has an impact on the phase constant of the uncoupled CPW and therefore causes a shift of the crossing point of the isolated modes' phase constants. Also shown in Figure 5.27 is the effect of the coupling strength on the bandwidth of the 0-dB coupler: the stronger the coupling, the wider the bandwidth of nearly complete power transfer. For a coupling level of at least -0.2 dB (95 %), the achievable bandwidth is 12.7 % for d = 127 μm, 7 % for d = 381 μm, and 5 % for d = 635 μm. This means that wideband transitions between CPW and SIW can be designed, if strong coupling is guaranteed, which also promotes lower insertion losses as a result of the shorter coupling length. Concerning the 3-dB coupler, maximally flat amplitude balance is achieved for a certain coupling strength. An SIW height of d = 381 μm is close to an optimum for the given coupler. It is for this reason that such a wide bandwidth was obtained in prior simulations. Greater design flexibility is possible, if uniformity of the coupling structure is abandoned. By shaping the CPW slot width (variable coupling coefficient) and by varying the SIW width (alters dispersion behavior and frequency of equal phase

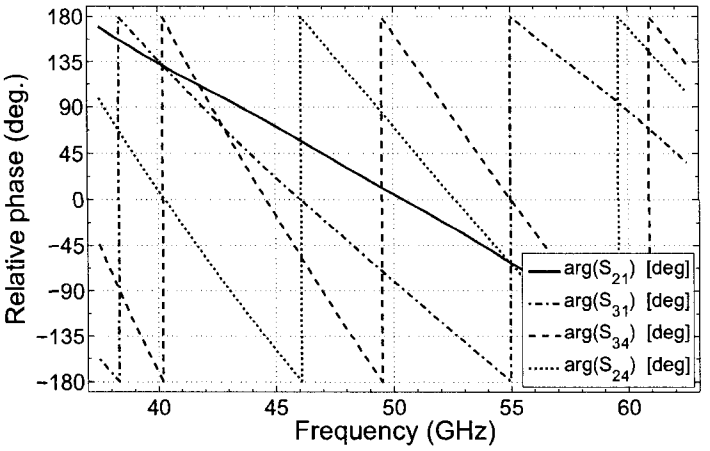

Figure 5.28 Phase relations at the output ports of the 3-dB coupler. A phase difference of 90°is only obtained for the symmetric case around 50 GHz.

constant), an even better performance is feasible. It is shown in [142], for example, that nearly complete power transfer in a 0-dB coupler with non-uniform coupling distribution requires

$$\left|\int_{z_1}^{z_2}(\beta_1-\beta_2)dz\right| \ll \frac{\pi}{2} \;\; ; \;\; 0 < z_1, z_2 < l \, , \tag{5.23}$$

which is a less restrictive requirement than $(\beta_1 - \beta_2)l \ll \pi/2$ for the uniform structure, where l is the length of the coupling section.

So far, the phase difference $\angle S_{21} - \angle S_{31}$ at the output ports was not considered. Unlike symmetrical couplers, a frequency-independent 90° phase difference is not inherently obtained for asymmetric coupling structures. Figure 5.28 shows the phase relations of the 3-dB coupler when the input and output reference planes of the SIW are identical to those of the CPW section. If a specific phase difference is needed, the technique proposed in [137] can be applied, which involves a shift of the reference planes and leads to relatively constant phase relations.

The coupling behavior of the hybrid SIW-CPW structure in Figure 5.16 was also examined for low-permittivity substrates. No significant difference is observed when the

dimensions, in particular the SIW width and the CPW slot width, are scaled appropriately. A disadvantage is the much longer coupling length due to the increased wavelengths in low-permittivity materials. Moreover, the CPW impedance has to be changed to a higher value ($\approx 90\ \Omega$), if the slot width should remain within a reasonable range.

5.4.3 Prototype fabrication and measurements

Both couplers, the 3-dB and the 0-dB version, were fabricated on polished alumina substrate from CoorsTek®. Instead of the continuous SIW side walls used for the preceding analysis, periodic metallized vias were used to realize the SIWs in a mechanically robust way. Long and large rectangular vias as those suggested in section 5.2 were used to ease the fabrication process. As a result, the SIW is operated between the first and second stop bands, caused by distributed Bragg reflection in the periodic structure. The gaps between the vias slightly increase the phase constant of the guided wave and therefore the SIW width a needs to be decreased from 1.47 mm to 1.44 mm to account for this effect [136]. All other dimensions were maintained as given in Table 5.2. Since any connection of the miniature SIW inputs to the coaxial ports of the network analyzer is extremely difficult at frequencies around 50 GHz, the CPW-SIW transition presented in subsection 5.3.1 was used to enable coplanar probe contacting on a probe station. A photograph of a fabricated 0-dB coupler is shown in Figure 5.29. Oblong holes for the vias were cut into the alumina substrate by a laser. The entire substrate was then covered with a 2 µm gold metallization by means of a sputtering process, followed by photolithographic etching of the CPW structures. Since the probe access was limited and only two probes were available, the free input and output ports were terminated by resistive 100-Ω thin-film pads in each of the CPW slots. In this way, reflections can be kept at moderate levels, although tolerances for the load impedances could not be tightly controlled. Isolation measurements could not be conducted because of the space restrictions. Figure 5.30 shows the measurement results for the 3-dB coupler in comparison to

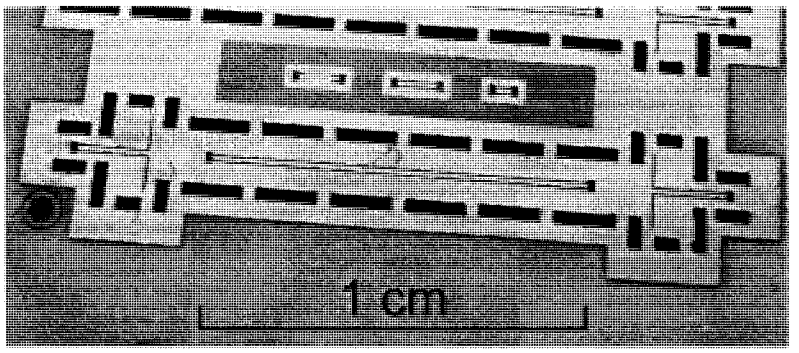

Figure 5.29 Photograph of a fabricated 0-dB CPW-SIW coupler with transitions from CPW to SIW for coplanar probe measurements.

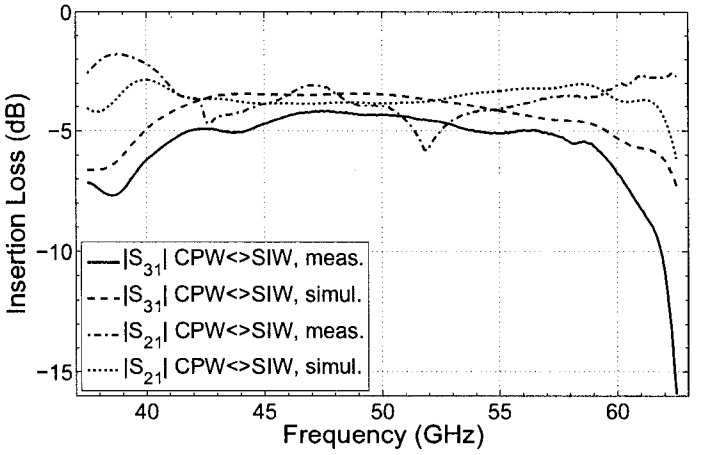

Figure 5.30 Measured and simulated S-parameters of the 3-dB coupler including the CPW-SIW transitions.

simulations of the lossy model, which also includes the transitions. Each of the measured curves was obtained from a different coupler with relocated load terminations. Since the reference plane of the calibration was at the probe tips, the insertion loss includes the transition loss. The discrepancy between simulation and measurement can be explained by underestimated losses in the CPW sections. Field singularities at the conductor edges and surface roughness are not properly taken into account in the simulations, so that the actual losses are generally higher. Another reason might be the poor quality of the gold

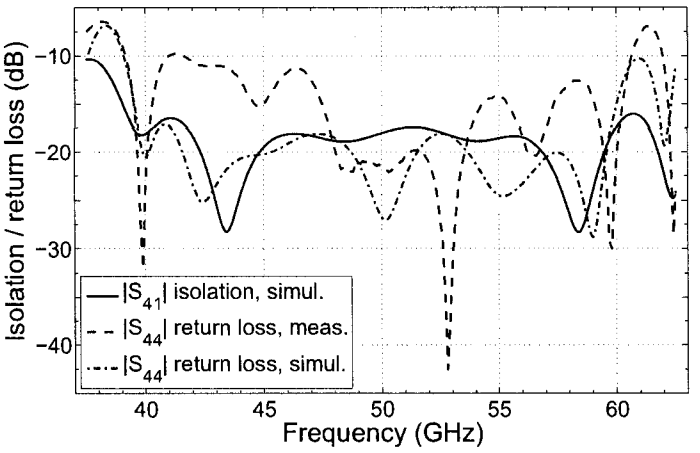

Figure 5.31 Simulated and measured isolation and return loss of the 3-dB coupler including the transitions.

metallization in the laser-cut vias with uneven walls. Measured S-parameters still confirm the wideband operation predicted by theory and simulations. Backward scattered waves caused by discontinuities cannot be determined by the provided theory and it is therefore not possible to calculate the level of isolation and return loss. 3-D simulations with CST-MWS indicate that both the isolation and the return loss are in the range of -20 dB to -15 dB, as shown in Figure 5.31. However, this relatively poor isolation can be greatly improved by using matching sections or tapers to reduce the reflections at the beginning and end of the coupling section.

Measured and simulated S-parameters for the 0-dB coupler are shown in Figure 5.32. The frequency of maximum power transfer from the CPW to the SIW matches the simulated result very precisely. Including the transition, the measured insertion loss at this point at 50 GHz is -2 dB.

Diverse applications can be considered for the presented hybrid coupling structure. They include, for example, transitions, six-ports, antenna feeding networks, active antennas, and distributed phase shifters or amplifiers in millimeter-wave front-ends. The

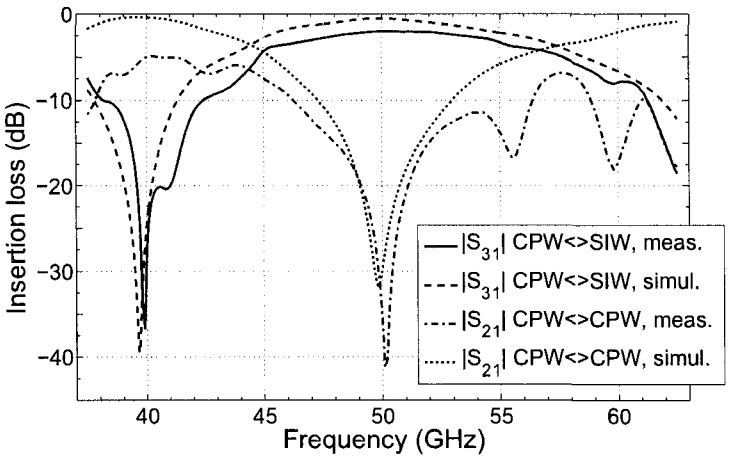

Figure 5.32 Measured and simulated S-parameters of the 0-dB coupler including the CPW-SIW transitions.

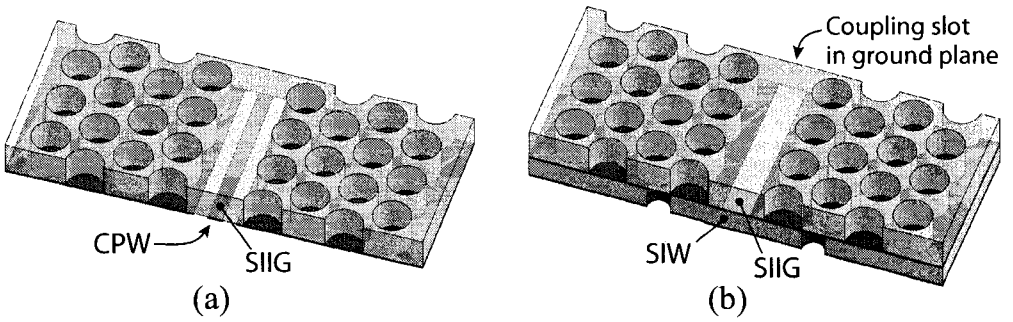

Figure 5.33 Examples for other possible hybrid coupling structures: (a) SIIG-CPW and (b) SIIG-SIW.

CPW-SIW coupler is also interesting for active traveling-wave antennas with distributed amplification in the feed path, similar to that presented in [143]. An optical modulator based on this coupling mechanism is proposed in [144]. Different hybrid coupling structures based on the same principle may be realized by combining other substrate integrated waveguide structures, e. g. an SIIG in combination with a CPW or an SIW, as shown in Figure 5.33. Furthermore, coupling from a CPW on the upper side of the SIW

to another CPW on the bottom side can be realized. This creates a great flexibility in the design of substrate integrated circuits.

5.5 Substrate integrated circuits

5.5.1 Concept

The ultimate goal that is strived for with substrate integrated waveguide technologies is to integrate planar and non-planar waveguide structures into a common medium, i. e. a planar dielectric substrate. The resulting technology is known as the substrate integrated circuits (SICs) [145]. One of the most advantageous features offered by the SIC technology is the feasibility of simple and precise interconnections between planar transmission lines and non-planar waveguide structures being synthesized in planar form. Post-production tuning is not necessary due to the attainable high fabrication and alignment precision. The transitions shown in this thesis enable the construction of hy-

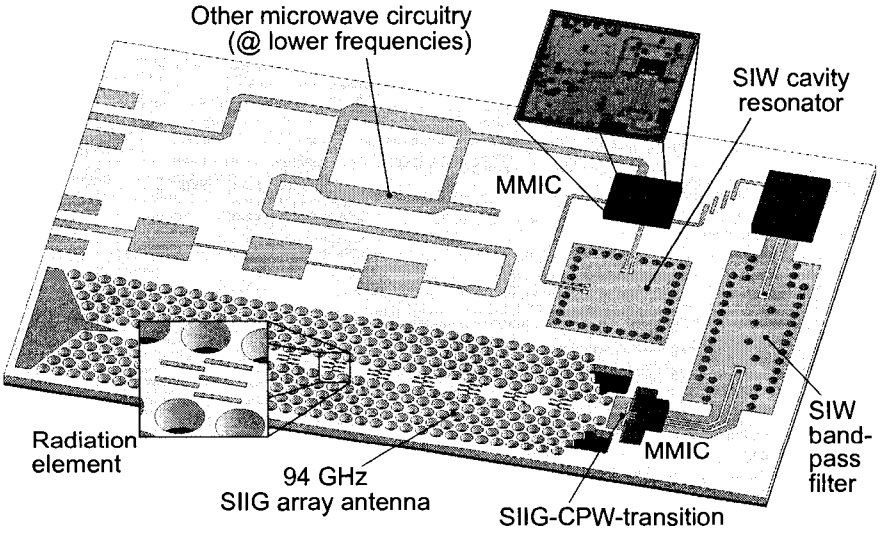

Figure 5.34 Example of a hybrid SIC: integration of various waveguide technologies on the same substrate.

brid SICs in which the specific benefits of each single guiding structure are exploited. Transmission lines like microstrip and CPW provide the necessary compatibility with lumped and active devices and with MMICs, whereas the shielded SIW is an ideal candidate for integrated cavity resonators and filters due to its high Q-factor. The open waveguide character and low attenuation of the SIIG allows for very efficient and flexible integrated front-end antennas in the mmW through terahertz ranges. An imaginable example of a hybrid SIC is shown in Figure 5.34. This single-layer example may be extended to a multi-layer structure and can be realized by an appropriate fabrication process, e. g. LTCC. Since the development of such a relatively complex hybrid fabrication process is a long and difficult task, the successful application of the SIC approach is demonstrated by a simplified example in the following subsection.

5.5.2 Hybrid integration of an MMIC with an SIIG antenna at 60 GHz

In order to demonstrate the feasibility of hybrid SIC integration of active devices with passive SIIG components, a 60-GHz receiver front-end was realized, comprising the SIIG rod antenna of section 3.1 and an LNA in MMIC die form. The planar rod antenna was selected among the the three different types of SIIG antennas in chapter 3, since it is easy to fabricate and because the inclined main beam direction allows for line-of-sight path measurements by means of a probe station. In this example, the miniature MMIC is interfaced with the relatively large antenna via the transition presented in section 2.3. The used LNA with part number HMC-ALH382 belongs to the Velocium™ product line from Hittite® Microwave Corporation. It has a specified gain of typically 21 dB, 3.8 dB noise figure, and a die size of 1.55 mm $\times$ 0.73 mm $\times$ 0.1 mm. The optional insulation film was omitted and a milled metal base was used as ground plane. The described assembly with part description is shown in Figure 5.35. Although flip-chip mounting of the MMIC on the alumina substrate can offer a considerable decrease in insertion loss [112], a more standard wire-bonding connection was used, where the MMIC is

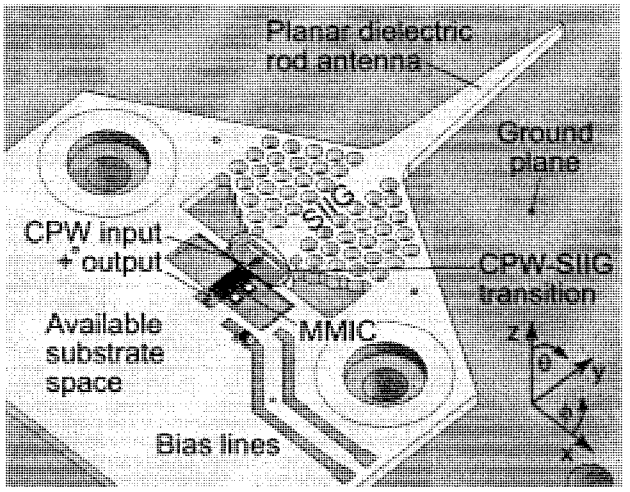

Figure 5.35 CAD assembly of the substrate integrated 60-GHz front-end (active SIIG rod antenna).

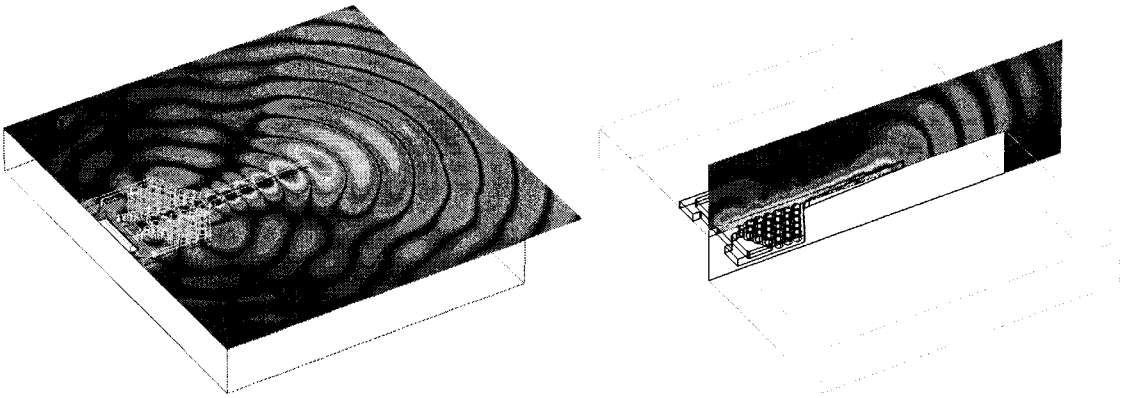

Figure 5.36 Simulated electric field at ground plane level and on a centered vertical plane.

mounted on the metal base by silver epoxy. This type of connection is also used and recommended in the LNA data sheet so that a direct comparison is possible. Alumina substrate of 0.635 mm thickness is suitable for single-mode operation of the SIIG in the 60-GHz band. Simulations were carried out by the CST-MWS time domain solver, respective E-fields are shown in Figure 5.36. This field visualization demonstrates how

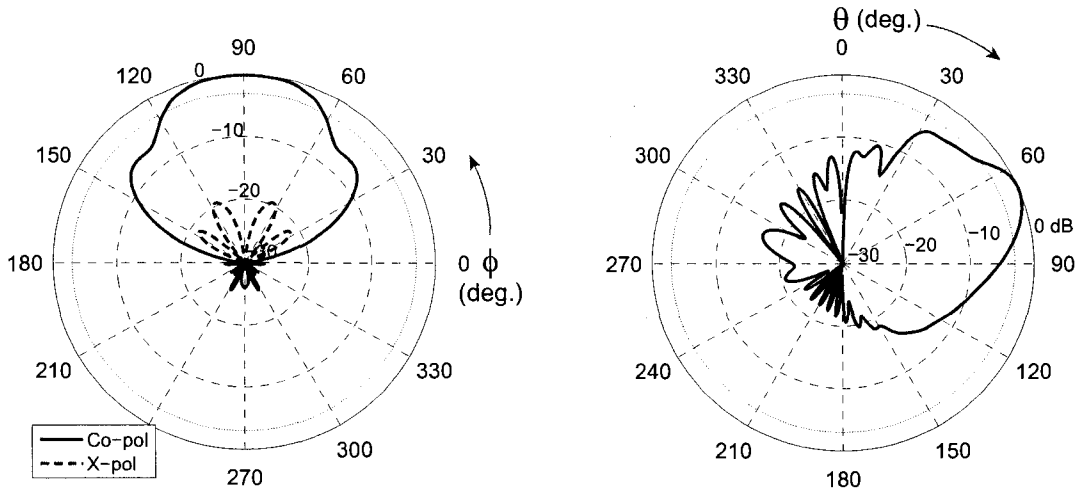

Figure 5.37 H-plane (l.) and E-plane (r.) radiation patterns of the simulated SIIG rod antenna including the CPW-SIIG transition at 60 GHz.

the guided wave in the SIIG is gradually matched and radiated into free space at an elevation angle of about 30° from the ground plane. Corresponding radiation patterns are shown in Figure 5.37. At 60 GHz, the theoretical peak gain is 11.5 dBi at $\phi = 90°$ and $\theta = 63°$. Based on an assumed conductivity of $2.0 \cdot 10^7$ S/m and $\tan\delta = 0.0005$ for the alumina substrate, the simulated radiation efficiency is 90 %. The use of cheaper, lossier materials degrades this very good value, but efficiencies between 60 % and 70% can still be expected in practical situations.

Prior to testing the performance of the entire active mmW front-end, the input return loss of the CPW-SIIG transition and rod antenna was measured without the LNA installed. Figure 5.38 shows the obtained results in comparison with simulations. Initial results for an optimized transition indicate a wide operating bandwidth with a return loss lower than -20 dB in the 60-GHz target band. Although the test results do not achieve the same low level, they attest a return loss better than -11 dB up to 65 GHz which is satisfactory for an antenna application. Fabrication tolerances that give rise to an air gap

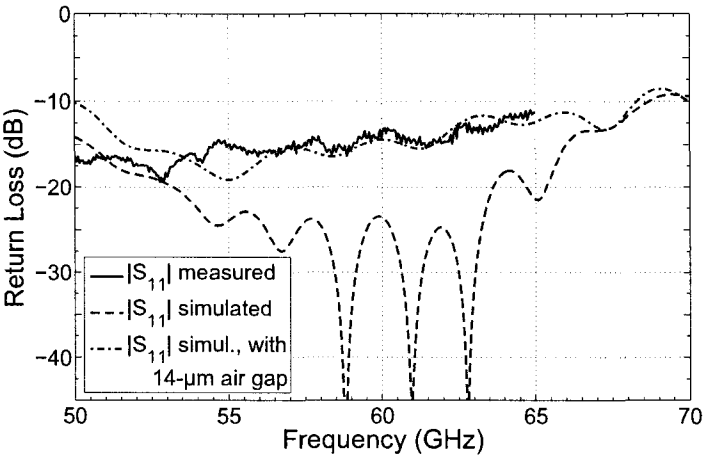

Figure 5.38 Measured and simulated input return loss of the SIIG rod antenna including the prior CPW-SIIG feed transition.

between the substrate and the ground plane are the most probable cause for the deterioration, as is confirmed by the second simulated curve in Figure 5.38.

The properties of the LNA MMIC were verified for the given environment in a separate experiment. The LNA's input and output were wire-bonded to short CPW sections on the surrounding alumina substrate in a similar assembly as later used for the active antenna. Due to fabrication difficulties, two parallel 25-µm gold wires were used for each connection instead of 75 µm × 13 µm gold ribbons as suggested in the data sheet. Test results are shown in Figure 5.39 for the recommended bias voltage of 2.5 V and a drain current of 64 mA. Compared to the specifications in the data sheet, the round bond wires are responsible for some additional insertion and return loss. In the target band, the gain is in the range of 18.5 dB to 19.5 dB.

In a next step, the performance of the entire active mmW front-end was evaluated. A photograph of the wire-bonded LNA die and the transition to the SIIG is shown in Figure 5.40. Antenna measurements of the prototype could not be carried out in the anechoic chamber, because a probe station is required for contacting the CPW output.

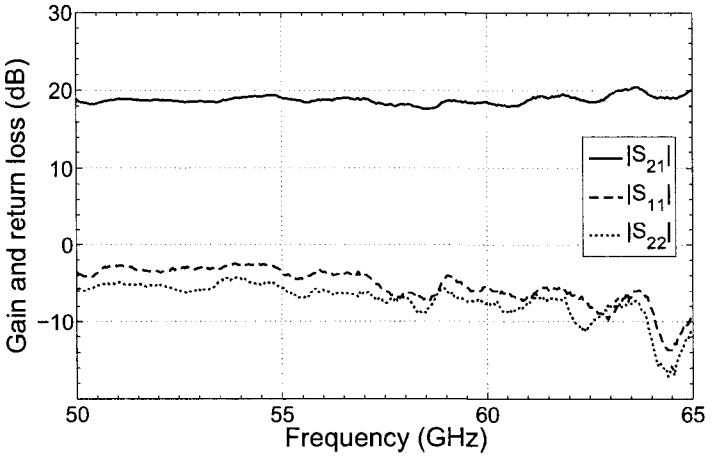

Figure 5.39 Measured gain, input and output return loss of the wire-bonded LNA die.

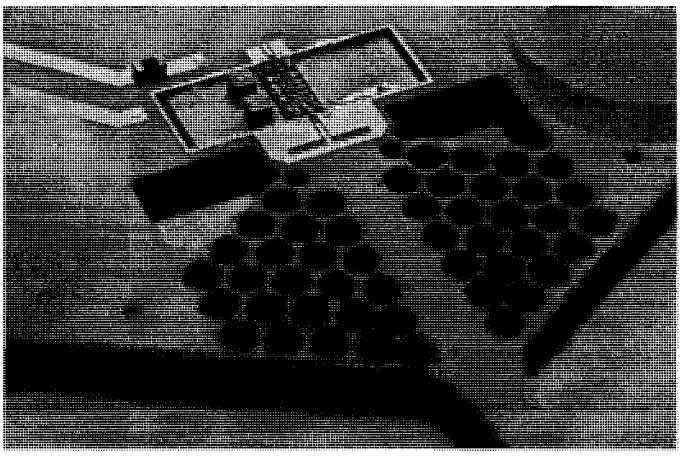

Figure 5.40 Photograph of the wire-bonded LNA die and SIIG transition.

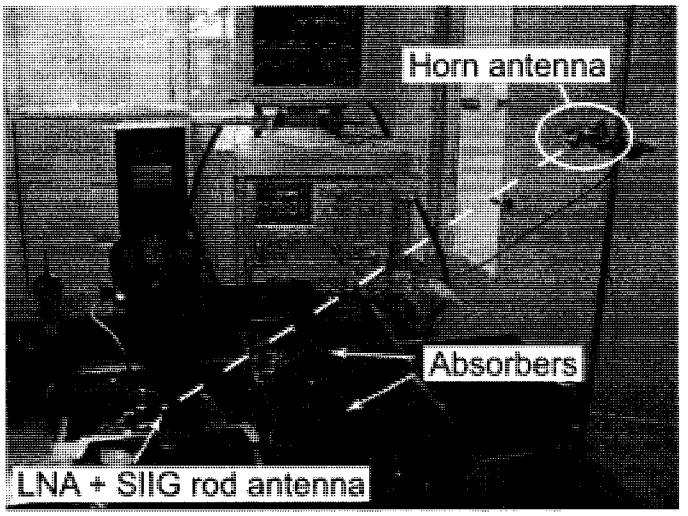

Figure 5.41 Photograph of the measurement setup. The transmitting antenna was located in a line of sight to the antenna under test and was aligned for minimum transmission loss.

Since good agreement of simulated and measured radiation patterns is already shown for the SIIG rod antenna in section 3.1, they were omitted in this experiment. However, it is possible to carry out path loss measurements with the active SIIG rod antenna placed on the chuck of the probe station. For this purpose, a prior LRM calibration to the probe tips was carried out on a calibration substrate. Then, one probe was removed and the free port of the VNA was connected to a standard gain horn antenna instead. The resulting measurement setup as shown in Figure 5.41 was used to determine the insertion loss between the transmitting horn antenna and the receiving SIIG rod antenna. This experiment was first conducted without the LNA installed. Subsequently, the MMIC was added and the insertion loss was again measured. Figure 5.42 shows both obtained curves over frequency. Test results are somewhat noisy as a consequence of the high added loss by the long 1.85 mm coaxial cables (approx. 1 m for each port), the free space loss between the antennas, and the limited receiver sensitivity of the VNA in this frequency range. This is especially true for the experiment without LNA amplification, which is why a subsequently smoothed curve was superposed. An insertion loss of -31.5 dB was measured

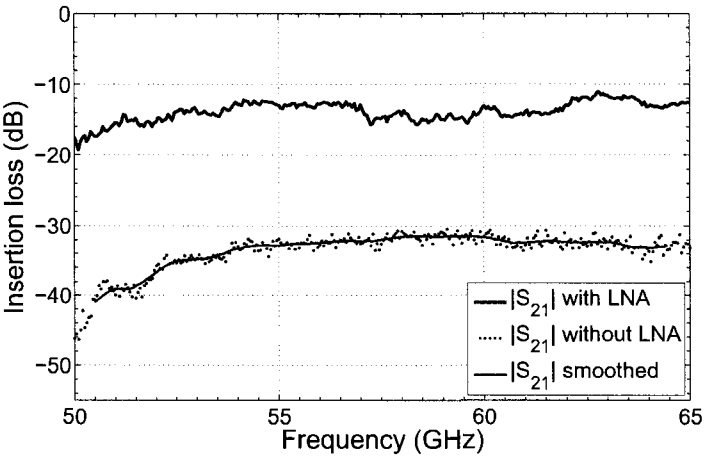

Figure 5.42 Measured insertion loss with and without mounted LNA.

around 60 GHz for optimal alignment of the antennas in the mutual beam maximum. The optimum was found at an inclination angle of 30° (θ = 60°), slightly more than the simulated 27°. The flat curve progression observable in Figure 5.42 indicates an almost frequency-independent main beam direction. The LNA adds effectively the gain which was obtained before in a separate measurement (see Figure 5.39, so that the concept of hybrid SIC integration is successfully demonstrated.

In good approximation, the rod antenna gain can be extracted from the determined insertion loss. A constant distance of 80 cm was kept between the horn antenna and the antenna under test. The free-space path loss (*FSPL*) for isotropic antennas is obtained by the Friis transmission equation:

$$FSPL = \frac{P_r}{P_t} = \left(\frac{\lambda}{4\pi R}\right)^2 , \tag{5.24}$$

where P_t and P_r are the transmitted and received powers, respectively, λ is the free-space wavelength, and R is the distance between the two isotropic antennas. The result is -66.1 dB for the given distance at 60 GHz. Of course, the antennas' gain must be taken into account to obtain the actual transmission loss. Although the atmospheric attenuation

Table 5.3 Summary of arising transmission losses.

Magnitude	Value [dB]
Free-space path loss (R = 80 cm)	–66.1
Predicted SIIG rod antenna gain	+11.5
Horn antenna gain	+20.2
Removed probe	+1.5
Expected insertion loss	= –32.9

is high in the 60 GHz band, it can be neglected for such small distances. Table 5.3 lists a summary of the described losses and gains. The removed waveguide probe accounts for a negative loss of 1.5 dB, a value which was determined in a separate test. Altogether, the expected transmission loss from the horn antenna input to the CPW output of the SIIG rod antenna (without following LNA) is -32.9 dB. The actually measured insertion loss is only -31.5 dB, however. The difference can be explained either by inaccuracies in the measurement procedure or by a higher gain of the SIIG rod antenna as predicted by simulations or a combination of both. In fact, the measured insertion loss is lower, which suggests that the hybrid circuit actually has very low loss.

In spite of small discrepancies due to the particular measurement procedure, the usefulness of the SIIG in SIC technology is successfully proven by this example. Future work will deal with more complex SICs which also involve the SIW as a waveguide structure that is particularly suitable for planar mmW band-pass filters.

CONCLUSION

Communication systems operating at mmW frequencies are expected to have a bright future [146, 147]. Upcoming high definition video streaming and other applications like fast data synchronization of mobile devices require the huge bandwidth capacities offered by mmW technology. The unlicensed 60-GHz band could have a particular impact in this sector. Radar for civil applications, especially the automotive sector, also take advantage of the high resolution and favorable propagation characteristics of millimeter waves. It is beyond controversy that parts of the electromagnetic spectrum in the upper mmW and terahertz ranges are essential for all kinds of imaging systems, spectroscopy of chemical substances, and material science. The shift to higher frequencies, or equivalently, to shorter wavelengths, simultaneously involves a change of the underlying technologies. A multitude of problems arise, which were formerly not known at lower frequencies. This is especially true for the lossy wave propagation in integrated waveguides that are used in all kinds of mmW components and entire circuits. The main cause are the considerable conduction losses, which rise disproportionately with frequency. Traditional hollow metal waveguide, although offering outstanding performance, is definitely not an option for commercial products by reason of its cost, size, and weight. Although extensive research on alternative dielectric technologies was conducted in the past decades, many of those approaches are not suitable for actual implementation in a high-volume production chain. Dielectric waveguides are nowadays still seen as too bulky and, since they require complex fabrication procedures, too expensive for mass products.

The novel approach followed in this thesis is the consequent integration of the dielectric image guide in a planar substrate. Today, planarity is the most significant requirement for large-scale integration and mass production. Planar substrates are used in almost all high-frequency circuits and systems and are indispensable as soon as integra-

tion in small spaces and the lowering of manufacturing costs for high-volume production are important. It is for this reason that originally non-planar waveguide structures with superior performance need to be embedded into planar substrates. The image guide is one of the simplest geometries among a multitude of integrable dielectric waveguides and was therefore preferred over others. In a first step it was shown how the conventional dielectric image guide can be synthesized on an ordinary planar substrate by perforation of specific zones in the substrate. This new waveguide structure, the so-called substrate integrated image guide (SIIG), was then analyzed for its guidance properties. A brief review of existing approximate analytical and rigorous numerical methods of analysis for uniform dielectric waveguides showed that these are not applicable to the SIIG. The SIIG's non-uniformity demands for numerical techniques which are capable of discretizing the complex periodic structure accurately. Two different methods of analysis were proposed, which are compatible with commercial full-wave simulation software and provide accurate and connsistent results. Those methods were subsequently used to carry out extensive simulation studies on the SIIG's propagation characteristics in dependence on its dimensional parameters. Design guidelines were developed in order to optimize the operating bandwidth, attenuation, and leakage of the SIIG. Particular attention has to be paid to electromagnetic band gaps and leaky-wave radiation due to the periodic structure of the SIIG. In this context, the differences between the SIIG and sometimes similar-looking 2-D photonic crystal (PC) defect waveguides were clarified. The wave guidance in the SIIG is exclusively based on total reflection due to a refractive index contrast, whereas the PC waveguide uses an electromagnetic band gap effect in at least one lateral dimension. This has important consequences on the operating range, the propagation behavior, and potential leakage. For this reason, those two waveguides have to be regarded from two separate perspectives. Indispensable novel transitions were developed in order to be able to interface the SIIG with standard measurement systems and integrated circuit technology. Besides a wideband transition to metal waveguide, a novel transition to CPW was developed. It fulfills major requirements such as very low radi-

ation loss, large bandwidth, high directivity, and eased fabrication on high-permittivity substrates at very high frequencies. CPW was chosen because of its compatibility with mmW MMICs and with thick substrates. Due to the open, unshielded character of the SIIG, a main field of application are integrated dielectric antennas. Three different versions of SIIG antennas for mmW front-ends were proposed. It is noteworthy that the field-trapping effect known from other antennas on high-permittivity substrates like alumina or silicon is easily overcome by the proposed designs. In this manner, dielectric antennas can be fabricated on the same substrate as MMICs, resulting in the lowest connection and feeding loss possible. The presented antenna types have medium to high gain and either a static or a frequency-steerable beam. An advantage shared by all presented dielectric antennas is the exceptionally high efficiency at mmW frequencies, which is a consequence of the low conductor loss.

As a dielectric waveguide, the SIIG suffers from severe radiation at sharp bends. Although possible but complex ways to improvement were identified, no effective and simple solution to that general problem of dielectric waveguides could be found so far. Preferred applications for the SIIG are therefore those which can be realized with straight or only slightly bent SIIG sections. In order to still enable efficient power dividing into a number of parallel SIIG channels regardless of this problem, a slab-mode power divider with superimposed planar lenses was studied in detail. Simulation results showed good amplitude and phase balance. Relatively high insertion loss can be explained by *TM-TE* mode coupling and reflections from the abrupt lens interfaces. Nevertheless, it can be expected that the developed design achieves very low loss if the multitude of interdependent parameters is carefully adjusted. As a continuation of this project, it would then be possible to realize quasi-optical slab-mode power combiners with wider bandwidth, lower loss, and lower cost than any comparable solution can offer. In an effort to combine differing substrate integrated wave-guiding structures in hybrid SICs, the properties of microstrip, CPW, SIW, SINRD, and SIIG were compared with each other. The

SIIG was found to be the one with the lowest loss in high-permittivity substrates. Due to its very low conductor loss, the SIIG is furthermore a promising submillimeter and terahertz waveguide. In order to achieve compatibility between the SIIG and the SIW on a common substrate, the SIW was adapted for fabrication on electrically thick high-permittivity substrates. Basically, this involves enlarged vias and a rectangular shape, so that the leakage is reduced at simultaneously increased structural stability. However, wider gaps between adjacent vias also cause increased reflections towards the SIW input. To mitigate this effect, improved matching was achieved by properly taking into account the Bloch impedance of the periodic structure. Appropriate transitions between SIW and SIIG were designed for indispensable interconnections on the common substrate. A novel forward coupling mechanism between the SIW and a CPW in the top broad wall was studied in detail and prototypes were realized. SIC components such as distributed phase shifters or amplifiers can be designed on the basis of this geometry. In order to demonstrate the usefulness of the SIC concept, an active SIIG rod antenna was realized. The prototype has proven the feasibility of hybrid integration of a miniature MMIC with a highly efficient directional 60-GHz antenna, thus enabling the design of high-performance mmW front-ends.

So far, the conducted research work has resulted in eight journal and conference publications (several others submitted or planned) and one international patent application under the *Patent Cooperation Treaty (PCT)*.

The principal scientific contributions of this thesis are the following:

- A novel synthesized dielectric waveguide structure, the SIIG, was proposed and analyzed. Compared to the existing standard image guide, it has similar low-loss wave guidance properties, but possesses decisive advantages concerning ease of manufacturing, fabrication tolerances, cost-efficiency, integrability, and alignment precision in hybrid circuits.

- Two different techniques for accurate analysis of the SIIG's propagation properties were developed, which allow to include leakage and radiation phenomena that occur in connection with the periodic open dielectric waveguide.

- The practicability of the fabrication and the predicted performance were proven by means of realized prototypes.

- In-depth investigation of several potential approaches led to an original transition concept, which uses a simple but efficient and broadband dielectric slab-mode launcher. In this manner, it is possible to interconnect two absolutely dissimilar waveguides, the CPW and the SIIG, with minimum radiation loss.

- Considering the proposed SIIG as a feed line, the well-known dielectric rod antenna was modified to a planar version. The result is a highly efficient wideband antenna of simple geometry.

- An original design of SIIG linear array antenna was developed. Other than ordinary leaky wave antennas, it uses specially designed radiation elements which enable frequency steering through broadside direction without inducing an electromagnetic bandgap, as it is common for this type of antennas. An extended theory is presented, which describes the exact scan limits of the main beam at simultaneous avoidance of grating lobes.

- A new design concept led to a patent-pending "dielectric slab-mode antenna". The proposed antenna is compact, capable of hybrid integration, provides medium to high gain, and has a very high radiation efficiency.

- Two-dimensional quasi-optical power splitting using a grounded dielectric slab as waveguiding medium and a planar lens configuration was shown to be feasible. This approach exploits the low transmission loss of an open dielectric technology, whereas radiation losses can be kept at a much lower level than by use of SIIG Y-branches or bends.

- Different SIC waveguides were compared quantitatively for the first time and it was shown that the SIIG is, by far, the guiding structure with the lowest transmission loss. The fact that conduction loss is the less important loss mechanism may anticipate its use in the terahertz range.

- Hybrid CPW-SIW forward couplers were developed for the mmW range together with a corresponding coupled-mode theory. Such couplers can be designed for an arbitrary coupling level up to 0 dB, which also makes them useful as transitions.

- Successful integration of a 60-GHz LNA MMIC with an SIIG antenna demonstrates the benefits of active SICs at very high frequencies.

As for the future development of the SIIG technology, many other components are still to be designed in this low-loss technology in order to build up a comprehensive library. A large variety of devices in standard image guide technology were published in the last decades, which suggests a knowledge-transfer similar to that from metal waveguide to SIW. Although the extensive guided electromagnetic fields around the actual SIIG guiding channel may be considered as a disadvantage for large-scale integration, they can facilitate all kinds of coupling structures. The desired coupling coefficient, e. g. to a whispering gallery dielectric resonator, is much better to accomplish in practice at very high frequencies. The coupling behavior between adjacent image guides was studied intensively. Asymmetric image guide forward couplers seem to yield the largest bandwidth and flattest transfer function [140]. Integrated dielectric narrowband filters [15] are based on coupled dielectric gratings that are operated in a DBR mode. Although difficult to design, they might become the preferred choice for future developments in the upper mmW and terahertz ranges, because the conductor losses of other technologies are to significant at those frequencies. The high achievable Q-factors depend predominantly on dielectric dissipation losses. Commercial suppliers today offer ceramics with custom permittivity and extremely low dielectric loss. In addition, pre-

cise micro-fabrication techniques such as DRIE are very well suited for semiconductors, which also have very low dissipation factors up to very high frequencies if they are in a pure, undoped state. Moreover, ion etching is less expensive for miniature terahertz components that require thinner substrates and very high alignment precision can easily be achieved by the SIIG technology. Electronically controlled millimeter-wave phase shifters are realizable by using a piezoelectric transducer which approaches or removes a dielectric material. In this way, the propagation constant of the SIIG is influenced locally without adding significant loss. Using semiconductor substrates such as silicon or gallium arsenide, infrared (IR)-controlled SIIG components are feasible. The resistivity of those materials rises drastically under the incidence of IR light due to a generation of free charge carriers and so does the dissipation factor. Simple, but effective variable attenuators were demonstrated by applying this technique to standard image guides [119]. The Q-factor of dielectric resonators and filters can be influenced in the same way, allowing for switches and reconfigurable multiplexers.

The revived interest in dielectric technologies can be noticed in the rising number of related publications. More researchers and engineers again start to consider dielectric technologies with a view to systematic mmW circuit and system integration. The SIIG is definitely a promising candidate in this field. However, the full potential of the SIIG and other substrate integrated waveguide structures can only be exploited by combining them in hybrid SICs. It is therefore imperative to advance and refine the manufacturing processes in order to be able to accommodate the differing structures on a common platform. The future of millimeter-wave technology lies in successful hybrid integration.

REFERENCES

[1] D. R. Vizard, "Millimeter-wave applications: from satellite communications to security systems," *Microwave Journal, Euro-Global Edition*, vol. 49, no. 7, pp. 22–36, Jul. 2006.

[2] D. Hondros and P. Debye, "Electromagnetic waves on dielectric wires {Elektromagnetische Wellen an dielektrischen Drähten (in German)}," *Annalen der Physik*, vol. 32, pp. 465–476, Jun. 1910.

[3] G. C. Southworth, "Hyper-frequency waveguides—general considerations and experimental results," *Bell System Technical Journal*, vol. 15, pp. 284–309, Apr. 1936.

[4] M. S. P. Carson, J. R. and S. A. Schelkunoff, "Hyper-frequency waveguides—mathematical theory," *Bell System Technical Journal*, vol. 15, pp. 310–333, Apr. 1936.

[5] G. E. Mueller and W. A. Tyrell, "Polyrod antennas," *Bell System Technical Journal*, vol. 26, pp. 837–851, Oct. 1947.

[6] C. H. Chandler, "An investigation of dielectric rod as waveguide," *Journal of Applied Physics*, vol. 20, pp. 1188–1192, Dec. 1949.

[7] W. M. Elsässer, "Attenuation in a dielectric circular rod," *Journal of Applied Physics*, vol. 20, pp. 1193–1196, Dec. 1949.

[8] D. D. King, "Dielectric image line," *Journal of Applied Physics*, vol. 23, pp. 699–700, Jun. 1952.

[9] R. M. Knox and P. O. Toulios, "Integrated circuits for the millimeter through optical frequency range," in *Proc. Symposium on Submillimetre Waves*, New York, NY, USA, Mar. 1970, pp. 497–516.

[10] T. Itoh, "Inverted strip dielectric waveguide for millimeter-wave integrated circuits," *IEEE Transactions on Microwave Theory and Techniques*, vol. MTT-24, no. 11, pp. 821–827, Nov. 1976.

[11] T. Yoneyama and S. Nishida, "Nonradiative dielectric waveguide for millimeter-wave integrated circuits," *IEEE Transactions on Microwave Theory and Techniques*, vol. MTT-29, no. 11, pp. 1188–1192, Nov. 1981.

[12] T. Rozzi and S. J. Hedges, "Rigorous analysis and network modeling of the inset dielectric guide," *IEEE Transactions on Microwave Theory and Techniques*, vol. MTT-35, no. 9, pp. 823–834, Sep. 1987.

[13] R. M. Knox, "Dielectric waveguide microwave integrated circuits—an overview," *IEEE Transactions on Microwave Theory and Techniques*, vol. MTT-24, no. 11, pp. 806–814, Nov. 1976.

[14] K. Solbach, *Review of dielectric image-line antennas*, ser. Infrared and Millimeter Waves. Orlando, FL: Academic Press, 1986, vol. 15, pp. 193–219.

[15] G. L. Matthaei, D. C. Park, Y. M. Kim, and D. L. Johnson, "A study of the filter properties of single and parallel-coupled dielectric-waveguide gratings," *IEEE Transactions on Microwave Theory and Techniques*, vol. MTT-31, no. 10, pp. 825–835, Oct. 1983.

[16] D. I. Kim, D. Kawabe, K. Araki, and Y. Naito, "Directly-connected image guide 3-dB couplers with very flat couplings," *IEEE Transactions on Microwave Theory and Techniques*, vol. MTT-32, no. 6, pp. 621–627, Jun. 1984.

[17] R. E. Horn, H. Jacobs, and E. Freibergs, "Integrated tunable cavity gunn oscillator for 60-GHz operation in image line waveguide," *IEEE Transactions on Microwave Theory and Techniques*, vol. MTT-32, no. 2, pp. 171–176, Feb. 1984.

[18] T. H. Oxley, J. Ondria, P. L. Lowbridge, N. Williams, and R. A. Gelsthorpe, "Dielectric guide W-band (75–100 GHz) receiver with partially integrated oscillator," in *1983 IEEE MTT-S Int. Microwave Symposium Digest*, Boston, MA, USA, Jun. 1983, pp. 287–289.

[19] Y. W. Chang and L. T. Yuan, "ICs for 94 GHz radar applications in dielectric image guide," *Microwave Journal*, vol. 24, no. 6, pp. 81–88, Jun. 1981.

[20] K. Wu, "Integration and interconnect techniques of planar and non-planar structures for microwave and millimeter-wave circuits - current status and future trend," in *Proc. Asia-Pacific Microwave Conference*, vol. 2, Taipei, Taiwan, Dec. 2001, pp. 411–416.

[21] D. Deslandes and K. Wu, "Integrated microstrip and rectangular waveguide in planar form," *IEEE Microwave and Wireless Components Letters*, vol. 11, no. 2, pp. 68–70, Feb. 2001.

[22] Y. Cassivi and K. Wu, "Substrate integrated nonradiative dielectric waveguide," *IEEE Microwave and Wireless Components Letters*, vol. 14, no. 3, pp. 89–91, Mar. 2004.

[23] A. Patrovsky and K. Wu, "Substrate integrated image guide (SIIG)—a planar dielectric waveguide technology for millimeter-wave applications," *IEEE Transactions on Microwave Theory and Techniques*, vol. 54, no. 6, pp. 2872–2879, Jun. 2006.

[24] ——, "Substrate integrated circuits (SICs)—providing a low-cost and low-loss approach for millimeter-wave circuit and system integration (invited paper)," in *Proceedings 8th MINT Millimeter-Wave Int. Symp. and 9th Topical Symp. on Millimeter Waves, Seoul, Korea, February 26-27, 2007*, Seoul, South Korea, Feb. 2007, pp. 9–14.

[25] P. Bhartia and I. J. Bahl, *Millimeter Wave Engineering and Applications*. New York: Wiley, 1984.

[26] T. Rozzi and M. Mongiardo, *Open Electromagnetic Waveguides*. London, UK: IEE Press, 1997.

[27] R. B. Adler, "Waves on inhomogeneous cylindrical structures," *Proceedings of the Institute of Radio Engineers*, vol. 40, no. 3, pp. 339–348, Mar. 1952.

[28] S. Shindo and T. Itanami, "Low-loss rectangular dielectric image line for millimeter-wave integrated circuits," *IEEE Transactions on Microwave Theory and Techniques*, vol. MTT-26, no. 10, pp. 747–751, Oct. 1978.

[29] S.-T. Peng and A. A. Oliner, "Guidance and leakage properties of a class of open dielectric waveguides. Parts I and II," *IEEE Transactions on Microwave Theory and Techniques*, vol. MTT-29, no. 9, pp. 843–869, Sep. 1981.

[30] A. Patrovsky and K. Wu, "Substrate integrated image guide (SIIG) - a low-loss waveguide for millimetre-wave applications," in *Proc. 35th European Microwave Conference*, Paris, France, Oct. 2005, pp. 897–900.

[31] M. J. Vaughan, K. Y. Hur, and R. C. Compton, "Improvement of microstrip patch antenna radiation patterns," *IEEE Transactions on Antennas and Propagation*, vol. 42, no. 6, pp. 882–885, Jun. 1994.

[32] G. P. Gauthier, A. Courtay, and G. M. Rebeiz, "Microstrip antennas on synthesized low dielectric-constant substrates," *IEEE Transactions on Antennas and Propagation*, vol. 45, no. 8, pp. 1310–1314, Aug. 1997.

[33] Y. Cassivi and K. Wu, "Substrate integrated circuits concept applied to the nonradiative dielectric guide," *IEE Proceedings – Microwaves, Antennas and Propagation*, vol. 152, no. 6, pp. 424–433, Sep. 2005.

[34] E. A. J. Marcatili, "Dielectric rectangular waveguide and directional coupler for integrated optics," *Bell System Technical Journal*, vol. 48, no. 7, pp. 2071–2102, Sep. 1969.

[35] W. Schlosser, "The rectangular dielectric wire {Der rechteckige dielectrische Draht (in German)}," *Archiv der Elektrischen Üebertragung*, vol. 18, no. 7, pp. 402–410, Jul. 1964.

[36] J. E. Goell, "A circular-harmonic computer analysis of rectangular dielectric waveguides," *Bell System Technical Journal*, vol. 48, no. 7, pp. 2133–2160, Sep. 1969.

[37] K. Solbach and I. Wolff, "The electromagnetic fields and the phase constants of dielectric image lines," *IEEE Transactions on Microwave Theory and Techniques*, vol. MTT-26, no. 4, pp. 266–274, Apr. 1978.

[38] K. Ogusu, "Numerical analysis of the rectangular dielectric waveguide and its modifications," *IEEE Transactions on Microwave Theory and Techniques*, vol. MTT-25, no. 11, pp. 874–885, Nov. 1977.

[39] J. Kot and T. E. Rozzi, "Rigorous modelling of single and coupled rectangular dielectric waveguide by transverse resonance diffraction," in *Proc. 14th European Microwave Conference*, Liege, Belgium, Sep. 1984, pp. 424–429.

[40] U. Rogge and R. Pregla, "Method of lines for the analysis of dielectric waveguides," *IEEE/OSA Journal of Lightwave Technology*, vol. 11, no. 12, pp. 2015–2020, Dec. 1993.

[41] J. S. Bagby, D. P. Nyquist, and B. C. Drachman, "Integral formulation for analysis of integrated dielectric waveguides," *IEEE Transactions on Microwave Theory and Techniques*, vol. MTT-33, no. 10, pp. 906–915, Oct. 1985.

[42] R. E. Collin and D. A. Ksienski, "Boundary element method for dielectric resonators and waveguides," *Radio Science*, vol. 22, no. 7, pp. 1155–1167, Dec. 1987.

[43] E. Schweig and W. B. Bridges, "Computer analysis of dielectric waveguides: a finite-difference method," *IEEE Transactions on Microwave Theory and Techniques*, vol. MTT-32, no. 5, pp. 531–541, May 1984.

[44] K. Bierwirth, N. Schulz, and F. Arndt, "Finite-difference analysis of rectangular dielectric waveguide structures," *IEEE Transactions on Microwave Theory and Techniques*, vol. MTT-34, no. 11, pp. 1104–1114, Nov. 1986.

[45] T. K. Sarkar, M. Manela, V. Narayanan, and A. R. Djordjevic, "Finite difference frequency-domain treatment of open transmission structures," *IEEE Transactions on Microwave Theory and Techniques*, vol. 38, no. 11, pp. 1609–1616, Nov. 1990.

[46] G. Mur, "Absorbing boundary conditions for the finite-difference approximation of the time-domain electromagnetic-field equations," *IEEE Transactions on Microwave Theory and Techniques*, vol. EMC-23, no. 4, pp. 377–382, Nov. 1981.

[47] D. H. Choi and W. J. R. Hoefer, "The finite difference-time domain method and its application to eigenvalue problems," *IEEE Transactions on Microwave Theory and Techniques*, vol. MTT-34, no. 12, pp. 1464–1470, Dec. 1986.

[48] V. J. Brankovic, D. V. Krupezevic, and F. Arndt, "An efficient two-dimensional graded mesh finite-difference time-domain algorithm for shielded or open waveguide structures," *IEEE Transactions on Microwave Theory and Techniques*, vol. 40, no. 12, pp. 2272–2277, Dec. 1992.

[49] P. P. Silvester, D. A. Lowther, C. J. Carpenter, and E. A. Wyatt, "Exterior finite elements for 2-dimensional field problems with open boundaries," *Proceedings of the Institution of Electrical Engineers*, vol. 124, no. 12, pp. 1267–1270, Dec. 1977.

[50] M. Ikeuchi, H. Sawami, and H. Niki, "Analysis of open-type dielectric waveguides by the finite-element iterative method," *IEEE Transactions on Microwave Theory and Techniques*, vol. MTT-29, no. 3, pp. 234–239, Mar. 1981.

[51] B. M. A. Rahman and J. B. Davies, "Finite-element analysis of optical and microwave waveguide problems," *IEEE Transactions on Microwave Theory and Techniques*, vol. MTT-32, no. 1, pp. 20–28, Jan. 1984.

[52] H. H. Chen, S. F. Yeh, Y. H. Chou, and R. C. Hsieh, "Finite-element method-method of lines approach for the analysis of three-dimensional electromagnetic cavities," *IET Microwaves, Antennas and Propagation*, vol. 1, no. 3, pp. 751–756, Jun. 2007.

[53] T. Weiland, "A discretization method for the solution of Maxwell's equations for six-component fields," *Archiv fur Elektronik und Üebertragungstechnik*, vol. 31, no. 3, pp. 116–120, Mar. 1977.

[54] Y. Cassivi, "Étude et développement de la technologie hybride circuit planaire/guide NRD dans le contexte d'un émetteur/récepteur onde millimétrique," Ph.D. dissertation, University of Montreal, École Polytechnique, Montreal, QC, Canada, 2004.

[55] M. D. Janezic and J. A. Jargon, "Complex permittivity determination from propagation constant measurements," *IEEE Microwave and Guided Wave Letters*, vol. 9, no. 2, pp. 76–78, Feb. 1999.

[56] R. E. Collin, *Field Theory of Guided Waves*, 2nd ed. New York: IEEE Press, 1991.

[57] F. Xu, A. Patrovsky, and K. Wu, "Fast simulation of periodic guided-wave structures based on commercial software," *Microwave and Optical Technology Letters*, vol. 49, no. 9, pp. 2180–2182, Sep. 2007.

[58] R. Kashyap, *Fiber Bragg Gratings*. San Diego, CA: Academic Press, 1999.

[59] R. J. Collier and R. D. Birch, "The bandwidth of image guide," *IEEE Transactions on Microwave Theory and Techniques*, vol. MTT-28, no. 8, pp. 932–935, Aug. 1980.

[60] J. D. Joannopoulos, R. D. Meade, and J. N. Winn, *Photonic Crystals – Molding the Flow of Light*. Princeton, NJ: Princeton Univ. Press, 1995.

[61] M. Loncar, T. Doll, J. Vuckovic, and A. Scherer, "Design and fabrication of silicon photonic crystal optical waveguides," *IEEE/OSA Journal of Lightwave Technology*, vol. 18, no. 10, pp. 1402–1411, Oct. 2000.

[62] H. Mosallaei and Y. Rahmat-Samii, "Photonic band-gap (PBG) versus effective refractive index: a case study of dielectric nanocavities," in *2000 IEEE Antennas and Propagation Society Int. Symposium Digest*, vol. 1, Salt Lake City, UT, USA, Jul. 2000, pp. 338–341.

[63] S. W. H. Tse and P. R. Young, "Photonic crystal non-radiative dielectric waveguide," in *2005 IEEE MTT-S Int. Microwave Symposium Digest*, Long Beach, CA, USA, Jun. 2005, pp. 1079–1081.

[64] N. Marcuvitz, *Waveguide Handbook*. New York: McGraw-Hill, 1951.

[65] G. Matthaei, E. M. T. Jones, and L. Young, *Microwave Filters, Impedance-Matching Networks, and Coupling Structures*. New York: McGraw-Hill, 1964.

[66] K. Solbach, "The fabrication of dielectric image lines using casting resins and the properties of the lines in the millimeter-wave range," *IEEE Transactions on Microwave Theory and Techniques*, vol. MTT-24, no. 11, pp. 879–881, Nov. 1976.

[67] V. V. Parshin, "Dielectric materials for gyrotron output windows," *Int. Journal of Infrared and Millimeter Waves*, vol. 15, no. 2, pp. 339–348, Feb. 1994.

[68] V. B. Braginsky, V. S. Ilchenko, and K. S. Bagdassarov, "Experimental observation of fundamental microwave absorption in high-quality dielectric crystals," *Physics Letters A*, vol. 120, no. 6, pp. 300–305, Mar. 1987.

[69] M. N. Afsar, "Precision millimeter-wave measurements of complex refractive index, complex dielectric permittivity, and loss tangent of common polymers," *IEEE Transactions on Instrumentation and Measurement*, vol. IM-36, no. 2, pp. 530–536, Jun. 1987.

[70] R. A. Woode, E. N. Ivanov, M. E. Tobar, and D. G. Blair, "Measurement of dielectric loss tangent of alumina at microwave frequencies and room temperature," *Electronics Letters*, vol. 30, no. 25, pp. 2120–2122, Aug. 1994.

[71] N. M. Alford, X. Wang, S. J. Penn, M. Poole, and A. Jones, "Effect of ceramic binders on microwave dielectric loss of alumina," *British Ceramic Transactions*, vol. 99, no. 5, pp. 212–214, 2000.

[72] J. W. Lamb, "Miscellaneous data on materials for millimetre and submillimetre optics," *Int. Journal of Infrared and Millimeter Waves*, vol. 17, no. 12, pp. 1997–2034, Dec. 1996.

[73] K. Solbach, "Electric probe measurements on dielectric image lines in the frequency range of 26-90 GHz," *IEEE Transactions on Microwave Theory and Techniques*, vol. MIT-26, no. 10, pp. 755–758, Oct. 1978.

[74] R. W. Klopfenstein, "A transmission line taper of improved design," *Proceedings of the Institute of Radio Engineers*, vol. 44, no. 1, pp. 31–35, Jan. 1956.

[75] R. P. Hecken, "A near-optimum matching section without discontinuities," *IEEE Transactions on Microwave Theory and Techniques*, vol. MTT-20, no. 11, pp. 734–739, Nov. 1972.

[76] D. D. King, "Circuit components in dielectric image lines," *IEEE Transactions on Microwave Theory and Techniques*, vol. MTT-3, no. 6, pp. 35–39, Dec. 1955.

[77] R. H. DuHamel and J. W. Duncan, "Launching efficiency of wires and slots for a dielectric rod waveguide," *IEEE Transactions on Microwave Theory and Techniques*, vol. MTT-6, no. 3, pp. 277–284, Jul. 1958.

[78] W. K. McRitchie and J. C. Beal, "Yagi-Uda array as a surface-wave launcher for dielectric image lines," *IEEE Transactions on Microwave Theory and Techniques*, vol. MTT-20, no. 8, pp. 493–496, Aug. 1972.

[79] F.-R. Yang, Y. Qian, and T. Itoh, "A novel high-Q image guide resonator using band-gap structures," in *1998 IEEE MTT-S Int. Microwave Symposium Digest*, vol. 3, Baltimore, MD, USA, Jun. 1998, pp. 1803–1806.

[80] H. Tehrani, M.-Y. Li, and K. Chang, "Broadband microstrip to dielectric image line transitions," *IEEE Microwave and Guided Wave Letters*, vol. 10, no. 10, pp. 409–411, Oct. 2000.

[81] A. Schary, G. C. Dalman, and C. A. Lee, "Dielectric waveguide-to-coplanar transmission line transitions," U.S. Patent 5 225 797, Jul., 1993.

[82] W. H. Haydl, "On the use of vias in conductor-backed coplanar circuits," *IEEE Transactions on Microwave Theory and Techniques*, vol. 50, no. 6, pp. 1571–1577, Jun. 2002.

[83] D. M. Pozar, *Microwave Engineering*, 3rd ed. Hoboken, NJ: Wiley, 2005.

[84] A. Nesic, "Slotted antenna array excited by a coplanar waveguide," *Electronics Letters*, vol. 18, no. 6, pp. 275–276, Mar. 1982.

[85] N. G. Alexopoulos, P. B. Katehi, and D. B. Rutledge, "Substrate optimization for integrated circuit antennas," *IEEE Transactions on Microwave Theory and Techniques*, vol. MTT-31, no. 7, pp. 550–557, Jul. 1983.

[86] S. P. Schlesinger and A. Vigants, "Experimental comparison of image line radiators and polyrod antennas," *IEEE Transactions on Antennas and Propagation*, vol. AP-8, no. 5, pp. 521–522, Sep. 1960.

[87] F. J. Zucker, *Antenna Engineering Handbook*, 3rd ed. New York: McGraw-Hill, 1992, ch. 12: Surface-wave antennas.

[88] S. Kobayashi, R. Mittra, and R. Lampe, "Dielectric tapered rod antennas for millimeter-wave applications," *IEEE Transactions on Antennas and Propagation*, vol. AP-30, no. 1, pp. 54–58, Jan. 1982.

[89] H. W. Ehrenspeck and H. Poehler, "A new method for obtaining maximum gain from yagi antennas," *IEEE Transactions on Antennas and Propagation*, vol. AP-7, no. 4, pp. 379–386, Oct. 1959.

[90] J. W. Duncan and R. H. DuHamel, "A technique for controlling the radiation from dielectric rod waveguides," *IEEE Transactions on Antennas and Propagation*, vol. AP-5, no. 3, pp. 284–289, Jul. 1957.

[91] H. W. Cooper, M. Hoffman, and S. Isaacson, "Image line surface wave antenna," in *Proc. IRE National Convention Record*, vol. 6, USA, 1958, pp. 230–239.

[92] G. Baumann, H. Richter, A. Baumgartner, D. Ferling, R. Heilig, D. Hollmann, H. Muller, H. Nechansky, and M. Schlechtweg, "51-GHz frontend with flip chip and wire bond interconnections from GaAs MMICs to a planar patch antenna," in *1995 IEEE MTT-S Int. Microwave Symposium Digest*, vol. 3, Orlando, FL, USA, May 1995, pp. 1639–1642.

[93] F. K. Schwering and S.-T. Peng, "Design of dielectric grating antennas for millimeter-wave applications," *IEEE Transactions on Microwave Theory and Techniques*, vol. MTT-31, no. 2, pp. 199–209, Feb. 1983.

[94] A. A. Oliner, *Antenna Engineering Handbook*, 3rd ed. New York: McGraw-Hill, 1992, ch. 10: Leaky-wave antennas.

[95] A. Hessel and T. Tamir, *Antenna Theory, Part 2*. New York: McGraw-Hill, 1969, ch. 19 and 20: General characteristics of leaky-wave antennas.

[96] S. Kobayashi, R. Lampe, R. Mittra, and S. Ray, "Dielectric rod leaky-wave antennas for millimeter-wave applications," *IEEE Transactions on Antennas and Propagation*, vol. AP-29, no. 5, pp. 822–824, Sep. 1981.

[97] W. L. Stutzman and G. A. Thiele, *Antenna Theory and Design*. New York: Wiley, 1998.

[98] T. Itoh, "Application of gratings in a dielectric waveguide for leaky-wave antennas and band-reject filters," *IEEE Transactions on Microwave Theory and Techniques*, vol. MTT-25, no. 12, pp. 1134–1138, Dec. 1977.

[99] K. Solbach and I. Wolff, "Dielectric image line groove antennas for millimeter waves. II. Experimental verification," *IEEE Transactions on Microwave Theory and Techniques*, vol. AP-33, no. 7, pp. 697–706, Jul. 1985.

[100] K. Solbach, "E-band leaky wave antenna using dielectric image line with etched radiating elements," in *1979 IEEE MTT-S Int. Microwave Symposium Digest*, Orlando, FL, USA, Apr. 1979, pp. 214–216.

[101] K. L. Klohn, R. E. Horn, H. Jacobs, and E. Freibergs, "Silicon waveguide frequency scanning linear array antenna," *IEEE Transactions on Microwave Theory and Techniques*, vol. MIT-26, no. 10, pp. 764–773, Oct. 1978.

[102] J. R. James and P. S. Hall, "Microstrip antennas and arrays, part II: New array-design technique," *IEE Journal on Microwaves, Optics and Acoustics*, vol. 1, no. 5, pp. 175–781, Sep. 1977.

[103] K. Solbach and B. Adelseck, "Dielectric image line leaky wave antenna for broadside radiation," *Electronics Letters*, vol. 19, no. 16, pp. 640–641, Aug. 1983.

[104] M. Ghomi, B. Lejay, J. L. Amalric, and H. Baudrand, "Radiation characteristics of uniform and nonuniform dielectric leaky-wave antennas," *IEEE Transactions on Antennas and Propagation*, vol. 41, no. 9, pp. 1177–1186, Sep. 1993.

[105] A. F. Perkons, Y. Qian, and T. Itoh, "TM surface-wave power combining by a planar active-lens amplifier," *IEEE Transactions on Microwave Theory and Techniques*, vol. 46, no. 6, pp. 775–783, Jun. 1998.

[106] H. F. Hammad, Y. M. M. Antar, A. P. Freundorfer, and S. F. Mahmoud, "Uniplanar CPW-fed slot launchers for efficient TM_0 surface-wave excitation," *IEEE Transactions on Microwave Theory and Techniques*, vol. 51, no. 4, pp. 1234–1240, Apr. 2003.

[107] H. F. Hammad, "A CPW-based slab beam quasi-optical power combiner at Ka-band," Ph.D. dissertation, Queen's University, Kingston, ON, Canada, 2002.

[108] G. M. Whitman, C. Pinthong, W.-Y. Chen, and F. K. Schwering, "Rigorous TE solution to the dielectric wedge antenna fed by a slab waveguide," *IEEE Transactions on Antennas and Propagation*, vol. 54, no. 1, pp. 101–114, Jan. 2006.

[109] D. H. Evans and P. J. Gibson, "A coplanar waveguide antenna for MMICs," in *Proc. 18th European Microwave Conference*, Stockholm, Sweden, Sep. 1988, pp. 312–317.

[110] A. Babakhani, X. Guan, A. Komijani, A. Natarajan, and A. Hajimiri, "A 77-GHz phased-array transceiver with on-chip antennas in silicon: receiver and antennas," *IEEE Journal of Solid-State Circuits*, vol. 41, no. 12, pp. 2795–2806, Dec. 2006.

[111] R. M. Emrick and J. L. Volakis, "Antenna requirements for short range high speed wireless systems operating at millimeter-wave frequencies," in *2006 IEEE MTT-S Int. Microwave Symposium Digest*, San Francisco, CA, USA, Jun. 2006, pp. 974–977.

[112] W. Heinrich, "The flip-chip approach for millimeter wave packaging," *IEEE Microwave Magazine*, vol. 6, no. 3, pp. 36–45, Sep. 2005.

[113] E. A. J. Marcatili, "Bends in optical dielectric guides," *Bell System Technical Journal*, vol. 48, no. 7, pp. 2103–2132, Sep. 1969.

[114] E.-G. Neumann and H.-D. Rudolph, "Radiation from bends in dielectric rod transmission lines," *IEEE Transactions on Microwave Theory and Techniques*, vol. MTT-23, no. 1, pp. 142–149, Jan. 1975.

[115] R. M. Knox, P. P. Toulios, and J. Q. Howell, "Radiation losses in curved dielectric image waveguides of rectangular cross section," in *1973 IEEE MTT-S Int. Microwave Symposium Digest*, Boulder, CO, USA, Jun. 1973, pp. 25–27.

[116] K. Solbach, "The measurement of the radiation losses in dielectric image line bends and the calculation of a minimum acceptable curvature radius," *IEEE Transactions on Microwave Theory and Techniques*, vol. MTT-27, no. 1, pp. 51–53, Jan. 1979.

[117] E.-G. Neumann and W. Richter, "Sharp bends with low losses in dielectric optical waveguides," *Applied Optics*, vol. 22, no. 7, pp. 1016–1022, Apr. 1983.

[118] C. Manolatou, S. G. Johnson, S. Fan, P. R. Villeneuve, H. A. Haus, and J. D. Joannopoulos, "High-density integrated optics," *IEEE/OSA Journal of Lightwave Technology*, vol. 17, no. 9, pp. 1682–1692, Sep. 1999.

[119] S. Lin, S. Gigoyan, J. Wilson, and A. E. Fathy, "Novel Ka-band IR controlled dielectric image guide components," in *2006 IEEE MTT-S Int. Microwave Symposium Digest*, San Francisco, CA, USA, Jun. 2006, pp. 1389–1392.

[120] K. Ogusu, "Experimental study of dielectric waveguide Y-junctions for millimeter-wave integrated circuits," *IEEE Transactions on Microwave Theory and Techniques*, vol. MTT-33, no. 6, pp. 506–509, Jun. 1985.

[121] H. Tehrani, M.-Y. Li, and K. Chang, "Planar dielectric image line antenna arrays using Y-junctions," in *2001 IEEE Antennas and Propagation Society Int. Symposium Digest*, vol. 3, Boston, MA, USA, Jul. 2001, pp. 570–573.

[122] J. Hirokawa and M. Ando, "Single-layer feed waveguide consisting of posts for plane TEM wave excitation in parallel plates," *IEEE Transactions on Antennas and Propagation*, vol. 46, no. 5, pp. 625–630, May 1998.

[123] C. Warns, W. Menzel, and H. Schumacher, "Transmission lines and passive elements for multilayer coplanar circuits on silicon," *IEEE Transactions on Microwave Theory and Techniques*, vol. 46, no. 5, pp. 616–622, May 1998.

[124] R. E. Collin, *Field Theory of Guided Waves*, 2nd ed. New York: McGraw-Hill, 1992.

[125] M. Zedler, C. Caloz, and P. Russer, "Circuital and experimental demonstration of a 3D isotropic LH metamaterial based on the rotated TLM scheme," in *2007 IEEE MTT-S Int. Microwave Symposium Digest*, Honolulu, HI, USA, Jun. 2007, pp. 1827–1830.

[126] D. Deslandes and K. Wu, "Integrated transition of coplanar to rectangular waveguides," in *2001 IEEE MTT-S Int. Microwave Symposium Digest*, vol. 2, Phoenix, AZ, USA, May 2001, pp. 619–622.

[127] ——, "Analysis and design of current probe transition from grounded coplanar to substrate integrated rectangular waveguides," *IEEE Transactions on Microwave Theory and Techniques*, vol. 53, no. 8, pp. 2487–2494, Aug. 2005.

[128] S. Yamamoto, J. Hirokawa, and M. Ando, "A beam switching slot array with a 4-way Butler matrix installed in a single layer post-wall waveguide," in *2002 IEEE Antennas and Propagation Society Int. Symposium Digest*, vol. 1, San Antonio, TX, USA, Jun. 2002, pp. 138–141.

[129] X. Xu, R. G. Bosisio, and K. Wu, "A new six-port junction based on substrate integrated waveguide technology," *IEEE Transactions on Microwave Theory and Techniques*, vol. 53, no. 7, pp. 2267–2273, Jul. 2005.

[130] E. Moldovan, R. G. Bosisio, and K. Wu, "W-band multiport substrate-integrated waveguide circuits," *IEEE Transactions on Microwave Theory and Techniques*, vol. 54, no. 2, pp. 625–632, Feb. 2006.

[131] G. Leuzzi, A. Silbermann, and R. Sorrentino, "Mode propagation in laterally bounded conductor-backed coplanar waveguides," in *1983 IEEE MTT-S Int. Microwave Symposium Digest*, Boston, MA, USA, Jun. 1983, pp. 393–395.

[132] R. N. Simons, G. E. Ponchak, K. S. Martzaklis, and R. R. Romanofsky, "Channelized coplanar waveguide: discontinuities, junctions, and propagation characteristics," in *1989 IEEE MTT-S Int. Microwave Symposium Digest*, Long Beach, CA, USA, Jun. 1989, pp. 915–918.

[133] K. Wu, R. L. Vahldieck, J. L. Fikart, and H. Minkus, "The influence of finite conductor thickness and conductivity on fundamental and higher-order modes in miniature hybrid mic's (mhmic's) and mmic's," *IEEE Transactions on Microwave Theory and Techniques*, vol. 41, no. 3, pp. 421–430, Mar. 1993.

[134] K. Wu, Y. Xu, and R. G. Bosisio, "Theoretical and experimental analysis of channelized coplanar waveguides (CCPW) for wideband applications of integrated microwave and millimeter-wave circuits," *IEEE Transactions on Microwave Theory and Techniques*, vol. 42, no. 9, pp. 1651–1659, Sep. 1994.

[135] N. K. Das, "Methods of suppression or avoidance of parallel-plate power leakage from conductor-backed transmission lines," *IEEE Transactions on Microwave Theory and Techniques*, vol. 44, no. 2, pp. 169–181, Feb. 1996.

[136] D. Deslandes and K. Wu, "Accurate modeling, wave mechanisms, and design considerations of a substrate integrated waveguide," *IEEE Transactions on Microwave Theory and Techniques*, vol. 54, no. 6, pp. 2516–2526, Jun. 2006.

[137] P. K. Ikalainen and G. L. Matthaei, "Wide-band, forward-coupling microstrip hybrids with high directivity," *IEEE Transactions on Microwave Theory and Techniques*, vol. MTT-35, no. 8, pp. 719–725, Aug. 1987.

[138] S. A. Schelkunoff, "Conversion of maxwell's equations into generalized telegraphist's equations," *Bell System Technical Journal*, vol. 34, no. 5, pp. 995–1043, Sep. 1955.

[139] S. E. Miller, "Coupled wave theory and waveguide applications," *Bell System Technical Journal*, vol. 33, pp. 661–719, May 1954.

[140] P. K. Ikalainen and G. L. Matthaei, "Design of broad-band dielectric waveguide 3-dB couplers," *IEEE Transactions on Microwave Theory and Techniques*, vol. MTT-35, no. 7, pp. 621–628, Jul. 1987.

[141] W. H. Louisell, "Analysis of the single tapered mode coupler," *Bell System Technical Journal*, vol. 34, no. 4, pp. 853–870, Jul. 1955.

[142] F. Sporleder and H.-G. Unger, *Waveguide Tapers, Transitions, and Couplers*. London, UK: IEE Press, 1979.

[143] F. P. Casares-Miranda, C. Camacho-Penalosa, and C. Caloz, "High-gain active composite right/left-handed leaky-wave antenna," *IEEE Transactions on Antennas and Propagation*, vol. 54, no. 8, pp. 2292–2300, Aug. 2006.

[144] E. Mortazy, J. Yao, X. Zhang, R. Kashyap, and K. Wu, "Substrate integrated optoelectronic devices for radio over fiber applications," in *Proc. Int. Symposium on Signals, Systems and Electronics (ISSSE '07)*, Montreal, QC, Canada, Jul. 2007, pp. 467–470.

[145] K. Wu, D. Deslandes, and Y. Cassivi, "The substrate integrated circuits - a new concept for high-frequency electronics and optoelectronics," in *Proc. 6th Int. Conference on Telecommunications in Modern Satellite, Cable and Broadcasting Services. (TELSIKS 2003)*, vol. 1, Nis, Yugoslavia, Oct. 2003, pp. III–X.

[146] J. Laskar, S. Pinel, D. Dawn, S. Sarkar, B. Perumana, and P. Sen, "The next wireless wave is a millimeter wave," *Microwave Journal*, vol. 50, no. 8, pp. 22–32, Aug. 2007.

[147] D. Razavi, "Gadgets gab at 60 GHz," *IEEE Spectrum*, vol. 45, no. 2, pp. 46–58, Feb. 2008.

APPENDIX I

PUBLICATIONS RESULTING FROM THIS RESEARCH WORK

I.1 Peer-reviewed journal publications

- A. Patrovsky, M. Daigle, and K. Wu, "Coupling mechanism in hybrid SIW-CPW forward couplers for millimeter wave substrate integrated circuits," *IEEE Transactions on Microwave Theory and Techniques*, submitted for publication.
- A. Patrovsky and K. Wu, "Substrate integrated image guide array antenna for the upper millimeter-wave spectrum," *IEEE Transactions on Antennas and Propagation*, vol. 55, pp. 2994-3001, Nov. 2007.
- F. Xu, A. Patrovsky and K. Wu, "Fast simulation of periodic guided-wave structures based on commercial software," *Microwave and Optical Technology Letters*, vol. 49, pp. 2180-2182, Sept. 2007.
- A. Patrovsky and K. Wu, "94-GHz planar dielectric rod antenna with substrate integrated image guide (SIIG) feeding," *IEEE Antennas and Wireless Propagation Letters*, vol. 5, pp. 435-437, Dec. 2006.
- A. Patrovsky and K. Wu, "Substrate integrated image guide (SIIG)-A planar dielectric waveguide technology for millimeter-wave applications," *IEEE Transactions on Microwave Theory and Techniques*, vol. 54, pp. 2872-2879, June 2006.

I.2 Conference papers

- A. Patrovsky, M. Daigle, and K. Wu, "Millimeter-wave wideband transition from CPW to substrate integrated waveguide on electrically thick high-permittivity substrates," in *Proceedings of the 37th European Microwave Conference*, Munich, Germany, Oct. 8-12, 2007, pp. 138-141.
- A. Patrovsky and K. Wu, "94-GHz broadband transition from coplanar waveguide to substrate integrated image guide (SIIG)," in *IEEE MTT-S International Microwave Symposium Digest*, Honolulu, Hawai'i, USA, June 3-8, 2007, pp. 1551-1554.

- A. Patrovsky and K. Wu, "Substrate integrated circuits (SICs)—Providing a low-cost and low-loss approach for millimeter-wave circuit and system integration (invited paper)," in *Proceedings of the 8th MINT Millimeter-Wave Int. Symp. and 9th Topical Symp. on Millimeter Waves*, Seoul, Korea, February 26-27, 2007, pp. 9-14.

- A. Patrovsky and K. Wu, "Substrate integrated image guide (SIIG)—A low-loss waveguide for millimetre-wave applications," in *Proceedings of the 35th European Microwave Conference*, Paris, France, Oct. 4-6, 2005, pp. 897-900.

I.3 **Patents**

- A. Patrovsky and K. Wu, "Compact dielectric slab-mode antenna," *international patent application* # PCT/CA2007/001973, Nov. 2007.